UNIVERSITAT JAUME·I

"Advanced Semiconductors for Photo-electrocatalytic Solar Fuel Production"

Drialys Cárdenas Morcoso

Director
Dr. Sixto Giménez Juliá

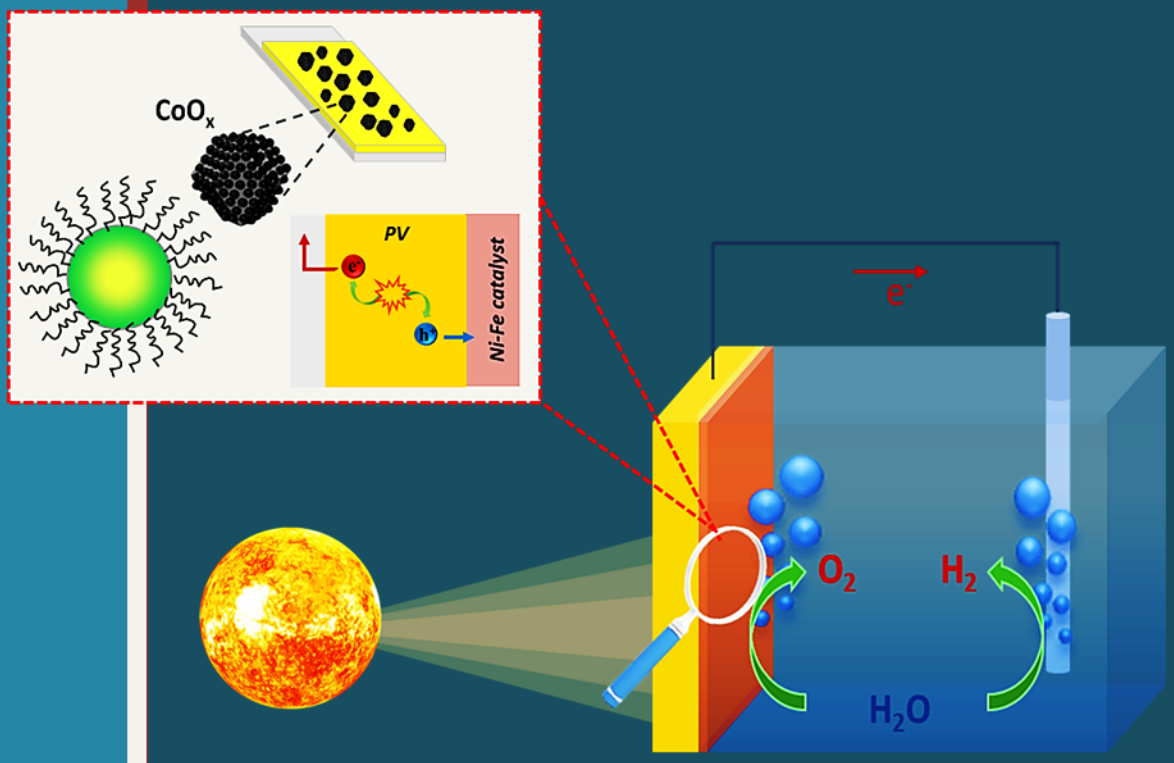

Doctoral Thesis
June, 2020

UNIVERSITAT JAUME I

Doctoral Programme in Sciences

Doctoral School of the Universitat Jaume I

"Advanced semiconductors for photo-electrocatalytic solar fuel production"

Report submitted by Drialys Cárdenas Morcoso in order to be eligible for a doctoral degree awarded by the Universitat Jaume I.

Drialys Cárdenas Morcoso
Ph. D. Candidate

Dr. Sixto Giménez Juliá
Director

Castelló de la Plana, June 2020

Funding

The present doctoral thesis was carried out thanks to the financial support from the following sources:

- Grant: Santiago Grisolia Program, Generalitat Valenciana, reference 2015-031.

- Project: "Sistemas cuánticos para el desarrollo de dispositivos optoelectrónicos" (Q-Devices), Generalitat Valenciana, reference Prometeo/2018/098.

- Project: "An Artificial Leaf: a photo-electrocatalytic cell from earth-abundant materials for sustainable solar production of CO_2-based chemicals and fuels" (A-LEAF), European Union Horizon 2020, reference 732840.

Acknowledgments

En primer lugar, quisiera expresar mi agradecimiento a mi director, el Dr. Sixto Giménez Juliá. Gracias por darme la oportunidad de incorporarme a su equipo, por la confianza depositada en mí y por toda la atención recibida para la realización de esta tesis doctoral y, en general, toda la preocupación por mi trabajo durante este tiempo. Sin duda alguna, estos cinco años han sido un largo trayecto de crecimiento profesional y personal, en el cual su guía y apoyo en ambos aspectos han sido imprescindibles para mí.

Quiero expresar mi gratitud hacia el director del INAM, el Prof. Juan Bisquert, así como a sus miembros, por la acogida y toda la atención recibida durante mi estancia en el instituto. Mi agradecimiento a aquellos que de forma directa han contribuido en los trabajos realizados en esta tesis. Al Dr. Miguel García Tecedor, por toda la ayuda en cuestiones experimentales, discusión de resultados y revisiones en los manuscritos; así como todo el apoyo y valiosos consejos profesionales y personales compartidos. A mis compañeros Sandheep Ravishankar y Agustín Bou Catalán, por la colaboración en aspectos teóricos.

Al Prof. Iván Mora Seró y los miembros del grupo GAS, por la oportunidad de explorar el fascinante mundo de los puntos cuánticos de perovskita. Mi especial agradecimiento a Andrés Fabián Guadrón Reyes, Seog Joon Yoon, Ana Beatriz Vitorretti y Mauricio Solís de la Fuente, por la maravillosa colaboración realizada.

La consecución de esta tesis también es resultado de importantes colaboraciones con grupos e instituciones externos, a los cuales también quiero transmitir mi agradecimiento.

I want to express my gratitude to our colleagues from the Department of Chemistry, Ilse Katz Institute for Nanoscale Science and Technology, at the Ben-Gurion University of the Negev. To Prof. Idan Hod, as well as Raya Ifraemov and Itamar Liberman, for the nice collaboration about the metal-organic-frameworks.

To the colleagues from the IEK-5 Photovoltaik, at Forschungszentrum Jülich, for the opportunity to do my research stay at their labs. My sincerely gratitude to Dr. Tsvetelina Merdzhanova and Dr. Vladimir Smirnov, for the welcome they gave me, and all their support and help received during my stay. To Prof. Friedhelm Finger for all the good advices, and to all the member of IEK-5 that assisted and supported me with the solar cells and samples preparation, and in general, in the work at the labs.

I would also like to thanks to Professors Bernhard Kaiser and Wolfram Jaegermann, from the Institute of Materials Science, at TU Darmstadt, for the opportunity to perform the XPS experiment at the DAISY-FUN installations. Many thanks to Paula and Céline, for all the help at the labs and with the experiments' discussion.

Mi agradecimiento al personal técnico de los Servicios Centrales de Instrumentación Científica de la UJI, por el apoyo para la realización de los análisis estructurales y morfológicos, en especial a José Javier Gómez, María del Carmen (Maruxa) Peiró, José Miguel Pedra y Gabriel Peris. Mi agradecimiento también a la Dra. Encarna Blasco, del Instituto de Tecnología Cerámica de la UJI, por el apoyo para los análisis de XPS.

Quiero agradecer al Prof. Francisco Fabregat, por su gran ayuda en cuestiones de impedancia. A Franziska e Issac, por el placer que ha sido haber trabajado juntos y por todo lo aprendido en el laboratorio gracias a ustedes.

Al personal de administración del INAM, especialmente a Loles Merchan, por todo el apoyo y la ayuda inestimables que me ha brindado todo este tiempo.

A mis compañeros/as de Centralita, Marta, Roser, Nuria y Ramón, con los que he tenido el placer de compartir mi día a día. A Eva, por cada consejo. Gracias por tantos momentos de risas, de Rossegó y Círculo. Por ser más que compañeros/as, por ser amigas y amigo

para toda la vida. A Bea, Sandra y Elena, gracias por todo el apoyo y cariño que me han brindado, junto a Eva y Loles, han sido como mamis para mí.

A mi querida amiga Marisé, que llegó como un rayito de luz a aportarme alegrías y fuerzas. Gracias por la complicidad, la paciencia y, sobre todo, por todo el cariño. A Fabi, por todas las atenciones; tenerlos a ambos ha sido para mí tener la familia cerca.

Agradezco también el apoyo y el cariño recibido por los amigos surgidos durante mi estancia aquí en Castellón, a los cuales considero mi familia española. A Claudia, por la amistad tan linda y sincera, siempre tan atenta y llena de detalles tan bonitos. A Irene, Marc, Elisa y Edurne, gracias por acogerme y hacerme sentir en Castellón como si hubiese sido siempre de aquí. A Nacho, Rubén y María, mis compis de piso, por tan lindos momentos de convivencia compartidos.

A mis amigas de siempre, Mariela, Geyla, Mariam y Adriana. No importa cuán lejos estemos físicamente, siempre están cerca.

Quiero agradecer a mi familia en Cuba. En especial a mis tíos Roberto y Beatriz y mis primas Claudia y Melany, por todo su apoyo, preocupación y ánimos siempre oportunos.

Y, por último, mi más eterno agradecimiento a mis padres, Cristina y Rafael, y mi abuela Pilar, que a pesar de la distancia consiguen estar siempre cerca de mí cuando más los necesito. A ellos les agradezco lo que soy y todo lo que he alcanzado, que ha sido gracias su apoyo e invaluables esfuerzos y sacrificios para que yo saliera adelante. A ellos he dedicado siempre cada meta conseguida, y para ellos es también esta tesis.

A mis padres, Cristina y Rafael, y a mi abuela Pilar.

A mis abuelos Emilia y Rafael, siempre presentes.

Resumen

Hoy en día, uno de los grandes retos que enfrentan la ciencia y la tecnología es el desarrollo de fuentes de energía alternativas a los combustibles fósiles. Este contexto motiva al desarrollo y utilización de fuentes de energías limpias, sostenibles y seguras, con el fin de sustituir el uso de combustibles fósiles y a la vez, minimizar el impacto medioambiental. La energía solar, un recurso abundante y benigno desde el punto de vista medioambiental, es considerada como la única alternativa viable a las actuales fuentes energéticas. Por otra parte, la energía solar puede convertirse y almacenarse en forma de energía química en enlaces moleculares, mimetizando el proceso de la fotosíntesis natural. Dicho proceso puede ser adaptado para la producción de hidrógeno, que posteriormente puede utilizarse como combustible, o para la síntesis de productos con alto interés industrial. Las estrategias más destacadas para este fin son: la fotocatálisis, la electrocatálisis asistida con dispositivos fotovoltaicos y las celdas fotoelectroquímicas. En todas ellas se requieren materiales semiconductores que puedan absorber y transformar la energía solar en portadores de cargas. Sin embargo, muchos de los materiales investigados sufren de importantes desventajas que limitan su aprovechamiento y, por tanto, su implementación tecnológica. Por lo tanto, la principal motivación de esta tesis doctoral consistió en el estudio de materiales semiconductores para la mejora de la eficiencia del proceso de obtención de combustibles solares. Para ello se abordaron diferentes estrategias, que abarcan: la implementación de co-catalizadores a partir de marcos-metal-orgánicos en fotoánodos para la oxidación de agua fotoelectroquímica; la integración de electrocatalizadores de oxidación de agua y dispositivos fotovoltaicos basados en materiales abundantes; y la evaluación de nuevos materiales con potencial aplicación en procesos foto-electrocatalíticos.

En particular, la producción de hidrógeno a partir de agua requiere la ruptura de esta molécula, en cuyo proceso el paso limitante tanto cinética- como termodinámicamente, es la semirreacción de oxidación. De ahí que, es de alto interés estudiar materiales y estrategias que permitan mejorar la cinética de dicha reacción. Entre los materiales investigados, el $BiVO_4$ se ha destacado como un candidato muy atractivo por sus propiedades ópticas para la oxidación fotoelectroquímica de agua. Sin embargo, este semiconductor presenta limitaciones intrínsecas que obstaculizan su implementación práctica. De ahí que sea necesario el uso de co-catalizadores para mejorar su desempeño. Por otra parte, los marcos-metal-orgánico, y los compuestos derivados de ellos, han demostrado tener relevantes aplicaciones catalíticas. Por tanto, en esta tesis se abordó el empleo del CoO_x derivado del marco-metal-orgánico ZIF-67, como co-catalizador en la superficie del $BiVO_4$. Esta estrategia conllevó a una mejora significativa desempeño del fotoánodo, para un aumento de alrededor de cuatro veces la fotocorriente del $BiVO_4$ sin modificar. Además, estudios de mecanismos sugirieron que el papel del CoO_x es verdaderamente catalítico, a diferencia de otros materiales que suelen actuar como pasivadores de estados superficiales.

Precisamente, la comprensión de los mecanismos de operación y limitaciones de los materiales semiconductores empleados como fotoelectrodos, es fundamental para la implementación de estrategias para su mejora. Para ello, es frecuente utilizar técnicas basadas en pequeñas perturbaciones del potencial, la corriente o la luz incidente, cuya interpretación es de gran complejidad, y está sujeta a modelos teóricos. Como parte de esta tesis se abordó el estudio de un efecto observado en medidas de espectroscopia de fotocorriente modulada (IMPS) incidente en fotoánodos de $BiVO_4$, relacionado con el cambio de signo de la función de transferencia. A partir de este estudio de demostró

experimentalmente que dicho efecto está asociado con la derivada de la fotocorriente en función de la intensidad de fotones incidentes. A partir de esta interpretación, se ha establecido las medidas de las curvas 'fotocorriente vs intensidad de la luz incidente' como una nueva fuente de información relevante sobre los mecanismos de operación de los fotoelectrodos.

A pesar de las mejoras conseguidas en materiales empleados como fotoánodo en celdas fotoelectroquímicas, esta estrategia aún está lejos de la implementación tecnológica, debido a las bajas eficiencias reportadas. Sin embargo, la integración de electrocatalizadores para la oxidación de agua con dispositivos fotovoltaicos, basados en materiales abundantes y de bajo coste ofrece una estrategia tecno-económicamente viable. En consecuencia, se consiguió desarrollar un dispositivo compuesto por la combinación de las fases NiO, α-Fe_2O_3 and $NiFe_2O_4$ en el componente electrocatalizador, y una celda solar basada en películas finas de silicio, que actúa como fotoánodo. Con este dispositivo se consiguió un 7.7% de eficiencia de conversión solar-a-hidrogeno, competitiva con aquellas reportadas en dispositivos y materiales similares. Estos resultados representan un gran paso de avance hacia el desarrollo de dispositivos para conseguir la "fotosíntesis artificial", sustituyendo los costosos materiales que actualmente se utilizan.

Finalmente, debido a la importancia del reconocimiento y aplicación de nuevos materiales en estrategias de conversión de energía solar a química, se abordó el estudio de los puntos cuánticos de perovskita en aplicaciones fotocatalíticas y fotoelectroquímicas. Por la novedad del sistema, en primer lugar, se establecieron las condiciones para la realización de medidas con la adecuada estabilidad. Posteriormente, se determinó la alineación de bandas de puntos cuánticos con diferentes composiciones ($CsPb_{1-x'}Sn_{x'}X_3$; X = Br, I o $Br_{0.5}I_{0.5}$) a través de técnicas electroquímicas y espectroscópicas, lo que permitió evaluar su potencial para conducir una determinada reacción química. Como prueba de concepto, se estudió la degradación fotocatalítica y fotoelectroquímica de un contaminante orgánico (2-mercaptobenzotiazol) con puntos cuánticos de la perovskita $CsPbBr_3$, demostrando la viabilidad de estos sistemas en aplicaciones foto-electrocatalíticas. En efecto, la futura aplicación de esta metodología abre perspectivas prometedoras en el estudio de nuevos materiales con potencial aplicación en estrategias de conversión y almacenamiento de la energía solar

Style of the Thesis

This thesis is written as a journal article compilation style, and includes eight chapters organized as follows:

Chapter 1 provides a background on the state-of-the-art on solar energy conversion and storage, with particular emphasis on photoelectrochemical and photocatalytic applications. Therefore, the different strategies for solar to chemical energy conversion are discussed, and particular focus on the semiconductor materials used as photoelectrodes is given, highlighting the recent advances and current challenges.

Chapter 2 offers a broad description of the synthesis and deposition routes used to prepared the materials investigated; as well as a detailed view of the structural, optical and (photo-) electrochemical characterization methods employed during the development of this thesis.

In *Chapter 3*, the goals of this thesis and the strategies proposed to achieve them are presented. Also, a critical overview of the works included is provided, together with the significance of the contributions made as result of the developed research.

Chapters 4-7 collects the author's version manuscripts of the publications included in this thesis. Details on the candidate contribution in each manuscript are also provided.

Finally, *Chapter 8* offers the general conclusions of the obtained results, highlighting their relevance in the actual context. Finally, the outlook for futures advances on the developed activities of this thesis is given.

List of Publications Included in the Thesis

1. Cardenas-Morcoso, D.; Ifraemov, R.; García-Tecedor, M.; Liberman, I.; Giménez, S.; Hod, I. "A metal-organic framework converted catalyst that boosts photo-electrochemical water splitting". *Journal of Materials Chemistry A*, **2019**, 7, 11143-11149. DOI: 10.1039/c9ta01559k. *Impact factor: 10.733.*

2. Cardenas-Morcoso, D.; Bou, A.; Ravishankar, S.; Garcia-Tecedor, M.; Giménez, S.; Bisquert, J. "Intensity-Modulated Photocurrent Spectroscopy for Solar Energy Conversion Devices: What Does a Negative Value Mean?". *ACS Energy Letters*, **2020**, 5, 187-191. DOI: 10.1021/acsenergylett.9b02555. *Impact factor: 16.331.*

3. Cardenas-Morcoso, D.; García Tecedor, M; Merdzhanova, T.; Smirnov, T.; Finger, F.; Kaiser, B.; Jaegermann, W; Gimenéz, S. "An Integrated Photoanode Based on Non-Critical Raw Materials for Robust Solar Water Splitting". *Submitted.*

4. Cardenas-Morcoso, D.; Gualdrón-Reyes, A.Fabián; Vitoreti, A.Beatriz Fe; Garcia-Tecedor, M.; Yoon, S.Joon; de la Fuente, M.Solis; Mora-Seró, I.; Giménez, S. "Photocatalytic and photoelectrochemical degradation of organic compounds with all-inorganic metal halide perovskite quantum dots." *The Journal of Physical Chemistry Letters*, **2019**, 10, 630-636. DOI: 10.1021/acs.jpclett.8b03849. *Impact factor: 7.329.*

This thesis has been accepted by the co-authors of the publications listed above that have waived the right to present them as part of another Ph.D. thesis.

List of Publications not Included in the Thesis

1. Lemsi, A.; Cardenas-Morcoso, D.; Haro, M.; Gil-Barrachina, C.; Aranda, C.; Maghraoui-Meherzi, H.; García-Tecedor, M.; Giménez, S.; Julián-López, B. "PbS Nanocubes for Solar Energy Storage". *Energy Technology*, **2020**. *In press*

2. Shaddad, M.*; Cardenas-Morcoso, D.*; García-Tecedor, M.l; Fabregat-Santiago, F.; Bisquert, J.; Al Mayouf, A.; Gimenez, S. "TiO_2 nanotubes for solar water splitting: vacuum annealing and Zr doping enhance water oxidation kinetics." *ACS Omega,* **2019**, 4, 16095−16102.

3. Liu, Kai; Ma, M.; Wu, Longfei; Valenti, M.; Cardenas-Morcoso, D.; et ál. "Electronic effects determine the selectivity of planar Au-Cu bimetallic thin films for electrochemical CO_2. reduction". *ACS Applied Materials & Interfaces*, **2019**, 8,11, 16546-16555.

4. García-Tecedor, M.*; Cardenas-Morcoso, D.*; Fernadez-Climent, R.; Gimenez, S. "The role of underlayers and overlayers in thin film $BIVO_4$ photoanodes for solar water splitting." *Advanced Materials Interfaces*, **2019,** 1900299, 1-8.

5. Perez-Rodriguez, P.; Cardenas-Morcoso, D.; Digdaya, I.A.; Raventos, A.Mangel; Procel, P.; Isabella, O.; Giménez, S.; Zeman, M.; Smith, W.A.; Smets, A.H.M. "Improving the back surface field on an amorphous silicon carbide thin-film photocathode for solar water splitting." *ChemSusChem*, **2018**, 11, 1797– 1804.

6. Shaddad, M.N.*; Cardenas-Morcoso, D.*; Arunachalam, P.; Garcia-Tecedor, M.; Ghanem, M.A.; Bisquert, J.; Al-Mayouf, A.; Giménez, S. "Enhancing the optical absorption and interfacial properties of $BiVO_4$ with Ag_3PO_4 nanoparticles for efficient water splitting." *The Journal of Physical Chemistry C*, **2018**, 122 (22), 11608–11615

7. Hegner, F. S.; Herraiz-Cardona, I.; Cardenas-Morcoso, D.; López, N.; Galan-Mascaros, J. R.; Giménez, S. "Cobalt hexacyanoferrate on $BiVO_4$ photoanodes for robust water splitting". *ACS Applied Materials & Interfaces* **2017** 9 (43), 37671-37681

8. Hegner, F. S.; Cardenas-Morcoso, D.; Giménez, S.; López, N.; Galan-Mascaros, J. R. "Level alignment as descriptor for semiconductor/catalyst systems in water splitting: The case of hematite/cobalt hexacyanoferrate photoanodes". *ChemSusChem* **2017**, 10, 4552.

9. Safshekan, S.; Herraiz-Cardona, I.; Cardenas-Morcoso, D.; Ojani, R.; Haro, M.; Gimenez, S., "Solar energy storage by a heterostructured $BiVO_4$-PbOx photocapacitive device." *ACS Energy Letters* **2017**, 2 (2), 469-475

10. Cardenas-Morcoso, D.; Peiro-Franch, A.; Herraiz-Cardona, I.; Gimenez, S., "Chromium doped copper vanadate photoanodes for water splitting." *Catalysis Today*. **2017**, 290, 65-72.

*Both authors have equally contributed.

Appendix

List of acronyms, abbreviations and symbols.

APCE	Absorbed Photon-to-Current Efficiency
AQY	Apparent Quantum Yield
AZO	Aluminium-doped Zinc Oxide
CE	Counter Electrode
Co-Fe PB	Cobalt hexacyanoferrate
Co-Pi	Cobalt phosphate
CV	Cyclic Voltammetry
CVD	Chemical Vapor Deposition
DFT	Density Functional Theory
DMSO	Dimethyl sulphoxide
DOS	Density Of States
EC	Electrocatalyst
ECM	Equivalent Circuit Model
EDS	Energy Dispersion X-Ray Spectroscopy
EQE	External Quantum Efficiency
FE	Faradaic Efficiency
FTO	Fluorine-doped Tin Oxide
GC	Gas Chromatography
HER	Hydrogen Evolution Reaction
IMPS	Incident Modulated Photocurrent Spectroscopy
IMVS	Incident Modulated Photovoltage Spectroscopy
IPCE	Incident Photon-to-Current Efficiency
IQE	Internal Quantum Efficiency
IS	Impedance Spectroscopy
ITO	Indium-doped Tin Oxide
LSV	Linear Sweep Voltammetry
NHE	Normal Hydrogen Electrode
OCP	Open Circuit Potential

OER	Oxygen Evolution Reaction
PB	Prussian Blue
PC	Photocatalytic
PEC	Photoelectrochemical
PECVD	Plasma Enhanced Chemical Vapor Deposition
PIAS	Photo-Induced Absorption Spectroscopy
PL	Photoluminescence
PLQY	Photoluminescence Quantum Yield
PSC	Perovskite solar cell
PV	Photovoltaic
PV–EC	Integrated Photovoltaic-Electrocatalyst device
QD	Quantum dots.
QY	Quantum Yield
RE	Reference Electrode
RHE	Reversible Hydrogen Electrode
SAED	Selected Area Electron Diffraction
SCLJ	Semiconductor-Liquid Junction
SCR	Space Charge Region or depletion zone
SEC	Spectro-Electrochemistry
SECM	Scanning Electrochemical Microscopy
SEM	Scanning Electron Microscopy
STH	Solar-To-Hydrogen conversion
TAS	Transient Absorption Spectroscopy.
TCO	Transparent Conductive Oxide
TEM	Transmission Electron Microscopy
TRPL	Time-Resolved Photoluminescence Spectroscopy
UPS	Ultraviolet Photoelectron Spectroscopy
UV	Ultraviolet
WE	Working Electrode
XPS	X-Ray Photoelectron Spectroscopy
A	Absorbance

C	Capacitance
$E°$	Standard potential
G	Charge generation upon illumination
R	Reflectance
T	Transmittance
V	Applied potential
W	Width of the depletion zone
ct	Charge transfer
$j-V$	Current-Voltage characteristic
n	Electron density
p	Hole density
rec	Charge recombination
t	Time
tr	Charge transport
C_{SC}	Space Charge Capacitance
$E_B; BE$	Binding energy
$E_{F,n}$	Quasi-Fermi level for electrons
$E_{F,p}$	Quasi-Fermi level for holes
E_F	Fermi level energy
E_K	Kinetic energy
E_{cb}	Conduction band edge
E_g	Band gap energy
E_{redox}	Redox potential of the electrolyte
E_{vb}	Valence band edge
H_L	Helmholtz's layer
$h\nu$	Photon energy
j_G	Ideal photocurrent density
j_{abs}	Theoretical maximum photocurrent
j_{dark}	Dart current density
j_e	Photocurrent density
j_ϕ	Incident photons current density

L_{min}	Minority carrier diffusion length
N_C	Effective density of states in the conduction band
N_D	Doping density
N_V	Effective density of states in the valence band
R_{ct}	Charge transfer resistance
R_s	Series resistance
R_{tr}	Charge transport resistance
V_{fb}	Flat band potential
$\Delta\phi_{SC}$	Potential drop across the space charge region
ΔV_{ph}	Photovoltage
u_{min}	Minority carrier mobility
α	Absorption coefficient
Φ	Incident light power
ε_r	Relative permittivity
η_{e^-/h^+}	Absorptance
η_{cat}	Charge injection efficiency
η_{cs}	Charge separation efficiency
η_{ox}	Overpotential for the oxidation reaction
η_{red}	Overpotential for the reduction reaction
μ_i	Chemical potential
μ_i^0	Standard chemical potential
$\bar{\mu}_i$	Electrochemical potential
τ_{min}	Minority carrier lifetime
ϕ	Work function

List of physical constants

h	Plank's constant	$6.626 \times 10^{-34}\ kg\ m^2 s^{-1}$
q	Elementary charge	$1.602 \times 10^{-19}\ C$
k_B	Boltzmann's constant	$1.38064 \times 10^{-23}\ J\ K^{-1}$
ε_0	Permittivity in vacuum	$8.85418 \times 10^{-12}\ F\ m^{-1}$
R	Ideal gas constant	$8.3144\ J\ (mol \cdot K)^{-1}$
F	Faraday's constant	$96485\ C\ mol^{-1}$

Table of Content

Chapter 1: Introduction

Outline

This chapter aims to provide a broad description of the state-of-the-art of the main strategies for solar energy conversion and storage into chemical energy through water splitting. The considered approaches are: particulate photocatalysis (PC), integrated photovoltaic-electrocatalyst devices (PV–EC), and photoelectrochemical (PEC) cells. Especial attention to both the functional and techno-economical aspects toward the practical implementation of each approach will be given. In all these configurations, the fundamental component, –and consequently the backbone of this doctoral thesis– is the semiconductor material acting as photo-absorber. Hence, a section will be devoted to defining important concepts regarding the physics and electrochemistry of the semiconductor materials. In addition, the requirements that the semiconductor materials must fulfill for efficient solar-assisted fuel production, as well as relevant strategies for improved performance, will be discussed. An especial attention to $BiVO_4$ was given, as a promising candidate as photoanode for photoelectrochemical (PEC) water splitting. Moreover, since integrated PV–EC devices offer a more techno-economically achievable approach to PEC cells, the recent advances in the individual components, with special emphasis on thin-film Si technology and Earth-abundant electrocatalyst, are presented. Finally, and motivated by the interest to search for novel and potential semiconductor materials for solar fuel production, the outstanding optoelectronic properties of all-inorganic perovskites QDs, and the recent progress in photo-electrocatalytic applications, will be discussed.

1.1. Motivation for the development of solar energy-based systems.

"If our black and nervous civilization, based on coal, shall be followed by a quieter civilization based on the utilization of solar energy, that will not be harmful to progress and to human happiness."

-G. Ciamician, 1912

The up-growing world population and economy demand an incremental energy consumption, which nowadays primarily relies on fossil fuels, with the subsequent environmental degradation. According to the latest *BP Statistical Review of World Energy, 2019*, the global primary energy consumption has grown during the last year at a rate of 2.9%, which almost doubles the 10-year average of 1.5 % per year and it is the fastest since 2010. As a consequence, carbon emissions grew by 2.0 %, rising at the highest rate for seven years.[1] Moreover, the *U.S. Energy Information Administration* (EIA) predicts an increase of nearly 50 % of world energy consumption between 2018 and 2050. The industrial sector, which includes refining, mining, manufacturing and construction, accounts for the largest share of the energy consumption of any end-use sector, more than half of end-use energy consumption throughout the foreseen period.[2]

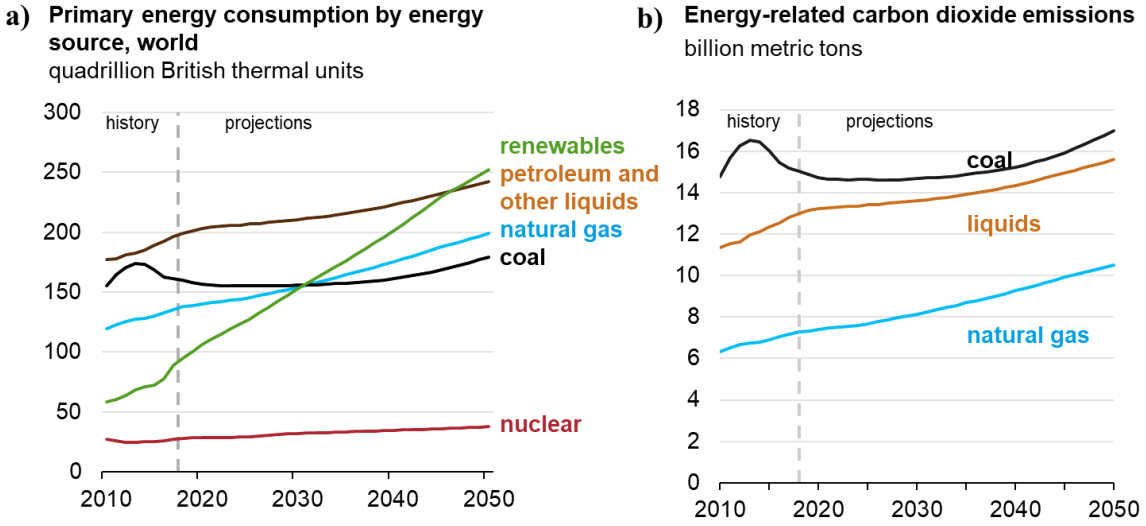

Figure 1.1. a) Projections for world energy consumption and **b)** CO_2 emissions by energy source. Adapted from the *International Energy Outlook 2019, U.S. Energy Information Administration (EIA).*[2]

Figure 1.1a shows the projections of primary energy sources consumption within thirty years from the present year. With the fastest growth, renewable energy sources (including solar, wind, and hydroelectric power) will become the most used energy source, surpassing petroleum and other liquids. However, fossil fuels are expected to continue to meet much of the world's energy demand. Then, a major problem arises since the inevitable exhaustion of this limited resource, in addition to the environmental damage especially related to the emission of CO_2 as result of fossil fuels combustion.[3] On the other hand, **Figure 1.1b** shows the projections for energy-related CO_2 emissions. In the short term, the CO_2 emission growth is slowed-down, due to the increase in energy efficiency and a gradual shift from coal toward natural gas and renewable energy sources. Therefore, CO_2 emissions are

expected to grow at an average rate of 0.6 % per year between 2018 and 2050, compared to the average growth rate of 1.8 % per year from 1990 to 2018.[4] However, in the long term, the broad population and economic growth lead to an increased CO_2 emission.

This context motivates the development and utilization of clean, sustainable, and secure energy sources, to balance the consumption of fossil fuels and mitigate the concomitant impact on climate change. Solar energy, as an inexhaustible and environmentally friendly resource, is considered nowadays the only viable alternative. **Figure 1.2** shows the world map distribution of the solar resources on the Earth's surface. On average, 1.05×10^5 terawatts (TW) of solar radiation reach the Earth's surface, exceeding by four orders of magnitude the global electricity consumption average of 2.5×10^1 TW.[1]

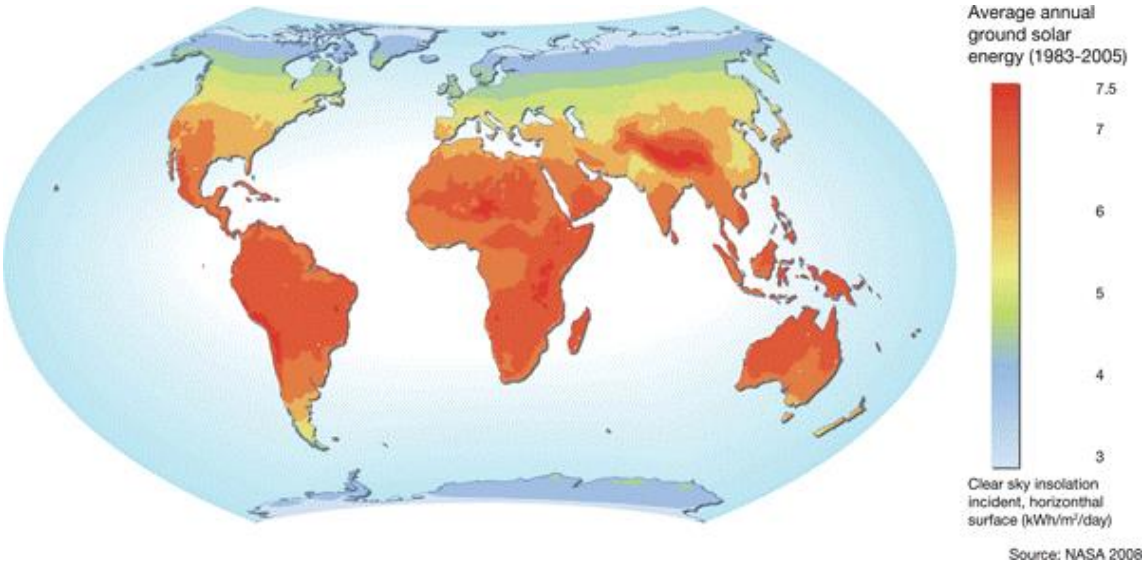

Figure 1.2. a. World solar resource distribution. Source: *NASA Surface meteorology and Solar Energy (SSE).*[5]

Solar energy conversion into chemical energy in the form of fuels or added value products offers an attractive approach for harnessing this abundant resource. The switch from fossil fuels to sunlight through technical photochemistry devices inspired by natural photosynthesis in green plants, algae and cyanobacteria was firstly proposed by G. Ciamician in 1912. However, it was fifty years later when Fujishima and Honda reported the first experimental report on artificial photosynthesis using TiO_2.[6] Thenceforth, several investigations have been devoted to the development of different materials and strategies for efficient, stable, low-cost and environmentally friend solar energy harvesting through chemical processes. Despite many efforts being made to accomplish that goal, the widespread application of solar-to-fuel strategies is still hampered by the struggling search of efficient materials and devices that meet the techno-economical requirements for the implementation of this technology.

In this context, the main motivation of the present doctoral thesis is contributing to the development of solar-fuel conversion technologies by the study of promising semiconductors materials and device architectures, which can be competitive for future deployment.

1.2. Strategies toward solar energy conversion and storage.

Solar energy systems convert solar radiation into heat and electricity. Solar thermal systems use solar collectors to absorb solar radiation to heat water or air. Moreover, solar thermal power plants use concentrating solar collectors to focus the sun rays to heat a fluid to a high temperature. This fluid generates steam to power a turbine and a generator. On the other hand, photovoltaic (PV) systems use solar electric cells that convert solar radiation directly into electricity. In a PV solar cell, a photo-absorber material is used to generate, and efficiently separate, charge carriers upon irradiation with an incident photon flux, which are further extracted with selective contacts. Individual PV cells can be arranged into modules (panels) of variable capacity for electricity production. Therefore, PV systems range from single PV cells for powering calculators to large power plants with hundreds of modules to generate large amounts of electricity, in the order of megawatts (MW). For example, the world's biggest solar power plant, the Bhadla Solar Park in India, have a fully operational total capacity of 2.245 MW, which has recently surpassed the previous largest solar park at Pavagada, Karnataka, with a capacity of 2.050 MW.[7] Globally, solar energy capacity in power plants has increased by approximately 60% over the last five years, rising to 485.82 GW in 2018.[8]

From the different energy conversion approaches described above, PV is the fastest growing technology, and hence, the most widely disseminated. **Figure 1.3** shows the evolution of the record solar conversion efficiencies of several PV technologies, in the last 45 years. Silicon-based PV has been widely explored and is currently at the forefront of the technological deployment of solar conversion systems. Furthermore, its cost has significantly decreased in the last years.[9] However, this technology suffers from several drawbacks, since silicon is not so efficient absorbing sunlight and semiconductor films must be thick (order of μm). Additionally, this material is brittle and, in order to avoid cracking, the deposition onto a very heavy piece of glass is generally required. Those limitations have motivated the development of new PV materials and approaches, including single junction gallium arsenide (GaAs) based cells and thin-film technologies involving copper indium gallium (di)selenide (CIGS), cadmium telluride (CdTe) and amorphous hydrogen-doped silicon (a-Si:H).

More recently, the outstanding optoelectronic properties of lead halide-based semiconductor materials with perovskite crystal structure motivated their application as photo-absorber materials in solar cells.[10] In 2009, Miyasaka and co-workers reported the first organic lead halide compounds ($CH_3NH_3PbBr_3$ and $CH_3NH_3PbI_3$) as sensitizers in photoelectrochemical dye solar cells, with photon-to-current efficiencies up to 3.81% and 3.13%, respectively.[11] Later in 2012, the groups of Grätzel and Park reported a long-term durable solid-state perovskite solar cell (PSC) with a photon conversion efficiency of 9.7%,[12]. Since then, PSC have shown significant progress in PV, reflected on the rapid growth of reported record cell efficiencies in the last seven years (see **Figure 1.3**, yellow-red circles), reaching a certified efficiency of 25.2%, comparable to commercial thin-film solar cell technologies.[13] However, instability of the perovskite in ambient conditions, mainly resulting from the high volatility of hydrophilic organic cations in the hybrid perovskite framework, concomitant to the difficult reproducibility of the devices, are important drawbacks for up-scaling and commercializing PV devices. Therefore, all-inorganic perovskite materials recently emerged as a promising alternative to organic-inorganic hybrid compounds, due to their outstanding thermal stability.

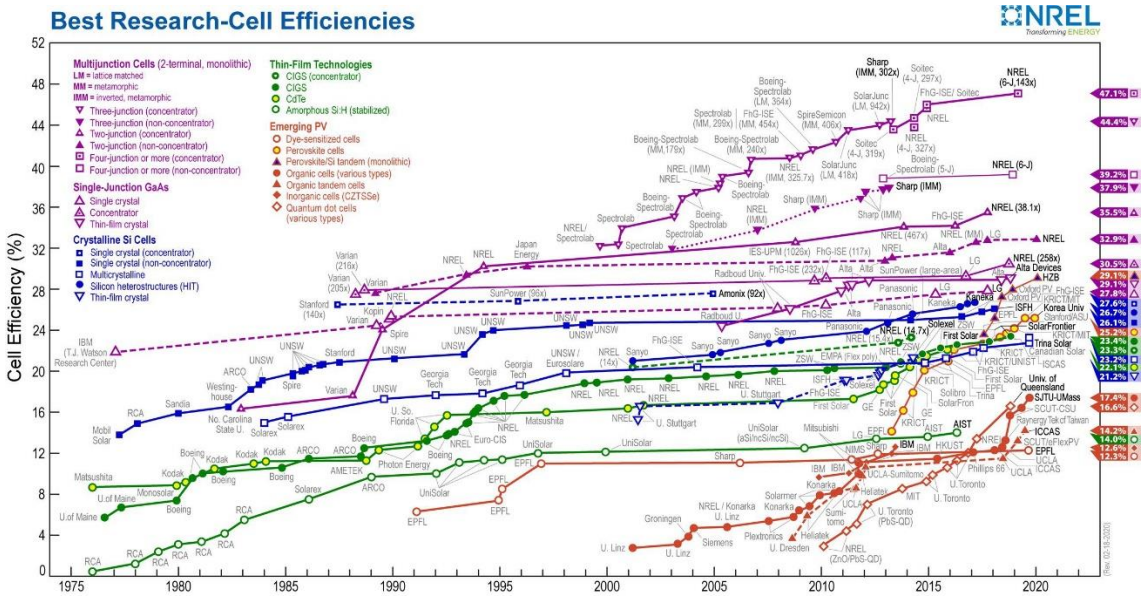

Figure 1.3. Best research-cell efficiency chart for photovoltaic technologies from 1976 to the present. Source: *National Renewable Energy Laboratory (NREL).*[14]

Despite the promising future of PV technologies, the realization of direct solar energy conversion to electricity is only possible during the day hours, making necessary an efficient and inexpensive storage technology for solar energy to provide a significant contribution to the primary energy supply.[15] Nevertheless, considering the present cost of electrical storage, (batteries and supercapacitors), the total costs remain uncompetitive with fossil fuel resources. Thus, improvements in both solar energy conversion and storage are urgently needed to accelerate its deployment into the energy market.[15-16] In this scenario, solar energy storage in the chemical bonds of high energy molecules, as molecular hydrogen (H_2) obtained by solar-assisted water splitting, offers an attractive alternative. Indeed, there are currently significant developments in solar-to-hydrogen conversion and big investment projects for large-scale implementation. For example, four key hydrogen projects utilizing $42 million are already underway in South Australia. One of the projects, Neoen Australia, is investigating the introduction of a 50 MW hydrogen super-hub to produce about 25.000 kg of hydrogen a day.[17] In Spain, the energy group Iberdrola will invest €150 million on the development of a large-scale green hydrogen production project in Puertollano, Ciudad Real, with up to 100 MW of capacity, which will become one of the largest green hydrogen production plants in Europe.[18]

1.2.1 Solar-to-fuel. Hydrogen economy.

Molecular hydrogen is a valuable reservoir of chemical energy, –120 J g^{-1}; c.a. three times the energy mass density of gasoline[19]– which can be stored, transported and converted into electricity using fuel cells producing clean combustion product (water). Moreover, H_2 can be supplied as a feedstock for reduction of atmospheric CO_2 to produce added-value products or other industry processes of high interest such as the Fischer-Tropsch reaction and ammonia synthesis.[20]

As shown in **Figure 1.4**, the vast majority (around 90 %) of H_2 is currently produced from fossil fuels. Approximately 45% is produced from natural gas, using steam methane reforming (SMR) without carbon capture; 30% is obtained during the refining process of petroleum; 18% is produced from coal; while 4% is produced through water electrolysis.[16,

[21] From a techno-economic point of view, the production of solar H_2 requires efficient and stable solar water splitting reactors, with very cheap production costs. It had been calculated that, depending on the system architecture, solar H_2 could be produced at a cost between \$1.60-\$10.40 per kg H_2, indicating that commercial-scale solar-assisted water splitting could be cost-competitive with fossil-based fuels.[22]

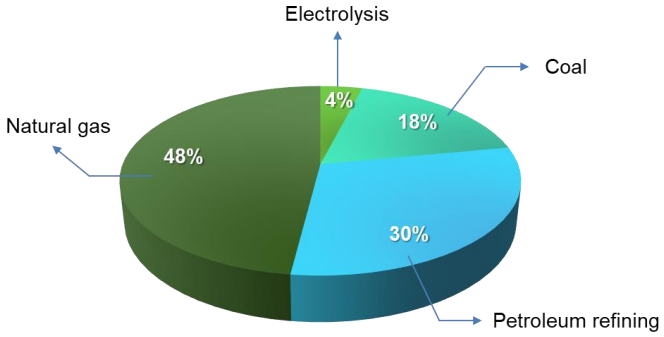

Figure 1.4. Current status of H_2 production. Data source from reference [21].

1.2.2 Solar-assisted water splitting.

Solar energy conversion to fuels technology is inspired by natural photosynthesis of green plants, which convert CO_2 and water in sugars and other carbohydrates, with an energy input from sunlight, as depicted in **Figure 1.5a**. The first step in natural photosynthesis is the splitting of water, which is a fundamental step in artificial systems for energy storage in the form of molecular H_2. Hence, artificial photosystems mimic natural photosynthesis with the use of a catalytic system to absorb the solar energy and drive the water splitting reactions, as depicted in **Figure 1.5b**.[23]

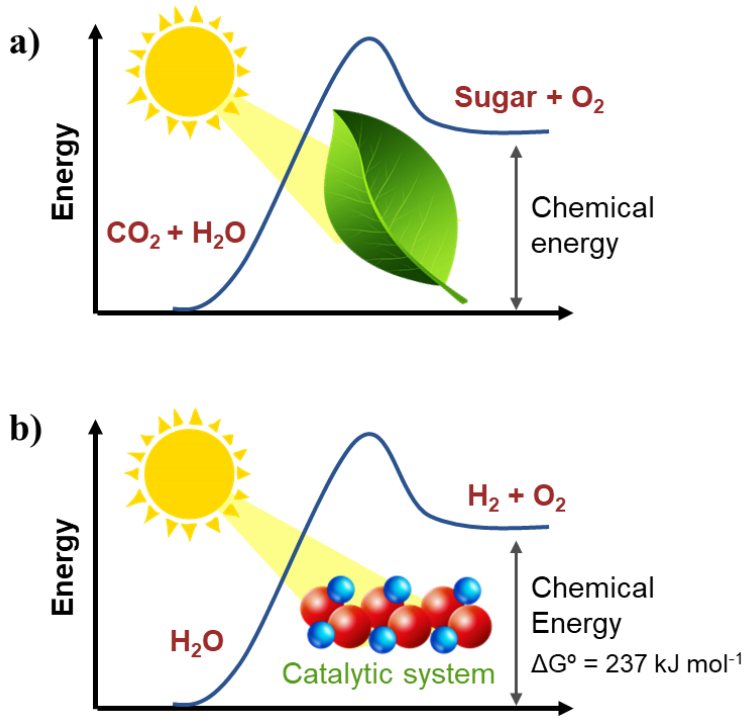

Figure 1.5. a) Schematic representation of plant photosynthesis and **b)** artificial photosynthesis by a catalytic system.

In this process, the water molecule is decomposed into H_2 and O_2 through the half-reactions (in acid media):

$$2H_2O \rightarrow O_2(g) + 4H^+ + 4e^- \quad (E° = 1.23\,V\ vs.NHE) \tag{1.1}$$

$$2H^+ + 2e^- \rightarrow H_2(g) \quad (E° = 0\,V\ vs.NHE) \tag{1.2}$$

$$2H_2O \rightarrow O_2(g) + 2H_2(g) \quad (E = 1.23\,V\ vs.NHE) \tag{1.3}$$

Note that, $E°$ is the standard potential of the half-reaction, expressed respect to the Normal Hydrogen Electrode (NHE). The global water splitting process, at standard temperature and concentrations, demands a free Gibbs energy of 237 kJ mol^{-1}, corresponding to the overall 1.23 V *vs* NHE (obtained by the Nernst equation) which can be supplied by an external electrical bias, in a conventional electrolysis cell using electrocatalytic materials. However, in practice, electrochemical water splitting occurs at a considerably higher voltage associated with the large overpotentials needed to drive the kinetically sluggish water oxidation half-reaction. Such energy input can be provided by the sunlight, with a suitable material able to absorb and convert the energy of the photon into charge carriers. The obtained H_2 can be taken as an energy vector, as discussed in Section 1.2.2, using the energy stored at the chemical bonds through the back reaction in a fuel cell.

In 1972, Fujishima and Honda reported the first demonstration of photoelectrochemical (PEC) water splitting, using a titanium dioxide (TiO_2) photoelectrode under ultraviolet (UV) light irradiation, where the O_2 evolution reaction (OER) took place, and a platinum (Pt) counter electrode, were the H_2 evolution reaction (HER) was observed.[6] This discovery stimulated scientists and technologists to explore efficient photoelectrodes based on semiconductor materials, not only for H_2 production but also for other relevant applications such as CO_2 reduction, production of added-value chemicals, and degradation of organic pollutants.

Solar-assisted water splitting using semiconductor materials includes the following steps:

1. *Photon absorption and charge carrier generation:* The absorption of a photon ($h\nu$) with energy higher than the semiconductor band gap (E_g) leads to the generation of an electron-hole pair.

2. *Charge separation:* The efficient separation of the photogenerated charge carriers requires the presence of an electrical field or a gradient of carrier density.

3. *Charge injection and water splitting reactions:* The photogenerated charge carriers are transferred to the electrolyte to drive the chemical reactions.

The primary metrics for solar water splitting is the Solar-To-Hydrogen conversion (STH) efficiency, defined as the fraction of the incident solar power that is stored as chemical energy in the H_2 produced.[24] The STH efficiency is determined under standard solar irradiation generated with the Air Mass 1.5 global (AM 1.5 G) filter or 1 sun (100 mW cm^{-2}) with no applied bias in a two-electrode photoelectrochemical cell.[25] Water splitting theoretically requires an input free Gibbs energy corresponding to 1.23 V, which represents the amount of high-quality (low-entropy) work that can be extracted from the

H_2. The excess voltage that is required to split water at a reasonable rate is lost as heat and does not enter into the efficiency calculation.[16] Therefore, STH efficiency is calculated as:

$$STH\ (\%) = \frac{j_e \times 1.23\ V}{\Phi} \times FE \qquad (1.4)$$

where j_e is the photocurrent density (in mA cm^{-2}) –considering the electrode surface area– measured at short-circuit conditions (refers to zero voltage in the external circuit), Φ is the incident total integrated light power, and FE is the Faradaic efficiency for H_2 evolution. Note that Eq, 1.4 is valid *only* if the stoichiometric evolution of evolved gases (H_2 and O_2) is confirmed, in the absence of sacrificial agents. From Eq. 1.4, it is clear that high photocurrent is critical to maximizing the STH efficiency.

Solar-assisted water splitting can be accomplished by three different methods: particulate photocatalysis, photovoltaic-assisted water electrolysis and PEC cells, which are described below.

1.2.2.1 Particulate photocatalysis.

Photocatalytic (PC) water splitting using particulate semiconductor materials is conceptually the simplest approach of hydrogen production.[26-27] In a particulate photocatalyst, the photogenerated charge carriers are spatially separated and transported to the particle surface, where the redox reactions take place. Provided that a suitable band alignment exists between the photocatalyst and the redox potential of the liquid solution, the photogenerated electrons and holes can induce the reduction and oxidation half-reactions, respectively. Simultaneously, both bulk and surface recombination processes can compete with charge extraction, directly affecting the photocatalytic efficiency. Besides the STH efficiency, the efficiency of the photocatalyst is often evaluated through the Apparent Quantum Yield (AQY). This figure of merit relates the number of electrons involved in the photocatalytic reaction and the production rate of molecules with the rate of incident photons. As the AQY is dependent on the wavelengths of photons, this metrics is usually determined under monochromatic irradiation.

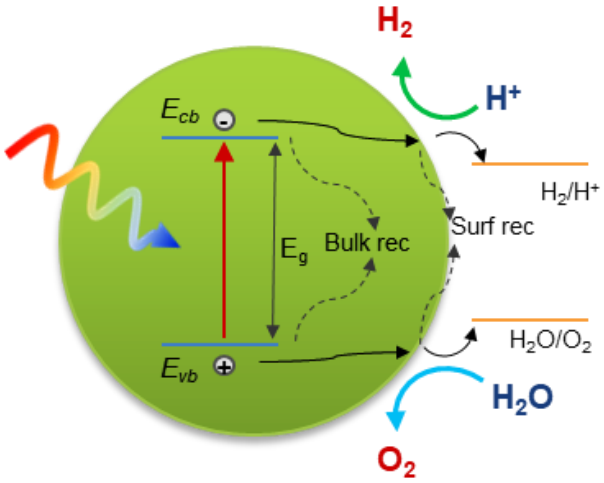

Figure 1.6. Schematic representation of particulate photocatalyst, carrying out the overall water splitting process.

There is a large variety of semiconductor materials, which have been investigated as photocatalysts, such as TiO_2, g-C_3N_4, CdS, Cu_2O, $BiVO_4$, Fe_2O_3, and perovskite oxides.[27-29] However, the majority of the reported photocatalytic materials are only effective for one of the half-reactions. Hence, two narrower E_g semiconductors: an OER photocatalyst and a HER photocatalyst, can be connected via an electron mediator (e. g. a redox couple), then both reactions occur at separated photocatalysts. This approach is also called "Z-scheme" artificial photosynthesis.[30]

Since recombination processes are usually the main limiting factor for efficient water splitting, the photocatalytic particles are commonly modified by the incorporation of co-catalysts at the photo-absorber semiconductor surface, to facilitate the charge separation and surface reactions. Moreover, the use of co-catalysts may reduce the possibility of photo-corrosion and therefore, enhance the chemical stability of the particulate photocatalyst. Other strategies such as improvement of material crystallinity and charge mobility, the decrease of surface and grain boundary defects and the reduction of particle size to shorten charge transport distance have been also explored in order to reduce recombination losses.

Overall water splitting using particulate photocatalysts offers attractive advantages for large-scale solar H_2 production, as a low-cost technology supported by the readily synthesis of the photocatalysts, and the simple reactor and facility designs. In terms of efficiency, to reach the maximum achievable STH efficiency corresponding to the E_g of the photocatalyst, an AQY of ~100% is required. However, the AQY is only 16 % (at 420 nm), and 2% STH, for the best PC reported system for overall water splitting (Carbon nanodots–C_3N_4).[31] Moreover, current STH efficiencies for this approach at the laboratory scale are only about 1%,[32] while values of 5-10% are needed to allow PC overall water splitting to be economically viable for solar H_2 production.[28]

1.2.2.2 Photovoltaic-powered electrocatalysis.

As discussed in the sections above, the water splitting process demand an energy input equivalent to the required thermodynamic potential plus the overpotentials resulting from the sluggish kinetics, especially from the water oxidation half-reaction, which involves the participation of four holes (see reaction 1.1). Such power input can be electrically provided, in a classical electrolysis cell, using electrocatalytic materials as anode and cathode, where the OER and HER take place, respectively, and an aqueous solution containing a redox species as the electrolyte. The electricity can be provided from PV technologies, externally connected to the electrolyzer system (PV+electrolyser), as represented in **Figure 1.7**. This approach is indeed, in terms of efficiency, the most straightforward to solar fuel production, with separated light harvesting and catalytic functions, further integrated by a series connection. However, in large scale applications, hydrogen production from such integrated approach is not competitive with current fossil fuels prices.[22] Moreover, industrial electrolyzers run at large current densities (hundred mA cm^{-2}), and require precious metal catalysts that are stable only under this operational condition, then easily corrodes when their power source is removed.[33]

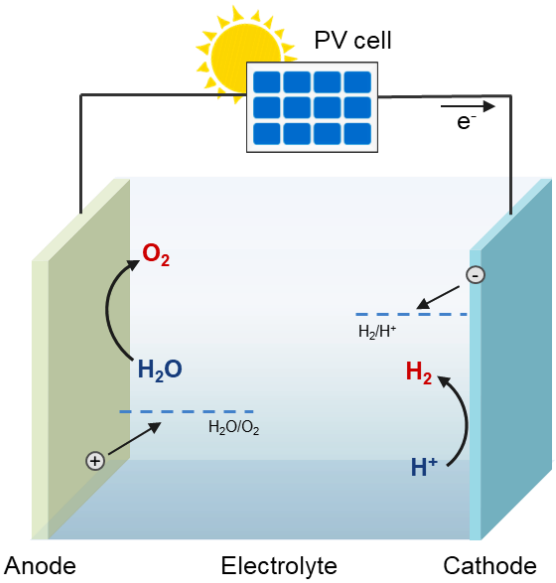

Figure 1.7. Schematic representation of an electrochemical water splitting cell, powered with a PV device.

Furthermore, The PV component and the electrocatalyst can be arranged in an integrated photovoltaic-electrocatalyst (PV–EC) electrode, as depicted in **Figure 1.8**. Usually in such configuration, a protective layer between the PV component and the electrocatalyst is needed, in order to avoid that the electrolyte contacts the solar cell, which may lead to partial degradation of the PV component. The integrated PV–EC systems offer several advantages, including:

(i) Flexibility for electrochemical reactions: The power generated by the underlying solar cell is entirely available for the water electrolysis.[34] That means that the solar cell can be adjusted in order to be able to provide the adequate voltage to drive any electrochemical reaction,[35-36] with no need for an externally applied bias.

(ii) High efficiency: Due to the flexibility of this approach and the maturity of the individual components, integrated PV–EC devices would become feasible to reach higher efficiencies compared to other solar fuel strategies (PC and PEC), over 10%.[34]

(iii) Accurately prediction of the PV–EC device performance: In PV–EC systems the individual components can be separately optimized. Also, the current–voltage characteristics of the electrocatalysts can be merged with that of the PV component. Therefore, the accurate prediction of the viability and final performance of the integrated PV–EC device is possible.[34, 37]

In addition, this approach offers a compact and less complex design compared to externally connected PV+electrolyser systems, with a more efficient thermal management. Moreover, the intimate connection of the PV and EC components in monolithic devices is of particular interest for further development of a practical “artificial leaf”.

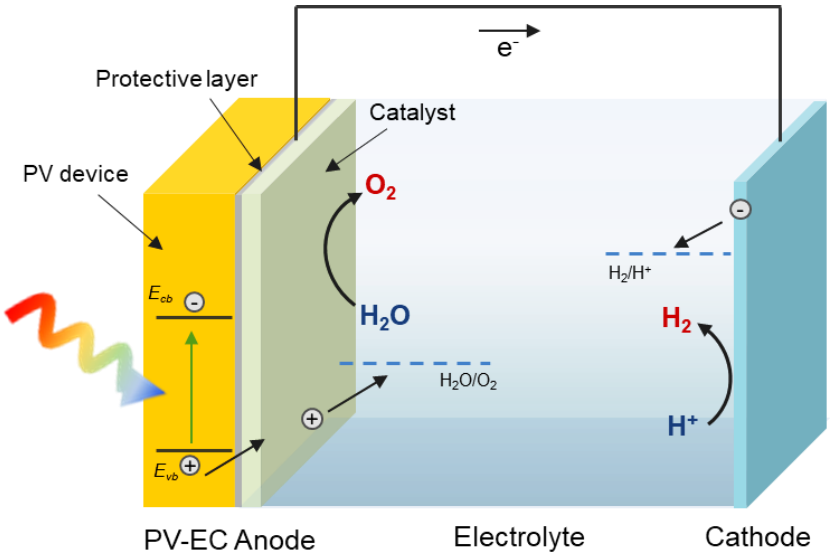

Figure 1.8. Schematic representation of an PV–EC integrated photoelectrode, acting as photoanode in a solar water splitting cell.

Although both solar cells and water oxidation electrocatalysts are commercially available, the large-scale implementation of PV–EC architectures is not still economically competitive with the much cheaper methane steam reforming,[38] mainly due to the high cost of the electrocatalytic materials that currently provide the best efficiencies and stability. A detailed discussion about the materials used as PV and EC components will be addressed below in Section 1.5.

1.2.2.3 Photoelectrochemical cells.

PEC water splitting is a "Z-scheme" of the photocatalysis approach, where OER and HER half-reactions occur at separated photoelectrodes. This is a more direct but challenging approach for solar fuel production compared to PV–EC configurations, since the reactions are directly driven by the photo-absorber material at the semiconductor/liquid interface. In a PEC cell, one of both electrodes consists of a photo-active semiconductor, able to absorb photons, to efficiently separate the photogenerated charges, and to drive the desired reactions at their interface with the liquid solution. Often, and mainly due to the thermodynamic and kinetic barriers imposed by the water oxidation reaction, the energy provided by light absorption is not enough to drive the water splitting reaction. Therefore, an external bias is needed to overcome the different losses.

Figure 1.9 shows a schematic representation of a PEC water splitting cell, where both electrodes integrate photo-absorber materials. In that configuration, photoexcited holes at the photoanode will oxidize water and produce O_2, while at the photocathode the photoexcited electrons will drive the hydrogen evolution reaction. It is worth noting that, either in electrocatalysis or PEC systems it is possible to prevent gas mixing, since OER and HER take place at different electrodes. Therefore, the use of an adequate membrane allows H_2 and O_2 to evolve at separate compartments, facilitating the collection of gases. The maximum attainable STH efficiency for this approach has been calculated as 16.6 % with both semiconductors E_g equals to 1.4 eV, which represents a moderate increase over a single absorber configuration. Moreover, integrated tandem approaches –were the absorbers are placed one on top of the other, allowing a more efficient photon harvesting–, are able to reach up to 30 % of solar conversion to hydrogen.[39]

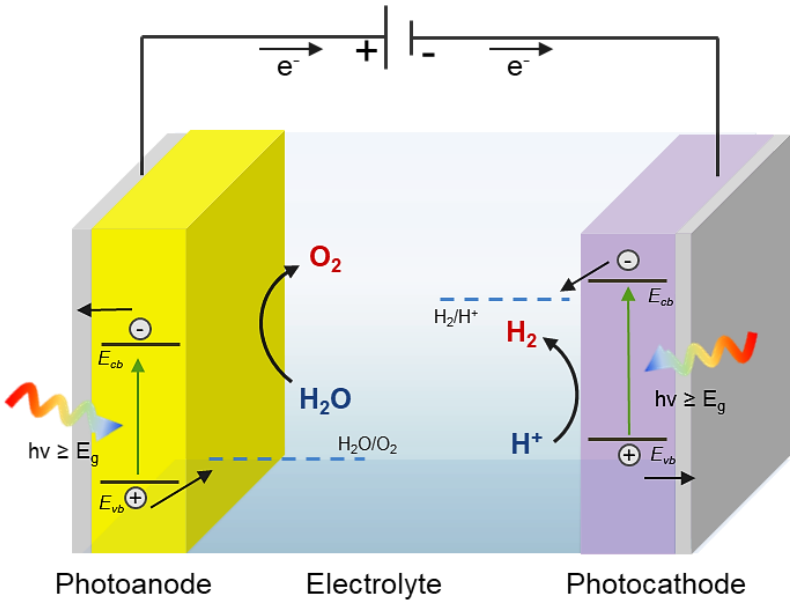

Figure 1.9. Schematic representation of a tandem PEC water splitting cell.

An important advantage of PEC approach is the potential simplicity of an integrated design, where the photo-absorber semiconductor can act itself as electrocatalyst for the desired reactions.[40] For that purpose, the semiconductor material should possess both adequate optoelectronic properties for efficient carrier generation and transport, and high catalytic activity towards the desired chemical reaction. However, the identification of low-cost and stable materials fulfilling the above requirements for both photoelectrodes in the configuration represented in **Figure 1.9** is not easily achievable. Therefore, investigations on PEC systems often use a simpler configuration, with a single photoelectrode under study, while a noble metal is used as counter electrode.[41]

Generally, the photo-active semiconductor is deposited on a transparent conductive oxide (TCO) on glass; the most commonly employed ones are fluorine-doped tin oxide (FTO) or indium tin oxide (ITO). However, metal-based substrates are used in some cases. As discussed in Section 1.2.2.1, usually a co-catalyst material is needed at the surface of the photo-absorber material, in order to overcome the recombination dynamics of the water splitting reactions. Due to the importance of the semiconductor materials used as photoelectrodes in PEC cell for the development of the present thesis, a detailed discussion about the photoelectrodes requirements and the more relevant strategies applied in order to improve their efficiency, including co-catalyst materials, will be described below in this chapter (Section 1.4).

1.2.3 Techno-economical perspectives of Solar–To–Hydrogen approaches.

Realization of a solar hydrogen economy, to substitute the current fossil fuels as a primary energy source, requires the development and up-scaling of efficient, deployable and cost-effective solar-assisted hydrogen production systems. In terms of efficiency, a single junction device should be able to theoretically reach up to 10% STH.[39] Moreover, ~30 % STH can be achieved by an integrated PEC water splitting system from two-component or two-junction light absorbers.[39, 42] In PV–EC system, the STH depends on the power conversion efficiency of the PV component. Therefore, a maximum STH of 28.7% was calculated using an efficient bipolar alkaline electrolyzer and tandem PV cells, while an STH of 31.8% was calculated using the same electrolyzer and a triple junction III–V

material-based PV cells. On the other hand, reaching 10% STH with PC systems, requires of photo-absorbers with AQY of 62, 40 and 30% at wavelengths of 600, 700 and 800 nm, respectively.[43]

Figure 1.10 depicts a technological map of the different solar-assisted fuel production approaches. Therein, the latest reported STH efficiencies in PV–EC, PEC and PC devices, as a function of the system complexity, recently reviewed by Kim and co-workers, are shown.[25]. Note that, PV–EC devices also accounts for externally connected PV and electrolyzer systems in the figure. As expected from the discussion above, there is a clear trend for efficiency, led by the PV–EC systems, followed by PEC, while the PC systems show the lowest STH efficiency values. Therefore, the highest STH efficiency, over 20%, are reported for PV–EC approaches using III/V-based PV devices and polymer electrolyte membrane (PEM) electrolyzers, which use expensive noble metal catalysts. As highlighted in **Figure 1.10**, a remarkable 19.3% STH was achieved by Cheng and co-workers with the monolithic RuO_2–GaAs/GaInAs/GaInP/AlInP/TiO_2–Rh device.[44] On the other hand, at the forefront of the integration of PV and photoelectrodes, Pihosh and co-workers have reported the best efficiency using a $BiVO_4$-based photoanode, reaching up to 8.1% STH with the architecture Co-Pi/$BiVO_4$/WO_3–GaAs/InGaAsP–Pt.[45] Conversely, PC approaches are still below 2% STH.

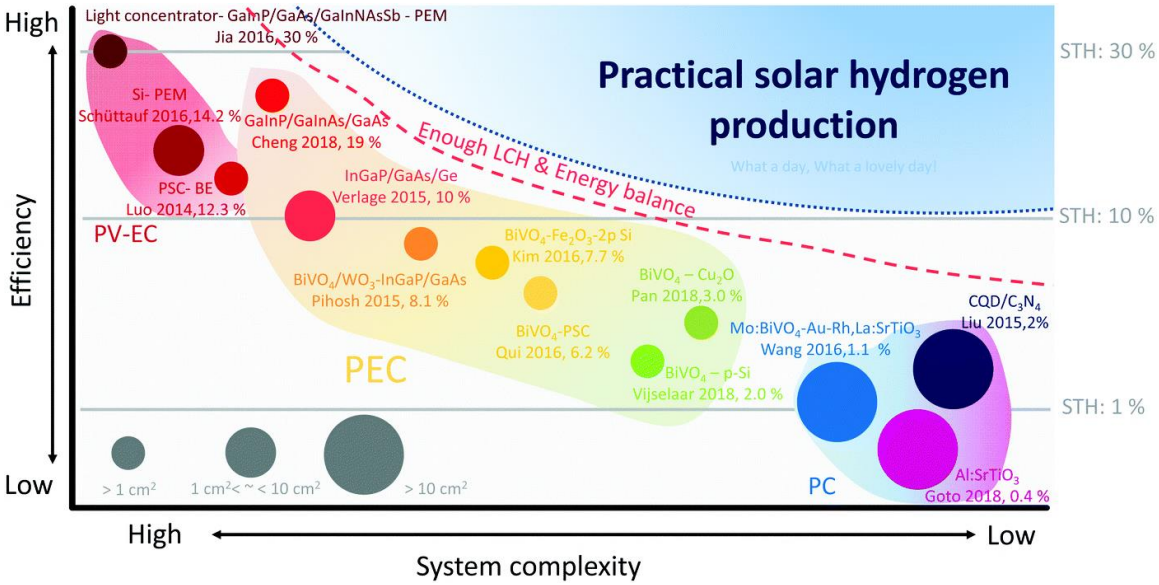

Figure 1.10. Technological map of the different approaches for practical solar-assisted fuels production. Relevant systems with experimentally demonstrated efficiency as function of the system complexity, are shown. Figure reprinted with permission from reference [25]. PEC devices are subdivided into PE buried, PE–PV and PE–PE devices.

On the other hand, the analysis of the cost of Solar-To-Hydrogen systems has provided estimates ranging from ~\$3–10 kg^{-1} for PEC systems, and ~\$5–8 kg^{-1} for integrated PV–EC approaches.[40] Despite the similitude in the ranging costs, the PV–EC systems is at a much higher technological readiness level due to the maturity of both PV and EC technologies, and particularly the thin-film silicon-based solar cells.[16] However, the practical implementation of hydrogen production *via* PV–EC approaches is hampered by the nature of the electrocatalytic materials. In particulate PC systems, the estimated average cost of hydrogen production is in the range of \$1.6–3.5 kg^{-1}, assuming STH efficiency

values of 5–10% and a system lifetime of 5 years.[26-27]. These costs seem attractive compared to PEC and PV–EC approach. However, despite the attempts to scale-up PC system for hydrogen production through solar water-splitting, this approach unfortunately has fallen short of the efficiency values required for practical applications. This analysis evidences that continued search for materials and strategies to practical realization and technological deployment of solar-assisted hydrogen production is needed.

1.3. Fundamentals of semiconductor materials.

In all the systems described in the sections above (particulate PC, integrated PV-EC and PEC devices), the semiconductor materials acting as photo-absorber have a fundamental role. Their fundamental properties have a direct influence on efficient light harvesting and subsequent solar to chemical energy conversion. In this context, this section is aimed at providing a summary on semiconductor electrochemistry, in order to introduce important concepts that will be further used along with this thesis.

In a semiconductor material the electron energy levels are grouped into the valence and conduction bands, which are separated by a forbidden energy gap (E_g), such as:

$$E_g = E_{cb} - E_{vb} \tag{1.5}$$

Where E_{cb} and E_{vb} are the conduction band minimum and the valence band maximum edges, respectively. The electron occupation probability for a distribution of energy levels, $f(E)$, is defined by the Fermi-Dirac function:

$$f(E) = \frac{1}{1 + \exp\left(\frac{E - E_F}{k_B T}\right)} \tag{1.6}$$

where E_F is the Fermi energy, k_B is Boltzmann's constant and T is the temperature. From Eq. 1.6 it can be noted that for $E > E_F$, the occupation probability falls to zero, over an energy interval of a few $k_B T$. When $E < E_F$ the $f(E)$ rises to one. Finally, for $E = E_F$, the occupation probability is 0.5. [46]

In a semiconductor material, the electrons can be thermally excited across the forbidden gap, leaving an electron vacancy (hole) in the valence band. Considering an ultrapure (intrinsic) semiconductor, the concentration of charge carriers (electrons and holes) in the semiconductor can be expressed in terms of the Fermi-Dirac probability function in the presence (f) or absence ($1 - f$) of electrons:[46]

$$n = \int_{E_{cb}}^{\infty} DOS_C(E)\ f(E)\ dE \tag{1.7}$$

$$p = \int_{\infty}^{E_{vb}} DOS_V(E)\ [1 - f(E)]\ dE \tag{1.8}$$

Where DOS_C and DOS_V are the density of state (DOS) distribution at the conduction and valence bands, respectively. With N_C and N_V being the effective DOS in the conduction and valence band, respectively, the equilibrium concentrations of charge carriers are related by the mass balance equation:

$$np = N_C N_V exp\left(\frac{E_g}{k_B T}\right) \tag{1.9}$$

For an intrinsic semiconductor $N_C = N_V$, indicating the Fermi energy is situated at the mid-gap position, as shown in **Figure 1.11a**. Note that, from the exponential term in Eq. 1.9, it follows that the electrons and holes concentration in an intrinsic semiconductor rapidly increase with T.[46]

1.3.1 Doped semiconductors.

Intrinsic semiconductors exhibit a rather low conductivity, since the carrier concentrations under ambient conditions are very low. Therefore, for practical applications, the semiconductors are usually doped. Doped semiconductors contain donor (n-type doping) or acceptor (p-type doping) atoms or vacancies in the lattice, that can produce electrons and holes according to the equilibria[46]:

$$D \rightarrow D^+ + e^-_{cb} \tag{1.10}$$

$$A \rightarrow A^- + h^+_{vb} \tag{1.11}$$

In this case, the concentrations of free charges are determined by the doping level, rather than by the excitation of electrons across the band gap. Therefore, under equilibrium conditions, the concentration of electrons and holes in the conduction and valence bands, respectively is given by the expressions:

$$n = N_C exp\left(-\frac{E_{cb} - E_F}{k_B T}\right) \tag{1.12}$$

$$p = N_V exp\left(\frac{E_{vb} - E_F}{k_B T}\right) \tag{1.13}$$

From Eqs. 1.12 and 1.13, it is clear that E_F is determined by N_C and N_V.Therefore, in an n-type semiconductor, E_F shifts towards the E_{cb} edge, while in a p-type doped semiconductor, E_F shifts towards the E_{vb} edge, in order to preserve charge neutrality. **Figure 1.11a-c** shows the relative position of the E_F in an intrinsic, an n-type and a p-type semiconductor, respectively.

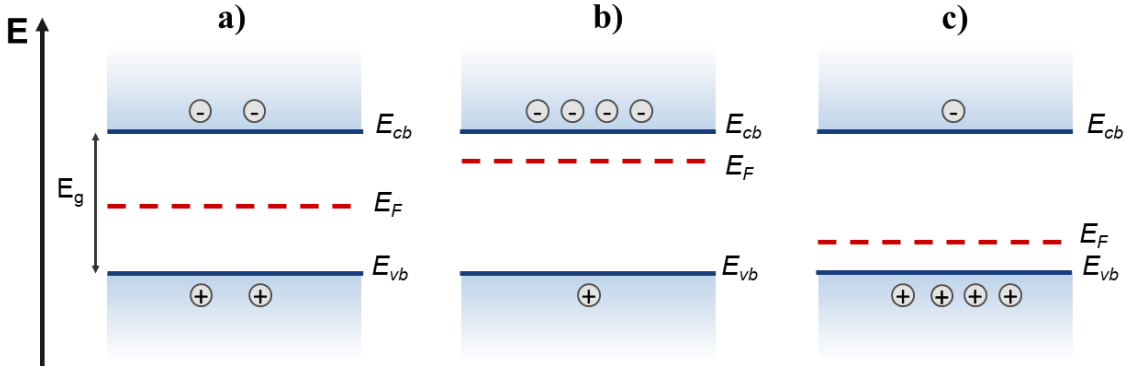

Figure 1.11. Schematic representation of the relative position of E_F in **a)** an intrinsic semiconductor, **b)** a p-type semiconductor and **c)** an n-type semiconductor.

1.3.2 Electrochemical potential of the semiconductor.

The electrochemical potential of a charged species i, ($\bar{\mu}_i$), describes the change of the free Gibbs energy G of a system when i is added to a phase of inner potential φ:

$$\bar{\mu}_i = \left(\frac{\partial \bar{G}}{\partial n_i}\right) \tag{1.14}$$

Note that, molar quantities are represented by a bar over the quantity. Moreover, $\bar{\mu}_i$ can be conceptually split into the 'chemical' and the 'electrical' components as:

$$\bar{\mu}_i = \mu_i + z_i F\varphi \tag{1.15}$$

Where μ_i is the chemical potential of the species and $z_i F\varphi$ represents the electrical work done to transfer one mole of charge $z_i F$. The chemical potential of electrons and holes depends on their concentrations.[46]

Considering the density instead of the molar concentration, μ_i for electrons and holes are:

$$\mu_n = \mu_n^0 + k_B T ln \frac{n}{N_C} \tag{1.16}$$

$$\mu_p = \mu_p^0 + k_B T ln \frac{p}{N_V} \tag{1.17}$$

Where μ_n^0 and μ_p^0 are the standard chemical potentials for electrons and holes, respectively. From Eqs. 1.15 and 1.16 it follows that N_C and N_V corresponds to the standard states for electrons and holes, respectively.

Note that, the electrochemical potentials of electrons and holes in a semiconductor material are related to the Fermi energy as[47]:

$$\bar{\mu}_n = E_F \tag{1.18}$$

$$\bar{\mu}_p = -E_F \tag{1.19}$$

1.3.3 The semiconductor material under illumination.

An incident photon flux may produce excitation of charges in a semiconductor. Depending on the nature of the optical transitions, the semiconductor band gap is direct or indirect. The band gap is considered direct if the minimum of the E_{cb} and the maximum of the E_{vb} lie at the same *k*-point in the reciprocal space, as represented in **Figure 1.12a**. Otherwise, when the E_{cb} minimum and E_{vb} maximum are at different *k*-points in the reciprocal space, as shown in **Figure 1.12b,** the band gap is called indirect.[41] Note that in indirect semiconductors, the photon must be coupled to a lattice vibration (phonon), to compensate for the missing crystal momentum *k*, according to the principle of momentum conservation. Involving a third entity leads that indirect transitions are much less likely to occur, therefore showing a weaker optical absorption.[41] Thus, a direct band gap semiconductor is usually preferred in photoelectrochemical applications.

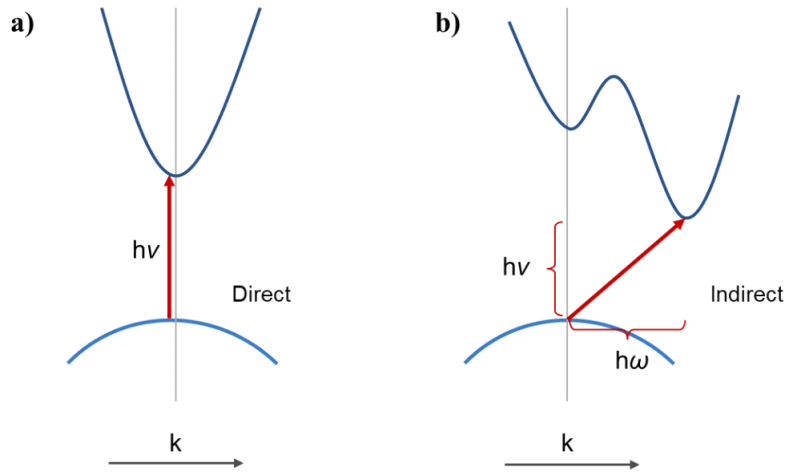

Figure 1.12. Schematic representation of the optical transitions in semiconductors with **a)** direct and **b)** indirect band gap. Note that indirect transition requires a phonon with energy $h\omega$.

The absorption of photons with energies $h\nu \geq E_g$ leads to the excitation of electrons from the valence band to the conduction band, resulting in the (photo)generation of electron-hole pairs. It worth mentioning that besides 'interbands' transitions, light absorption by free carries within the bands is possible, where the photon energy is converted into heat (intraband absorption), as well as by charge carries localized at impurity atoms or lattice imperfections (impurities absorption).[48] However, in photoelectrochemistry, we will only refer to interband transitions.

Under steady illumination and open circuit conditions (no current flow), the electron-hole pairs generation is balanced by charge recombination. Note that, recombination process may involve interband recombination, Auger process, or recombination via impurities or defect states, either in the bulk or at the semiconductor surface.[46] Considering only bulk recombination in a doped semiconductor, the concentration of majority carries remains constant upon illumination, if the concentration of photo-generated majority carriers is lower than the equilibrium dark concentration. Therefore, the recombination process will determine the minority carrier lifetime, τ_{min}, which is an important bulk property of semiconductor materials.[46] With τ_{min} long enough, the carriers can diffuse to the semiconductor surface, if the carrier diffusion length L_{min} is comparable with the sample thickness:

$$L_{min} = \sqrt{\frac{k_B T}{q} u_{min} \tau_{min}} \tag{1.20}$$

where u_{min} is the mobility of the minority carriers.

Photo-generation of electron-hole pairs perturbs the thermal equilibrium described in terms of E_F in Section 1.3.1, leading to an excess of charge carriers, where their concentration depends on the generation rate and on the bulk τ_{min}. Since the electron and hole densities are increased to above their equilibrium value, the electron and hole densities cannot be determined by the same E_F. Therefore, it becomes necessary to define 'quasi-Fermi' levels, $E_{F,n}$ and $E_{F,p}$, for electrons and holes, respectively. Hence, Eqs 1.11 and 1.12 can be re-written as:

$$n + \Delta n = N_C exp\left(-\frac{E_{cb} - E_{F,n}}{k_B T}\right) \quad (1.21)$$

$$p + \Delta p = N_V exp\left(\frac{E_{vb} - E_{F,p}}{k_B T}\right) \quad (1.22)$$

Where Δn and Δp are the additional photo-generated electrons and holes, respectively. **Figure 1.13a** shows an n-type semiconductor under equilibrium dark conditions. Upon illumination, as represented in **Figure 1.13b**, the concentration of minority carrier (holes in the valence band) increases, particularly near the semiconductor surface, leading to the split of the Fermi level into the $E_{F,n}$ and $E_{F,p}$. Note that, the quasi-Fermi level of the majority carriers (electrons in **Figure 1.13b**) stays nearly constant upon illumination, whilst the quasi-Fermi level of the minority carriers (holes in **Figure 1.13b**) varies with the distance from the excitation area.

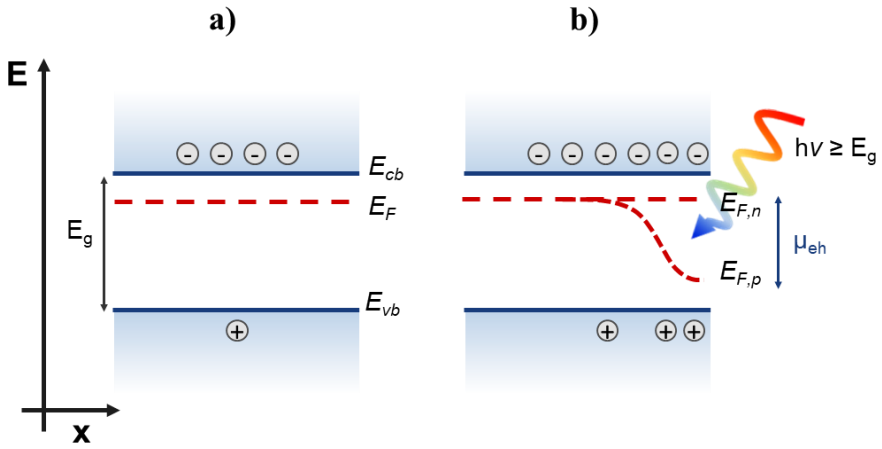

Figure 1.13. a) Schematic representation of an n-type semiconductor in the dark (equilibrium) and **b)** under illumination conditions. Photon absorption with energies $h\nu \geq E_g$ promotes the electron-hole pair generation, leading to E_F splitting into separated quasi-Fermi levels for holes ($E_{F,p}$) and electrons ($E_{F,n}$). The difference between the quasi-Fermi energies gives the chemical potential of the electron-hole pairs, μ_{eh}.

The free energy of electron-hole pairs is given by the sum of their chemical potentials or, considering Eqs. 1.17 and 1.18 now referred in terms of $E_{F,n}$ and $E_{F,p}$, respectively, the difference between the quasi-Fermi energies:

$$\mu_{eh} = \mu_n + \mu_p = E_{F,n} - E_{F,p} \quad (1.23)$$

The main objective of a practical semiconductor-based solar energy conversion device is to extract the largest possible fraction of this chemical energy (μ_{eh}), either as electrical power (PV cells) or as chemicals (PEC cells), as fuels or added valued products. [46]

1.3.4 The semiconductor/liquid interface.

Figure 1.14a represents an n-type semiconductor and an electrolyte in aqueous solution, before and after contact. When the semiconductor and the electrolyte are in contact, thermodynamic equilibrium requires that the electrochemical potential of the

semiconductor (i.e. the Fermi level, see Eq. 1.18 and 1.19) and that of the electrolyte solution (E_{redox}) are equal. Therefore, electrons will flow between the semiconductor and the solution producing an interfacial electric field, whose electrostatic potential balances the initial difference between the electrochemical potentials of semiconductor and the electrolyte.[49] In an n-type semiconductor, as that depicted in **Figure 1.14a**, there will be an excess of positive charge, arising from the ionized dopant atoms in the semiconductor, which is spread out over a space charge region (SCR) or depletion zone of width *W*. Due to the drop of the electric field in the semiconductor, a band bending near the semiconductor/liquid interface takes place. On the other hand, the solution will have an excess negative charge that spread over a much narrower region in the solution close to the electrode, called the Helmholtz layer (H_L). Analogously, **Figure 1.14b** represents the formation of a semiconductor/liquid junction (SCLJ) with a p-type semiconductor. I this case, there will be an excess negative charge at the semiconductor resulting in a depletion zone, while at the solution side, there will be an excess of positive charge forming the H_L.

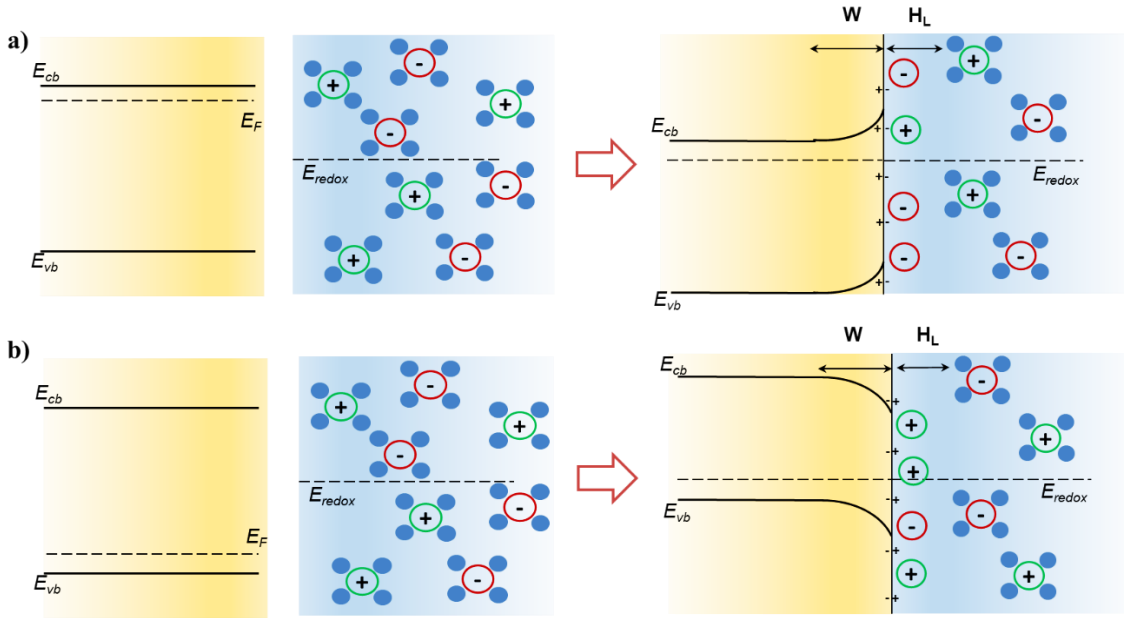

Figure 1.14. Schematic representation of the semiconductor/liquid junction: **a)** n-type semiconductor, **b)** p-type semiconductor. Note that, due to the large dipole moment of water, the ions in the solution are solvated with water molecules, represented with the blue circles.

The charge distribution across the SCLJ leads to a potential gradient at the surface, as represented in **Figure 1.15a**, with an n-type semiconductor as an example. The potential gradient at the surface of the semiconductor is given by the abrupt depletion approximation[46] as:

$$\left.\frac{d\phi}{dx}\right|_{x=0} = \frac{qN_DW}{\varepsilon_0\varepsilon_r} \tag{1.24}$$

Where q is the elemental charge, ε_0 is the permittivity in vacuum, and ε_r is the relative permittivity of the semiconductor material. Integration of Eq. 1.24 gives the dependence of the depletion zone (W) with the potential drop $\Delta\phi_{SC}$ and the doping density N_D:

$$W = \left(\frac{2qN_D\Delta\phi_{SC}}{\varepsilon_0\varepsilon_r}\right)^{1/2} \quad (1.25)$$

Note that, if the redox potential of the electrolyte is equal to the E_F in the semiconductor, there is no charge distribution and hence, no SCR (or depletion zone). The potential at which the SCR vanishes, i.e. W=0, is the flat band potential, V_{fb}.

The effect of the applied potential on the SCLJ can also be considered. Starting from the equilibrium condition between the semiconductor E_F and the E_{redox}, in reverse bias (positive applied potentials), the E_F moves downward to the relative position of E_{redox}, while the band bending increases. Therefore, the electrons flow from the redox systems to the semiconductor becomes thermodynamically possible. Conversely, in forward bias (more negative applied potentials), the band bending decreases and the electrons flow from the semiconductor to the electrolyte is possible. Beyond the V_{fb}, the electrons accumulate near the surface of the semiconductor, which behaves like a metal electrode in this condition. [46]

Moreover, since the stored charge at the depletion layer (Q_{SC}) is proportional to W_{SC} , the variation of the capacitance at the space charge region (C_{SC}) as a function of the applied potential gives an important relation, known as the Mott-Schottky equation:

$$\left(\frac{1}{C_{SC}}\right)^{-2} = \left(\frac{dQ_{SC}}{d\Delta\phi_{SC}}\right)^{-2} = \frac{2}{\varepsilon_0\varepsilon_r e N_D A^2}\left(\Delta\phi_{SC} - \frac{k_B T}{q}\right) \quad (1.26)$$

Where A is the surface area of the semiconductor material. Note that $\Delta\phi_{SC}$ can be replaced by the difference $V - V_{fb}$, where V is the applied potential. This relationship is fundamental for the determination of the intrinsic properties of the semiconductor materials, such as the type of doping and the density of dopants. As shown in **Figure 1.15b**, the plot of Eq. 1.26 follows a linear trend with a positive slope for an n-type semiconductor, and a negative slope for a p-type semiconductor and its magnitude is directly related to the doping density. Furthermore, the *x*-axis intercept is used to calculate V_{fb}, and hence, knowing the band gap, the band alignment of the semiconductor can be estimated.

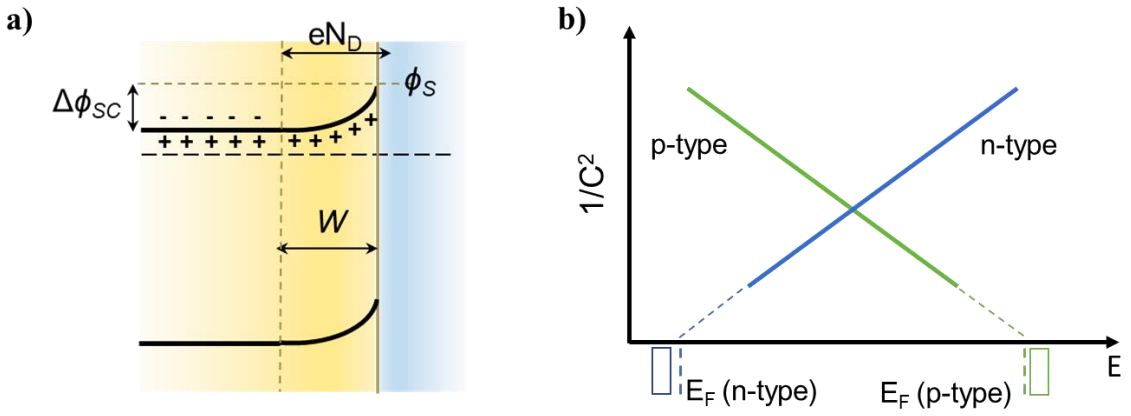

Figure 1.15. a) Charge distribution at the SCLJ in an n-type semiconductor, showing the depletion zone of width W. **b)** Representative Mott-Schottky plots for n-type and p-type semiconductor materials.

The presence of surface states (electronic states generally located inside the energy gap) affects the electronic at the SCLJ and, therefore, the processes occurring in this region

including charge accumulation, charge transfer, and recombination. In a pristine solid in vacuum conditions, surface states arise from the symmetry-breaking discontinuity of the crystalline lattice.[46] In contrast, extrinsic surface states arise from crystal defects or from bonding interactions when in contact with a liquid or solid phase. In the presence of surface states, the relationship between $\Delta\phi_{SC}$ and V is no longer linear, due to the change of the surface charge. For example, a sufficient density of surface states located close to the conduction band edge of an n-type semiconductor, leads to equilibration of the E_F in the bulk of the semiconductor material with the energy of these states rather than with E_{redox}, a phenomenon referred as *Fermi level pinning*. Since E_F is pinned to the surface states, any additional voltage –either provided by a more positive E_{redox}, or by an external V–, results in the charging of the surface states rather than an increase in band bending in the semiconductor. Although the key role that surface states play in reactions taking place at the semiconductor/liquid interface is recognized, their nature and catalytic impact are still under debate.[50-52]

1.3.5 The semiconductor/liquid interface under illumination.

So far, the behaviour of the semiconductor/liquid interface in dark conditions has been described. Now, the case of the semiconductor material in contact with a liquid, and under illumination, will be addressed (see **Figure 1.16**). As already described in the sections above, when an ideal semiconductor contacts the electrolyte, the equilibrium reached between the semiconductor E_F and the E_{redox} leads to a charge distribution, concomitant to the conduction and valence band bending along the depletion zone of width W. [53-54] In addition, photon absorption for $h\nu \geq E_g$ leads to the generation of an electron-hole pair, which can be separated due to the electric field at the depletion zone. Also, E_F splitting into separated quasi-Fermi levels ($E_{F,p}$ and $E_{F,n}$ for holes and electrons, respectively), leads to a (photoelectro-)chemical potential difference ($\Delta\mu_{eh}$), between the SCLJ and the counter electrode.[54-55] Solar-assisted water splitting requires for $q\Delta\mu_{eh}$ to exceed the water splitting redox potential, 1.23 V, (see reactions 1.1-3) plus the electrochemical overpotentials (η_{ox} for oxidation and η_{red} for reduction reactions respectively).[54] In particular, to drive the water oxidation reaction, four holes need to be transferred at the SCLJ of a n-type semiconductor acting as photoanode, as the one depicted in **Figure 1.16**.

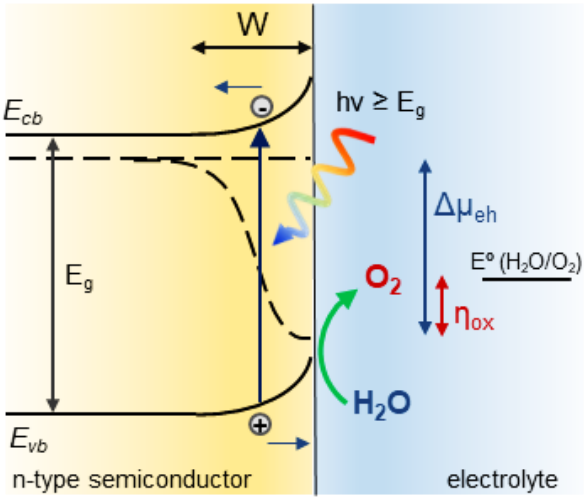

Figure 1.16. Schematic representation of an n-type semiconductor under illumination, acting as photoanode, in contact with a liquid electrolyte.

1.3.6 Current-voltage characteristic of the semiconductor/liquid interface.

Figures **1.17 a** and **b** summarize the concepts described so far for the semiconductor materials. For the interest of this thesis, most of the concepts have been addressed with an n-type semiconductor. Hence, **Figure 1.17a** and **b** show the band diagram of an n-type semiconductor in contact with the electrolyte in the dark and under illumination conditions, respectively.

In dark conditions, the current-voltage characteristic ($j-V$) of the SCLJ corresponds to that of a diode (see Section 1.3.4 for the effect of the applied potential). At reverse bias, (positive applied voltage), there is an energy barrier determined by the energy difference between the E_c and the E_F , that restricts the current density j_{dark} to small values, as represented in **Figure 1.17c**.

Under illumination, charge generation (G) leads to the E_F rise as depicted in **Figure 2.15b**. Consequently, the band bending is reduced, while near the SCLJ, E_F is split into the $E_{F,n}$ and $E_{F,p}$. The potential difference between the E_F and $E_{F,n}$ is also called photovoltage, ΔV_{ph}. The transfer of (photogenerated) holes to the electrolyte (ct) –or electrons accepted by the semiconductor– produces an electron flow, leading to a photocurrent density (j_G), that depends on the generation, collection and reaction rates at the SCLJ.[46, 55] Note that holes generated beyond the SCR have limited diffusion lengths, L_{min}, (Eq. 1.20), and if they reach the W, it is assumed that they will reach the surface to be transferred to the electrolyte. Also, direct charge injection from the valence band is considered (and not indirect charge injection from surface states).The ratio of the electron flux measured in the external circuit to the incident photon flux, Φ, which is referred as the External Quantum Efficiency (EQE) or Incident Photon-to-Current Efficiency (IPCE) is expressed as:

$$EQE = \frac{j_G}{q\Phi_{in}} = 1 - \frac{\exp(-\alpha W)}{1+\alpha L_{min}} \tag{1.27}$$

Where α is the absorption coefficient of the semiconductor material. Eq. 1.27 is also known as the *Gärtner equation*,[56] and assumes that there is no recombination at the SCLJ.

Since water oxidation is a four-hole reaction, this process leads to a positive j_G, which can be measured with a potentiostat. However, in real systems, recombination processes (rec) are difficult to eliminate. In consequence, the experimental photocurrent density, j_{ph}, is determined by the difference between the j_G and the current density related to charge recombination, j_{rec}.[46] In **Figure 2.15c,** the difference between the ideal and the experimental $j-V$ characteristic plots gives the j_{rec}. Furthermore, due to current density losses by charge recombination, the measured EQE is also much lower compared to that predicted by Eq. 1.27.

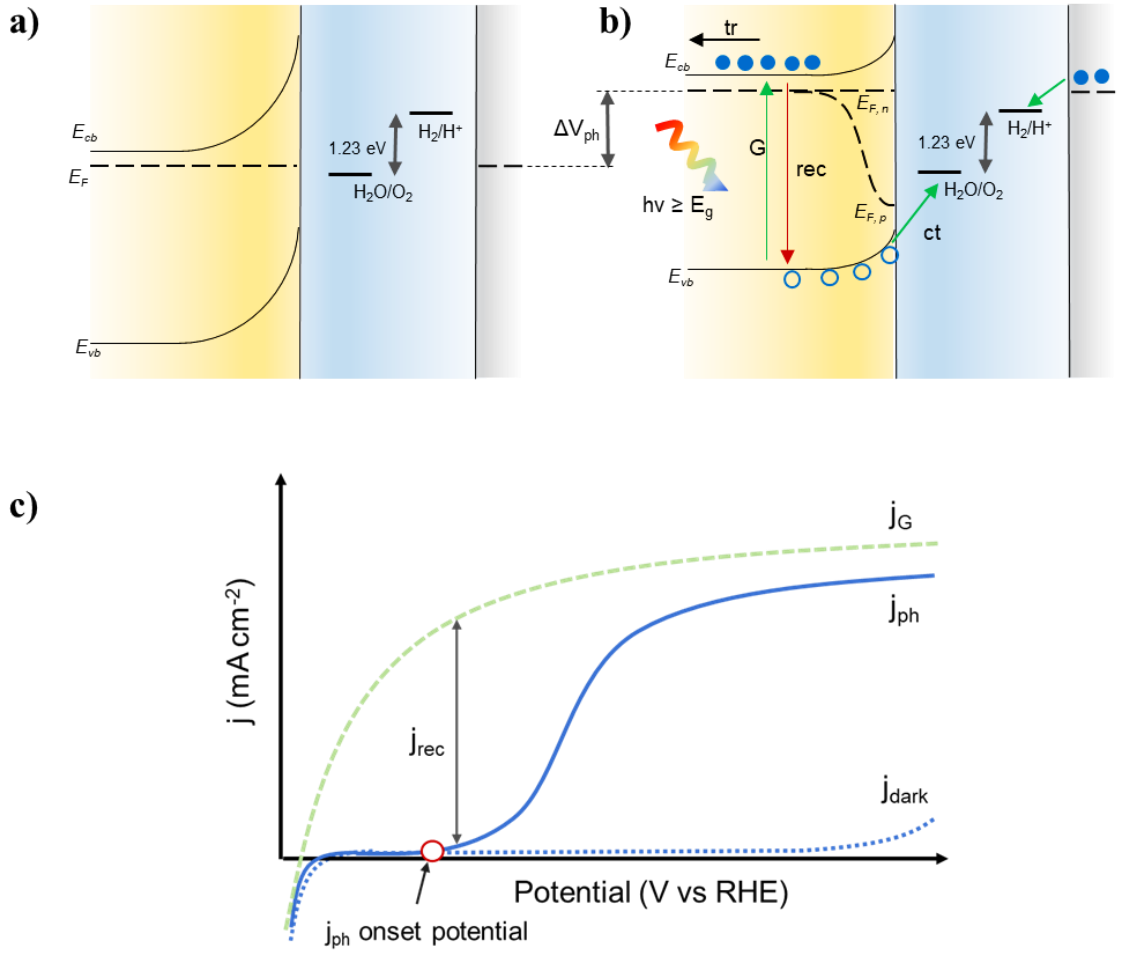

Figure 1.17. a) Energy diagram of a photoanode/electrolyte junction in the dark and **b)** under illumination conditions, where the fundamental processes taking place: G represents the charge generation, rec is the charge recombination, ct the charge transfer and tr the charge transport are represented. **c)** Representative $j-V$ plots of a photoanode: j_{dark} is the dark current density; j_G the ideal photocurrent density from the Gärtner equation and j_{ph} the experimental photocurrent density. The difference between j_G and j_{ph} gives the recombination current density, j_{rec}.

1.4. Metal oxide-based semiconductors for PEC water splitting.

The PEC technology, using photo-active semiconductor materials as photoelectrodes to drive the water splitting reactions, has significantly advanced toward the practical realization of solar fuel production.[53, 55, 57] Since the first demonstration of PEC water splitting by Fujishima and Honda in 1972 using TiO_2,[6] various semiconductor materials have been designed and prepared as photoelectrodes, but their efficiencies are still too low for practical application. Therefore, exploring suitable semiconductor photoelectrodes and modification strategies in order to achieve higher solar-to-fuel conversion efficiencies is still a challenge. This section is aimed at providing, in first place, the requirements that a semiconductor material should fulfill to be a candidate photoelectrode, as well as the state-of-the-art on semiconductor materials as photoanodes in PEC water splitting cells.

1.4.1 Requirements for efficient and stable photoelectrode photoelectrodes.

The intrinsic optoelectronic properties of a semiconductor material govern the photon absorption, charge separation in the bulk and electrode surface, and charge injection to the electrolyte, needed for efficient solar production of hydrogen or added-value chemicals. Therefore, an ideal semiconductor material should fulfill the following requirements for optimal performance as photoelectrode, and subsequent high solar–to–fuel conversion efficiency, including:

(i) *Strong visible light absorption:* The spectral region for light absorption is determined by the semiconductor E_g. As water splitting is not a spontaneous process but requires an energy supply of 1.23 eV, plus the overpotentials due to thermodynamic and kinetic losses, a minimum of 1.9 eV E_g value is required.[58] On the other hand, the maximum $E_g$value is determined by the solar spectrum, as shown in **Figure 1.18**. Since below 400 nm, the sunlight intensity falls abruptly, the absorption below this wavelength would use only a very small fraction of the solar spectrum.[58] Therefore, the optimal semiconductor E_g value have been considered must be between 1.9-3.1 eV (corresponding to 650-400 nm of the visible region, as represented with the grey area in **Figure 1.18**). However, it worth noting that 3.1 eV for the E_g will lead to photocurrents values too low (~ 3 mA cm^{-2}) for practical applications.

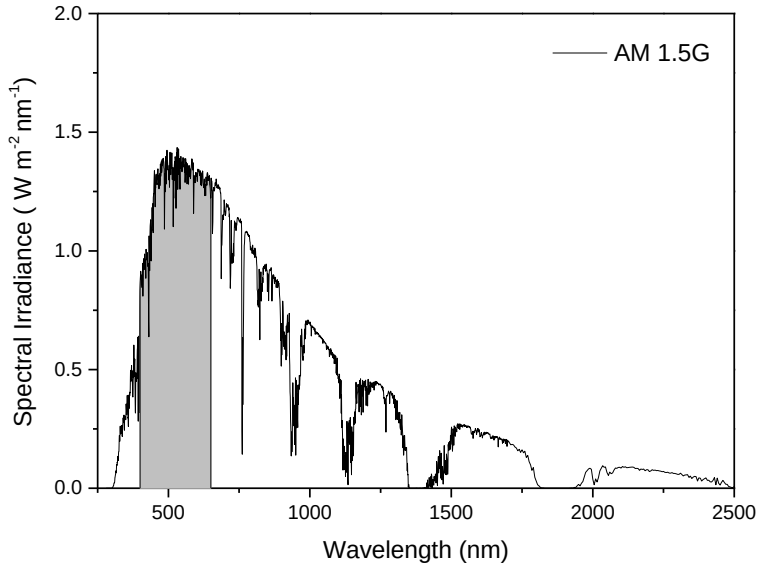

Figure 1.18. Reference Air Mass 1.5G Spectra for terrestrial solar spectral irradiance. Data source: NREL.[59] The grey area represents the interval for optimal E_g value of a semiconductor for PEC water splitting.

(ii) *Efficient charge separation and transport:* The photogenerated charges need to reach the semiconductor/electrolyte interfaces to drive the water splitting reaction. Consequently, an efficient charge separation at the SCLJ, and transport to the interfaces is required. This requirement depends on both the intrinsic properties –conductivity and carriers mobility– and the extrinsic properties –crystallinity, nanostructuring– of the material.[60] Therefore, materials with good conductivity and charge mobility are required in order to reduce losses due to electron-hole recombination, mainly in the bulk material.

(iii) *Effective charge injection:* For effective charge transfer to drive the oxidation or reduction reactions, an adequate alignment between the semiconductor band edge positions

and the redox potential of the reaction, is required. The semiconductor band edges must straddle the electrochemical potentials for water oxidation and hydrogen reduction: the valence band edge must be located below the water oxidation potential, to allow hole injection to drive the OER, while the conduction band edge must be located above the HER, driven by the electron injection.

(iv) *Low overpotentials:* Charge transfer at the semiconductor/electrolyte interface must be fast, to avoid charge accumulation at the surface, which increases the electron-hole recombination. Although several semiconductor materials have appropriate band-edge positions, the sluggish reaction kinetics at the bare semiconductor surface requires a stronger driving force, i.e. an overpotential, to drive the desired chemical reaction. In turn, the overpotential lowers the usable voltage output and hence, lowers the efficiency of the photoelectrode.[57]

(v) *High chemical stability:* For practical purposes, the semiconductor material should be stable in aqueous media for long times, in both dark and under illumination conditions. A semiconductor material is generally stable against oxidation by photogenerated holes if its oxidation potential is lower than the E_{vb} or the water oxidation potential. Likewise, a material is generally stable against reduction by photogenerated electrons if its reduction potential is higher than the E_{cb} or the hydrogen evolution potential.[61] However, several factors may affect the semiconductor stability, including the electrolyte composition and pH, the synthetic and deposition route, the presence of dopants and the oxygen stoichiometry.

(vi) *Low-cost processing and Earth-abundant components:* To be economically competitive with other fuel production technologies, the semiconductor materials for PEC water splitting must be obtained through low cost and environmentally friend synthetic routes, from Earth-abundant and non-toxic materials. That includes low-temperature and easily controllable synthesis and post-synthetic treatments. **Figure 1.19** shows the relative abundance of chemical elements on the Earth's upper continental crust. Clearly, transition metal-based compounds, including Ti, Fe, Mn, Co, Ni, W, etc.., are the most attractive candidates due to their relative abundance.

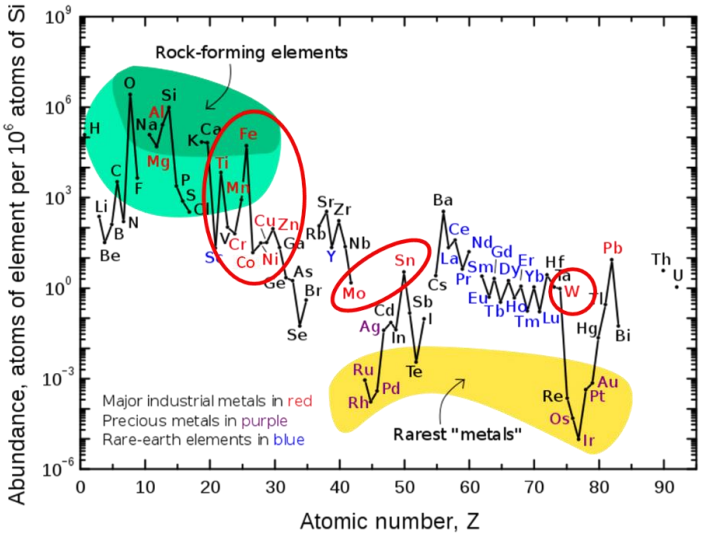

Figure 1.19. Abundance (atomic fraction) of the chemical elements in Earth's upper continental crust as a function of atomic number. Figure adapted with permission from reference [62].

Although the photo-electrocatalytic properties of several semiconductor materials have been extensively investigated, there is not a single material fulfilling all the requirements listed above. **Figure 1.20** shows the energy diagram for several semiconductor materials. Materials like $BiVO_4$ and α-Fe_2O_3 stand as semiconductor metal oxides with sufficient band gap value for light absorption, and adequate valence band position for water oxidation. However, their poor electronic properties hamper the practical realization of water oxidation at high efficiency. The requirement of high conductivity and charge mobilities in the bulk material along with adequate surface properties for fast charge transfer, constitute the main barriers for efficient solar conversion with these materials. On the other hand, photo-corrosion is a major problem for many candidate water splitting semiconductors, in particular metal sulfides, as depicted in **Figure 1.20**.[60] However, common photoanode materials such as TiO_2 and α-Fe_2O_3, even when their anodic deposition potential is above the E_{vb}, are thermodynamically stable because of their very slow decomposition reaction kinetics.[60]

Facing those challenges involves the discovery of new materials with unique properties for PEC water splitting or the improvement of the existing materials with different strategies comprising: doping, the introduction of suitable co-catalysts, heterostructuring, etc…, which will be detailed in Section 1.4.2. In this context, the engineering of novel semiconductor materials remains as a prevalent challenge for competitive PEC performance.

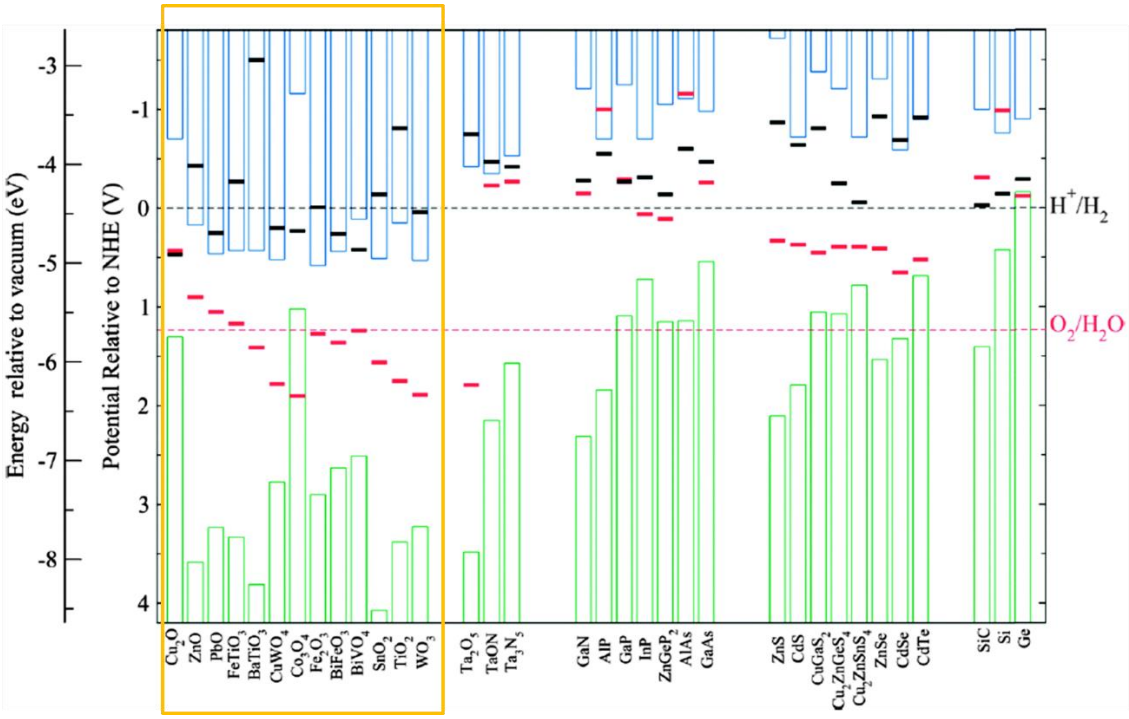

Figure 1.20. Band structure of some semiconductor materials, relative to the NHE and vacuum levels pH=0. Red and black bars represent the calculated oxidation and reduction potentials in solution at pH=0 and ambient temperature, which define the thermodynamic stability of photoelectrodes against photo-corrosion. Promising metal oxide-based materials for OER are highlighted. Figure adapted with permission from reference [61].

1.4.2 Metal oxide-based photoanodes for PEC water splitting.

From Eq. 1.1 and 1.2 it is clear that the OER is the more challenging step of the overall water splitting process, due to the kinetic and thermodynamic limitations as a result of the participation of four holes. Therefore, the efficient operation of the photoanode is a fundamental requirement for efficient Solar-To-Hydrogen conversion in PEC water splitting cells.[54] As discussed above, an oxygen-evolving photoanode must be an n-type semiconductor, such that the electric field generated by the band bending drives holes toward the surface. Several metal oxides from transition elements have shown attractive features to become promising candidates as photoanodes, including suitable optical properties and high stability (see **Figure 1.20)**.[19, 63] In addition, there are well stabilized low-cost synthetic routes to prepare a variety of metal oxide with a wide range of optoelectronic properties.[19]

Moreover, among the semiconductor materials investigated as photoanode for PEC water splitting, $BiVO_4$ has received great attention, due to its suitable E_g value, 2.4–2.5 eV, which allows visible light absorption up to 590 nm, together with its low cost and non-toxicity.[64] This E_g value predicts a theoretical maximum photocurrent density of 7.5 mA cm^{-2}, which is translated into a 9% STH efficiency.[42] Therefore, in the context of the present PhD thesis, the discussion about materials and strategies for efficient PEC performance will be focused on metal oxide semiconductors as photoanodes for the water oxidation reaction, with especial attention to $BiVO_4$.

Due to the requirement of stability under oxidizing conditions, most of the photoanode materials that have been investigated are metal oxides (see **Figure 1.20**, materials highlighted), or metal oxide anions (oxometallates) in pure, mixed, or doped forms. A general trend in the electronic structure of these oxides and oxometallates is that the valence band consists of O 2p orbitals, and the conduction band is formed by the valence orbitals of one or more metals.[57] As a consequence, E_{vb} stays relatively unchanged at 3.0±0.5 *vs* NHE for most metal oxides including TiO_2, WO_3 and Fe_2O_3. The OER requires that E_{vb} lies below the water oxidation potential, to allow holes to diffuse to the SCLJ to oxidise water. Therefore, the disparity between E_{vb} of some metal oxides and the water oxidation potential represents a major challenge for the development of high-performance photoanodes.[57] As a consequence, the poor charge transfer and separation properties leading to sluggish kinetics, naturally hamper the PEC activity of metal oxide photoelectrodes.[63] On the other hand, the band alignment of $BiVO_4$ is strategically more convenient compared to other metal oxides, providing a smaller E_g that allows accessing to a wider fraction of the solar spectrum.[65]

$BiVO_4$ has three main crystal forms: monoclinic scheelite, tetragonal zircon-type and tetragonal scheelite structure, being the monoclinic scheelite, represented in **Figure 1.21a**, the most commonly used structure in photocatalysis because of its highest photoactivity compared to the other polymorphs.[66] It worth to note that, an irreversible transition from the tetragonal zircon-type to the monoclinic scheelite structure occurs at the calcination temperatures of 400–500°C, which is considered in most of the synthetic strategies for $BiVO_4$ preparation.[65] The poor electron mobility observed in $BiVO_4$ (~0.01 $cm^2\ V^{-1}s^{-1}$)[67] has been related to the disconnection of the VO_4 tetrahedra in the $BiVO_4$ structure, which constrains the efficient flow of the photogenerated electrons towards the conducting support.[68] In contrast, a long carrier lifetime of 40 ns has been reported in $BiVO_4$ photoanodes, which translates into a relatively long L_{min} of 70 nm.[67] The optical properties of $BiVO_4$ have been also extensively studied, in particular the nature of it fundamental band gap. Cooper and co-workers determined that the fundamental bandgap of monoclinic

scheelite $BiVO_4$ is indirect, by using a range of spectroscopic measurements (**Figure 1.21 b** and **c**).[69] However, since the direct band gap is slightly larger than the indirect band gap, $BiVO_4$ is considered a direct band gap semiconductor.

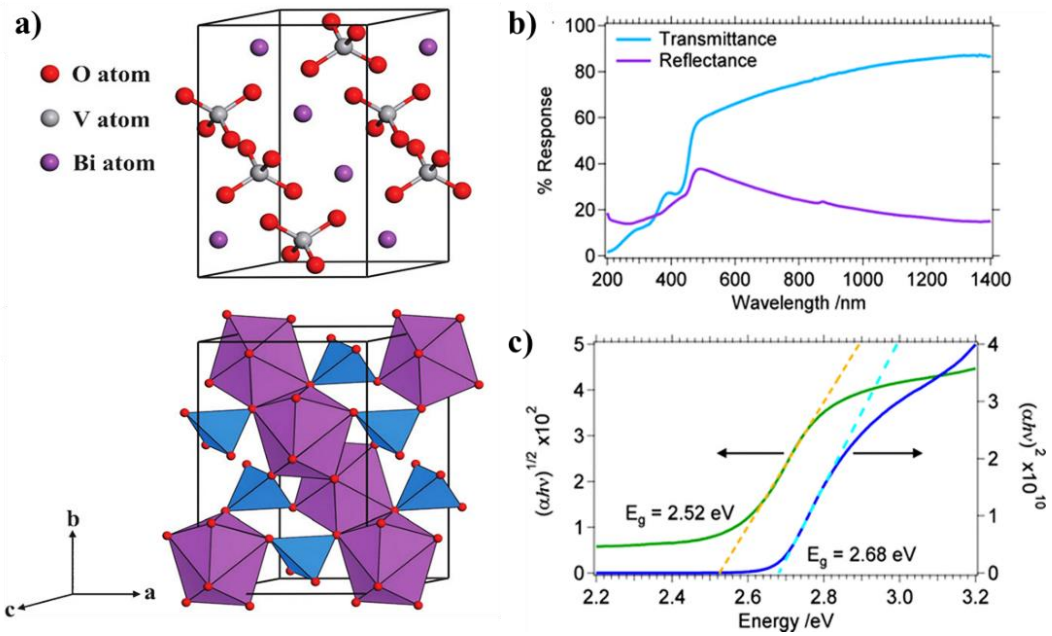

Figure 1.21. a) Unit cell of the monoclinic $BiVO_4$ crystal structure, formed by VO_4 tetrahedron and BiO_8 dodecahedron. Figure adapted with permission from reference[68]. **b)** Transmission and reflection plot of monoclinic $BiVO_4$. **c)** Band gap calculations for indirect (left axis) and direct (right axis) transitions. Figures adapted with permission from reference [69].

Regarding stability, the calculated oxidation potential of $BiVO_4$ is predicted to be slightly more positive than the water oxidation potential, as showed in **Figure 1.20**, suggesting that this material could be resistant to photoinduced corrosion under water splitting conditions.[61] However, several reports have demonstrated its photoelectrochemical instability in both near-neutral and alkaline pH conditions.[70-72] While the bulk chemical instability has been attributed to kinetic factors that limit room-temperature structural transformation of the V-deficient degradation product into a stable Bi oxide phase, the photodegradation has been related to the accumulation of holes at the surface of $BiVO_4$ that destabilize the lattice and increase the dissolution rate.[71] However, in several reports the photo-corrosion of $BiVO_4$ has been also correlated with vanadium leaching from the surface into the electrolyte solution.[72] Nonetheless, the poor photochemical stability of $BiVO_4$ undermines its practical application in large-scale integrated devices, adding a further challenge for the technological deployment of this material.

1.4.3 Strategies for improved efficiency and stability of metal oxide-based photoanodes.

The drawbacks of the metal oxide-based semiconductors as photoanode, including the $BiVO_4$, have been tackled trough different strategies attending to the particular needs of each material:[16, 19, 43, 58, 60, 73] *(i)* morphology and size control of the semiconductor material; *(ii)* introduction of dopants; *(iii)* combination of both or more semiconductors to form a

heterostructured photoelectrode; *(iv)* deposition of surface co-catalyst layers or (nano)particle dispersions. Alternatively, other methods[74-75] such as *(v)* attachment of quantum dots as sensitizers, [19] *(vi)* control of the crystal orientation,[76] and *(vi)* application of post-synthetic treatments have been employed.[77] Usually, different strategies can be simultaneously employed in order to achieve the higher PEC performance on the photoelectrode. Since there are several recent reviews in the literature concerning the development of photoanodes for water splitting employing the above-mentioned strategies, herein the focus will be given to those strategies more relevant in the context of this thesis.

1.4.3.1 Morphology and size control.

The optoelectronic properties of the semiconductors are strongly dependent on their sizes and morphology.[19, 57-58, 73, 78] Therefore, controlling the morphology at the surface of the electrode is crucial for light absorption, surface recombination, and the (photo-) electrochemical active area when designing high-performance photoelectrodes. The photo-absorber must be thick enough to absorb all the incident light and possess good structural properties so that the excited minority carriers that are photogenerated in the bulk are able to diffuse to the surface (see Eq. 1.20). As depicted in **Figure 1.22a,** in a planar device the photogenerated carriers must traverse the entire thickness of the material, $\sim 1/\alpha$, before collection. In a rod-array material as shown in **Figure 1.22b**, the carriers must only reach the rod surface before recombination (increased L_{min}). Several works have shown that a high surface area in semiconductor structures with short minority carrier diffusion lengths, reduces the distance that minority carriers must travel and hence, the electrocatalysis losses in the form of overpotentials are also reduced, leading to near-unity collection efficiencies.[57] It worth noting that, the increased surface area can also lead to increased recombination at surface defects. Therefore, for improved overall performance, the surface area needs to increase without proportionally increasing the density of surface defects.[79] Nevertheless, micro- and nanostructuring as strategies for morphology and size control have been successfully applied in semiconductor materials with poor electronic properties, such as $BiVO_4$ and α-Fe_2O_3.[80] **Figure 1.22b** shows a dual bandgap system $WO_3/BiVO_4$, where porous $BiVO_4$ film allows the contact of the electrolyte to the bottom layer with enhanced surface area, promoting the oxidation reaction. Whereas, one-dimensional (1D) WO_3 nanorods, directly grown on the FTO substrate, are advantageous for transporting electrons to the back contact. Furthermore, as shown in **Figure 1.22c** the magnitude of the photocurrent enhancement was associated with the morphological changes induced by the different preparation conditions.[81]

In addition, it was demonstrated by Kim and co-workers that nanoporous morphology on bare $BiVO_4$ photoelectrodes can effectively suppress bulk carrier recombination.[70] Such enhancement was achieved by improving the synthetic process, specifically with the substitution of the vanadium precursor solvent to dimethylsulfoxide (DMSO). Moreover, Kan and co-workers further improved the $BiVO_4$ deposition technique, by preparation of high-surface-area dendritic Bi electrodes, instead of the previous BiIO, via electrodeposition, with subsequent drop-casting of the vanadium precursor previously optimized. [82] This synthetic method is nowadays one of the most popular for the preparation of $BiVO_4$ photoelectrodes. Further details about the experimental procedure of this synthetic method will be provided in **Chapter 2**.

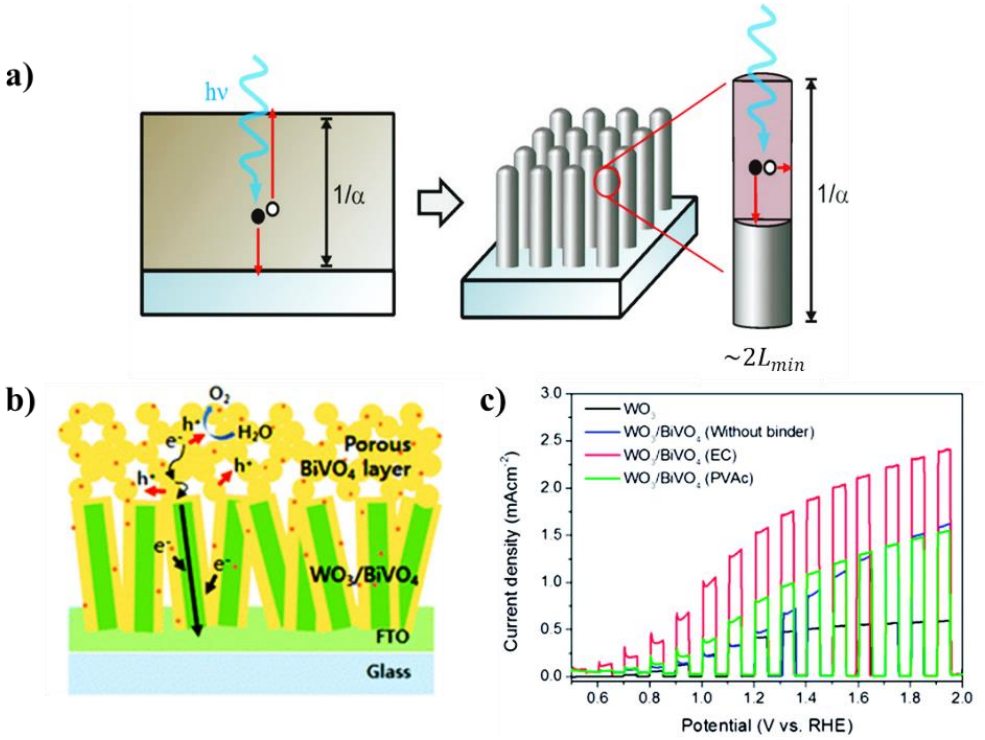

Figure 1.22. a) Effect of nanostructures arrays in the L_{min}. Figure adapted with permission from reference [57] **b)** Dual bandgap system formed by 1D WO_3 nanorods bottom layer and porous $BiVO_4$. **c)** Photocurrent densities of WO_3 and $WO_3/BiVO_4$ photoanodes using various organic binders Figures b) and c) are adapted with permission from reference [81].

1.4.3.2 Doping.

Depending on the type and nature of the impurity, doping a semiconductor may have different effects, including: the extension of optical absorption toward longer wavelengths; improved adsorption of the chemical species at the surface; enhancement of the electrical conductivity and hence, of the efficient separation of photogenerated charge carriers.[83] It has been reported that charge carriers in metal oxides tend to be localized as small polarons, leading to a polaron-hopping transport mechanism predominant in metal oxides.[84] Consequently, the mobility of majority carriers in metal oxides is generally low. In a photoanode, this effect can affect the electrons collection at the back contact, leading to increased bulk recombination losses. Therefore, extrinsic doping is often used to improve the optoelectronic properties of semiconductors. For example, optimal Cr doping of $Cu_3V_2O_8$ photoanodes,–an attractive semiconductor material due to the Earth-abundance of its components–, leads to improved electronic properties, particularly reflected on an increased charge separation efficiency.[85] Cr has an atomic radii of 0.74Å, close to that of Cu^{2+} (0.73Å), making feasible the exchange of both atoms on the crystalline structure, enhancing the extrinsic n-type doping of the $Cu_3V_2O_8$.

Doping can also promote the optical and catalytic properties of the photoelectrode. Recently, the homovalent doping of TiO_2 nanotubes with Zr was reported,[86] which in combination with annealing treatment in vacuum conditions, leads to the creation of surface oxygen vacancies that enhance the optical scattering, which slightly enhances the light harvesting efficiency. More relevant, those strategies induced a surface stress and an anodic band shift, both beneficial effects for the enhanced photo-electrocatalytic activity of the TiO_2 nanotubes toward water oxidation.[86]

Metal doping into $BiVO_4$ can significantly minimize recombination losses by enhancing the mobility of photoinduced charge carriers.[64] Parmar and co-workers screened several dopants (Mo, W, Ti, Cr, Fe, Zn, Nb, Ru, Pt, Sn, Ce, and Ta) in $BiVO_4$ photocatalyst, covering most common cationic elements. As shown in **Figure 1.23a** and **b**, they observed a drastic improvement in the visible-light induced water oxidation activity with W and Mo doping.[83] Consequently, W and Mo have been the most common dopants in $BiVO_4$ photoelectrodes, and the beneficial doping effect has been enhanced by complementary strategies.[87-90] In spite of the substantial improvements in the PEC performance reported for doped $BiVO_4$ photoanodes, the nature of such effect, especially on the catalytic activity, is often difficult to clarify. In recent studies, experimental and theoretical studies suggested that W doping improves both bulk charge separation and surface charge transfer. The enhanced bulk charge separation was related to the improved carrier density resulting from W doping. In addition, W doping promotes the V atoms to be active reaction sites, as shown in **Figure 1.23c**, which promotes the adsorption of species involved in the water oxidation process. Consequently, the surface charge transfer resistance is significantly decreased.[87] On the other hand, the increased charge separation efficiency with Mo doping has been related to a decrease of trap states, together with the improved carrier mobility resulting from the increase of electron density. Transient absorption spectroscopy (TAS) measurements showed that both electron and hole traps are reduced upon Mo doping, inhibiting the electron–hole recombination.[90] The effect of doping on the surface states was also reported in In-doped $BiVO_4$ photoanodes. Density functional theory (DFT) calculations indicate that In^{3+} partially substitute Bi^{3+} sites. Such substitution passivates surface states of $BiVO_4$ and thus inhibiting the surface charge recombination, improving the PEC water oxidation activity.[91]

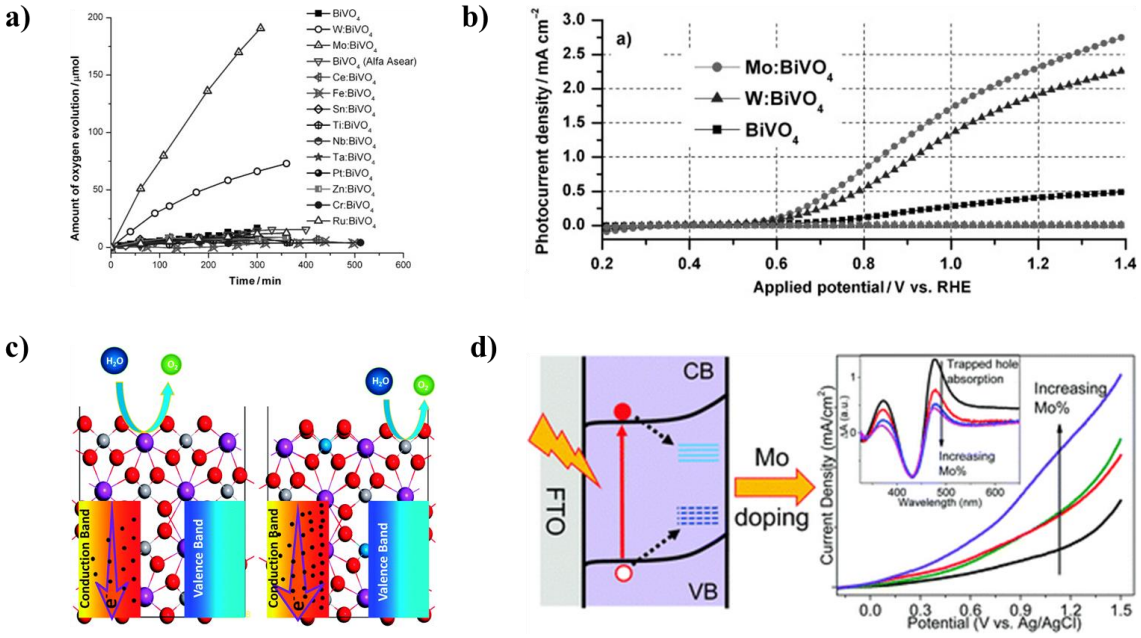

Figure 1.23. a) Screening of different dopants in $BiVO_4$ photoelectrodes, presented as evolved O_2 from the photoelectrochemical water oxidation reaction and **b)** Current densities with optimal W- and Mo-doped photoanodes. Figures adapted with permission from reference [83] **c)** Proposed mechanism of the effect of W doping on the performance of the $BiVO_4$ photoanodes. **d)** Effect of Mo-doping of $BiVO_4$ in surface trap states. Figures c) and d) are reprinted with permission from references [87] and [90]respectively.

Non-metal doping in $BiVO_4$ photocatalyst has been also reported, using P,[92] C,[93] S,[94] or N atoms[95] acting as anionic dopants that enhance the catalytic activity. More recently, doping with rare elements as Gd has been reported in PEC water oxidation [96], leading to significant improvements in the overall performance of the photoelectrode.

1.4.2.3 Heterostructures.

Another common strategy to enhance the photoelectrodes performance is the combination of different materials to harvest the qualities of all of them, in the form of heterojunctions. For example, a conductive and high surface area support material (host) can be coated with a highly dispersed visible light absorber (guest), leading to a guest-host systems,[97] as that presented in **Figure 1.22b**. In particular, the $WO_3/BiVO_4$ heterojunction has attracted significant attention, due to the highest water oxidation photocurrents obtained (6.72 $mA \cdot cm^{-2}$ at 1.23 V vs RHE), close to the theoretical maximum (7.5 $mA \cdot cm^{-2}$).[98] This heterojunction synergistically combines the excellent conductivity of WO_3 with the good absorption properties of $BiVO_4$, in a favorable type-II band alignment (see **Figure 1.24a**) to promote charge separation leading to a significant reduction of charge recombination.[99] Similar architecture was reported with $Ta:TiO_2/BiVO_4$ nanowire photoanode, in which $BiVO_4$ acts as a visible light-absorber and $Ta:TiO_2$ acts as a high surface area electron conductor, as shown in **Figure 1.24b**.[97] Several heterojunctions explored for $BiVO_4$ photoanodes have been discussed in a recent review about the role of overlayers and underlayers on $BiVO_4$ photoanodes.[100]

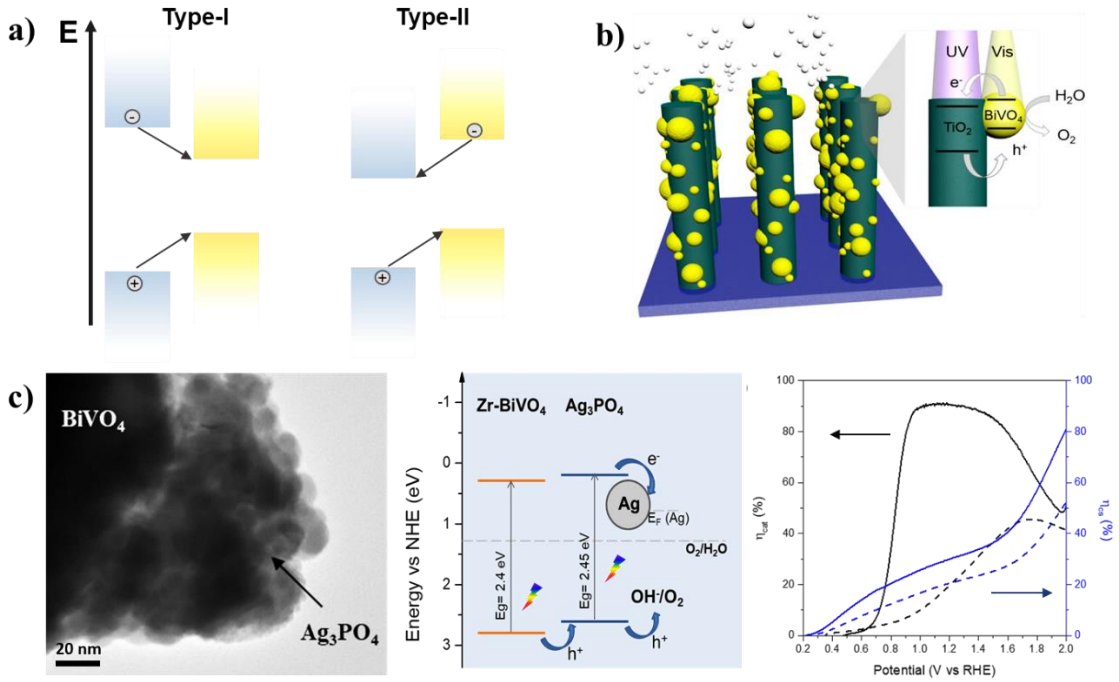

Figure 1.24. a) Representation of the type-I and type II band alignments. **b)** $Ta:TiO_2/BiVO_4$ nanowire heterostructure photoanode. Figure adapted from reference [97]. **c)** Ag_3PO_4 nanoparticle over Zr-$BiVO_4$ **d)** Band alignment (type-II) between the materials forming the $Ag/Ag_3PO_4/Zr\text{-}BiVO_4$ heterostructure. **e)** Enhanced charge injection efficiency (η_{cat}) in the $Ag/Ag_3PO_4/Zr\text{-}BiVO_4$ (straight black line) photoanode, compare to bare Zr-$BiVO_4$. Figures c)-e) are adapted with permission from reference [101].

More recently, the enhanced performance of Zr-$BiVO_4$ photoanodes through the Ag/Ag_3PO_4/Zr-$BiVO_4$ heterostructure, was reported [101] as showed in **Figure 1.24c**. Such heterostructure allowed to achieve a remarkable enhancement of the charge injection efficiency, up to nearly 90%. It was demonstrated that the increase of above-band gap absorbance and the decrease of surface losses after the optimized deposition of Ag/Ag_3PO_4 nanoparticles were responsible for this notable performance.

Moreover, the construction of heterostructures allows exploring novel applications, beyond the classical solar conversion to chemicals, for example, solar storage using photoanodes. Such is the case of the photo-capacitive system based on the $BiVO_4$/PbS type-II heterostructure, as depicted in **Figure 1.25a** and **b,** which after controlled oxidation evolves to $BiVO_4/PbO_x$. The $BiVO_4$ acts as the photoactive core, while the photogenerated holes are subsequently stored in a capacitive PbO_x top layer. This storage platform is obtained through controlled photo-oxidation of PbS quantum dots. The resulting $BiVO_4/PbO_x$ system is capable of converting and storing solar energy within an intrinsically single structure with outstanding stability toward charge–discharge cycling and fast charge rate without applying any electrical bias under only solar illumination.[102]

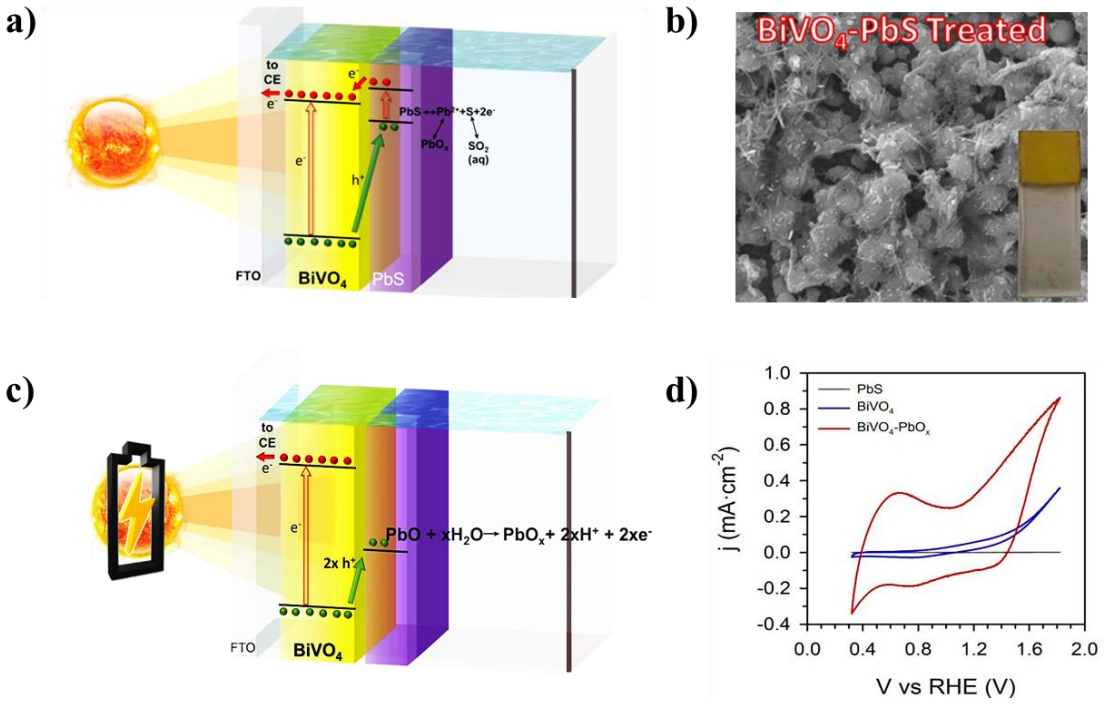

Figure 1.25. a) The $BiVO_4$/PbS heterostructure, and evolution from PbS to PbO_x through controlled oxidation. **b)** SEM image of the $BiVO_4$/PbS photoelectrode after the oxidation treatment. **c)** Photo-charging mechanism of the resulting $BiVO_4/PbO_x$ photocapacitor. **d)** Synergic effect of both semiconductor on the photocapacitor performance. Figures adapted with permission from reference [102].

1.4.2.4 Surface co-catalysts.

As shown in reaction 1.1 and **Figure 1.16,** water oxidation suffers from a kinetic barrier associated to the participation of four electrons to drive the reaction. Thus, a common strategy to improve the performance of photoanodes is the incorporation of co-catalytic materials at the photoactive semiconductor surface, in order to boost the reactions kinetic at the SCLJ by reducing the η_{ox} by improving the charge transfer at the SCLJ. The addition

of catalyst particles fundamentally changes the energetics of the electron transfer process at the semiconductor surface, as shown in **Figure 1.26**, favoring the charge injection to the electrolyte. Usually, the co-catalysts are deposited as thin layers or as dispersed nanoparticles, to avoid excessive light absorption or reflection, and preserve the desired interfacial energetics.

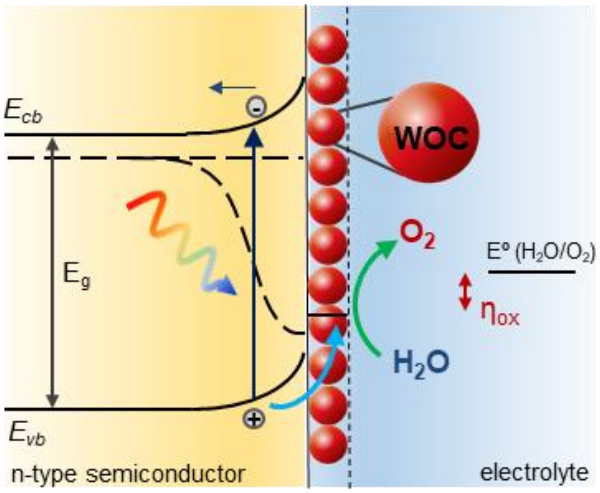

Figure 1.26. Schematic representation of a photoanode formed by an n-type semiconductor and a surface co-catalyst.

Noble metal-based catalysts such as IrO_2 and RuO_2 are among the highest performing water oxidation evolution catalysts in neutral and acid media, respectively, but are prohibitively expensive due to their low Earth-abundance (see **Figure 1.19**). In recent years, significant effort has concentrated on developing low-cost first-row transition metal oxide OER catalysts. Therefore, catalysts composed by Earth-abundant materials, such as the Co, Ni and Fe oxide/hydroxide, have emerged as affordable and efficient candidates.[19, 54]

Co-based electrocatalysts have emerged as affordable and efficient electrocatalysts, which can be easily deposited by electro- and photo-depositions methods, from Co^{2+} solutions at relatively low overpotentials.[19] The cobalt phosphate (Co-Pi) has been widely explored as co-catalyst for OER in combination with metal oxide photoanodes as α-Fe_2O_3, $BiVO_4$ and WO_3, resulting in improved PEC performances, comparable to those achieved with noble metal catalysts.[19] The highest performance for a $BiVO_4$ photoelectrode was reported by Pihosh and co-workers, with a WO_3/$BiVO_4$/Co-Pi core-shell nanostructured photoanode, represented in **Figure 1.27a**, that nearly achieved the maximum theoretical water splitting efficiency due to the combination of several strategies such as nano-structuring, heterostructured design and use of a surface co-catalysts.[45] With this system, a photocurrent of 6.72 mA cm^{-2} was obtained under 1 sun illumination at 1.23 V $_{vs}$ RHE, see **Figure 1.27b**, corresponding to ~90% of the theoretically possible value for $BiVO_4$.

Despite several authors have reported an increased charge injection efficiency and consequently, enhanced water oxidation kinetics when using Co-Pi modified photoanodes[103-104], the origin of such improvements is not yet fully understood and is currently under debate, since two different mechanisms can explain the observed enhanced photoelectrochemical behavior: *(i)* suppression of surface recombination at the SCLJ,[103] and *(ii)* "true" catalytic activity via Co-Pi enhancing charge transfer kinetics. From one side, it has been reported that Co-Pi did not significantly contribute to the overall water

oxidation photocurrent. A detailed mechanistic study was carried out by Durrant and co-workers using Photo Induced Absorption Spectroscopy (PIAS) and Spectro-electrochemistry (SEC). The significantly larger PIAS signal observed on Co-Pi modified $BiVO_4$, was attributed to additional photoinduced species, rather than to photogenerated holes in $BiVO_4$. The analysis of both techniques revealed the hole transfer kinetics from $BiVO_4$ was still faster compared to that via Co-Pi oxidation states. Hence, it was concluded that Co-Pi did not significantly contribute to the overall water oxidation photocurrent, which was instead enhanced by the capability of Co-Pi to retard electron/hole recombination at the $BiVO_4$/solution interface.[105] Similar conclusions were obtained by Abdi and co-workers, using Incident Modulated Photocurrent Spectroscopy (IMPS) and in situ UV-Vis absorption measurements.[51] On the other hand, different insights were observed by Boettcher and co-workers, through Atomic Force Microscopy (AFM) and dual-working electrode measurements. In this study, Co-Pi was found to act as a hole reservoir of photogenerated charges at $BiVO_4$, behaving as a "true" oxygen evolution catalyst, since holes involved in the oxidation of water are first transferred to the Co-Pi catalyst, whereby OER does not take place on the $BiVO_4$ surface.[52]

Ni-based oxides and oxyhydroxides have been also extensively studied as OER electrocatalyst in alkaline conditions (pH 13-14). NiO_x films generally convert to either $Ni(OH)_2$ or NiOOH during the water oxidation reaction in alkaline electrolytes, according to:

$$Ni(OH)_2 + OH^- \leftrightarrow NiOOH + H_2O + e^- \quad (1.28)$$

NiO_x and $Ni(OH)_2$ can be converted to NiOOH, the active phase for OER, through consecutive CV scans.[106] Moreover, it has been reported that Fe impurities from the electrolyte can spontaneously incorporate into NiOOH during the water oxidation reaction, considerably enhancing its catalytic performance.[107] Despite the clear positive effect of Fe incorporation, its nature is not clearly understood. Therefore, several studies are still under progress in order to provide a reasonable explanation for the role of Fe incorporation on Ni-based catalysts.

Ni and Fe oxyhydroxide electrocatalysts have been applied to $BiVO_4$ photoelectrodes. Kim and co-workers reported a remarkable enhanced PEC performance in $BiVO_4$ photoanodes with a dual-layered catalyst (NiOOH/FeOOH),[70] as depicted in **Figure 1.27c**. Experiments using a sacrificial agent showed that, although NiOOH shows faster water oxidation kinetics as an electrocatalyst, the interface recombination at the $BiVO_4$/NiOOH junction is more substantial compared to that at the $BiVO_4$/FeOOH junction. After optimization and understanding the $BiVO_4$/catalyst and catalyst/electrolyte interfaces, the optimal performance was obtained with the dual structure NiOOH/FeOOH/ $BiVO_4$.[70] Remarkable performance has also been reported with the combination of CoO_x and NiOOH as co-catalyst in $BiVO_4$ photoelectrodes,[108] showed in **Figures 1.27d** and **e**. Here, the in situ formation of NiOOH at the photoanode, prior deposition of NiO by atomic layer deposition, enables the formation of a hydroxyl-rich and hydroxyl-ion permeable surface, leading to a dual catalytic effect of CoO_x and NiOOH for improved OER activity.[108] Moreover, CoO_x deposited by atomic layer deposition, has also been reported as surface catalytic and protective layer against photo-corrosion in $BiVO_4$ photoanodes, resulting in a remarkable improvement of PEC performance compared to pristine $BiVO_4$.[109]

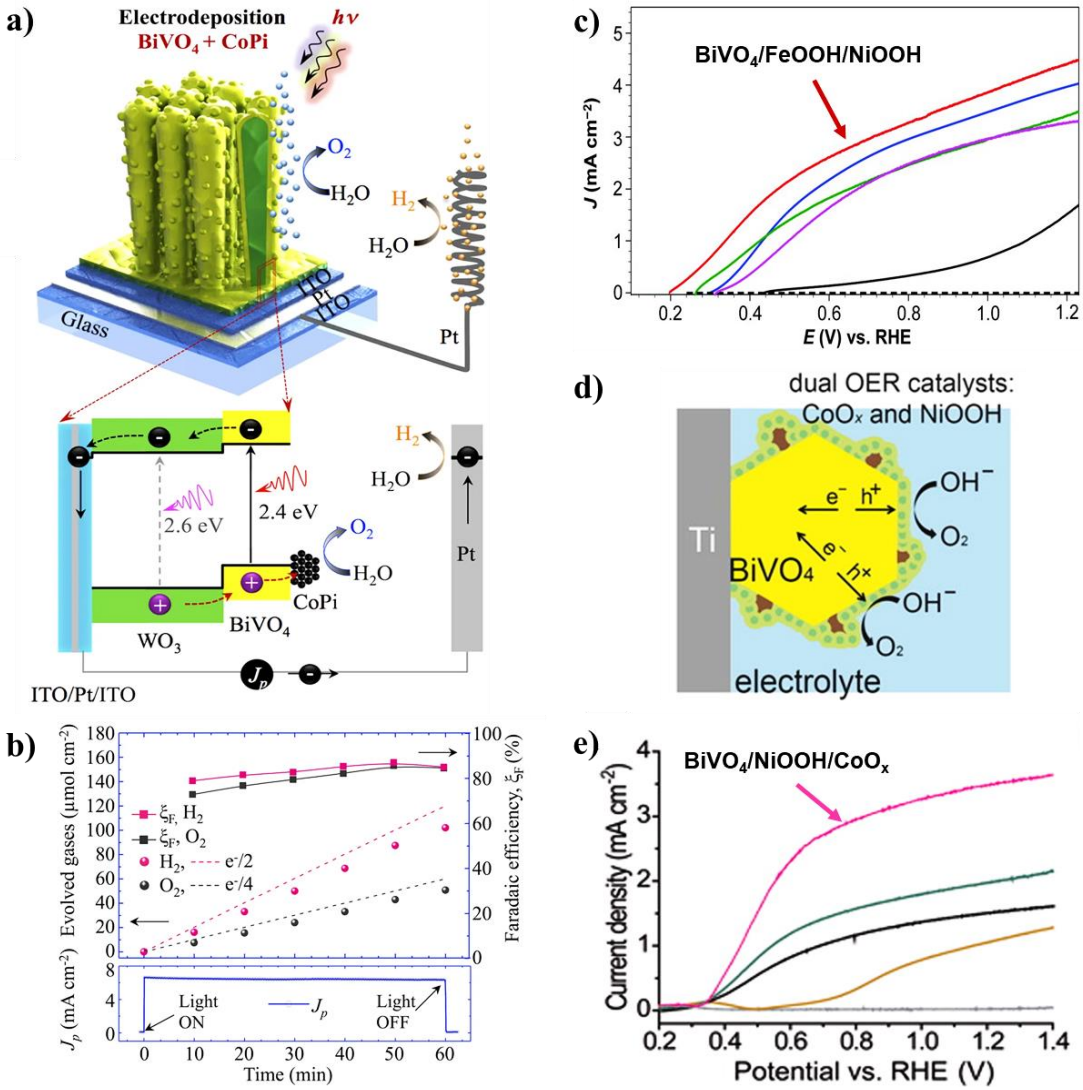

Figure 1.27. a) Schematic illustration of a core-shell $WO_3/BiVO_4$/Co-Pi photoanode, fabricated by glancing angle deposition (GLAD) of WO_3 nanorods, followed by electrodeposition of $BiVO_4$ and Co-Pi. **b)** Gas evolution rates (circles) and FE (rectangles) at 1 sun. Figures adapted with permission from reference [45]. **c)** $j-V$ plots of $BiVO_4$ photoanodes modified with NiOOH and FeOOH electrocatalysts in a 0.5 M phosphate buffer (pH 7). The best performance was obtained with the dual-layered $NiOOH/FeOOH/BiVO_4$ (red curve) photoelectrode. Figure adapted with permission from reference [70]. **d)** Representation of recombination/separation processes of the photogenerated carriers in a $NiOOH/NiO/CoO_x/BiVO_4/Ti$ photoanode. **e)** $j-V$ plots of $BiVO_4$ photoanodes modified with NiOOH and CoO_x co-catalysts, where the best performance with the $NiOOH/NiO/CoO_x/BiVO_4/Ti$ photoanode is highlighted. Figures d)-e) were adapted with permission from reference [108].

On the other hand, although different Fe-based catalysts have been investigated as co-catalysts in water oxidation photoanodes, the use of α-Fe_2O_3 nanoparticles as OER catalyst in combination with $BiVO_4$ as photoanode has been less explored. Shaddad and co-workers reported a remarkable enhancement of the water oxidation kinetics in $BiVO_4$ photoanodes, due to the cooperative catalytic effect of monoclinic ZrO_2 and α-Fe_2O_3 nanoparticles, as represented in **Figure 1.28**.[110] Both the optimized photoelectrode and their preparation route –electrochemical deposition with the sequential addition of Zr and Fe precursors– provides a versatile and fully reproducible platform, facile to scale-up on large area conductive substrates with attractive implications for technological deployment.[110]

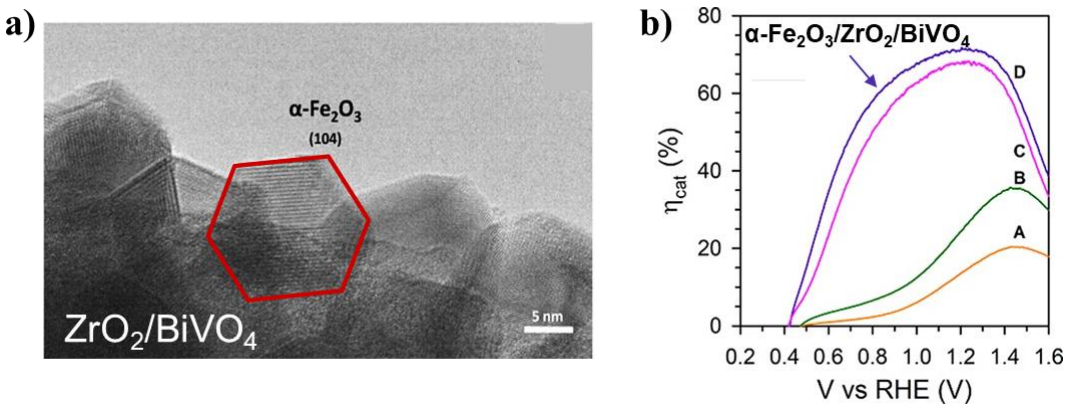

Figure 1.28. a) Nanostructured α- Fe_2O_3 particles over $ZrO_2/BiVO_4$. **b)** Improved charge injection efficiency with the α-$Fe_2O_3/ZrO_2/BiVO_4$. The labels correspond to A: reference $BiVO_4$, B: $ZrO_2/BiVO_4$, C: α-$Fe_2O_3/BiVO_4$, and D: α-$Fe_2O_3/ZrO_2/BiVO_4$. samples. Figures adapted with permission from reference [110].

As a very attractive alternative to metal oxide-based water oxidation catalysis, the Prussian Blue-type networks (metal hexacyanometallate structures) outstands due to their exceptional activity and stability in neutral and acidic media[111], in addition to the possibility of easy preparation and processing by soft chemistry methods, both as nanoparticles and thin film.[112-115] The electrocatalytic activity for water oxidation of Prussian Blue (PB) analogs was firstly investigated by Galán-Mascaros and co-workers in 2013 with cobalt hexacyanoferrate; (CoFe-PB[112]). Hegner et al. reported a heterostructured CoFe-PB/$BiVO_4$ photoanode (**Figure 1.29a**) with a 10-fold enhancement of the photocurrent compared to bare $BiVO_4$, an onset potential shift of 0.8 V vs RHE, as depicted in **Figure 1.29b,** and excellent stability through c.a. 50 h,[116] exceeding the performance observed for other state-of-the-art photoanodes as Co-Pi/$BiVO_4$ and $CoO_x/BiVO_4$.[116] Moreover, mechanistic studies with impedance spectroscopy and hybrid DFT calculations demonstrated the existence of a strong energetic offset (thermodynamic driving force) for holes transfer between the $BiVO_4$ valence band and CoFe-PB, as shown in **Figure 1.29c**. Since the electronic Co states of CoFe-PB lie above the $BiVO_4$ E_{vb} and below H_2O HOMO, the hole transfer via the CoFe-PB is favoured, acting as a true catalyst.[116] Further mechanistic studies with optical spectroscopy confirmed this assessment. [117]

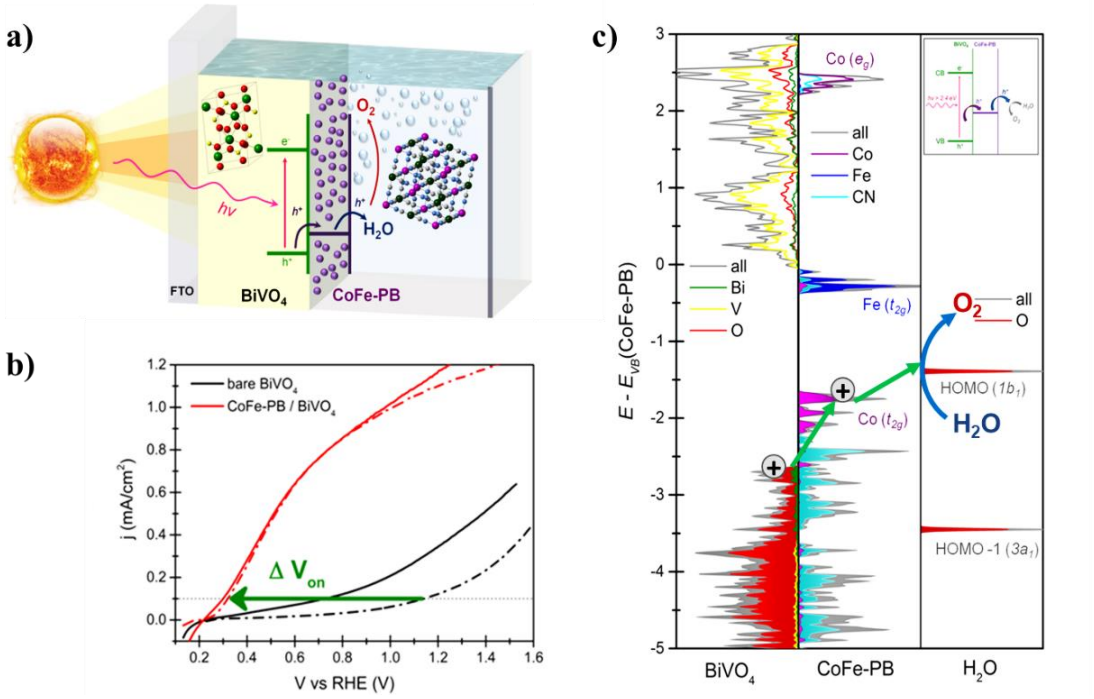

Figure 1.29. a) Schematic representation of the CoFe-PB/$BiVO_4$ photoelectrode. **b)** $j-V$ plot of bare and modified $BiVO_4$ photoanode, showing the remarkable shift of the onset potential and enhanced photocurrent. **c)** Densities of states of $BiVO_4$ (left), CoFe-PB (middle), and solvated H_2O molecule (right) aligned by their O 2s bands. Filled electronic states are represented by filled areas. A simplified representation is given as the inset (top right). Figures adapted with permission from reference [116].

1.5. Integrated PV–EC photoelectrodes.

In an integrated PV–EC photoelectrode, light absorption by the PV component (a solar cell or module of several series-connected cells) produces a photovoltage and a photocurrent, that are used to power an electrochemical reaction in a suitable catalytic material, intimately connected to the PV device, as illustrated in **Figure 1.8**. As discussed in Section 1.2, the best performance PV–EC devices are based on scarce and expensive materials. Therefore, PV–EC systems based on non-critical raw materials are imperative for further development and large-scale implementation. In this context, the integration thin-film silicon solar cells and water oxidation electrocatalysts based on Earth-abundant elements such as Ni and Fe, is an attractive alternative to III–V based PC and noble metal EC, leading the current PV–EC efficiency records.

1.5.1 Thin-film Si solar cells for solar fuel production.

For solar-assisted water splitting, the PV component should be able to generate a photovoltage above 1.6 V, considering the minimum thermodynamic potential difference under standard conditions for water splitting, plus the overpotentials. This requirement can be achieved with tandem and multijunction thin films silicon solar, as suggested in several studies. [34, 37, 118] The widespread use of PV–EC approaches using III–V based, CIGS, crystalline silicon, or perovskite solar cells has been mainly hampered by stability issues and cost limitations. In contrast, silicon-based thin-film technology, which outstands by its

chemical resistance, earth abundance and low-cost production, has achieved a leading position in PV-powered electrocatalytic systems, due to their ability to provide high photovoltages, above the required potential for photo-electrolysis, particularly with multijunction configurations.[34, 36]

Thin-film silicon devices allow the fabrication of monolithic cells, which can be integrated into compact water splitting photoelectrodes. This concept was theoretically and experimentally demonstrated by Urbain and co-workers in a photocathode based on a hydrogenated amorphous silicon thin-film tandem junction *(a-Si:H/a-Si:H)* device.[37] The solar cell was adapted to provide sufficient photovoltage to drive the water splitting reactions, while an Ag/Pt layer stack and a RuO_2 counter electrode were used as catalyst for HER and OER, respectively, to achieve a 6.8% STH efficiency. More recently, the fabrication of multijunction solar cells consisting of stack layers of amorphous (*a-Si:H*) and microcrystalline (*μc-Si:H*) silicon thin films was reported. It worth noting that, the combinations of *a-Si:H* and *μc-Si:H* films allow a more precise adjustment of the PV parameters, while the PV devices suffer less from stability issues under long term illumination compared to their all-amorphous counterparts. **Figure 1.30a** shows the schematic drawing of the multijunction solar cells: *a-Si:H/a-Si:H/μc-Si:H* and *a-Si:H/μc-Si:H/μc-Si:H* triple junction, and *a-Si:H/a-Si:H/μc-Si:H/μc-Si:H* quadruple junction; while the characteristic $j-V$ plots of each device is represented in **Figure 1.30b**, indicating the available open circuit potential range (OCP).[34] Note that the $j-V$ curves of the solar cells are linked with the theoretical operation point of an integrated PV–EC device, at 1.23 V (red dashed vertical line). However, in real PV–EC devices this operation point is shifted due to overpotential losses.

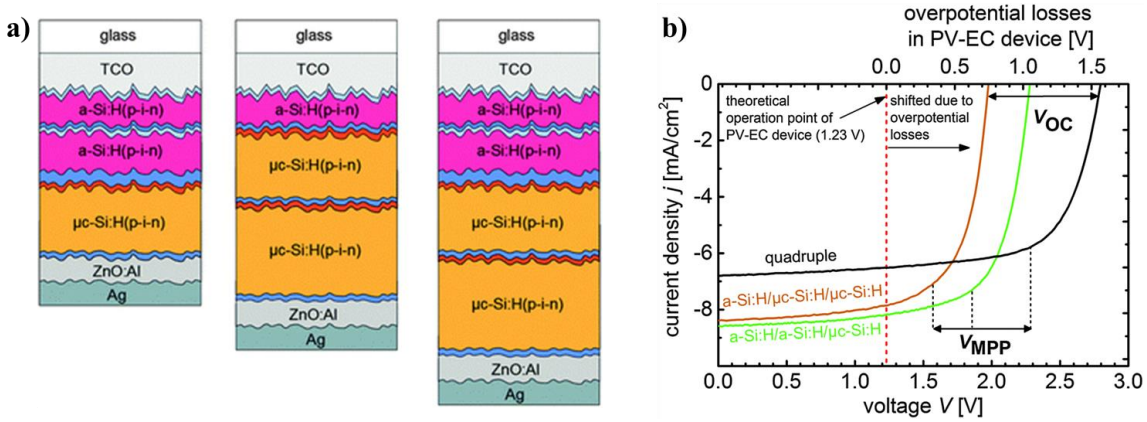

Figure 1.30. a) Schematic representation of the triple and quadruple junction solar cell structures. **b)** Characteristic $j-V$ plots of the triple and quadruple junction solar cells. Figure adapted with permission from reference [34].

The applicability of the multijunction solar cells as photocathodes in an integrated PV–EC device was further demonstrated using thin Pt and Ni layers as catalysts for the HER, directly connected on top of the solar cells, while a RuO_2 counter electrode was used for the OER, as shown in **Figure 1.31a,** where a *a-Si:H/a-Si:H/μc-Si:H* triple junction cell is used as an example.[34] **Figure 1.31b** and **c** show the PEC performance of the water splitting cell, indicating the operation point at zero-bias (black line), where the best results are obtained with the *a-Si:H/a-Si:H/μc-Si:H* triple junction solar cell and noble-metal based electrocatalysts (Pt and RuO_2), reaching a maximum of 9.5% STH efficiency.

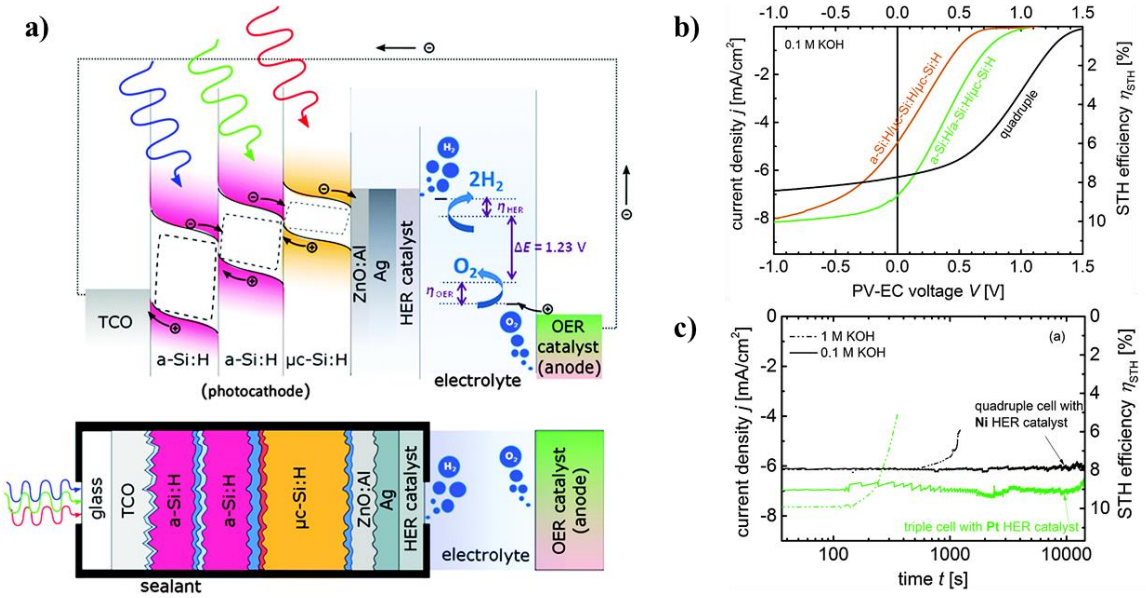

Figure 1.31. Representation of an integrated PV–EC photocathode in a solar-assisted water splitting cell, under bias-free operation conditions. **b)** *j–V* plots of the PV–EC devices based on thin-film silicon multijunction cells. A 150 nm thick Pt layer is used as HER catalyst while OER reaction takes place in a RuO_2 counter electrode**. c)** Long-term stability of the *a-Si:H/a-Si:H/μc-Si:H* and the quadruple junction-based PV–EC devices with Pt and Ni catalyst layers, at 0 V applied bias. Figures adapted with permission from reference [34].

Since the outstanding performance of the PV component is already provided with thin-films multijunction silicon solar cells, the major challenge for practical application of integrated PV–EC devices lies in the substitution of noble metal-based electrocatalyst with Earth-abundant and low-cost processed materials.

1.5.2 OER electrocatalysts.

A good catalyst for application in PV–EC devices must satisfy two basic requirements: *(i)* The catalyst must be highly active toward the desired reaction, which means that it must be capable of producing large quantities of H_2 or O_2 as quickly as the photo-absorber can supply charge carriers to the catalyst; and *(ii)* the catalyst must be robust enough in order to sustain a high efficiency over time scales relevant to commercial applications. Materials fulfilling the listed requirements are generally noble-metal based compounds, as shown in **Figure 1.31.** Therefore, the identification of Earth-abundant materials as electrocatalytic components in PV–EC photoelectrodes, with long-term stability and robust performance, is currently a challenge.

As discussed in the section above, Earth-abundant transition metal compounds, and mainly those based on Co, Fe, Mn and Ni oxides, have been extensively used as OER electrocatalysts in combination with photo-active semiconductors. Moreover, the possibility of synthesizing transition metal oxides via electrodeposition allows preparing large-geometrical area devices, a desirable condition for commercial perspectives. However, the lack of standardization in the reported electrocatalytic data precludes the objective evaluation of their OER efficiency, due to the different measurement conditions and variety of substrates tested. McCrory and co-workers reported a benchmarking protocol for evaluating the activity, stability, and electrochemically active surface area for heterogeneous OER catalysts under standard conditions, providing comprehensive plots

for facile evaluation of the materials, as the one showed in **Figure 1.32**.[119] In this figure, the color of each point represents the roughness factor of the catalyst, while the size of each point is inversely proportional to the standard deviation in electrochemical surface area measurements. From that plot, clearly $NiFeO_x$ stands out due to its lower surface area and hence higher specific activity, providing a specific current density ~10 times higher compared to the other non-noble metal catalyst.

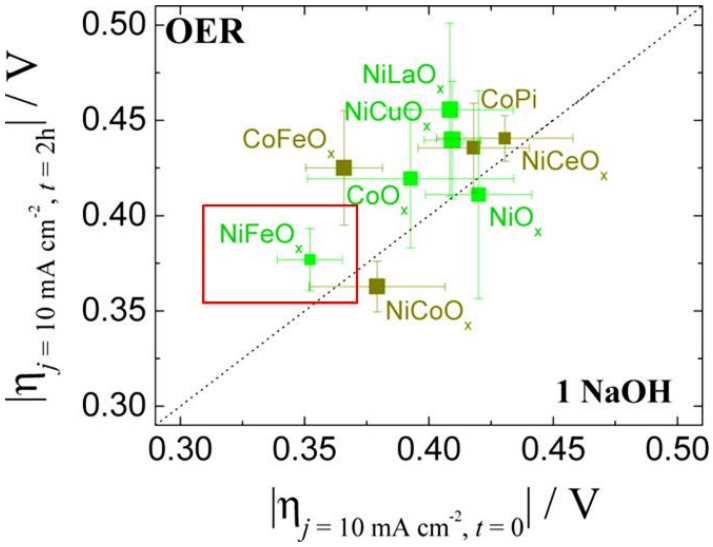

Figure 1.32. Catalytic activity and stability of transition metal-based OER electrocatalysts in alkaline solution. The *x*-axis is the overpotential required to achieve 10 mA cm^{-2} per geometric area at time $t = 0$. The *y*-axis is the overpotential required to achieve 10 mA cm^{-2} per geometric area at time $t = 2$ h. The diagonal dashed line is the expected response for a stable catalyst. Figure adapted with permission from reference [119].

Transition metal compounds have been successfully used as electrocatalysts in PV–EC applications for solar water splitting. As an example, Welter and co-workers used NiMo and $NiFeO_X$ catalysts for HER and OER, respectively, in an integrated PV–EC cassette system with a triple junction *a-Si:H/a-Si:H/μc-Si:H* solar cell.[120] The NiMo/$NiFeO_X$ catalyst system has demonstrated robust electrocatalytic performance, comparable to that obtained with a precious metal-based catalyst system (Pt/IrO_X). Furthermore, their integration in the PV–EC device lead to an STH efficiency of 5.1%, slightly higher compared to that obtained with the Pt/IrO_X system (STH =4.8%).[120]

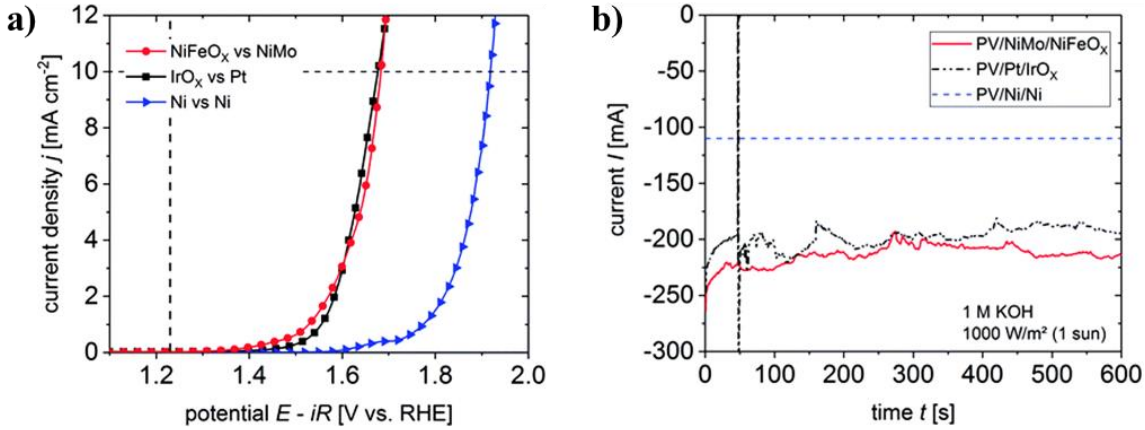

Figure 1.34. a) $j - V$ curves of the $NiFeO_X$/NiMo catalyst pair deposited on 50.3 cm^2 nickel sheets, compared to precious metal-based IrO_X/Pt catalysts and pure Ni/Ni sheets. **b)** Stability measurement of the fully integrated PV–EC device under bias-free conditions featuring different catalyst systems in 1 M KOH and under 100 mW m^{-2} illumination. Figures adapted with permission from reference [120].

Moreover, among the transition metal oxide-based compounds proposed as OER electrocatalysts, the spinel-type oxides including MCo_2O_4, MFe_2O_4 and MMn_2O_4, with M = Ni, Zn, Cu, etc. outstand due to their high stability and electrocatalytic activity in alkaline solution, added to the low cost of their constituent elements. The general formula of the spinel structure (AB_2O_4) is $[A^{2+}][B_2^{3+}][O_4^{2-}]$, where A is a divalent cation and B is a trivalent cation. This structure consists of a closely packed array of 32 oxygen ions that form 64 tetrahedral cations and 32 octahedral cations in a single unit cell.[121] The spinel structure can be classified into three types: normal, inverse, and mixed spinel based on the cation occupancy. In a normal spinel, the A cations preferentially occupy tetrahedral sites, and the B cations occupy octahedral sites. In contrast, in the inverse-spinel structure, which is denoted as $[B^{3+}][A^{2+}B^{3+}]O_4$, the octahedral sites are occupied by the A cations and half of the B cations, while the other half of the B cations occupy the tetrahedral sites. $NiFe_2O_4$ is an example of the inverse-spinel structure, represented in **Figure 1.33**. The inversed spinel $NiFe_2O_4$ has been reported as a promising OER electrocatalyst in neutral and alkaline media.[122-123] However, the finite number of surface-active sites and low conductivity of $NiFe_2O_4$ often hamper its catalytic activity for technological implementation. Therefore, significant effort is needed on engineering modified $NiFe_2O_4$ catalysts for further application.

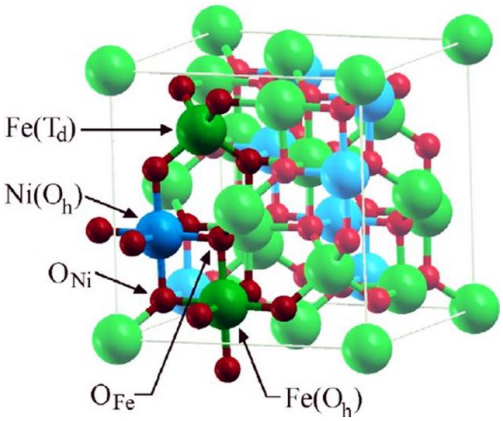

Figure 1.33. Unit cell of the inverse-spinel structure of $NiFe_2O_4$. Figure adapted with permission from reference [121].

In general, from the discussion on this section and Section 1.4.2.4, the NiFe-based oxides are clearly promising catalysts for the OER. Their high activity and stability, the Earth-abundance of their components, and the possibility of low-cost and facile synthetic routes allow their implementation in commercial and large-area devices.

1.6. Inorganic perovskite quantum dots: Harvesting their exceptional properties in PC and PEC applications.

In the last years, metal halide compounds with perovskite-type crystal structure, and chemical formula ABX_3 where A can be a monovalent organic cation (e.g., $CH_3NH_3^+$) or an inorganic cation (e.g., Cs^+), B is a divalent metal cation (e.g., Pb^{2+}, Sn^{2+}), and X is a halide ion (e.g., Cl^-, Br^-, I^-, or mixed halides), have attracted increasing attention for optoelectronic applications, due to their excellent optical and photoelectric properties, low cost, and simple preparation method.[124-126] Therefore, the applications of metal halide perovskite materials have been expanding from their original application field of PVs to light-emitting diodes, photodetectors, lasers, memories and transistors.[124, 126]

However, the instability of the organic functional groups has been a great obstacle to the practical application of hybrid organic-inorganic perovskite materials. Consequently, the substitution of the organic functional groups with inorganic cations, leading to an all-inorganic halide perovskite structure has become a hot research topic.[29] The intrinsic ionic characteristics of all-inorganic perovskites make them prone to decompose in polar solvents –such as water, ethanol, acetone, etc.–, leading to structural instability. However, due to the absence of organic functional groups, the inorganic-halide perovskites are more stable compared to organic and hybrid perovskites.[127] In order to improve the stability, as well as the optoelectronic properties of the all-inorganic-halide perovskites, several strategies including compositional engineering, surface engineering, matrix encapsulation and device encapsulation, have been developed,[127-129] resulting in a notable increase of their stability and, hence, their applications in different fields.[29] Nonetheless, the low long-term stability, added to their thermal stability and the high sensitivity to humidity, make difficult the commercialization of devices based on these materials.[130] A successful alternative to face these problems involves the size reduction of the perovskite material.[131] Colloidal quantum dots (QDs) have demonstrated to potentially provide novel opportunities for next-generation of light-emitting devices, owing to their high photoluminescence quantum yield (PLQY), and tuneable and narrow emission bandwidth.[129, 132-133]

In this context, all-inorganic perovskite QDs have become an attractive choice for optoelectronic applications, including photocatalysis, due to their enhanced chemical stability compared to their bulk counterpart. Furthermore, their broadly tunable photoluminescence (PL) in the range of 400-700 nm, small PL full width at half-maxima (fwhm) of 12−40 nm, and high PL quantum yields (QY) up to 90% provide an optimal platform for optoelectronic applications.[134-136] The typical crystal structure of the inorganic perovskites, depicted in **Figure 1.35a**, is the cubic phase, consisting of a 3D framework where divalent metal cations (Pb^{2+}, Sn^{2+}), and halide anions (Cl^-, Br^-, I^-, or mixed halides) form the corner-sharing BX_6^{4-} octahedra, while the vertexes of the octahedral cavity are occupied by the monovalent inorganic cations Cs^{1+}. Such framework allows the charge carriers to move in the limited 3D grid, leading to a relatively high carrier mobility. [29, 137]

Li and co-workers[136] showed that cubic-phase $CsPbBr_3$ QD the E_{vb} and E_{cb} positions are determined by the 4p orbital of Br element and the 4p orbital of Pb element, respectively, while the Cs element has a less significant influence on the energy band

positions.[136] As a consequence, the band structure of all-inorganic perovskites QDs can be controlled either by changing the ratio of the halogen element to adjust the E_{vb} position, or replacing the Pb with other metal elements such as Sn, or doping with other elements, to adjust the E_{cb} position.[29] Therefore, all-inorganic colloidal perovskites QDs exhibit tuneable E_g, as well as E_{vb} and E_{cb} positions, depending on size and composition, covering the entire visible spectral region with narrow and bright emission, as shown in **Figure 1.35b**. Those properties are, in fact, crucial to evaluation of photocatalytic and photoelectrochemical activities and further applications.

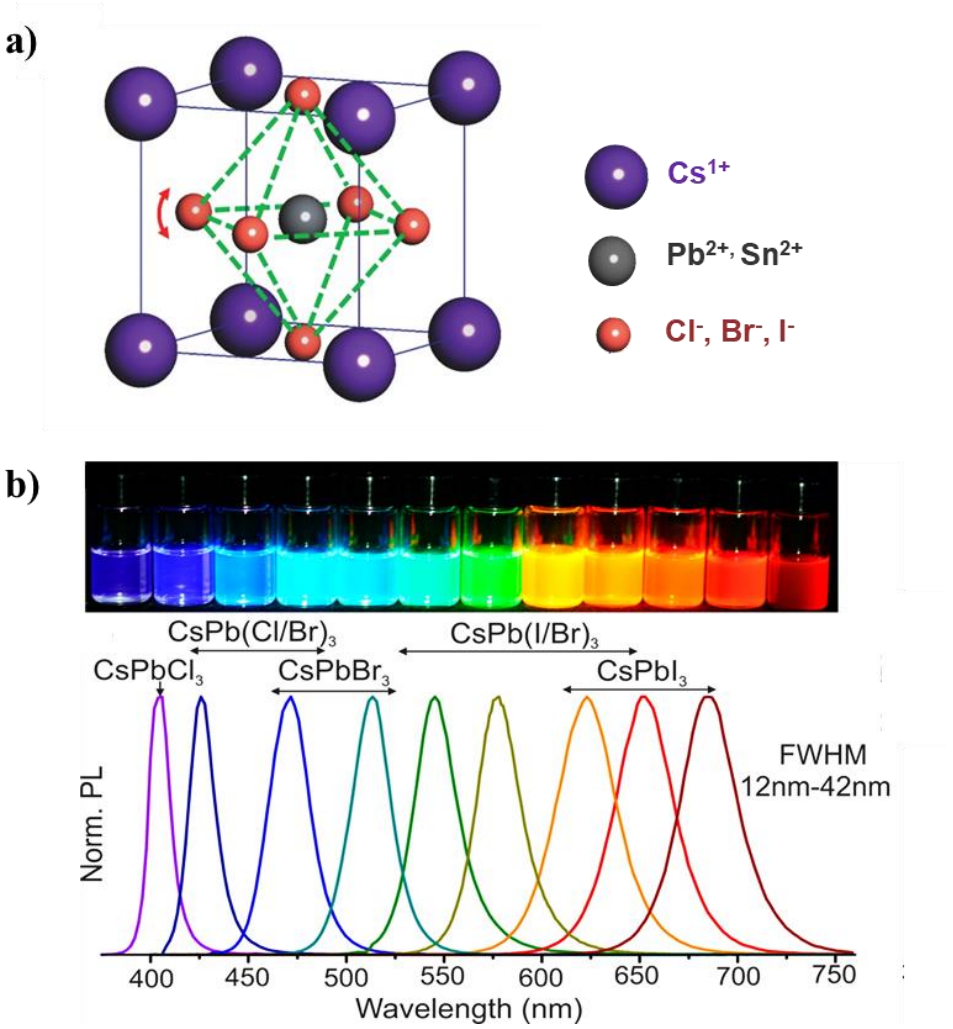

Figure 1.35. a) All inorganic perovskites crystal structure (cubic). **b)** Colloidal QDs solutions under UV lamp (λ = 365 nm) and representative PL spectra (λ_{exc} = 400 nm; 350 nm for $CsPbCl_3$). Figures adapted with permission from references [127] and [135].

The first report of photocatalysis with metal halide perovskites was made in 2016, by Park and co-workers.[138] They outlined a strategy for photocatalytic-driven HI splitting, using methyl-ammonium lead iodide ($MAPbI_3$) perovskite, by exploiting the dynamic equilibrium of the dissolution and reprecipitation of this material in saturated HI aqueous solutions.[138] This demonstration opened a gate for the research of several halide perovskite-based materials in photocatalytic applications.

More recently, the PC degradation of organic dyes using all-inorganic perovskite QDs was reported by Gao and co-workers.[139] They evaluated the ability of $CsPbCl_3$ and $CsPbBr_3$ QDs for degrading methyl orange (MO) solution under visible light irradiation.[139]

Interestingly, both materials show excellent photocatalytic activities to decompose the MO solution into a colorless solution within 100 min, with a better performance of $CsPbCl_3$, as shown in **Figure 1.36a**. Furthermore, they proposed a mechanism for MO degradation, depicted in **Figure 1.36b**, based on the principal role of $\cdot O_2^-$, rather than holes and ·OH in the PC process.[139] However, in this study there is not a stability assessment for reliable operational conditions or further experimental evidence of effective energy transfer from the QD to the organic dye to drive the degradation reactions.

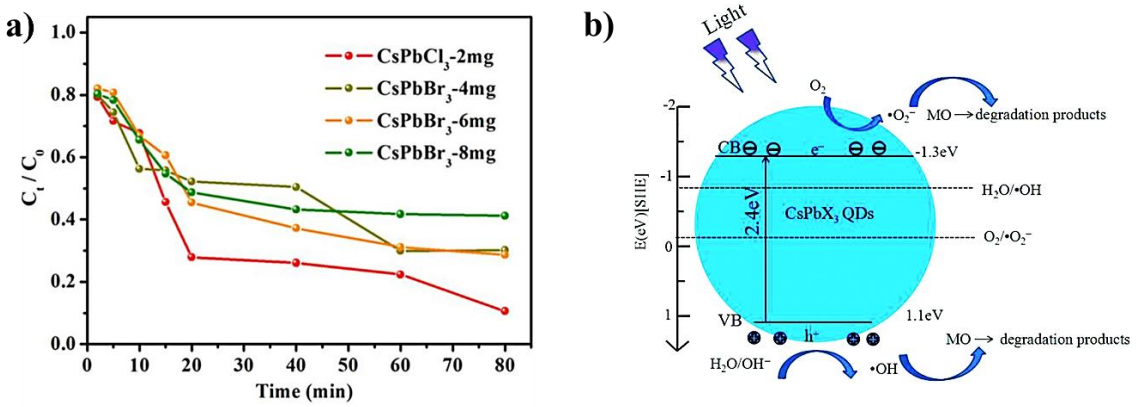

Figure 1.36. a) Degradation of MO, expressed in terms of concentration (C_t/C_0), with $CsPbCl_3$ and $CsPbBr_3$ QDs as photocatalyst, under visible light irradiation. **b)** Proposed mechanism for the PC reaction of MO using the all-inorganic perovskite QDs. Figures adapted with permission from reference [140].

Conversion of CO_2 into solar fuels with $CsPbBr_3$ QDs as photocatalyst was reported by the first time by Xu and co-workers in 2017.[141] They found that the individual $CsPbBr_3$ QDs could catalyze the CO_2 reduction reaction at a rate of 23.7 μmol g^{-1} h^{-1} for CH_4 production with a selectivity over 99.3%, in a non-polar solvent (acetonitrile?) under AM 1.5G simulated illumination. Moreover, $CsPbBr_3$ QD/graphene oxide ($CsPbBr_3$ QD/GO) composite, represented in **Figure 1.37a**, led to an improved CO_2 reduction rate up to 29.8 μmol g^{-1} h^{-1}, as shown in **Figure 1.37b**. Photoluminescence and photoelectrochemical impedance tests confirmed that the electron-extraction ability of conductive GO was responsible for the photocatalytic enhancement.[141] Hou and co-workers also used $CsPbBr_3$ QDs towards solar CO_2 reduction with high selectivity, greater than 99 %, achieving an efficient yield of 20.9 μmol g^{-1}, as depicted in **Figure 1.37c**. The estimation of band positions, showed in **Figure 1.37d**, through optical measurements, showed that the photogenerated electrons can react with adsorbed CO_2 and H_2O to produce CO and CH_4, since the E_{vb} of the $CsPbBr_3$ QDs is more negative compared to that of $E°_{CO2/CO}$ and $E°_{CO2/CH4}$. Simultaneously, the photogenerated holes in the valence band can oxidize water to produce oxygen and protons. Later on, Xu and co-workers also developed amorphous-TiO_2-encapsulated $CsPbBr_3$ nanocrystals for enhanced photocatalytic reduction of CO_2.[142] In this study, they showed that the amorphous TiO_2 matrix played a pivotal driving force for enhanced photocatalytic performance by improving the charge dynamics for extraction and separation of the photoinduced charges, and increasing the adsorption of the CO_2 simultaneously, as schematically represented in **Figure 1.37e**.[142] As a consequence, a nearly 6.5-fold enhancement on the consumption of the photoelectrons was achieved during the photocatalytic CO_2 reduction reactions, outperforming the previous tested systems. The photocatalytic activity for CO_2 reduction of a-TiO_2-encapsulated $CsPbBr_3$ prepared with different TiO_2 volumes is depicted in **Figure 1.37f**.

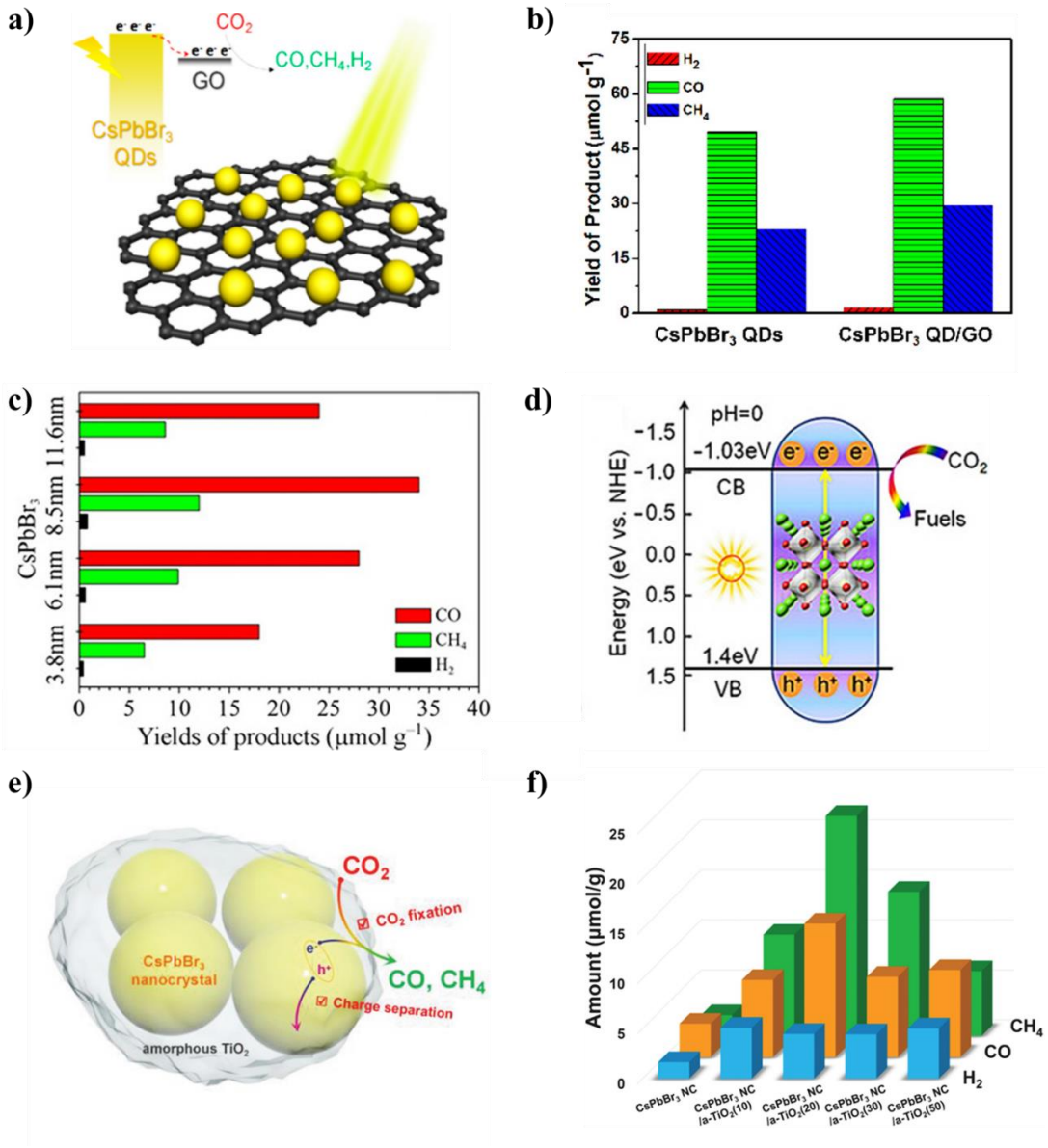

Figure 1.37. a) Schematic representation of CO_2 photoreduction over the $CsPbBr_3$ QD/GO photocatalyst. **b)** Photocatalytic activity of the $CsPbBr_3$ QD/GO composites, expressed in the yield of the CO_2 reduction products after 12 h of photochemical reaction. **c)** CO_2 reduction into fuels with $CsPbBr_3$ QDs, under 300 W Xe lamp irradiation. **d)** Proposed band diagram and CO_2 reduction mechanism with $CsPbBr_3$ QDs. **e)** Schematic illustration of the charge separation and CO_2 fixation in a-TiO_2-encapsulated $CsPbBr_3$ nanocrystals. **f)** Photocatalytic CO_2 reduction with a-TiO_2-encapsulated $CsPbBr_3$ nanocrystals. Figures adapted with permission from references [140-142].

These seminal reports on PC and PEC applications with all-inorganic perovskite QDs demonstrated the need for a systematic methodology that allows assessing their potential application in solar conversion and storage through photo-electrocatalytic approaches.

1.7. References

1. Petroleum, B. BP Statistical Review of World Energy Report. *BP: London, UK* **2019**.
2. U.S. Energy Information Administration. https://www.eia.gov/todayinenergy/detail.php?id=41433.
3. Hoffert, M. I.; Caldeira, K.; Jain, A. K.; Haites, E. F.; Harvey, L. D.; Potter, S. D.; Schlesinger, M. E.; Schneider, S. H.; Watts, R. G.; Wigley, T. M. Energy implications of future stabilization of atmospheric CO_2 content. *Nature* **1998,** *395* (6705), 881-884.
4. Yang, W.; Prabhakar, R. R.; Tan, J.; Tilley, S. D.; Moon, J. Strategies for enhancing the photocurrent, photovoltage, and stability of photoelectrodes for photoelectrochemical water splitting. *Chemical Society Reviews* **2019**.
5. Stackhouse, P. W. Surface meteorology and solar energy **2011**.
6. Fujishima, A.; Honda, K. Electrochemical Photolysis of Water at a Semiconductor Electrode. *Nature* **1972,** *238* (5358), 37-38.
7. Sanjay, P. With 2,245 MW of Commissioned Solar Projects, World's Largest Solar Park is Now at Bhadla. https://mercomindia.com/world-largest-solar-park-bhadla/.
8. The world's biggest solar power plant. https://www.power-technology.com/features/the-worlds-biggest-solar-power-plants/.
9. Battaglia, C.; Cuevas, A.; De Wolf, S. High-efficiency crystalline silicon solar cells: status and perspectives. *Energy & Environmental Science* **2016,** *9* (5), 1552-1576.
10. Kazim, S.; Nazeeruddin, M. K.; Grätzel, M.; Ahmad, S. Perovskite as Light Harvester: A Game Changer in Photovoltaics. *Angewandte Chemie International Edition* **2014,** *53* (11), 2812-2824.
11. Zhou, H.; Chen, Q.; Li, G.; Luo, S.; Song, T.-b.; Duan, H.-S.; Hong, Z.; You, J.; Liu, Y.; Yang, Y. Interface engineering of highly efficient perovskite solar cells. *Science* **2014,** *345* (6196), 542-546.
12. Kim, H.-S.; Lee, C.-R.; Im, J.-H.; Lee, K.-B.; Moehl, T.; Marchioro, A.; Moon, S.-J.; Humphry-Baker, R.; Yum, J.-H.; Moser, J. E.; Grätzel, M.; Park, N.-G. Lead Iodide Perovskite Sensitized All-Solid-State Submicron Thin Film Mesoscopic Solar Cell with Efficiency Exceeding 9%. *Scientific Reports* **2012,** *2* (1), 591.
13. A decade of perovskite photovoltaics. *Nature Energy* **2019,** *4* (1), 1-1.
14. NREL, N. Best Research-Cell Efficiency Chart. 2020.
15. Cook, T. R.; Dogutan, D. K.; Reece, S. Y.; Surendranath, Y.; Teets, T. S.; Nocera, D. G. Solar Energy Supply and Storage for the Legacy and Nonlegacy Worlds. *Chemical Reviews* **2010,** *110* (11), 6474-6502.
16. Yang, W.; Prabhakar, R. R.; Tan, J.; Tilley, S. D.; Moon, J. Strategies for enhancing the photocurrent, photovoltage, and stability of photoelectrodes for photoelectrochemical water splitting. *Chemical Society Reviews* **2019,** *48* (19), 4979-5015.
17. Spence, A. South Australia looks to take lead in green hydrogen race. https://indaily.com.au/news/2019/09/25/south-australia-looks-to-take-lead-in-green-hydrogen-race/.
18. Molina, P. S. Big solar+storage project linked to hydrogen production in Spain. https://www.pv-magazine.com/2020/03/17/big-solarstorage-project-linked-to-hydrogen-production-in-spain/.
19. Cho, S.; Jang, J.-W.; Lee, K.-H.; Lee, J. S. Research Update: Strategies for efficient photoelectrochemical water splitting using metal oxide photoanodes. *APL Materials* **2014,** *2* (1), 010703.
20. Lewis, N. S. Research opportunities to advance solar energy utilization. *Science* **2016,** *351* (6271), aad1920.

21. Körner, A.; Tam, C.; Bennett, S.; Gagné, J. Technology roadmap-hydrogen and fuel cells. *International Energy Agency (IEA): Paris, France* **2015**.
22. Pinaud, B. A.; Benck, J. D.; Seitz, L. C.; Forman, A. J.; Chen, Z.; Deutsch, T. G.; James, B. D.; Baum, K. N.; Baum, G. N.; Ardo, S.; Wang, H.; Miller, E.; Jaramillo, T. F. Technical and economic feasibility of centralized facilities for solar hydrogen production via photocatalysis and photoelectrochemistry. *Energy & Environmental Science* **2013,** *6* (7), 1983-2002.
23. Barber, J. Photosynthetic energy conversion: natural and artificial. *Chemical Society Reviews* **2009,** *38* (1), 185-196.
24. Chen, Z.; Dinh, H.; Miller, E. *Photoelectrochemical Water Splitting. Standards, Experimental Methods, and Protocols*. Springer-Verlag New York: 2013; p 126.
25. Kim, J. H.; Hansora, D.; Sharma, P.; Jang, J.-W.; Lee, J. S. Toward practical solar hydrogen production – an artificial photosynthetic leaf-to-farm challenge. *Chemical Society Reviews* **2019,** *48* (7), 1908-1971.
26. Hisatomi, T.; Domen, K. Reaction systems for solar hydrogen production via water splitting with particulate semiconductor photocatalysts. *Nature Catalysis* **2019,** *2* (5), 387-399.
27. Wang, Q.; Domen, K. Particulate Photocatalysts for Light-Driven Water Splitting: Mechanisms, Challenges, and Design Strategies. *Chemical Reviews* **2020,** *120* (2), 919-985.
28. Wang, Z.; Li, C.; Domen, K. Recent developments in heterogeneous photocatalysts for solar-driven overall water splitting. *Chemical Society Reviews* **2019,** *48* (7), 2109-2125.
29. Liang, J.; Chen, D.; Yao, X.; Zhang, K.; Qu, F.; Qin, L.; Huang, Y.; Li, J. Recent Progress and Development in Inorganic Halide Perovskite Quantum Dots for Photoelectrochemical Applications. *Small* **2019,** *n/a* (n/a), 1903398.
30. Wang, Y.; Suzuki, H.; Xie, J.; Tomita, O.; Martin, D. J.; Higashi, M.; Kong, D.; Abe, R.; Tang, J. Mimicking Natural Photosynthesis: Solar to Renewable H2 Fuel Synthesis by Z-Scheme Water Splitting Systems. *Chemical Reviews* **2018,** *118* (10), 5201-5241.
31. Liu, J.; Liu, Y.; Liu, N.; Han, Y.; Zhang, X.; Huang, H.; Lifshitz, Y.; Lee, S.-T.; Zhong, J.; Kang, Z. Metal-free efficient photocatalyst for stable visible water splitting via a two-electron pathway. *Science* **2015,** *347* (6225), 970-974.
32. Wang, Q.; Hisatomi, T.; Jia, Q.; Tokudome, H.; Zhong, M.; Wang, C.; Pan, Z.; Takata, T.; Nakabayashi, M.; Shibata, N.; Li, Y.; Sharp, I. D.; Kudo, A.; Yamada, T.; Domen, K. Scalable water splitting on particulate photocatalyst sheets with a solar-to-hydrogen energy conversion efficiency exceeding 1%. *Nature Materials* **2016,** *15* (6), 611-615.
33. Smith, W. A. Photoelectrochemical Cell Design, Efficiency, Definitions, Standards, and Protocols. In *Photoelectrochemical Solar Fuel Production: From Basic Principles to Advanced Devices*, Giménez, S.; Bisquert, J., Eds. Springer International Publishing: Cham, 2016; pp 163-197.
34. Urbain, F.; Smirnov, V.; Becker, J.-P.; Lambertz, A.; Yang, F.; Ziegler, J.; Kaiser, B.; Jaegermann, W.; Rau, U.; Finger, F. Multijunction Si photocathodes with tunable photovoltages from 2.0 V to 2.8 V for light induced water splitting. *Energy & Environmental Science* **2016,** *9* (1), 145-154.
35. Parkinson, B. On the efficiency and stability of photoelectrochemical devices. *Accounts of Chemical Research* **1984,** *17* (12), 431-437.
36. Urbain, F.; Wilken, K.; Smirnov, V.; Astakhov, O.; Lambertz, A.; Becker, J.-P.; Rau, U.; Ziegler, J.; Kaiser, B.; Jaegermann, W.; Finger, F. Development of Thin Film

Amorphous Silicon Tandem Junction Based Photocathodes Providing High Open-Circuit Voltages for Hydrogen Production. *International Journal of Photoenergy* **2014,** *2014*, 10.
37. Urbain, F.; Smirnov, V.; Becker, J.-P.; Rau, U.; Ziegler, J.; Kaiser, B.; Jaegermann, W.; Finger, F. Application and modeling of an integrated amorphous silicon tandem based device for solar water splitting. *Solar Energy Materials and Solar Cells* **2015,** *140*, 275-280.
38. Mason, J. E.; Zweibel, K. Baseline model of a centralized pv electrolytic hydrogen system. *International Journal of Hydrogen Energy* **2007,** *32* (14), 2743-2763.
39. Sivula, K. Advanced Device Architectures and Tandem Devices. 2016; pp 493-512.
40. Tan, C. S.; Kemp, K. W.; Braun, M. R.; Meng, A. C.; Tan, W.; Chidsey, C. E. D.; Ma, W.; Moghadam, F.; McIntyre, P. C. >10% solar-to-hydrogen efficiency unassisted water splitting on ALD-protected silicon heterojunction solar cells. *Sustainable Energy & Fuels* **2019,** *3* (6), 1490-1500.
41. Van de Krol, R.; Grätzel, M. *Photoelectrochemical hydrogen production*. Springer: 2012; Vol. 90.
42. Hu, S.; Xiang, C.; Haussener, S.; Berger, A. D.; Lewis, N. S. An analysis of the optimal band gaps of light absorbers in integrated tandem photoelectrochemical water-splitting systems. *Energy & Environmental Science* **2013,** *6* (10), 2984-2993.
43. Hisatomi, T.; Kubota, J.; Domen, K. Recent advances in semiconductors for photocatalytic and photoelectrochemical water splitting. *Chemical Society Reviews* **2014,** *43* (22), 7520-7535.
44. Cheng, W.-H.; Richter, M. H.; May, M. M.; Ohlmann, J.; Lackner, D.; Dimroth, F.; Hannappel, T.; Atwater, H. A.; Lewerenz, H.-J. Monolithic Photoelectrochemical Device for Direct Water Splitting with 19% Efficiency. *ACS Energy Letters* **2018,** *3* (8), 1795-1800.
45. Pihosh, Y.; Turkevych, I.; Mawatari, K.; Uemura, J.; Kazoe, Y.; Kosar, S.; Makita, K.; Sugaya, T.; Matsui, T.; Fujita, D.; Tosa, M.; Kondo, M.; Kitamori, T. Photocatalytic generation of hydrogen by core-shell $WO_3/BiVO_4$ nanorods with ultimate water splitting efficiency. *Scientific Reports* **2015,** *5* (1), 11141.
46. Peter, L. M. Semiconductor Electrochemistry. In *Photoelectrochemical Solar Fuel Production: From Basic Principles to Advanced Devices*, Giménez, S.; Bisquert, J., Eds. Springer International Publishing: Cham, 2016; pp 3-40.
47. Würfel, P.; Würfel, U. *Physics of solar cells: from basic principles to advanced concepts*. John Wiley & Sons: 2016.
48. Sato, N. *Electrochemistry at metal and semiconductor electrodes*. Elsevier: 1998.
49. Morrison, S. R. Electrochemistry at semiconductor and oxidized metal electrodes**1980**.
50. Trześniewski, B. J.; Digdaya, I. A.; Nagaki, T.; Ravishankar, S.; Herraiz-Cardona, I.; Vermaas, D. A.; Longo, A.; Gimenez, S.; Smith, W. A. Near-complete suppression of surface losses and total internal quantum efficiency in $BiVO_4$ photoanodes. *Energy & Environmental Science* **2017,** *10* (6), 1517-1529.
51. Zachäus, C.; Abdi, F. F.; Peter, L. M.; van de Krol, R. Photocurrent of $BiVO_4$ is limited by surface recombination, not surface catalysis. *Chemical Science* **2017,** *8* (5), 3712-3719.
52. Nellist, M. R.; Qiu, J.; Laskowski, F. A. L.; Toma, F. M.; Boettcher, S. W. Potential-Sensing Electrochemical AFM Shows CoPi as a Hole Collector and Oxygen Evolution Catalyst on $BiVO_4$ Water-Splitting Photoanodes. *ACS Energy Letters* **2018,** *3* (9), 2286-2291.
53. Grätzel, M. Photoelectrochemical cells. *Nature* **2001,** *414* (6861), 338-344.

54. Sivula, K. Metal Oxide Photoelectrodes for Solar Fuel Production, Surface Traps, and Catalysis. *The Journal of Physical Chemistry Letters* **2013,** *4* (10), 1624-1633.
55. Peter, L. M. Photoelectrochemical Water Splitting. A Status Assessment. *Electroanalysis* **2015,** *27* (4), 864-871.
56. Reichman, J. The current-voltage characteristics of semiconductor-electrolyte junction photovoltaic cells. *Applied Physics Letters* **1980,** *36* (7), 574-577.
57. Walter, M. G.; Warren, E. L.; McKone, J. R.; Boettcher, S. W.; Mi, Q.; Santori, E. A.; Lewis, N. S. Solar Water Splitting Cells. *Chemical Reviews* **2010,** *110* (11), 6446-6473.
58. van de Krol, R.; Liang, Y.; Schoonman, J. Solar hydrogen production with nanostructured metal oxides. *Journal of Materials Chemistry* **2008,** *18* (20), 2311-2320.
59. NREL. Reference Air Mass 1.5 Spectra. https://www.nrel.gov/grid/solar-resource/spectra-am1.5.html.
60. Jiang, C.; Moniz, S. J. A.; Wang, A.; Zhang, T.; Tang, J. Photoelectrochemical devices for solar water splitting – materials and challenges. *Chemical Society Reviews* **2017,** *46* (15), 4645-4660.
61. Chen, S.; Wang, L.-W. Thermodynamic Oxidation and Reduction Potentials of Photocatalytic Semiconductors in Aqueous Solution. *Chemistry of Materials* **2012,** *24* (18), 3659-3666.
62. Haxel, G. *Rare earth elements: critical resources for high technology*. US Department of the Interior, US Geological Survey: 2002; Vol. 87.
63. He, H.; Liao, A.; Guo, W.; Luo, W.; Zhou, Y.; Zou, Z. State-of-the-art progress in the use of ternary metal oxides as photoelectrode materials for water splitting and organic synthesis. *Nano Today* **2019,** *28*, 100763.
64. Tayebi, M.; Lee, B.-K. Recent advances in $BiVO_4$ semiconductor materials for hydrogen production using photoelectrochemical water splitting. *Renewable and Sustainable Energy Reviews* **2019,** *111*, 332-343.
65. Tolod, K. R.; Hernández, S.; Castellino, M.; Deorsola, F. A.; Davarpanah, E.; Russo, N. Optimization of $BiVO_4$ photoelectrodes made by electrodeposition for sun-driven water oxidation. *International Journal of Hydrogen Energy* **2020,** *45* (1), 605-618.
66. Martinez Suarez, C.; Hernández, S.; Russo, N. $BiVO_4$ as photocatalyst for solar fuels production through water splitting: A short review. *Applied Catalysis A: General* **2015,** *504*, 158-170.
67. Abdi, F. F.; Savenije, T. J.; May, M. M.; Dam, B.; van de Krol, R. The Origin of Slow Carrier Transport in $BiVO_4$ Thin Film Photoanodes: A Time-Resolved Microwave Conductivity Study. *The Journal of Physical Chemistry Letters* **2013,** *4* (16), 2752-2757.
68. Zhao, Z.; Li, Z.; Zou, Z. Electronic structure and optical properties of monoclinic clinobisvanite $BiVO_4$. *Physical Chemistry Chemical Physics* **2011,** *13* (10), 4746-4753.
69. Cooper, J. K.; Gul, S.; Toma, F. M.; Chen, L.; Liu, Y.-S.; Guo, J.; Ager, J. W.; Yano, J.; Sharp, I. D. Indirect Bandgap and Optical Properties of Monoclinic Bismuth Vanadate. *The Journal of Physical Chemistry C* **2015,** *119* (6), 2969-2974.
70. Kim, T. W.; Choi, K.-S. Nanoporous $BiVO_4$ Photoanodes with Dual-Layer Oxygen Evolution Catalysts for Solar Water Splitting. *Science* **2014,** *343* (6174), 990-994.
71. Toma, F. M.; Cooper, J. K.; Kunzelmann, V.; McDowell, M. T.; Yu, J.; Larson, D. M.; Borys, N. J.; Abelyan, C.; Beeman, J. W.; Yu, K. M.; Yang, J.; Chen, L.; Shaner, M. R.; Spurgeon, J.; Houle, F. A.; Persson, K. A.; Sharp, I. D. Mechanistic insights into chemical and photochemical transformations of bismuth vanadate photoanodes. *Nature Communications* **2016,** *7* (1), 12012.
72. Lee, D. K.; Choi, K.-S. Enhancing long-term photostability of $BiVO_4$ photoanodes for solar water splitting by tuning electrolyte composition. *Nature Energy* **2018,** *3* (1), 53-60.

73. Xiao, M.; Luo, B.; Wang, Z.; Wang, S.; Wang, L. Recent Advances of Metal-Oxide Photoanodes: Engineering of Charge Separation and Transportation toward Efficient Solar Water Splitting. *Solar RRL* **2020,** *n/a* (n/a), 1900509.
74. S, D. T. Recent Advances and Emerging Trends in Photo-Electrochemical Solar Energy Conversion. *Advanced Energy Materials* **2019,** *9* (2).
75. Tan, H. L.; Amal, R.; Ng, Y. H. Alternative strategies in improving the photocatalytic and photoelectrochemical activities of visible light-driven $BiVO_4$: a review. *Journal of Materials Chemistry A* **2017,** *5* (32), 16498-16521.
76. Han, H. S.; Shin, S.; Kim, D. H.; Park, I. J.; Kim, J. S.; Huang, P.-S.; Lee, J.-K.; Cho, I. S.; Zheng, X. Boosting the solar water oxidation performance of a $BiVO_4$ photoanode by crystallographic orientation control. *Energy & Environmental Science* **2018,** *11* (5), 1299-1306.
77. Lamm, B.; Trześniewski, B. J.; Döscher, H.; Smith, W. A.; Stefik, M. Emerging Postsynthetic Improvements of $BiVO_4$ Photoanodes for Solar Water Splitting. *ACS Energy Letters* **2018,** *3* (1), 112-124.
78. Wang, S.; Liu, G.; Wang, L. Crystal Facet Engineering of Photoelectrodes for Photoelectrochemical Water Splitting. *Chemical Reviews* **2019,** *119* (8), 5192-5247.
79. Thorne, J. E.; He, Y.; Wang, D. Nanostructured Materials. In *Photoelectrochemical Solar Fuel Production: From Basic Principles to Advanced Devices*, Giménez, S.; Bisquert, J., Eds. Springer International Publishing: Cham, 2016; pp 463-492.
80. Kondofersky, I.; Dunn, H. K.; Müller, A.; Mandlmeier, B.; Feckl, J. M.; Fattakhova-Rohlfing, D.; Scheu, C.; Peter, L. M.; Bein, T. Electron Collection in Host–Guest Nanostructured Hematite Photoanodes for Water Splitting: The Influence of Scaffold Doping Density. *ACS Applied Materials & Interfaces* **2015,** *7* (8), 4623-4630.
81. Chae, S. Y.; Jung, H.; Jeon, H. S.; Min, B. K.; Hwang, Y. J.; Joo, O.-S. Morphology control of one-dimensional heterojunctions for highly efficient photoanodes used for solar water splitting. *Journal of Materials Chemistry A* **2014,** *2* (29), 11408-11416.
82. Kang, D.; Park, Y.; Hill, J. C.; Choi, K.-S. Preparation of Bi-Based Ternary Oxide Photoanodes $BiVO_4$, Bi_2WO_6, and $Bi_2Mo_3O_{12}$ Using Dendritic Bi Metal Electrodes. *The Journal of Physical Chemistry Letters* **2014,** *5* (17), 2994-2999.
83. Parmar, K. P. S.; Kang, H. J.; Bist, A.; Dua, P.; Jang, J. S.; Lee, J. S. Photocatalytic and Photoelectrochemical Water Oxidation over Metal-Doped Monoclinic $BiVO_4$ Photoanodes. *ChemSusChem* **2012,** *5* (10), 1926-1934.
84. Reticcioli, M.; Diebold, U.; Kresse, G.; Franchini, C. Small Polarons in Transition Metal Oxides. In *Handbook of Materials Modeling: Applications: Current and Emerging Materials*, Andreoni, W.; Yip, S., Eds. Springer International Publishing: Cham, 2019; pp 1-39.
85. Cardenas-Morcoso, D.; Peiro-Franch, A.; Herraiz-Cardona, I.; Gimenez, S. Chromium doped copper vanadate photoanodes for water splitting. *Catalysis Today* **2017,** *290*, 65-72.
86. Shaddad, M. N.; Cardenas-Morcoso, D.; García-Tecedor, M.; Fabregat-Santiago, F.; Bisquert, J.; Al-Mayouf, A. M.; Gimenez, S. TiO_2 Nanotubes for Solar Water Splitting: Vacuum Annealing and Zr Doping Enhance Water Oxidation Kinetics. *ACS Omega* **2019,** *4* (14), 16095-16102.
87. Zhao, X.; Hu, J.; Chen, S.; Chen, Z. An investigation on the role of W doping in $BiVO_4$ photoanodes used for solar water splitting. *Physical Chemistry Chemical Physics* **2018,** *20* (19), 13637-13645.
88. Zhao, L.; Wei, J.; Li, Y.; Han, C.; Pan, L.; Liu, Z. Photoelectrochemical performance of W-doped $BiVO_4$ photoanode. *Journal of Materials Science: Materials in Electronics* **2019,** *30* (24), 21425-21434.

89. Kim, M.-W.; Kim, K.; Ohm, T. Y.; Joshi, B.; Samuel, E.; Swihart, M. T.; Yoon, H.; Park, H.; Yoon, S. S. Mo-doped $BiVO_4$ nanotextured pillars as efficient photoanodes for solar water splitting. *Journal of Alloys and Compounds* **2017,** *726*, 1138-1146.
90. Pattengale, B.; Huang, J. The effect of Mo doping on the charge separation dynamics and photocurrent performance of $BiVO_4$ photoanodes. *Physical Chemistry Chemical Physics* **2016,** *18* (48), 32820-32825.
91. Zhong, X.; He, H.; Yang, M.; Ke, G.; Zhao, Z.; Dong, F.; Wang, B.; Chen, Y.; Shi, X.; Zhou, Y. In^{3+}-doped $BiVO_4$ photoanodes with passivated surface states for photoelectrochemical water oxidation. *Journal of Materials Chemistry A* **2018,** *6* (22), 10456-10465.
92. Xia, T.; Chen, M.; Xiao, L.; Fan, W.; Mao, B.; Xu, D.; Guan, P.; Zhu, J.; Shi, W. Dip-coating synthesis of P-doped $BiVO_4$ photoanodes with enhanced photoelectrochemical performance. *Journal of the Taiwan Institute of Chemical Engineers* **2018,** *93*, 582-589.
93. Yin, C.; Zhu, S.; Chen, Z.; Zhang, W.; Gu, J.; Zhang, D. One step fabrication of C-doped $BiVO_4$ with hierarchical structures for a high-performance photocatalyst under visible light irradiation. *Journal of Materials Chemistry A* **2013,** *1* (29), 8367-8378.
94. Guo, M.; Wang, Y.; He, Q.; Wang, W.; Wang, W.; Fu, Z.; Wang, H. Enhanced photocatalytic activity of S-doped $BiVO_4$ photocatalysts. *RSC Advances* **2015,** *5* (72), 58633-58639.
95. Wang, M.; Liu, Q.; Che, Y.; Zhang, L.; Zhang, D. Characterization and photocatalytic properties of N-doped $BiVO_4$ synthesized via a sol–gel method. *Journal of alloys and compounds* **2013,** *548*, 70-76.
96. Baek, J. H.; Gill, T. M.; Abroshan, H.; Park, S.; Shi, X.; Nørskov, J.; Jung, H. S.; Siahrostami, S.; Zheng, X. Selective and Efficient Gd-Doped $BiVO_4$ Photoanode for Two-Electron Water Oxidation to H_2O_2. *ACS Energy Letters* **2019,** *4* (3), 720-728.
97. Resasco, J.; Zhang, H.; Kornienko, N.; Becknell, N.; Lee, H.; Guo, J.; Briseno, A. L.; Yang, P. TiO_2/$BiVO_4$ Nanowire Heterostructure Photoanodes Based on Type II Band Alignment. *ACS Central Science* **2016,** *2* (2), 80-88.
98. Pihosh, Y.; Turkevych, I.; Mawatari, K.; Uemura, J.; Kazoe, Y.; Kosar, S.; Makita, K.; Sugaya, T.; Matsui, T.; Fujita, D.; Tosa, M.; Kondo, M.; Kitamori, T. Photocatalytic generation of hydrogen by core-shell WO_3/$BiVO_4$ nanorods with ultimate water splitting efficiency. *Scientific Reports* **2015,** *5*, 11141.
99. Hong, S. J.; Lee, S.; Jang, J. S.; Lee, J. S. Heterojunction $BiVO_4$/WO_3 electrodes for enhanced photoactivity of water oxidation. *Energy & Environmental Science* **2011,** *4* (5), 1781-1787.
100. García-Tecedor, M.; Cardenas-Morcoso, D.; Fernández-Climent, R.; Giménez, S. The Role of Underlayers and Overlayers in Thin Film $BiVO_4$ Photoanodes for Solar Water Splitting. *Advanced Materials Interfaces* **2019,** *6* (15), 1900299.
101. Shaddad, M. N.; Cardenas-Morcoso, D.; Arunachalam, P.; García-Tecedor, M.; Ghanem, M. A.; Bisquert, J.; Al-Mayouf, A.; Gimenez, S. Enhancing the Optical Absorption and Interfacial Properties of $BiVO_4$ with Ag_3PO_4 Nanoparticles for Efficient Water Splitting. *The Journal of Physical Chemistry C* **2018,** *122* (22), 11608-11615.
102. Safshekan, S.; Herraiz-Cardona, I.; Cardenas-Morcoso, D.; Ojani, R.; Haro, M.; Gimenez, S. Solar Energy Storage by a Heterostructured $BiVO_4$–PbO_x Photocapacitive Device. *ACS Energy Letters* **2017,** *2* (2), 469-475.
103. Zhong, D. K.; Choi, S.; Gamelin, D. R. Near-Complete Suppression of Surface Recombination in Solar Photoelectrolysis by "Co-Pi" Catalyst-Modified W:$BiVO_4$. *Journal of the American Chemical Society* **2011,** *133* (45), 18370-18377.

104. Abdi, F. F.; Firet, N.; van de Krol, R. Efficient $BiVO_4$ Thin Film Photoanodes Modified with Cobalt Phosphate Catalyst and W-doping. *ChemCatChem* **2013,** *5* (2), 490-496.
105. Ma, Y.; Kafizas, A.; Pendlebury, S. R.; Le Formal, F.; Durrant, J. R. Photoinduced Absorption Spectroscopy of CoPi on $BiVO_4$: The Function of CoPi during Water Oxidation. *Advanced Functional Materials* **2016,** *26* (27), 4951-4960.
106. Stern, L.-A.; Hu, X. Enhanced oxygen evolution activity by NiOx and Ni(OH)2 nanoparticles. *Faraday Discussions* **2014,** *176* (0), 363-379.
107. Corrigan, D. A. The catalysis of the oxygen evolution reaction by iron impurities in thin film nickel oxide electrodes. *Journal of The Electrochemical Society* **1987,** *134* (2), 377-384.
108. Zhong, M.; Hisatomi, T.; Kuang, Y.; Zhao, J.; Liu, M.; Iwase, A.; Jia, Q.; Nishiyama, H.; Minegishi, T.; Nakabayashi, M.; Shibata, N.; Niishiro, R.; Katayama, C.; Shibano, H.; Katayama, M.; Kudo, A.; Yamada, T.; Domen, K. Surface Modification of CoO_x Loaded $BiVO_4$ Photoanodes with Ultrathin p-Type NiO Layers for Improved Solar Water Oxidation. *Journal of the American Chemical Society* **2015,** *137* (15), 5053-5060.
109. Lichterman, M. F.; Shaner, M. R.; Handler, S. G.; Brunschwig, B. S.; Gray, H. B.; Lewis, N. S.; Spurgeon, J. M. Enhanced Stability and Activity for Water Oxidation in Alkaline Media with Bismuth Vanadate Photoelectrodes Modified with a Cobalt Oxide Catalytic Layer Produced by Atomic Layer Deposition. *The Journal of Physical Chemistry Letters* **2013,** *4* (23), 4188-4191.
110. Shaddad, M. N.; Ghanem, M. A.; Al-Mayouf, A. M.; Gimenez, S.; Bisquert, J.; Herraiz-Cardona, I. Cooperative Catalytic Effect of ZrO_2 and α-Fe_2O_3 Nanoparticles on $BiVO_4$ Photoanodes for Enhanced Photoelectrochemical Water Splitting. *ChemSusChem* **2016,** *9* (19), 2779-2783.
111. Han, L.; Tang, P.; Reyes-Carmona, Á.; Rodríguez-García, B.; Torréns, M.; Morante, J. R.; Arbiol, J.; Galan-Mascaros, J. R. Enhanced Activity and Acid pH Stability of Prussian Blue-type Oxygen Evolution Electrocatalysts Processed by Chemical Etching. *Journal of the American Chemical Society* **2016,** *138* (49), 16037-16045.
112. Pintado, S.; Goberna-Ferrón, S.; Escudero-Adán, E. C.; Galán-Mascarós, J. R. Fast and Persistent Electrocatalytic Water Oxidation by Co–Fe Prussian Blue Coordination Polymers. *Journal of the American Chemical Society* **2013,** *135* (36), 13270-13273.
113. Goberna-Ferrón, S.; Hernández, W. Y.; Rodríguez-García, B.; Galán-Mascarós, J. R. Light-Driven Water Oxidation with Metal Hexacyanometallate Heterogeneous Catalysts. *ACS Catalysis* **2014,** *4* (6), 1637-1641.
114. Indra, A.; Paik, U.; Song, T. Inside Back Cover: Boosting Electrochemical Water Oxidation with Metal Hydroxide Carbonate Templated Prussian Blue Analogues (Angew. Chem. Int. Ed. 5/2018). *Angewandte Chemie International Edition* **2018,** *57* (5), 1419-1419.
115. Aksoy, M.; Nune, S. V. K.; Karadas, F. A Novel Synthetic Route for the Preparation of an Amorphous Co/Fe Prussian Blue Coordination Compound with High Electrocatalytic Water Oxidation Activity. *Inorganic Chemistry* **2016,** *55* (9), 4301-4307.
116. Hegner, F. S.; Herraiz-Cardona, I.; Cardenas-Morcoso, D.; López, N.; Galán-Mascarós, J.-R.; Gimenez, S. Cobalt Hexacyanoferrate on $BiVO_4$ Photoanodes for Robust Water Splitting. *ACS Applied Materials & Interfaces* **2017,** *9* (43), 37671-37681.
117. Moss, B.; Hegner, F. S.; Corby, S.; Selim, S.; Francàs, L.; López, N.; Giménez, S.; Galán-Mascarós, J.-R.; Durrant, J. R. Unraveling Charge Transfer in CoFe Prussian Blue Modified BiVO4 Photoanodes. *ACS Energy Letters* **2019,** *4* (1), 337-342.
118. Urbain, F.; Rau, U.; Jaegermann, W. *Light induced water splitting using multijunction thin film silicon solar cells*. Forschungszentrum Jülich: 2016.

119. McCrory, C. C. L.; Jung, S.; Peters, J. C.; Jaramillo, T. F. Benchmarking Heterogeneous Electrocatalysts for the Oxygen Evolution Reaction. *Journal of the American Chemical Society* **2013,** *135* (45), 16977-16987.
120. Welter, K.; Hamzelui, N.; Smirnov, V.; Becker, J. P.; Jaegermann, W.; Finger, F. Catalysts from earth abundant materials in a scalable, stand-alone photovoltaic-electrochemical module for solar water splitting. *Journal of Materials Chemistry A* **2018,** *6* (33), 15968-15976.
121. Perron, H.; Mellier, T.; Domain, C.; Roques, J.; Simoni, E.; Drot, R.; Catalette, H. Structural investigation and electronic properties of the nickel ferrite $NiFe_2O_4$: a periodic density functional theory approach. *Journal of Physics: Condensed Matter* **2007,** *19* (34), 346219.
122. Liu, G.; Wang, K.; Gao, X.; He, D.; Li, J. Fabrication of mesoporous $NiFe_2O_4$ nanorods as efficient oxygen evolution catalyst for water splitting. *Electrochimica Acta* **2016,** *211*, 871-878.
123. Liu, J.; Zhu, D.; Ling, T.; Vasileff, A.; Qiao, S.-Z. S-$NiFe_2O_4$ ultra-small nanoparticle built nanosheets for efficient water splitting in alkaline and neutral pH. *Nano Energy* **2017,** *40*, 264-273.
124. Stranks, S. D.; Snaith, H. J. Metal-halide perovskites for photovoltaic and light-emitting devices. *Nature nanotechnology* **2015,** *10* (5), 391.
125. Manser, J. S.; Christians, J. A.; Kamat, P. V. Intriguing optoelectronic properties of metal halide perovskites. *Chemical Reviews* **2016,** *116* (21), 12956-13008.
126. Amgar, D.; Aharon, S.; Etgar, L. Inorganic and Hybrid Organo-Metal Perovskite Nanostructures: Synthesis, Properties, and Applications. *Advanced Functional Materials* **2016,** *26* (47), 8576-8593.
127. Li, X.; Cao, F.; Yu, D.; Chen, J.; Sun, Z.; Shen, Y.; Zhu, Y.; Wang, L.; Wei, Y.; Wu, Y.; Zeng, H. All Inorganic Halide Perovskites Nanosystem: Synthesis, Structural Features, Optical Properties and Optoelectronic Applications. *Small* **2017,** *13* (9), 1603996.
128. Liu, F.; Ding, C.; Zhang, Y.; Ripolles, T. S.; Kamisaka, T.; Toyoda, T.; Hayase, S.; Minemoto, T.; Yoshino, K.; Dai, S.; Yanagida, M.; Noguchi, H.; Shen, Q. Colloidal Synthesis of Air-Stable Alloyed $CsSn_{1-x}Pb_xI_3$ Perovskite Nanocrystals for Use in Solar Cells. *Journal of the American Chemical Society* **2017,** *139* (46), 16708-16719.
129. Wei, Y.; Cheng, Z.; Lin, J. An overview on enhancing the stability of lead halide perovskite quantum dots and their applications in phosphor-converted LEDs. *Chemical Society Reviews* **2019,** *48* (1), 310-350.
130. Conings, B.; Drijkoningen, J.; Gauquelin, N.; Babayigit, A.; D'Haen, J.; D'Olieslaeger, L.; Ethirajan, A.; Verbeeck, J.; Manca, J.; Mosconi, E.; Angelis, F. D.; Boyen, H.-G. Intrinsic Thermal Instability of Methylammonium Lead Trihalide Perovskite. *Advanced Energy Materials* **2015,** *5* (15), 1500477.
131. Schmidt, L. C.; Pertegás, A.; González-Carrero, S.; Malinkiewicz, O.; Agouram, S.; Mínguez Espallargas, G.; Bolink, H. J.; Galian, R. E.; Pérez-Prieto, J. Nontemplate Synthesis of $CH_3NH_3PbBr_3$ Perovskite Nanoparticles. *Journal of the American Chemical Society* **2014,** *136* (3), 850-853.
132. Zhao, Y.; Li, J.; Dong, Y.; Song, J. Synthesis of Colloidal Halide Perovskite Quantum Dots/Nanocrystals: Progresses and Advances. *Israel Journal of Chemistry* **2019,** *59* (8), 649-660.
133. Li, Y.-F.; Feng, J.; Sun, H.-B. Perovskite quantum dots for light-emitting devices. *Nanoscale* **2019,** *11* (41), 19119-19139.
134. Krieg, F.; Ochsenbein, S. T.; Yakunin, S.; ten Brinck, S.; Aellen, P.; Süess, A.; Clerc, B.; Guggisberg, D.; Nazarenko, O.; Shynkarenko, Y.; Kumar, S.; Shih, C.-J.; Infante, I.; Kovalenko, M. V. Colloidal $CsPbX_3$ (X = Cl, Br, I) Nanocrystals 2.0:

Zwitterionic Capping Ligands for Improved Durability and Stability. *ACS Energy Letters* **2018,** *3* (3), 641-646.
135. Protesescu, L.; Yakunin, S.; Bodnarchuk, M. I.; Krieg, F.; Caputo, R.; Hendon, C. H.; Yang, R. X.; Walsh, A.; Kovalenko, M. V. Nanocrystals of Cesium Lead Halide Perovskites ($CsPbX_3$, X = Cl, Br, and I): Novel Optoelectronic Materials Showing Bright Emission with Wide Color Gamut. *Nano Letters* **2015,** *15* (6), 3692-3696.
136. Li, X.; Wu, Y.; Zhang, S.; Cai, B.; Gu, Y.; Song, J.; Zeng, H. CsPbX3 Quantum Dots for Lighting and Displays: Room-Temperature Synthesis, Photoluminescence Superiorities, Underlying Origins and White Light-Emitting Diodes. *Advanced Functional Materials* **2016,** *26* (15), 2435-2445.
137. Hong, W. L.; Huang, Y. C.; Chang, C. Y.; Zhang, Z. C.; Tsai, H. R.; Chang, N. Y.; Chao, Y. C. Efficient low-temperature solution-processed lead-free perovskite infrared light-emitting diodes. *Advanced materials* **2016,** *28* (36), 8029-8036.
138. Park, S.; Chang, W. J.; Lee, C. W.; Park, S.; Ahn, H.-Y.; Nam, K. T. Photocatalytic hydrogen generation from hydriodic acid using methylammonium lead iodide in dynamic equilibrium with aqueous solution. *Nature Energy* **2016,** *2* (1), 16185.
139. Gao, G.; Xi, Q.; Zhou, H.; Zhao, Y.; Wu, C.; Wang, L.; Guo, P.; Xu, J. Novel inorganic perovskite quantum dots for photocatalysis. *Nanoscale* **2017,** *9* (33), 12032-12038.
140. Hou, J.; Cao, S.; Wu, Y.; Gao, Z.; Liang, F.; Sun, Y.; Lin, Z.; Sun, L. Inorganic Colloidal Perovskite Quantum Dots for Robust Solar CO_2 Reduction. *Chemistry – A European Journal* **2017,** *23* (40), 9481-9485.
141. Xu, Y.-F.; Yang, M.-Z.; Chen, B.-X.; Wang, X.-D.; Chen, H.-Y.; Kuang, D.-B.; Su, C.-Y. A CsPbBr3 Perovskite Quantum Dot/Graphene Oxide Composite for Photocatalytic CO2 Reduction. *Journal of the American Chemical Society* **2017,** *139* (16), 5660-5663.
142. Xu, Y.-F.; Wang, X.-D.; Liao, J.-F.; Chen, B.-X.; Chen, H.-Y.; Kuang, D.-B. Amorphous-TiO_2-Encapsulated $CsPbBr_3$ Nanocrystal Composite Photocatalyst with Enhanced Charge Separation and CO_2 Fixation. *Advanced Materials Interfaces* **2018,** *5* (22), 1801015.

Chapter 2: Experimental Methods

In this chapter, a broad description of synthesis and deposition routes used for the preparation of the investigated materials and photoelectrodes, as well as the theoretical background of the techniques employed for their structural, morphological and photoelectrochemical characterization, are described. The specific details of reagents and conditions in the experimental methods used in each particular study are provided in the respective chapters.

2.1. Synthesis and deposition methods for photoelectrodes preparation.

The development of efficient and stable photoelectrodes requires critical control of the morphology, crystallinity and surface properties for achieving enhanced structural, optical, photo-electrocatalytic properties. These factors are directly related to the employed synthetic routes in the photoelectrodes preparation. There are several reported synthetic and deposition methods for semiconductor-based electrodes, with advantages and drawbacks that must be taken into account when selecting a synthetic strategy. Thus, it is fundamental to consider the balance between the semiconductor performance and the cost and scalability of the fabrication method. [1-3]

When preparing semiconductor-based photoelectrodes, the photo-absorber material is usually deposited over a glass substrate covered with a thin film of an optically transparent conductive oxide (TCO), acting as back contact. The reason for using a TCO is to provide an ohmic contact to ensure the optimal charge carrier transfer at the semiconductor/substrate interface while maintaining its high optical transparency.[3] In photoanodes, for example, a TCO material with a work function located below the conduction band of the n-type semiconductor used as photo-absorber is needed. **Table 2.1** summarizes some physical properties of common TCO materials: F-doped SnO_2 (FTO), Sn-doped In_2O_3 (ITO), and Al-doped ZnO (AZO). FTO and ITO are the most common and commercially available materials. Both of them exhibit high transparency and conductivity, however, FTO exhibits a broader electrochemical window and resists higher temperatures compared to ITO substrates, being the former more convenient for photoelectrochemical applications.[4]

Table 2.1 Material properties of some common transparent conductive oxides (TCO).[4]

TCO	*Work function (eV)*	*Conductivity ($S\ cm^{-1}$)*	*Carrier concentration (cm^{-3})*	*Mobility ($cm^2\ V^{-1}s^{-1}$)*	*Thermal stability (ºC)*
F:SnO_2 (FTO)	4.9	~1×10^3	4×10^{20}	~30	< 700
Sn:In_2O_3 (ITO)	4.7	~1×10^4	~10^{21}	~40	< 350
Al:ZnO (AZO)	4.6	~7×10^3	1.5×10^{21}	50-100	< 400

The strategies for photoelectrodes preparation over the TCO are usually based on: *i)* deposition of pre-synthesized or commercially provided particles, and *ii)* direct grown of the semiconductor over the conductive substrate. The first strategy involves the preparation of precursor solutions, through synthetic methods such as sol-gel, hydrothermal or solid-state synthesis. The as-prepared particles are further incorporated on the TCO with deposition techniques including dip coating, spin coating, screen printing and doctor blade.

Usually, the photoelectrodes prepared with these routes might suffer from poor contact between the semiconductor particles and at the semiconductor/TCO interface, leading to mechanical instability and deficient bulk charge separation and transport, with the concomitant loss of charge extraction on the TCO. However, due to the lower complexity of this approach, it can be attractive for the incorporation of previously synthesized particles.

On the other hand, the direct grown of the semiconductor material onto the TCO may overcome the limitations mentioned above, offering in most of the cases a better conductivity along the semiconductor and a good contact with the TCO. Among these strategies electrochemical deposition[5], physical vapor deposition (PVD), molecular beam epitaxy (MBE), atomic layer deposition (ALD) and chemical vapor deposition (CVD) are the most widely employed. There are several reviews on literature regarding the synthesis and growth of materials for PEC applications, providing a broad background of the techniques and control parameters.[1-2] Thus, the detailed description of all the above-mentioned techniques is out of the scope of this chapter, and only those techniques directly employed on the preparation of the materials investigated in this thesis will be described below.

2.1.1 Preparation of metal oxide-based photoelectrodes and electrocatalysts.

The preparation of the metal oxide semiconductor materials studied in this thesis, i. e. $BiVO_4$ photoelectrodes, investigated in **Chapters 4** and **5**, and Ni-Fe electrocatalyst, employed in **Chapter 6**, were based on electrodeposition as the synthetic method for direct growth over the supporting conductive substrate. This technique offers several advantages, including the compatibility with ambient atmosphere of the solutions containing the species to deposit and the easy manipulation of the synthetic variables. Then, this is a practical and inexpensive method to deposit highly reproducible metal oxide thin films or particles, depending on the control of the deposition conditions.[1, 5-6]

Figure 2.1 shows a schematic representation of the setup for electrochemical deposition of a metal, from a solution containing the oxidized specie. This particular case represents an anodic deposition, since a negative potential is applied to promote the reduction of the species in the solution at the surface of the substrate acting as the working electrode, concomitant with the deposition of the reduced species (metallic) on the substrate surface. By controlling the deposition variables, it is possible to obtain from nanoparticles to thin films of the electrodeposited metal. Usually, an annealing treatment is needed after the electrodeposition, in order to reach the desired phase of the material.

The simplicity of this technique allows the easy manipulation of the synthetic variables, such as the composition of the plating solution, pH, type of solvent, addition of doping and stabilizing agents, and temperature.[5] These factors remarkably affect the morphological characteristics of the deposited material, such as the surface area and nano-structure. Furthermore, the applied potential and the deposition current density can be used as additional variables for fine control of growth processes.[5]

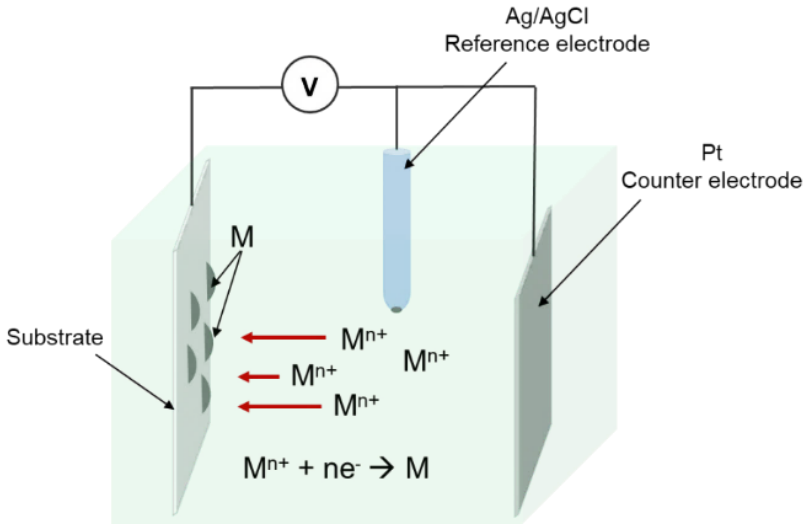

Figure 2.1. Schematic representation of the setup for electrochemical deposition, consisting of a three-electrode cell, where an FTO substrate or a metal foil acts as the working electrode, and the electrolyte containing the oxidized species to be deposited as metal (M), under an applied potential.

Since its first report by Seabold and Choi,[7] the preparation of $BiVO_4$ photoelectrodes through electrochemical deposition has been extensively used, with further modifications and improvements on the method. [8-13] The procedure used in this thesis for the fabrication of the $BiVO_4$ photoelectrodes studied in **Chapters 4** and **5,** is based on a two-step method also reported by Choi and co-workers.[13] First, a dendritic bismuth metal film is electrodeposited on the FTO substrate, from a non-aqueous plating bath containing the oxidized species Bi^{3+} (from $Bi(NO_3)_3{\cdot}5H_2O$) in ethylene glycol. The applied negative potential provides electrons to the FTO surfaces, where the reduction of Bi^{3+} takes place, concomitant to the formation and deposition of metallic bismuth, following the reaction:

$$Bi^{3+} + 3e^- \rightarrow Bi^0 \qquad E^0 = 0.308\,V \qquad (2.1)$$

The reason for using of a non-aqueous ethylene glycol solution is to increase the Bi^{3+} solubility, and simultaneously prevent the dissolution of the deposited bismuth, providing a good coverage and adhesion of the resulting films. Second, a $VO(acac)_2$ in dimethyl sulphoxide (DMSO) solution is drop casted over the as-deposited metallic Bi film, followed by a low-temperature treatment (around 80 ºC) to evaporate the solvent. Finally, the sample is annealed at 450 ºC for 2h, where the metallic bismuth and VO^{2+} are oxidized and reacted with each other to form crystalline $BiVO_4$ and amorphous V_2O_5. To obtain a pure $BiVO_4$ film, the excess V_2O_5 is dissolved by soaking the films in a 1M NaOH solution under stirring, for 30 min. **Figure 2.2a** shows the top view of an electrodeposited Bi film, recorded by Scanning Electron Microscopy (SEM), and as an inset, a digital image of the as-prepared film, whereas **Figure 2.2b** shows the resulting $BiVO_4$ film.

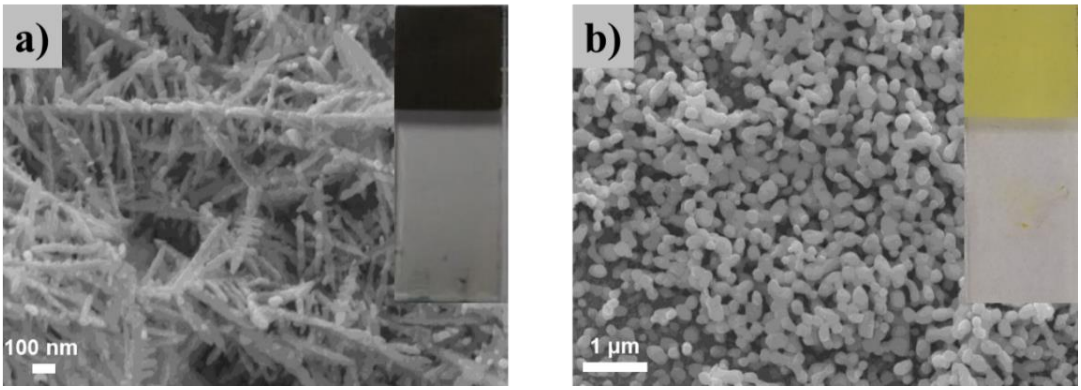

Figure 2.2 SEM micrographs of **a)** electrodeposited metallic Bi film, **b)** $BiVO_4$ film.

A similar procedure was used for the preparation of the Ni-Fe electrocatalyst, investigated in **Chapter 6**. In this case, the deposition was carried out over a bare Ni foil and the plating bath solution contains $FeCl_2 \cdot 4H_2O$ in DMSO as a source of oxidized species, further reduced under a negative applied potential as:

$$Fe^{2+} + 2e^- \rightarrow Fe^0 \qquad E^0 = -0.447\ V \qquad (2.2)$$

Very low deposition charges were used in order to obtain dispersed clusters of deposited Fe-rich particles, whereas larger deposition charges lead to the formation of a metallic Fe film over the substrate.[14] The Ni foil with the as-deposited metallic Fe was annealed at 450ºC for 2h, resulting in the conversion of the as-deposited Fe film into α-Fe_2O_3 and further transformation of the metallic Ni to NiO and the possible formation of the mixed oxide $NiFe_2O_4$, according to the phase diagram of Ni[15], Fe[16] and Ni-Fe alloys.[17]

2.1.2 Multijunction solar cells and modules preparation.

Thin-film Silicon devices used in the integrated PV-EC devices in **Chapter 6** were provided by our collaborators in IEK-5 Photovoltaik, Forschungszentrum Jülich. The devices were fabricated by Plasma-Enhanced Chemical Vapor Deposition (PECVD) technique, that offers an excellent alternative for thin-film silicon-based photovoltaic synthesis, with several advantages such as their low temperature, the tuneable control over the chemical composition and the high quality of the deposited films.[18-20]

The principles and setup of the PECVD technique for silicon thin films deposition are represented in **Figure 2.3**. A typical PECVD reactor is a low-pressure chamber of a few liters volume, in which silane (SiH_4), often diluted with H_2 or Ar, is pumped-in at a low flow rate and room temperature ***(a)***. Inside the chamber, two-parallel electrodes are placed: in the powered electrode (the lower in the scheme), or cathode, a radio-frequency (RF) oscillating voltage is applied, coupled to a capacitive glow discharge that initiates the plasma generation ***(b)***. Therefore, the neutral gases are dissociated into reactive radicals, ions, neutral atoms and molecules, and other highly excited species ***(c)***. The deposition processes occur at the substrate located at the grounded electrode (the upper in the scheme), or anode, due to the interaction with the atomic and molecular fragments generated ***(d)***.

Silicon is deposited in the substrate according to the equation:

$$SiH_x(plasma) \leftrightarrow Si(solid) + xH \qquad (2.3)$$

The efficient decomposition of the SiH_4 precursor occurs around 200-250 ºC. Therefore, to enhance the chemical processes leading to the plasma formation, the substrate is heated to a temperature of around 250 ºC. It worth noting that the film deposition rate can be favored by increasing the electron density in the plasma through an increase in the process pressure or the RF power. However, this is not suitable since the high energetic ion bombardment over the growing material may lead to potential damage of the film. Finally, the products of the chemical reactions that are not deposited are pumped away from the chamber ***(e)***.[19]

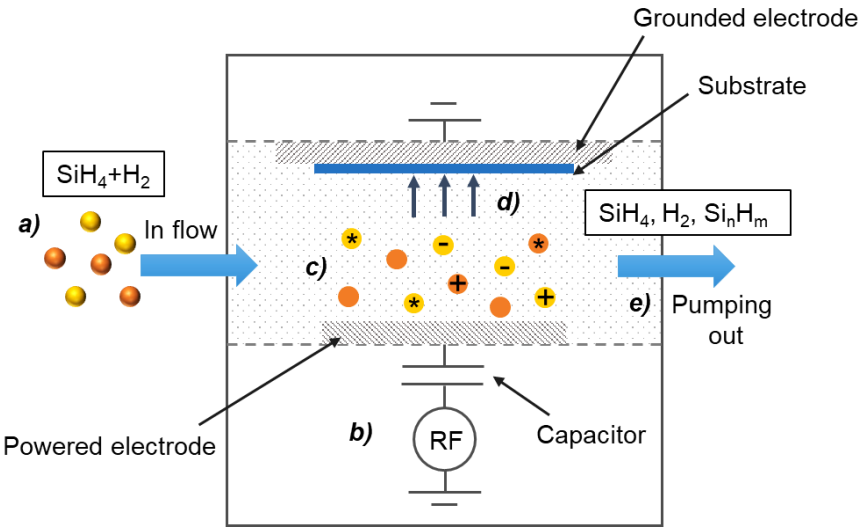

Figure 2.3. Scheme of a PECVD reactor, indicating the basic components and steps.

The process described above allows the deposition of two different allotropes: hydrogenated amorphous (*a-Si:H*) and micro-crystalline silicon (*μc-Si:H*) films, through the control of the process conditions, such as the gas flow composition, chamber pressure and RF power density.[21-23] In addition, *p*- and *n*- doped layers can be deposited by incorporation of doping gases such as B_2H_6, BF_3, $B(CH_3)_3$ or PH_3 in the inlet gas mixture.[24] Moreover, the refractive index and the electronic band gap and, consequently, the optical absorption of the material, can be modified through alloying with carbon and oxygen, using CH_4 or CO_2 in the gas mixture.[20] Compared to the conventional CVD process, PECVD requires lower temperature compared to those employed in CVD, due to the generation of dissociated species by electron impact instead of conventional thermal energy, whilst maintaining a good film quality and high deposition rates. These advantages make PECVD a very attractive strategy for large-scale implementation of silicon photovoltaics.

In **Chapter 6**, specific details about the precursors and depositions conditions are provided.

2.1.3 Synthesis of inorganic perovskite quantum dots and photoelectrodes preparation.

The outstanding optoelectronic properties of the inorganic halide perovskite quantum dots (QDs), motivates the development of new synthetic strategies for fabrication of high-quality semiconductor materials.[25-26] The synthesis by hot injection has become very popular to prepare colloidal quantum dots, providing good monodispersion, tuneable composition and luminescent properties. This leads to high fluorescence efficiency covering the whole visible region.[27] On the other hand, room temperature synthesis, such

as supersaturated recrystallization (SR) and ligand-assisted precipitation (LARP), offer more attractive approaches for large-scale productions, due to the lower costs.[28-29] More recently, novel strategies such as simple purified method[30] and in-situ crystallization synthesis[31] have been developed for the preparation of high-quality all-inorganic perovskite QDs.

In the present thesis, the perovskite QDs investigated in **Chapter 7** were provided through the collaboration with the Group of Advances Semiconductors (GAS) leaded by Prof. Iván Mora-Sero, and were prepared by the hot injection method. This synthetic route is based on the fast injection of the precursors in a supersaturated solution at an elevated temperature. Due to the fast nucleation and growth kinetics, the reaction time of the synthesis only takes a few seconds. Kovalenko and co-workers [32] introduced for the first time an adapted hot injection technique for preparation of all inorganic $CsPbX_3$ (X= F, Br or Cl) QDs, showing a photoluminescence quantum yield (PLQY) up to 90%, using a PbX_2 precursor (X= F, Br or Cl) together with oleylamine (OLA) and oleic acid (OA), dissolved in 1-octadecene (ODE). The injection of a Cs-oleate precursor at a temperature of 140-200 °C initiates the nucleation and growth of highly luminescent colloidal $CsPbX_3$ QDs with tuneable emission spectra. Furthermore, the dimension of the QDs can be adjusted by controlling the reaction temperature.[27] The hot injection process is schematically represented in **Figure 2.4**. This method is used in **Chapter 7** to prepared the $CsPbX_3$ (X = Br, I) and $CsPbBr_{1.5}I_{1.5}$ QDs, whilst a modified procedure, adapted from the reported method of Shen and co-workers[33], was employed for the preparation of $CsPb_{0.4}Sn_{0.6}I_3$ QDs.

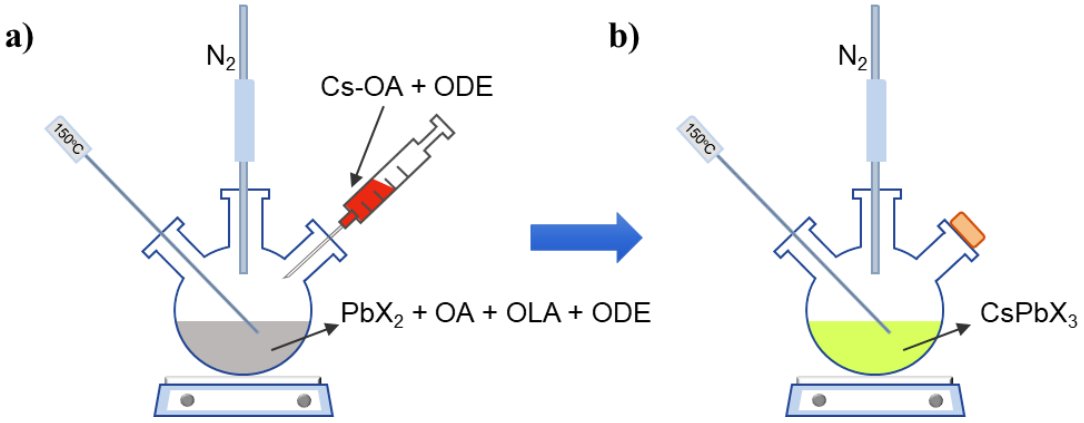

Figure 2.4. Schematic representation of the all inorganic perovskite quantum dots synthesis, by the hot injection method: **a)** The cesium precursor is rapidly injected on a saturated solution at high temperature, containing a lead halide and the ligands, **b)** nucleation and grown of luminescent colloidal quantum dots.

It worth noting that the optoelectronic applications of colloidal $CsPbX_3$ QDs are frequently hampered by the loss of colloidal stability and by the poor structural integrity, due to the facile desorption of surface capping molecules during isolation and purification.[34] Therefore, several strategies of ligand capping and purification processes have been reported in order to improve the chemical stability of the perovskite QDs.[34-36]

The colloidal perovskite QDs – in particular $CsPbBr_3$ nanocrystals– were immobilized on TiO_2-coated FTO glass electrodes, through spin-coating deposition, to get a photoelectrode for PEC measurements. In this technique, a small droplet of the colloidal solution is poured at the centre of the substrate, which is then rotated at high angular speed (ω), in order to spread the material by centrifugal force. A higher ω leads to a thinner film. This process is represented in **Figure 2.5a**. Herein, a compact layer of TiO_2 was firstly

deposited by spin coating from a commercial titanium-based precursor over an FTO-covered glass substrate, previously cleaned (details of the procedure and precursors are provided in **Chapter 7**). The film was heated at 150 °C for 10 min, and then annealed at 500 °C for 30 min. Thereafter, the purified colloidal QDs suspension was deposited by spin coating on the TiO_2 compact layer, followed by a rapid immersion of the film in a solution of $Pb(NO_3)_2$ in anhydrous methyl acetate (MeOAc), to partially substitute the ODE ligand and improve the deposition of additional QDs layers.[37] **Figure 2.5b and c** show the digital pictures under visible and UV light, respectively, of $CsPbBr_3$ photoelectrode, resulting from the deposition procedure described above.

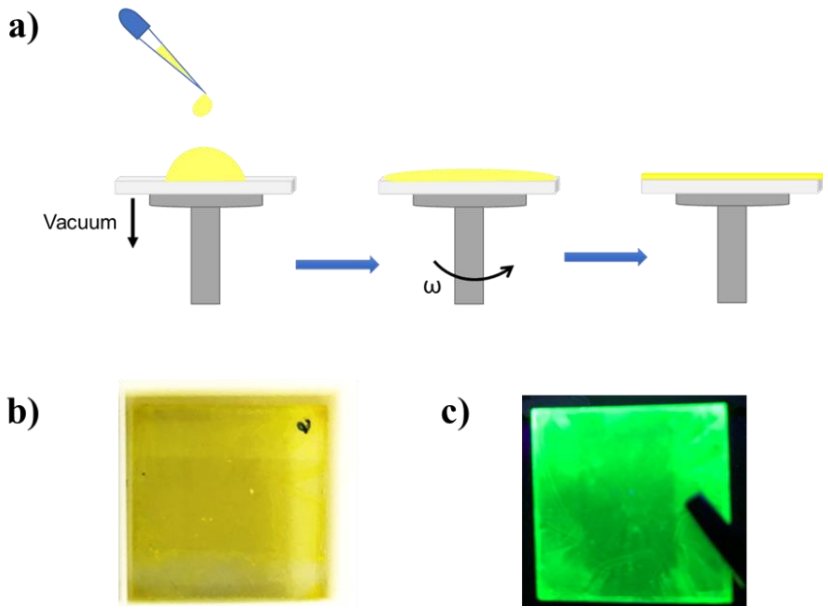

Figure 2.5. a. Schematic representation of the process of spin-coating of thin films. **b.** Digital picture under visible and **c.** UV light of the resulting $FTO/TiO_2/CsPbBr_3$ photoelectrode.

2.2. Characterization Techniques I: Structural, Morphological and Optical Techniques.

In this section, a broad description of the theory and setup of structural, morphological and optical characterization techniques employed in this thesis, is presented. The detailed information on specific measuring conditions is detailed at each particular chapter, depending on the system under investigation.

2.2.1 Scanning Electron Microscopy.

Electron microscopy is an important tool for the study of the morphology, structure and elemental composition of the materials. This technique is based on the concept of the interaction of an electron beam with a solid sample. This interaction emits different signals that are further collected by different types of detectors for specific measurements, as depicted in **Figure 2.6**.

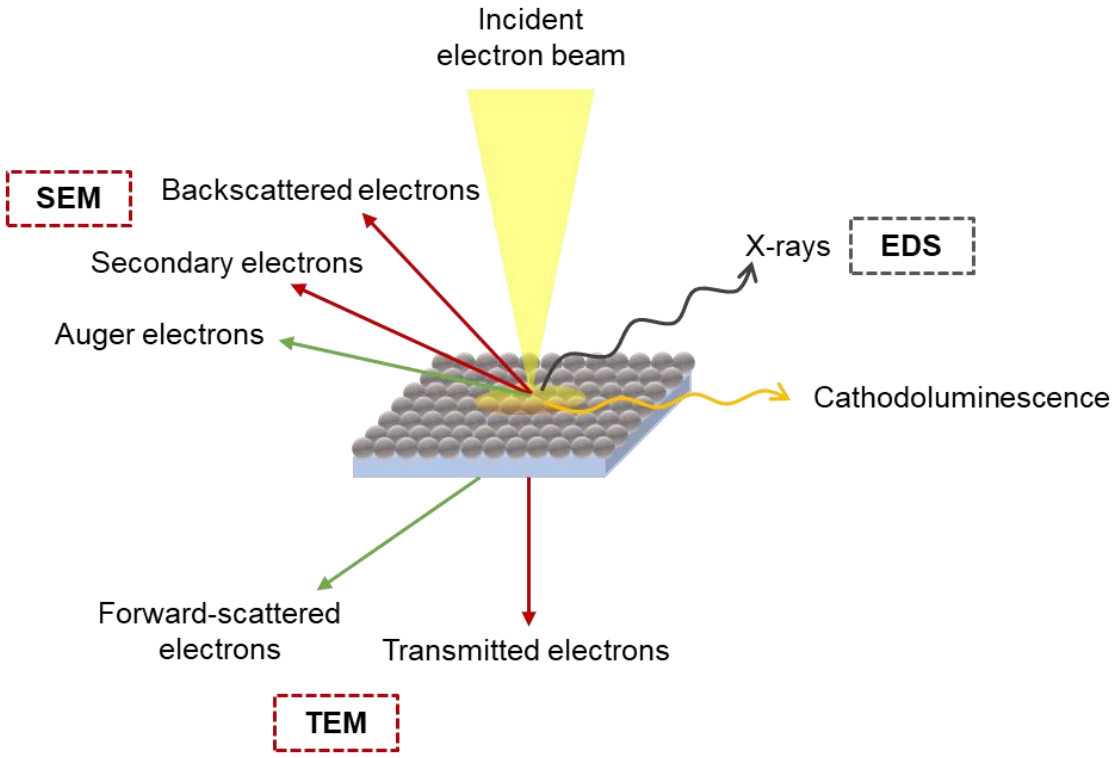

Figure 2.6. Representation of the interaction between an incident electron beam and the sample surface, and the generated useful signals for specific measurements.

Scanning Electron Microscopy (SEM) operates with secondary and/or backscattered. electrons. [38-39] Secondary electrons, arise from the sample surface (5-50 nm), with energies below 50 eV, allowing the accurate topography of the specimen surface with spatial resolution in the order of few nm.[38] Backscattered electrons, with energies above 50 eV, come up from the interaction with deeper atoms, and their signal is proportional to the average atomic number on the interaction volume. The contrast of the obtained image will vary due to both topographic and chemical contrast. Therefore, the backscattered image provides useful information about the specimen composition.[38] In a typical scanning electron microscope, the emitted electron beam is produced by resistive heating with a thermionic filament. The more advanced field emission microscopes (FE-SEM) use a potential difference between the anode and the cathode to produce the electron beam, instead of heating. Due to the sharper tip of the field emitter which produces a more collimated electron beam, the obtained images have higher resolution compared to those from thermionic sources.

2.2.2 Energy Dispersion X-Ray Spectroscopy.

Energy Dispersion X-Ray Spectroscopy (EDS or EDX) analysis uses the X-rays signals produced when the primary electrons from the incident beam knock an electron out of an atom, with the subsequent transition of a second electron between energy states, producing an X-ray of specific energy. Since each element produces characteristic X-rays, the EDS detectors are able to differentiate elemental presence and distribution in the scanned area.[38-39]

In this thesis, SEM and EDS analysis were fundamental for the morphology and compositional analysis of the investigated photoelectrodes. Unless otherwise specified, a Field Emission Scanning Electron Microscopy (FE-SEM) with a JSM-7000F JEOL FEG-

SEM system (Tokyo, Japan) equipped with an INCA 400 Oxford EDS analyser (Oxford, U.K.) operating at 15 kV was used for the measurements.

2.2.3 Transmission Electron Microscopy.

Transmission Electron Microscopy (TEM) is based on the detection of electrons which are able to penetrate through the material, providing information of the internal structure of the sample at atomic level.[29] These transmitted electrons have much higher energies compared to the case of SEM (typically between 80 and 300 keV).[38] Therefore, TEM has a higher spatial resolution, providing more detailed structural and analytical information.

Constructive and destructive interference of elastically coherent scattered electrons can generate strong beams of transmitted electrons, at specific angles to the incoming electrons determined by the crystal structure and orientation of the material. This phenomenon is called electron diffraction or Bragg scattering and is analogous to X-ray diffraction[38] (vide infra in **Section 2.2.7**). With Selected Area Electron Diffraction (SAED) technique, the detailed analysis of the obtained diffraction patterns at a certain area provides deep crystalline information of the sample, including the lattice system and parameters, crystal orientation and can also reveal the existence of different phases.

In this thesis, TEM analysis was complementary to SEM for the morphological and compositional characterization of the investigated materials. For analysis of metal oxide thin films, sample preparation consisted of scratching the film, followed by the dispersion of the material in ethanol by ultrasonication. Thereafter, the material was placed on a nickel grid. The colloidal dispersions of perovskite QDs were used as-prepared, by placing an aliquot on the nickel grid, and subsequently drying the solvent. Measurements were performed in a JEM-2100 JEOL Transmission Electron Microscope (TEM) operating at 200 kV.

2.2.4 X-Ray Photoelectron Spectroscopy.

X-Ray photoelectron spectroscopy, also called X-Ray photoemission, is one of the most employed techniques for surface analysis, in particular for both qualitative and quantitative surface chemical composition. The photoemission is based on the external photoelectric effect, where the interaction of photons with energies larger than the ionizing energy, causes the emission of free electrons from the sample. Depending on the excitation energy, there are different photoemission-based techniques: X-Ray Photoelectron Spectroscopy (XPS), Ultraviolet Photoelectron Spectroscopy, (UPS) and Synchrotron Radiation X-Ray Photoelectron Spectroscopy (SXPS), using as excitation sources X-rays, ultraviolet (UV) light and synchrotron radiation, respectively. In photoelectron spectroscopy, the information is contained in the energetic and spatial distribution of the emitted electrons, which under vacuum conditions have a mean free path large enough to travel through an energy analyzer to a detector without scattering.[40-41]

In particular, XPS uses soft X-rays, with a photon energy of 200-2000 eV, to examine electrons in core-levels. Therefore, it is a powerful tool to obtain the elemental composition (except for hydrogen and helium) of the top 10-200 Å of a solid surface, depending on the sample and instrumental conditions.[42] Furthermore, not only the atomic analysis but also the chemical environment and the oxidation state of the elements, can be provided. In this technique, the kinetic energy spectrum of ejected photoelectrons from the surface of a specimen by the irradiation of X-ray with constant energy, $h\nu$, is determined.[43] The relation between $h\nu$ and the kinetic energy of photoelectron, E_K, is expressed as:

$$E_K = h\nu - E_B - \phi \quad (2.4)$$

where E_B is the binding energy of an electron to the nucleus, relative to the Fermi level of the sample holder, and ϕ a work function of the analyzer. Note that ϕ is an instrumental parameter, which is adjusted by setting the Fermi edge emission of a clean metallic sample to zero E_B.[40]The value of E_B and difference from elemental state, also known as chemical shift, are used for the identification of a certain element and the estimation of its chemical bonding state in the specimen.[43]

Figure 2.7 shows a schematic representation of an XPS spectrometer, consisting of an X-ray source, the sample, and electron analysis components (collection lens, energy dispersive analyzer and detector). The XPS spectra are represented by the count rate electrons, i.e. intensity, versus the binding energy. Reference spectra for the different elements are compulsory for elemental analysis. Several databases provide sufficient data for the determination of the chemical states from the binding energies, such as the National Institute of Standards and Technology (NIST) Database.

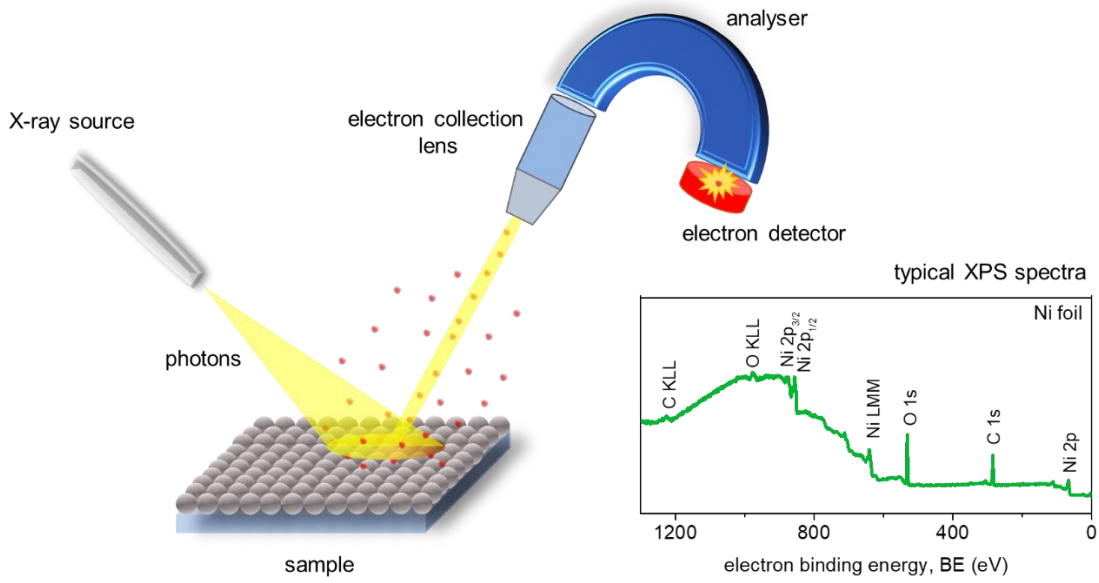

Figure 2.7. Schematic representation of XPS setup consisting of the X-ray source, the sample and the electron analyzer system. The XPS spectra (intensity *vs.* binding energy) of a Ni foil is shown as an example.

XPS analysis was used in **Chapters 4** and **6**, where a detailed description of the equipment used and measurement parameters are detailed.

2.2.5 Ultraviolet Photoelectron Spectroscopy.

UPS operates on the same principles described for XPS. However, unlike XPS, UPS uses UV irradiation, with photon energies between 10-45 eV, as the excitation source. Therefore, only valence band electrons states can be accessed. In addition, this technique is particularly sensitive to the surface region, up to 10 nm depth, due to the short range of the emitted photoelectrons, compared to X-rays.[40-41] Ultraviolet photons can be produced using a gas discharge lamp, typically filled with helium, although other gases such as argon and neon can also be used. There are two types of experiments performed using UPS: Valence band determination and electronic work function measurement.

In this thesis, this technique was used in **Chapter 7**, in combination with UV-Vis spectroscopy, for determination of the valence band of colloidal QDs, prepared as thin films, and further estimation of the energy band alignment. The measurements presented in this thesis were carried out by our collaborators at Berkeley University (USA).

2.2.6 Raman Spectroscopy.

Confocal Raman Microscopy is a powerful and non-destructive technique for material characterization, that can be complementary to other optical spectroscopy and photoelectronic techniques.[44] Raman spectroscopy theory relies on the inelastic scattering of photons by a molecule, which provides information about the vibrational modes of electrons and ions presents in the sample under study, as well as phonon and molecular vibrations. When the electromagnetic radiation interacts with a molecule, incident photons with energy equal to the difference energy between the ground and an excited state, are absorbed. After such excitation, a photon is emitted, leading to elastic or inelastic scattering, as depicted in **Figure 2.8**. Elastic or Rayleigh scattering is produced when the incident and scattered photons have the same energy. On the other hand, when the energies of the emitted and incident photons are different, inelastic or Raman scattering is produced. Furthermore, when the scattered photon has less energy than the incident photon, it is called Stokes Raman scattering, and anti-Stokes Raman scattering when a scattered photon has more energy than the incident photon. After the scattering event, the sample is in a different rotational or vibrational state.

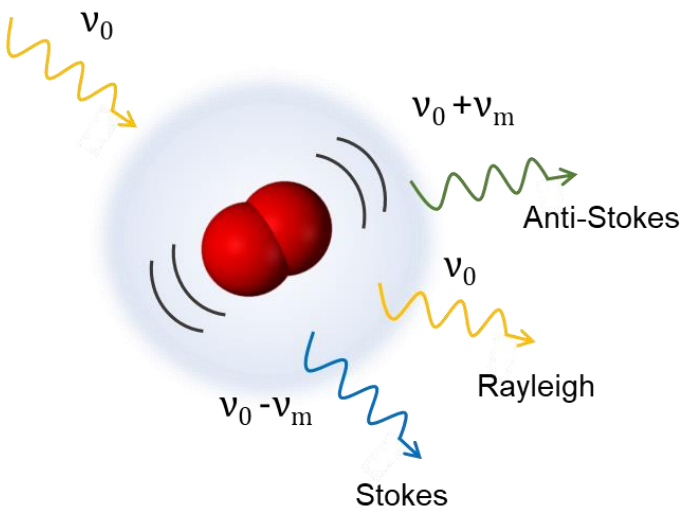

Figure 2.8. Rayleigh (elastic) and Raman (inelastic) scattering at a molecule.

In Raman spectroscopy, excitation with one fixed wavelength (laser), induces inelastic scattering related to all vibrational Raman-active modes, simultaneously. Since the vibrational frequencies are characteristic of chemical bonds and symmetry of a molecule, the Raman spectroscopy provides a fingerprint for molecular identification. Moreover, multiple Raman spectra can be collected at a certain region of a sample volume, which is further transformed into chemical images. Therefore, a compositional mapping of the sample volume is obtained, allowing the identification of different species.

Confocal Multi-Spectral Imaging (CMSI) Raman Spectroscopy, performed in a WiTec *apyron* system, is part of the structural characterization in **Chapter 5**.

2.2.7 X-Ray Diffraction.

X-ray diffraction is the elastic scattering of X-ray photons by atoms in a periodic lattice. X-Ray diffraction technique provides relevant information about the crystal structure of a solid and hence, the phases, preferred crystal orientations (texture), and other structural parameters, such as average grain size, crystallinity, strain, and crystal defects. The X-ray diffraction technique principles are represented in **Figure 2.9**. The X-ray photons impinging on the atoms of a volume of periodic atomic planes, separated by a distance *d*, are scattered in all directions, with a diffraction angle, θ, as represented. The periodic nature of a crystalline structure leads to constructive or destructive scattered radiation, which results in a characteristic diffraction pattern.[45] The geometrical interpretation of this phenomena is given by the Bragg's law:

$$n\lambda = 2d\ sin\theta \tag{2.5}$$

Where *n* is the order of diffraction, λ the wavelength of the incident beam, *d* the lattice spacing and θ the angle of the diffracted beam.

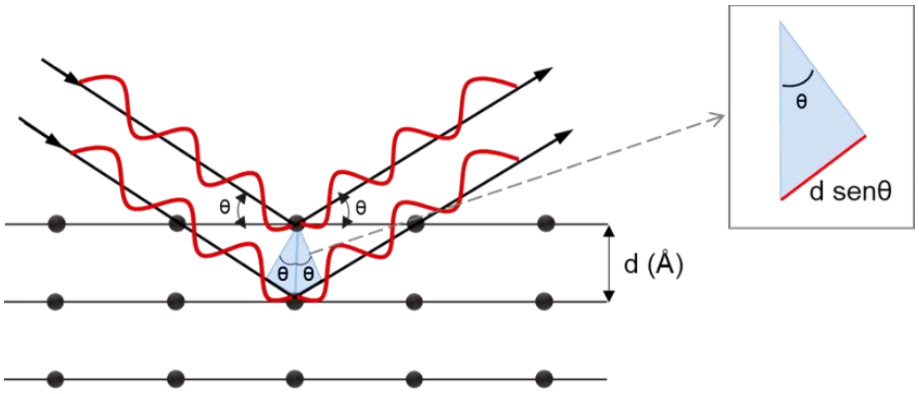

Figure 2.9. Representation of X-ray diffraction principles: X-rays are diffracted with an angle θ by two atoms, separated by a distance *d*, on the crystalline lattice. The distance $d\ sin\theta$ is shown in a magnified scheme for the sake of clarity.

The generated diffraction pattern contains information about the crystalline structure, including the lattice parameters and the distance between the lattice planes. The recorded diffraction data can be compared with the standard line patterns available for several compounds in the Powder Diffraction File (PDF) database, released and annually updated by the International Centre for Diffraction Data (ICDD). Then, a compound identification or the distinction between two or more possible phases can be done by comparing the characteristic lines of the reported crystallographic phases.[46]

XRD technique was used in **Chapters 6** and **7** as part of the structural characterization of the materials investigated. Measurements were performed in a Rigaku Miniflex 600 equipment, from Rigaku Corporation, Tokyo, Japan, using the copper K_α radiation (λ = 1.5418 Å). Specific details of measurement parameters are provided in the corresponding chapters.

2.2.8 UV-Vis Spectroscopy.

Ultraviolet-visible light (UV-Vis) spectroscopy provides relevant information about the electronic transitions through light absorption on the material, as a function of wavelength.

For example, UV-Vis is a convenient method to estimate the optical band gap (E_g) of semiconductor materials, since the electronic transitions between the valence and conduction bands, are provided.

For UV-Vis spectroscopy measurements, a spectrophotometer is used, involving an incident beam from a light source, a monochromator, a sample holder and a detector. **Figure 2.10** shows a schematic representation of the basic array for UV-Vis spectroscopy measurements. The absorbed, transmitted or reflected light can be measured as a function of the photon energy. The fraction of intensity measured after the interaction of light with the sample (I_0) versus the incident light (I) is dependent on the length of the optical path of the light through the sample (l), the absorption cross-section of the transition (σ), and difference of the population of the initial (N_1) and the final (N_2) state of the electronic levels,[3] as depicted in Eq. 2.6.

$$\frac{I}{I_0} = e^{-\sigma(N_1 - N_2 l)} \tag{2.6}$$

This relationship is also known as the Lambert-Beer's law, which can be also expressed as a function of the absorbance (A) as:

$$A = -log_{10}\left(\frac{I}{I_0}\right) \tag{2.7}$$

On the other hand, the efficiency of the photon absorption by the sample, formally known as absorptance, (η_{e^-/h^+}), is defined as the fractions of absorbed photons per those interacting with the sample.[3]

$$\eta_{e^-/h^+} = 1 - \frac{I}{I_0} = 1 - 10^{-A} \tag{2.8}$$

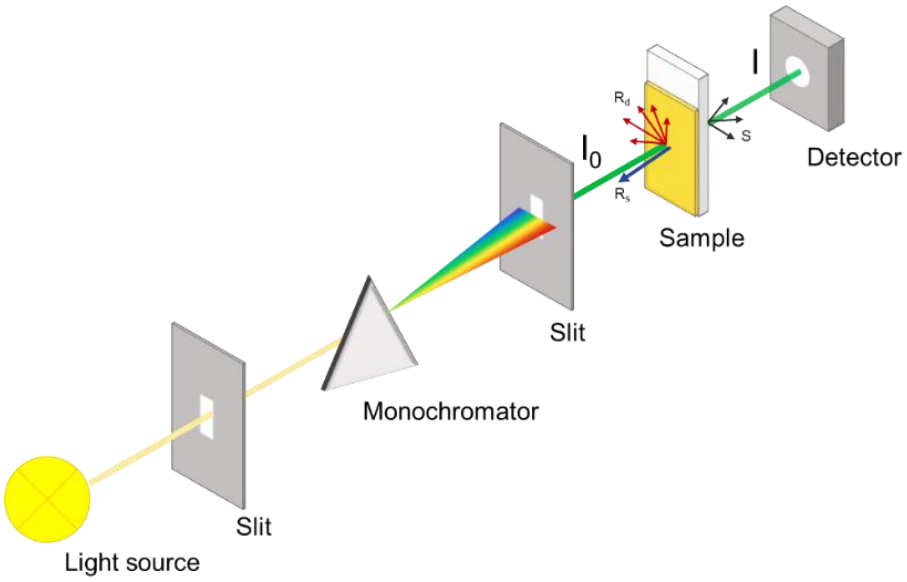

Figure 2.10. Scheme of the UV-Vis spectrophotometer array, in transmission configuration.

As depicted in **Figure 2.10**, after light-matter interaction, processes as reflection and scattering may occur at the sample. Then, the incident light after the interaction with the sample can be split in different components that include the absorptance, the transmitted light (T), the specularly reflected light (R_s), the diffuse reflected (or back-scattered) light

(R_d), and forward-scattered light (S), such that:

$$I_0 = \eta_{e^-/h^+} + T + R_s + R_d + S \tag{2.9}$$

When UV-Vis absorption is measured in thin films, it is convenient to separately measure the transmittance and the diffuse reflectance. The other reflective and scattering components can produce a decreased amount of light reaching the detector and, therefore, a non-zero baseline, which needs to be taken into account when analyzing the spectra. Hence, the absorbance can be calculated as:

$$A = -\log(T + R) \tag{2.10}$$

In highly scattering samples, an integrating sphere is used to provide a better diffuse reflectance spectrum, as depicted in **Figure 2.11**. The integrating sphere allows capturing the photons that are reflected from the sample in all directions. A specular reflectance plug, or sink, is used to minimize the noise due to R_s contribution.[3]

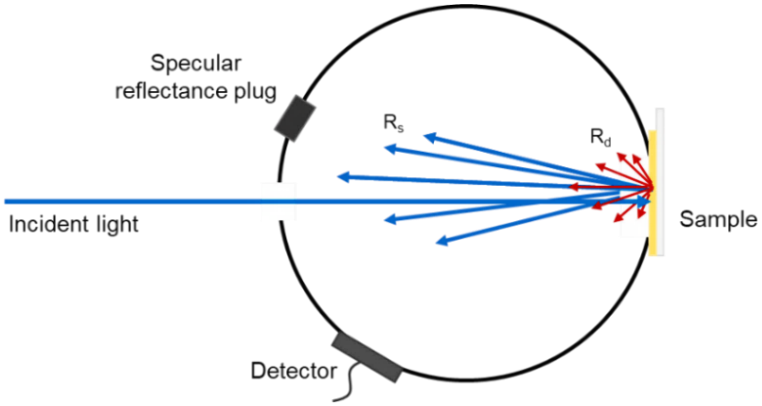

Figure 2.11. Scheme of the integrating sphere used for diffuse reflectance measurements, indicating the components resulting from the interaction of the incident light with the sample.

From the absorbance spectrum, the band gap energies can be analyzed by the Tauc plot, since:

$$(h\nu\alpha)^{1/n} = A(h\nu E_g) \tag{2.11}$$

Where α is the absorption coefficient (which depends on the film thickness, l, as $A = \alpha l$), $h\nu$ the incident light energy and n denotes the nature of the transition. Usually, the allowed transitions dominate the basic absorption processes, giving n=1/2 or n=2, for direct and indirect transitions, respectively. This relation is valid for materials with $\alpha > 10^4$ cm^{-1}. **Figure 2.12** shows the absorbance spectra of a semiconductor metal oxide, and the corresponding Tauc plot for the estimation of the band gap energy, considering an indirect transition (n=1/2).

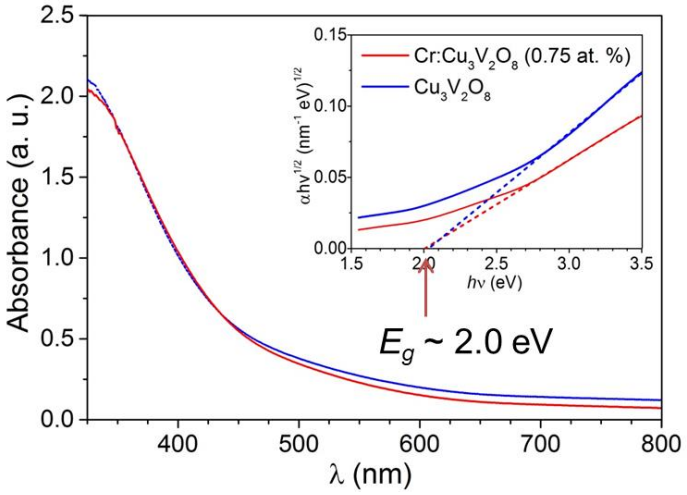

Figure 2.12. Representative absorbance spectra of the semiconductor material. As an inset, the Tauc plot used for estimation of the band gap value. Adapted from reference [47]

Another useful information from the absorbance spectra relates to the theoretical maximum photocurrent, j_{abs}, that can be achieved by the semiconductor material if all the absorbed light is converted into photocurrent. The j_{abs} value can be calculated from the absorbance spectra of the semiconductor material, and considering the spectral irradiance of the photon source, *I(λ),* according to the expression:

$$j_{abs} = \frac{q}{hc} \int \lambda \cdot I(\lambda) \cdot (1 - 10^{-A}) d\lambda \qquad (2.12)$$

In this thesis, for all the experiments involving UV-Vis absorption measurements, a Cary 300 UV−Vis Varian spectrophotometer was used, at the wavelength interval of 300 nm to 800 nm. From the absorbance spectra, Tauc plots were obtained to estimate the bag gap energy and the value provided by Eq. 2.12 was used to calculate charge separation and charge injection efficiencies during photoelectrochemical performance (vide infra in Section 2.3.2).

2.2.9 Photoluminescence Spectroscopy.

The photoluminescence (PL) effect consists of the emission of light after the absorption of a photon by a sample. This light absorption leads to the excitation of one electron to a higher electronic excited state, that further returns to a lower energy state, with the concomitant emission of a photon. This process is represented in **Figure 2.13**. If the material undergoes internal energy redistribution after the initial photon absorption, the radiated photon is of longer wavelength (i.e., lower energy) compared to the absorbed photon. The intensity and spectral content of the emitted photoluminescence is a direct measurement of different relevant material properties, including the electronic band gap, detection of impurities and defects levels, and recombination mechanisms.

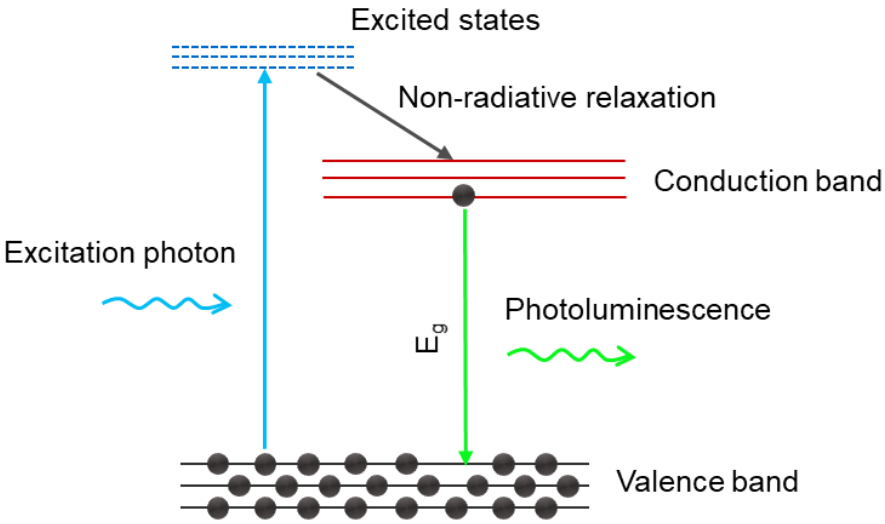

Figure 2.13. Schematic representation of the principle of photoluminescence.

Time-Resolved Photoluminescence Spectroscopy (TRPL) is an extension to steady-state PL spectroscopy involving, in this case, a short laser pulse to produce the excitation, and a fast detector to determine the emission as a function of time after the excitation. This technique allows the identification of spectral emissions with specific emissive states in a material, and the study of energy transfer from one component to another in mixed systems.

Both, steady-state photoluminescence and TRPL, were fundamental in the optical characterization of the colloidal inorganic perovskite QDs in **Chapter 7**. Furthermore, these techniques were also employed on the investigation of the photocatalytic activity of the QDs on the degradation of an organic pollutant.

2.3. Characterization Techniques II: (Photo-) Electrochemical Techniques.

This section aims to describe the experimental setup used for the (photo-) electrochemical characterizations of the materials investigated in this thesis. The specific parameters or conditions for each measurement are detailed in the respective chapters.

2.3.1 Setup for photoelectrochemical measurements and general considerations.

The photoelectrochemical measurements are imperative in the investigation of the electronic properties and performance of photoelectrodes used in PEC cells for solar-assisted energy conversion. The basic setup, depicted in **Figure 2.14**, involves:

1. A two- or three-electrode cell, including a working electrode (WE), a counter (CE) electrode, a reference electrode (RE), when appropriate, and an electrolyte.
2. A simulated sunlight source.
3. A potentiostat, coupled to a computer with a data acquisition and analysis software.

Figure 2.14 shows the experimental setup used for PEC measurements. Depending on the employed techniques, some additional modules may be needed; some examples are: a frequency response analyzer for small perturbation techniques measurements, a monochromator for the measurement of wavelength-dependent properties, or a gas

detection system for the quantification of products. Also, a Faraday cage is strongly recommended to avoid external electromagnetic interferences, when small perturbation techniques are employed.

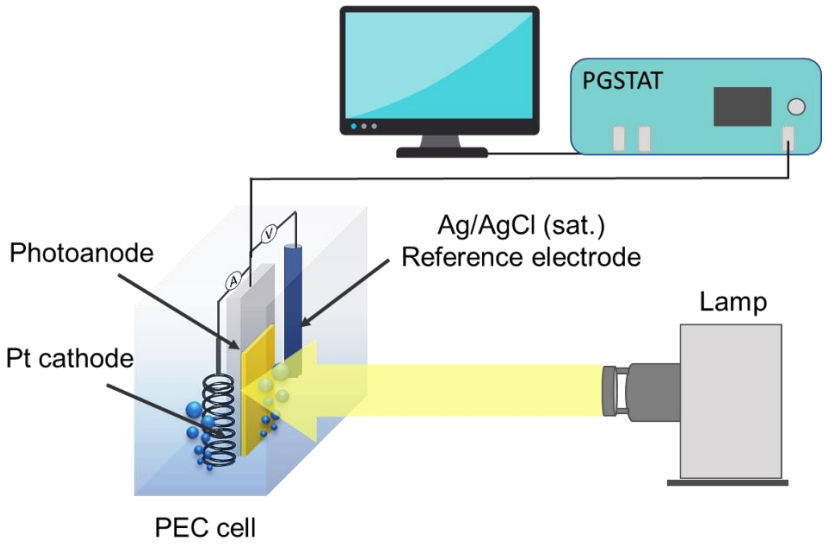

Figure 2.14. Experimental setup for photo-electrochemical (PEC) measurements, consisting of a three-electrode PEC cell, the solar simulator, and the potentiostat.

A PEC system consists of at least two electrodes to drive the oxidation and reduction reactions. However, for the study of the intrinsic properties of the photoelectrode, acting as WE, the potential should be measured respect to a fixed reference potential, in order to ensure that any change due to the applied potential is reflected only on the photoelectrode. Therefore, a third electrode with a fixed potential and legible current flow through it, is needed. Consequently, the potential of the WE is measured with respect to the potential of the RE. The most employed RE in photoelectrochemical measurements in aqueous electrolytes is the silver/silver chloride electrode (*Ag/AgCl, KCl sat.).*[4]In order to provide pH-independent metrics, the potentials measured using the *Ag/AgCl* RE, are conveniently transformed to the Reversible Hydrogen Electrode (RHE), using the Nernst equation:

$$V_{RHE} = V_{Ag/AgCl} + V^0_{Ag/AgCl} + \frac{\mathrm{RT}}{nF} \cdot pH \qquad (2.13)$$

where $V_{Ag/AgCl}$ is the recorded potential versus the reference, $V^0_{Ag/AgCl}$ is the standard potential of the *Ag/AgCl* redox couple, $\frac{\mathrm{RT}}{nF}$ at room temperature is a constant value, 0.0591, and the pH is that of the buffer solution used as the electrolyte.

On the other hand, when working in organic media, a non-aqueous electrode is used. The most commonly used is the *Ag/Ag*$^+$ electrode, consisting of an Ag wire immersed in a solution of silver nitrate or perchlorate and a supporting salt in an organic solvent.[48] The potential of the *Ag/Ag*$^+$ electrode depends on several factors including the solvent, the Ag^+ concentration and the nature and concentration of the supporting salt. Therefore, an internal reference should be used in order to further express the redox potentials measured relative to the redox potential of the internal reference compound.

For the selection of the CE, it should be kept in mind that the reaction taking place at the surface should be fast enough to avoid performance limitations, consequently, it needs a high catalytic activity and good chemical stability. Additionally, in order to ensure

homogeneous current densities, the surface area of the CE should be, at least, twice higher compared to the WE. A common choice is a platinum (Pt) wire, mesh, or foil.

The electrolyte contains the active species to be oxidized and reduced and provides a conductive media to ensure the current flow. In photoelectrochemical water splitting measurements, the electrolyte is an aqueous solution containing ionic species, with high electric conductivity, and low electrolyte resistance, which depends on both the type of ions and their concentration.[4] Moreover, the selection of the electrolytic solution strongly depends on the stability of the semiconductor material under study. For example, $BiVO_4$, which is stable between pH 3 and pH 11,[49] a Na_2SO_4 or K_2SO_4 solution is usually employed. However, in order to avoid local pH fluctuations, which may affect the flat band potential of the semiconductor, a buffer solution is preferred. Therefore, a potassium phosphate buffer, also named K-Pi buffer, which is formed by a mixture of KH_2PO_4 and K_2HPO_4, is widely used for PEC measurements with $BiVO_4$. The pH of the buffer solution depends on the concentration and the ratio of both components, being the most common condition a pH value close to neutral (6.8-7.5). Moreover, photoelectrodes containing nickel and ion oxides, require a strong alkaline solution due to stability issues. Then, KOH or NaOH solutions, are commonly used, in a pH range of 13-14. Note that, taking into account the electrolyte conductivity, potassium-based salts and buffers are preferred over the sodium-based ones.

On the other hand, photoelectrochemistry with colloidal perovskite QDs requires the use of non-polar organic solvents, due to their tendency to degradation in the presence of water or any other polar solvent. Additionally, it readily dissolves in the presence of supporting salts commonly used as the electrolyte.[50] Therefore, a careful investigation of a suitable combination of solvents and electrolytes is needed in order to ensure the stability of the materials and photoelectrodes and subsequent reliability of the measurements. In **Chapter 7**, the selection of the optimal combination of solvent and supporting salt for electro- and photoelectrochemical measurements are discussed in detail. It worth noting that even a small amount of water can significantly affect the stability of the colloidal perovskite QDs-based photoelectrodes. Hence, the solution must be prepared from anhydrous pure solvents and the salt is recommended to be previously dried.

On the other hand, tests under illumination conditions in PEC cells require a solar simulator that provides meaningful irradiation conditions for comparison with real sunlight. This is referred to the *AM1.5G* conditions, that stand the spectral distribution and intensity of sunlight on a 37º south-facing tilted surface, after traveling through 1.5 times the thickness of the Earth atmosphere.[4] The total *AM1.5G* spectrum has a total integrated intensity of 100 mW cm^{-1} (1 sun) and includes both direct and diffuse contributions of the incident sunlight. Xenon lamps, properly equipped with optical filters, are widely accepted to provide a good match with the solar spectrum. The light source is generally equipped with an electromechanical shutter to set the light on/off and a frequency controller for chopped-light measurements.

Finally, and more importantly, a potentiostat is essential for PEC measurements. In a potentiostat, there are three leads for the WE, CE, and RE, and an additional fourth lead (S) that "senses" the potential of the WE. Therefore, the potentiostat main function is to measure the potential difference between the S and the RE, ensuring that it is equal to the desired potential difference by adjusting the potential at the CE.[4] Additional internal modules can be present for specific measurements, such as a frequency response analyzer (FRA), for impedance measurements, or external modules as a LED driver for light intensity modulated measurements. A software is also needed to control the potentiostat and for data acquisition. During this thesis, potentiostats from different manufacturers were used: Metrohm Autolab and Gamry.

Once the main components of the PEC setup are presented, the PEC characterization techniques used in this thesis are described below. Note that particular conditions for measurements are specified at the respective chapter, depending on the system and the type of analysis.

2.3.2 Photocurrent–Voltage measurements.

The first step of the evaluation of the performance of a photoelectrode is the current density-voltage ($j-V$) curve. Note that, a broad theoretical background regarding the physics of the semiconductor, including their $j-V$ characteristic in both dark and illumination conditions, is provided in Chapter 1, Section 1.3.

$j-V$ measurements are performed by recording the current while sweeping the potential at a constant scan rate, either in linear sweep or cyclic voltammetry mode (LSV and CV, respectively). This can be done in dark conditions and under constant illumination or switching on/off the illumination with a constant frequency (chopped-light). valuable information can be extracted, including:

- The dark current and the photocurrent densities as a function of the applied potential.
- The sign (anodic or cathodic), the onset potential of the photocurrent, and consequently, the overpotentials for the reaction.
- Limitations from charge carrier recombination, either in the space charge region or at the surface, by using appropriate sacrificial agents.
- Transport limitations (from front and back-side illumination) and surface recombination (transient effects with chopped-light measurements).

In a photoelectrode for water splitting, the measured net current density is directly proportional to the rate of water photo-electrolysis, if the Faradaic efficiency is 100%. The evaluation of the limiting factors for the performance of the photoelectrode can be done, in a first step, using sacrificial agents on the electrolyte solution, which allows the deconvolution of surface and bulk recombination, as a function of the applied potential.[51] For example, for evaluation of photoanodes, species with less thermodynamic and kinetic demand than water oxidation are used, acting as "hole scavengers" that provide a fast charge injection and therefore, suppression of surface recombination. Some common hole scavengers are H_2O_2, especially used with hematite photoelectrode, and Na_2SO_3 used with $BiVO_4$ photoelectrodes. Therefore, if surface recombination is completely suppressed, then any difference between the maximum theoretical photocurrent, j_{abs} calculated from Eq. 2.13, and the observed photocurrent can be assigned to bulk recombination, or, in other words, the magnitude of the charge separation efficiency η_{cs}:

$$\eta_{cs} = \frac{j_{HS}}{j_{abs}} \tag{2.14}$$

Comparison of the photocurrent recorded in an electrolyte solution with and without a hole scavenger allows the quantification of the charge injection, or catalytic, efficiency η_{cat}:

$$\eta_{cat} = \frac{j_{H_2O}}{j_{HS}} \tag{2.15}$$

On the other hand, CV have been successfully used for the quantitative estimation of HOMO and LUMO levels of electro-active molecular species. Semiconductor quantum dots, like redox molecules, have discrete energy levels, and are expected to undergo electron transfer, through the valence and conduction band edges. Therefore, the respective anodic and cathodic peaks in the CV of a dispersion of quantum dots in a proper solvent can be attributed to the band edge positions. The difference between these two levels is defined as the quasi-particle band gap or electrochemical band gap, and can be correlated with the optical band gap.[52-53]

Both LSV and CV measurements were used in all the chapters of the present thesis, as a fundamental step in the PEC characterization of the studied materials. Furthermore, the application of cyclic voltammetry for the estimation of the band edges position was used in **Chapter 7**, for the determination of the band structure of colloidal all-inorganic halide perovskite QDs.

2.3.3 Quantum conversion efficiencies.

The spectral response measurements provide useful information about the limiting factors for the performance of a photoelectrode. The Incident Photon-to-Current Efficiency (IPCE), or External Quantum Efficiency (EQE) is the fraction of incident photons that is converted into electrons, which can be measured at the outer circuit. The IPCE is obtained by dividing the measured photocurrent at a constant applied potential, by the number of photons impinging the photoelectrode, as a function of the wavelength, through the expression:

$$IPCE\ \% = \frac{j_{ph}}{P_\lambda} \cdot \frac{1239.8}{\lambda} \cdot 100 \qquad (2.16)$$

where j_{ph} is the measured photocurrent density, in mA cm^{-1}, potentiostatically measured, the value 1239.8 corresponds to the product hc (Plank´s constant and speed of light respectively), P_λ is the power, in mW cm^{-2}, of the incident light at a particular wavelength, λ, in nm. Note that j_{ph} is an average value obtained for a chronoamperometric measurement for several minutes. The power of the incident light as a function of the wavelength is determined using a calibrated photodiode.

The experimental setup for IPCE measurements, represented in **Figure 2.15**, is similar to the basic setup for photoelectrochemical measurements, but including a monochromator to provide the wavelengths spectra, and optical lens to focus the incident beam.

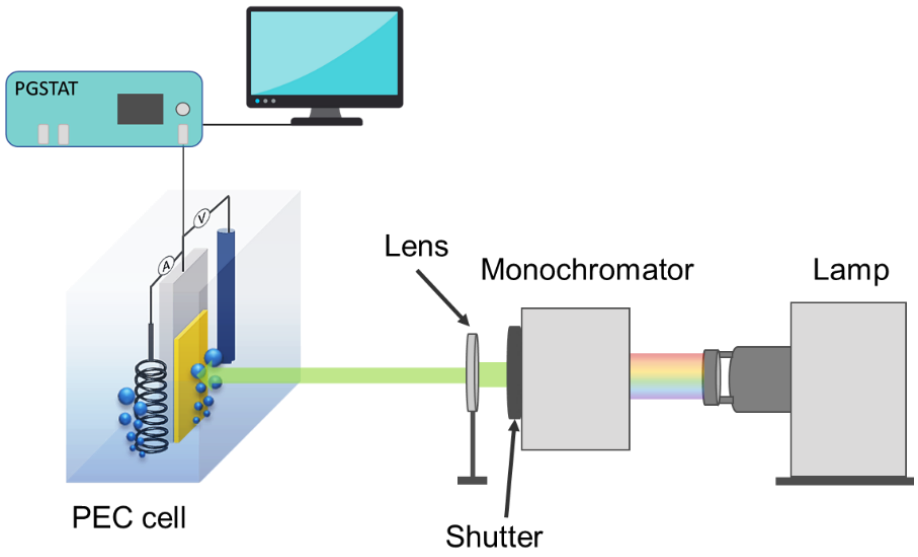

Figure 2.15 Experimental setup for quantum efficiency measurements in photoelectrochemical cells.

The difference between the maximum value, 100%, and the calculated IPCE reflects the contribution of both the portion of incidents photons that are reflected or transmitted, and the number of photogenerated carriers that recombine before reaching the outer circuit. In order to separate these contributions, the IPCE can be divided by absorptance of the photoelectrode, resulting in the Absorbed Photon-to-Current Efficiency (APCE), or Internal Quantum Efficiency (IQE):

$$APCE\ \% = \frac{IPCE}{\eta_{e^-/h^+}} \cdot 100 \tag{2.17}$$

Where η_{e^-/h^+} is the absorptance, defined as the fraction of photogenerated carriers (electron–hole pairs) per incident photon flux, and it is obtained from the absorbance (A) as:

$$\eta_{e^-/h^+} = 1 - 10^{-A} \tag{2.18}$$

The IPCE response, recorded under monochromatic irradiation, can be used to calculate the total photocurrent under solar irradiation by the integration of the IPCE spectra as a function of the wavelength, $IPCE\ (\lambda)$, and the solar photon flux $\Phi\ (\lambda)$ as:

$$j_{IPCE} = \int (IPCE\ (\lambda) \cdot \Phi\ (\lambda) \cdot q)\, d\lambda \tag{2.19}$$

The solar photon flux can be calculated from tabulated solar irradiance data. The comparison between the photocurrent calculated from the IPCE measurements and that recorded by voltammetry measurements under AM1.5G solar spectrum provides a validation of the experimental procedure for both measurements.

In this thesis, steady-state quantum efficiency measurements were performed as part of the PEC characterization of the photoelectrodes studied in **Chapter 4**, where specific details about the used equipment and measurements conditions are detailed.

2.3.4 Small perturbation techniques.

Small perturbation techniques include Impedance Spectroscopy (IS), Intensity Modulated Photocurrent Spectroscopy (IMPS), and Intensity Modulated Photovoltage Spectroscopy (IMVS). These techniques have become powerful tools for fundamental studies in solar energy conversion devices, including photoelectrodes for solar-assisted water splitting. Therefore, these techniques are especially useful for understanding the charge carrier dynamics and limitations for the performance of semiconductor materials in PEC cells.

As discussed in the section above, the photoelectrochemical characterization of a photoelectrode includes the 'photocurrent versus applied potential' plot, which is usually recorded at a single light intensity. However, an extended representation of the photoelectrode performance can be obtained by measuring the extracted steady-state photocurrent j_e, at different photon flux Φ, and applied potential E, to get a 3D representation of the Light-Current-Potential dependence,[54] as shown in **Figure 2.16a** for a $BiVO_4$ photoelectrode, as an example. Note that, the photon flux, Φ, can be expressed in units of electrical current density, $j_\phi = q\Phi$.

Figure 2.16b shows the surface representation of operation points determined by steady-state performance in terms of the variables j_e, Φ and E. Such a steady-state surface cannot provide detailed mechanistic information, being necessary to work in the dynamic regime by using methods such as small perturbation techniques. These techniques involve a small perturbation of the variables, with certain angular frequency ω, and measurement of the resulting output. When the variables are taken in output/input couples, the result of the frequency-modulated spectroscopy is a transfer function.[54] Note that, taking the variables in couples in **Figure 2.16b**, the slope of the curve is given by the zero-frequency value of the transfer function.

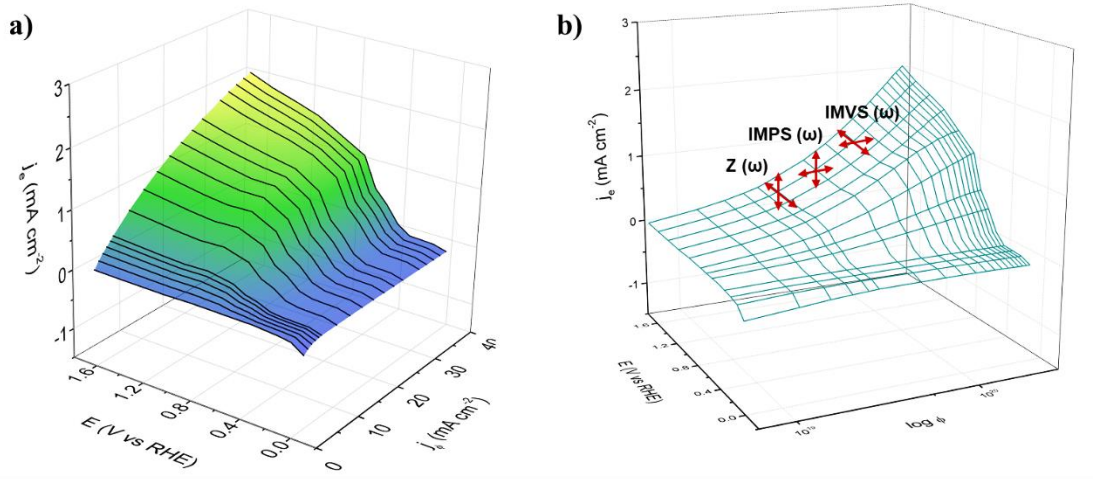

Figure 2.16. a. Light-Current-Potential performance 3D plot of a $BiVO_4$ photoelectrode. **b.** Surface representation of steady-state operation points.

Recently, an important general expression was established that relates the photo-current, $\hat{j}_e$, arising from a small perturbation of light, $\hat{j}_\phi$, or voltage, $\hat{V}$, at any frequency as a linear combination of the transfer functions expressed as coefficients,[54] such as:

$$\hat{j}_e = Q_\phi(\omega)\hat{j}_\phi + Z^{-1}(\omega)\hat{V} \qquad (2.20)$$

The derivation of this expression is detailed in reference[54]. The notation $\hat{x}$ is used to represent a small perturbation over the quantity x and indicates that $\hat{x}$ is the complex amplitude of a sinusoidal ac perturbation of x. For a linear response of measured variable with respect to the modulated quantity, so that the transfers function is independent of the amplitude of the perturbation (linear), the small $\hat{x}$ is required. From Eq. 2.20, the absence of a modulated illumination ($\hat{j}_\phi = 0$) gives the definition of impedance, where the photocurrent response with an ac perturbation of voltage is measured. With IMPS measurements, it is imposed that $\hat{V}$=0, and the modulated photocurrent under a modulated illumination is measured. Finally, with IMVS, $\hat{j}_e = 0$ holds, and the corresponding photovoltage perturbation is measured. The expressions of these transfer functions are summarized in **Table 2.2.**

Table 2.2 Definition of the transfer functions as a result of the measurement of small perturbations techniques.

Small Perturbation Technique	Transfer Function	
Impedance Spectroscopy **(IS)**	$Z(\omega) = \left.\frac{\hat{V}}{\hat{j}_e}\right\|_{\hat{j}_\Phi=0}$	(2.21)
Incident Modulated Photocurrent Spectroscopy **(IMPS)**	$Q(\omega) = \left.\frac{\hat{j}_e}{\hat{j}_\phi}\right\|_{\hat{V}=0}$	(2.22)
Incident Modulated Photovoltage Spectroscopy **(IMVS)**	$W(\omega) = \left.\frac{\hat{V}}{\hat{j}_\phi}\right\|_{\hat{j}_e=0}$	(2.23)

2.3.4.1 Impedance spectroscopy.

Electrochemical IS consists of the measurement of the ac electrical current density $\hat{j}_e$ at a certain angular frequency ω, when an ac voltage $\hat{V}$ is applied to the photoelectrode (Eq. 2.21), either in the dark or under constant illumination conditions. During an EIS measurement, the system is kept at a fixed steady-state (by imposing stationary constraints as dc voltage and constant incident light intensity) and the $Z(\omega)$ is measured by scanning multiple frequency values. Usually, a perturbation of 10 or 20 mV is reasonable for PEC measurements. Then, provided the PEC performance of a photoelectrode, as depicted in **Figure 2.16**, the analysis of the frequency domain response under an ac voltage perturbation can be performed at several points of the steady-state curve, at a constant light intensity, revealing specific kinetic and charge storage properties under PEC performance.

Figure 2.17a show the representative complex plane –imaginary impedance Z'' *versus* its real-value counterpart Z'– (Nyquist plots), while and **Figure 2.17b** show the plot of the module of the capacitance *versus* frequency (Bode plot) The analysis of different processes occurring in photoelectrodes by IS measurements have been widely described in the literature.[4, 16, 55] The equivalent circuit model (ECM) is frequently used to relate the basic electronic processes of charge transfer, accumulation and recombination to circuit elements as resistances and capacitors: the in-phase component provides resistances (charge transport and transfer) and out-of-phase component provides capacitances (charge accumulation). The simplest ECM is the Randles' circuit, represented as an inset in **Figure 2.17a**, consisting of a resistance in series with a parallel association of a capacitance and a

resistance, which appears as a single arc in the complex plane representation.[56]

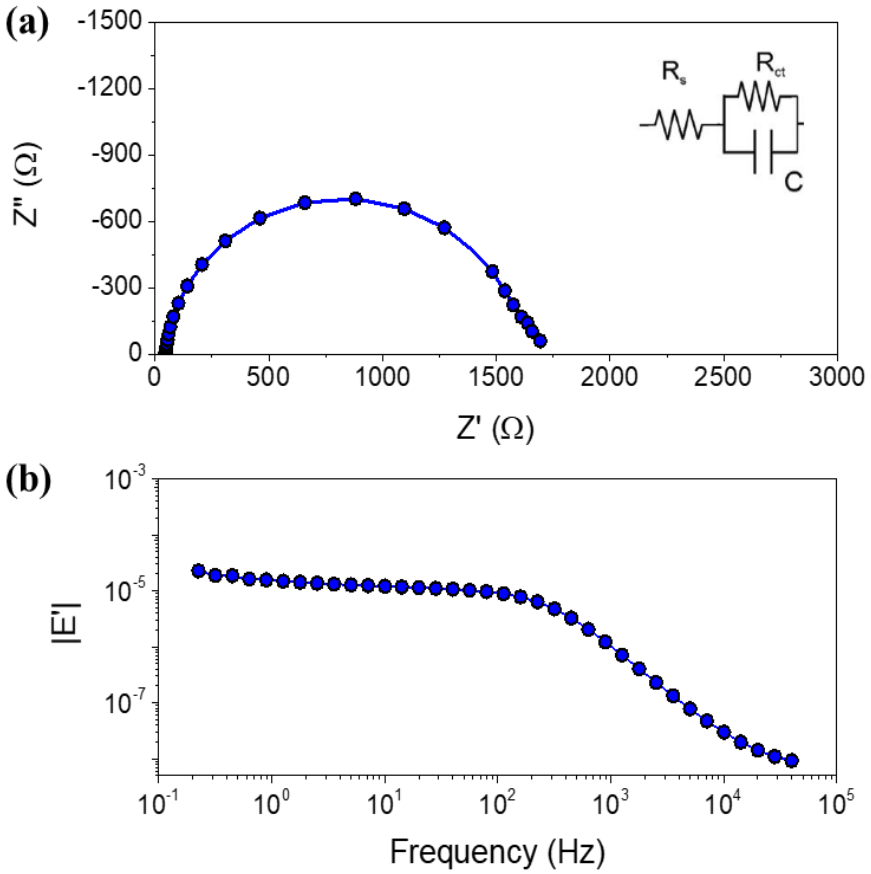

Figure 2.17. a. Representative complex plane (Nyquist plot) and **b.** Real part of the capacitance *vs* frequency (Bode plot) representations of an IS measurement on a metal oxide-based photoanode. As an inset in (a), the ECM (Randles' circuit) used for the analysis of the IS measurement is represented.

The resistances are associated with processes of carrier flux (charge transport and transfer), either inside the semiconductor or at the interfaces. The sum of all the resistive components when no frequency modulation is applied lead to the total dc resistance R_{dc}, which corresponds to the real value of $Z(\omega)$ when $\omega = 0$, i.e. the slope of the steady-state $j-V$curve. Then:

$$R_{dc} = \left(A\frac{dj}{dV}\right)^{-1} \tag{2.24}$$

where A is the geometrical surface area of the photoelectrode. Therefore, the sum of resistances obtained from the fitting can be integrated and compared to the $j-V$plot (dc values) extracted during the EIS measurements. Both plots can be compared, and their agreement support that the processes observed with the IS measurements correlate with the actual functional response of the photoelectrode, and hence its stability under investigation during the IS measurements.

On the other hand, the capacitances represent a charge storage mechanism. Moreover, the capacitances can be divided into two types: *(i)* the dielectric capacitance, associated to an internal electrical field produced by a spatial charge separation (discussed in detail in

the next section); and *(ii)* the chemical capacitance, resulting from the variation of the chemical potential, or carrier concentration. It worth noting, in some cases a non-ideal-capacitance response is observed, therefore, a constant-phase element (CPE) is used instead of a pure capacitance element. Since:

$$Z = Y^{-1}(i\omega)^{-n} \tag{2.25}$$

Depending on the value of n, the behavior of the CPE can vary from purely resistive (n=0) to purely capacitive (n=1) behavior.

For the simplest model represented in **Figure 2.17a**, R_s is the series resistance, that includes transport through the electrical contact and the electrolyte, and its value remains constant if all the experiments are performed in the same conditions; R_{ct} is the charge transfer resistance, that accounts for different interfacial charge transfer steps leading to the electrochemical reaction at the semiconductor/electrolyte interface; and C is capacitance. This assignment implicitly neglects the contribution of the transport resistance (R_{tr}) compared to the charge transfer resistance ($R_{tr} \ll R_{ct}$). The evolution of both R_{ct} and C components with the applied potential reveals significant information regarding kinetics and charge accumulation process, respectively, providing mechanistic insights into the overall performance of the photoelectrodes.

EIS measurements were performed as part of the PEC characterization of the photoelectrodes investigated in **Chapter 4** of the present thesis, where further details of the experimental parameters (dc applied potential, ac perturbation, and frequency interval) are provided.

2.3.4.2 Incident Modulated Photocurrent Spectroscopy.

The IMPS technique has been increasingly used for understanding the charge carrier dynamics and performance limitations of semiconductor materials in PEC cells. Usually, the IMPS results treatment involves the decoupling of electron transfer from other processes such as mass transfer and other chemical reactions at a semiconductor/electrolyte interface [57-64] With IMPS measurements, it is imposed that $\hat{V}$=0, and the modulated photocurrent $\hat{j}_e$ under a modulated illumination $\hat{j}_\phi$ is measured (Eq. 2.21 from **Table 2**). Note that, the experimental setup for IMPS measurements should include an external module to provide and control an intensity-modulated light. **Figure 2.18a** shows the representation of IMPS measurements in the complex plane. The low-frequency limit of the Q transfer function is given by:

$$Q(0) = \frac{\partial j_e}{\partial j_\phi} \tag{2.26}$$

An important feature of the IMPS spectra is the connection of the low-frequency values with the EQE. From Eq. 2.26, it can be noted that the low-frequency limit is a differential external quantum efficiency (EQE_{diff}), from a given steady state. A traditional EQE_{diff} measurement involves a small perturbation in an incident monochromatic light intensity from a given steady-state, and the corresponding response is measured. This measurement is also termed as a differential spectral response method. Therefore, IMPS measurements are a reflection of the EQE of the device under test.

Moreover, Eq. 2.26 denotes that the low-frequency intercept of the IMPS transfer function is directly connected to small perturbation of the $j_e - j_\phi$ steady-state curve, as represented in Figure **2.18b**. Specifically, $Q(0)$ is the slope of the steady-state extracted

photocurrent dependence on the photon flux. This is a powerful concept for further interpretation of IMPS features, which can be extended that the IMPS transfer function is the modulated EQE.[54, 65]

Chapter 5 of the present thesis includes a detailed discussion about the interpretation of the low-frequency values of IMPS measurements. Further detailed experimental setup and measurement considerations are also provided.

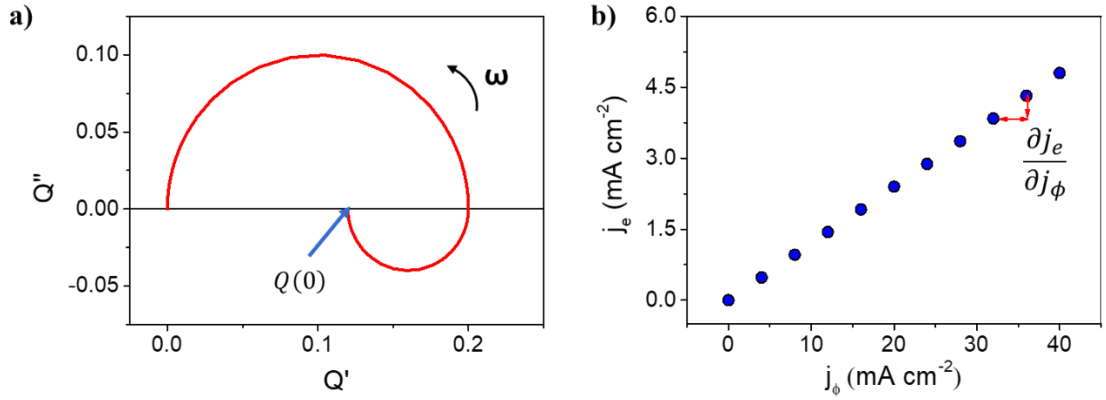

Figure 2.18. a. Representative complex plane representation of IMPS measurement on a $BiVO_4$ photoanode. **b.** $j_e - j_\phi$ steady-state curve; the derivative of the extracted current with respect to the photon current is represented.

2.3.5 Stability measurements.

One of the most significant drawbacks in semiconductor materials for PEC applications is their long-term stability. For example, the photogenerated charge carriers in a photoelectrode for water splitting can oxide or reduce the semiconductor itself, leading to photo-corrosion, instead of the desired water oxidation and reduction reactions. Therefore, a photocurrent stability test should be included in the PEC characterization of semiconductors materials. The standard stability test evaluates the current density versus the time under illuminated operational conditions, generally through a chronoamperometry measurement. Furthermore, in order to understand the nature of any degradation process, additional post-mortem morphological, structural and chemical characterization, such as SEM, XPS, XRD, etc., should be performed on the tested sample.[3] Stability tests through chronoamperometric measurements were included in the PEC characterization of materials studied in **Chapters 4** and **6**.

2.3.6 Detection and quantification of evolved gases.

The detection and quantification of gases resulting from the reactions occurring at the electrode surface are key when evaluating the performance of photoelectrodes for water splitting, in order to show the efficiency of the charge transferred to the electrode surface to be actually used in the water splitting process.[66]

In this thesis, the experimental detection of evolved gases, in particular evolved oxygen, was carried out by gas chromatography (GC) in **Chapters 4** and **6**, using a sealed cell coupled to an Agilent Micro-GC gas chromatograph. The detection and quantification of evolved oxygen were performed in a chronoamperometric measurement, usually at the thermodynamic water oxidation potential (1.23 V vs RHE) unless otherwise specified. The amount of detected gas is given as partial pressure by the calibration of the chromatograph,

which is further converted into a molar quantity as:

$$n\ (mol) = \frac{{p(O_2)}/{p^0}}{V_m}\ (\mathrm{P} \cdot t\ ) \tag{2.27}$$

where ${p(O_2)}/{p^0}$ is the partial pressure, V_m is the molar volume of the gas (calculated as 22.4 mol L^{-1} from the equation of ideal gases), P is the total gas flux, in L min^{-1}, and t the time, in min.

On the other hand, if all the current is related to the water oxidation reaction producing O_2, the amount of evolved gas can be theoretically predicted through the Faraday´s law:

$$n_{O_2}\ (mol) = \frac{I \cdot t}{z \cdot F} \tag{2.28}$$

Where I is the measured current by chronoamperometry, which is multiplied by the time, t, z is the number of transferred electrons, i.e. z =4 for the water oxidation reaction, and F is the Faraday constant (96 485 C mol^{-1}).

The ratio between the experimental and theoretical amount of evolved gas is called the Faradaic Efficiency (FE), and it is calculated by the expression:

$$FE\ (\%) = \frac{n_{O_2}\ (experimental)}{n_{O_2}\ (theoretical)} \cdot 100 \tag{2.29}$$

Therefore, if all the recorded current is involved in the desired reaction, e.g. water oxidation to produce O_2, the FE reaches 100%, indicating that the total current is used for the oxygen evolution reaction. Otherwise, side reactions, such as electrode corrosion, can take place at the electrode surface, affecting the evolved amount of gas and hence, decreasing the FE. However, in some cases the experimental conditions, including adequate cell selling, gas flux control and the gas detection technique, affect the sensitivity of the measurements, resulting in fluctuations in the FE values.

2.3.7 Scanning Electrochemical Microscopy.

Scanning Electrochemical Microscopy (SECM) is a scanning probe technique consisting of the use of a small-scale electrode (tip), with dimensions in the μm-nm range, which scan across the surface of an immersed sample electrode. The tip records a current response, which is dependent on both the surface topography and the electrochemical activity of the sample.[67-69] **Figure 2.19a** shows the setup with the essential components for SECM measurements, consisting of a bipotentiostat, the scanned sample and the tip (**Figure 2.19b**), a three-dimensional (3D) positioning control system for the tip, and a data acquisition system.

There are different operational modes for SECM experiments, among them, the "generation/collection" approach is commonly used for the measurements of concentration profiles or chemical flux from the sample.[67] In the substrate-generation/tip-collection mode, an electroactive species is generated at the sample substrate, and further collected at a biased tip, according to the reactions:

Substrate reaction: $R - ne^- \rightarrow O$ (2.30)

Tip reaction: $O + ne^- \rightarrow R$ (2.31)

These reactions represent the simplest description of this mode, assuming that the system contains only R, without the possibility of any other side reactions. Then, the faradaic current resulting from the electrochemical reactions is recorded at both at the probe and the substrate, and depends on the topography and the electrochemical activity of the substrate.

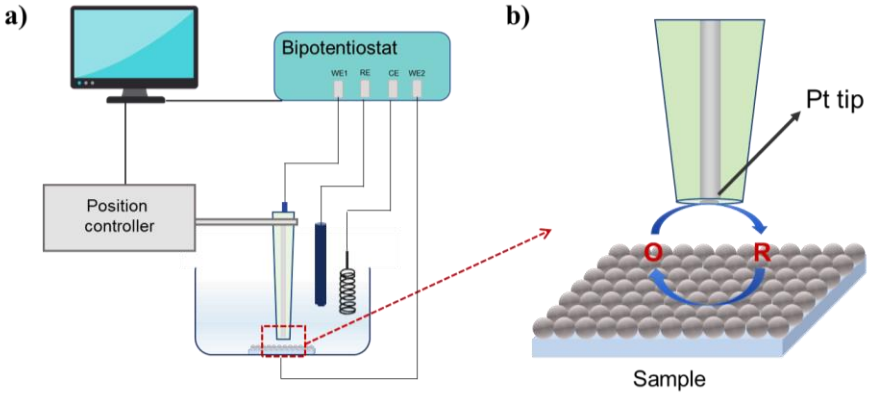

Figure 2.19. a) Experimental setup for SECM measurement. **b)** Magnification showing the sample and the scanning tip, in substrate-generation/tip-collection mode.

From this measurement, information regarding the local electrochemical behavior of the semiconductor/electrolyte interface can be obtained. In particular, the SECM technique was used in **Chapter 4** of this thesis for the direct detection of PEC O_2 evolution. For that purpose, the substrate (the photoanode under investigation) was anodically scanned, under illumination conditions, to generate O_2, whilst the tip potential was fixed at 0.1 V vs. RHE to effectively reduce the evolved O_2 by the sample. A direct confirmation for the photo-electrocatalytic O_2 generation is provided when the oxidative substrate photocurrent is followed by a reductive tip current. These measurements were carried out by our collaborators at Ben Gurion University of the Neguev.

2.4. References

1. Park, K.; Kim, Y. J.; Yoon, T.; David, S.; Song, Y. M. A methodological review on material growth and synthesis of solar-driven water splitting photoelectrochemical cells. *RSC Advances* **2019,** *9* (52), 30112-30124.
2. He, Y.; Hamann, T.; Wang, D. Thin film photoelectrodes for solar water splitting. *Chemical Society Reviews* **2019,** *48* (7), 2182-2215.
3. Chen, Z.; Dinh, H.; Miller, E. *Photoelectrochemical Water Splitting. Standards, Experimental Methods, and Protocols*. Springer-Verlag New York: 2013; p 126.
4. van de Krol, R. Photoelectrochemical Measurements. In *Photoelectrochemical Hydrogen Production*, van de Krol, R.; Grätzel, M., Eds. Springer US: Boston, MA, 2012; pp 69-117.
5. Kang, D.; Kim, T. W.; Kubota, S. R.; Cardiel, A. C.; Cha, H. G.; Choi, K.-S. Electrochemical Synthesis of Photoelectrodes and Catalysts for Use in Solar Water Splitting. *Chemical Reviews* **2015,** *115* (23), 12839-12887.
6. Therese, G. H. A.; Kamath, P. V. Electrochemical Synthesis of Metal Oxides and Hydroxides. *Chemistry of Materials* **2000,** *12* (5), 1195-1204.
7. Seabold, J. A.; Choi, K.-S. Efficient and Stable Photo-Oxidation of Water by a Bismuth Vanadate Photoanode Coupled with an Iron Oxyhydroxide Oxygen Evolution Catalyst. *Journal of the American Chemical Society* **2012,** *134* (4), 2186-2192.
8. McDonald, K. J.; Choi, K.-S. A new electrochemical synthesis route for a BiOI electrode and its conversion to a highly efficient porous $BiVO_4$ photoanode for solar water oxidation. *Energy & Environmental Science* **2012,** *5* (9), 8553-8557.
9. Smilyk, V. O.; Fomanyuk, S. S.; Kolbasov, G. Y.; Rusetskyi, I. A.; Vorobets, V. S. Electrodeposition, optical and photoelectrochemical properties of $BiVO_4$ and $BiVO_4/WO_3$ films. *Research on Chemical Intermediates* **2019,** *45* (8), 4149-4161.
10. Saada, H.; Abdallah, R.; Fabre, B.; Floner, D.; Fryars, S.; Vacher, A.; Dorcet, V.; Meriadec, C.; Ababou-Girard, S.; Loget, G. Boosting the Performance of $BiVO_4$ Prepared through Alkaline Electrodeposition with an Amorphous Fe Co-Catalyst. *ChemElectroChem* **2019,** *6* (3), 613-617.
11. Tolod, K. R.; Hernández, S.; Castellino, M.; Deorsola, F. A.; Davarpanah, E.; Russo, N. Optimization of $BiVO_4$ photoelectrodes made by electrodeposition for sun-driven water oxidation. *International Journal of Hydrogen Energy* **2020,** *45* (1), 605-618.
12. Kim, T. W.; Choi, K.-S. Nanoporous $BiVO_4$ Photoanodes with Dual-Layer Oxygen Evolution Catalysts for Solar Water Splitting. *Science* **2014,** *343* (6174), 990-994.
13. Kang, D.; Park, Y.; Hill, J. C.; Choi, K.-S. Preparation of Bi-Based Ternary Oxide Photoanodes $BiVO_4$, Bi_2WO_6, and $Bi_2Mo_3O_{12}$ Using Dendritic Bi Metal Electrodes. *The Journal of Physical Chemistry Letters* **2014,** *5* (17), 2994-2999.
14. Shaddad, M. N.; Ghanem, M. A.; Al-Mayouf, A. M.; Gimenez, S.; Bisquert, J.; Herraiz-Cardona, I. Cooperative Catalytic Effect of ZrO_2 and α-Fe_2O_3 Nanoparticles on $BiVO_4$ Photoanodes for Enhanced Photoelectrochemical Water Splitting. *ChemSusChem* **2016,** *9* (19), 2779-2783.
15. Index. In *Impedance Spectroscopy*, pp 583-595.
16. Lopes, T.; Andrade, L.; Ribeiro, H. A.; Mendes, A. Characterization of photoelectrochemical cells for water splitting by electrochemical impedance spectroscopy. *International Journal of Hydrogen Energy* **2010,** *35* (20), 11601-11608.
17. Aguado, S.; Quirós, J.; Canivet, J.; Farrusseng, D.; Boltes, K.; Rosal, R. Antimicrobial activity of cobalt imidazolate metal–organic frameworks. *Chemosphere* **2014,** *113*, 188-192.

18. Ramanujam, J.; Verma, A. Photovoltaic Properties of a-Si:H Films Grown by Plasma Enhanced Chemical Vapor Deposition: A Review. *Materials Express* **2012,** *2* (3), 177-196.
19. Krzhizhanovskaya, V. V.; Sloot, P. M. A.; Gorbachev, Y. E. Grid-Based Simulation of Industrial Thin-Film Production. *SIMULATION* **2005,** *81* (1), 77-85.
20. Gabriel, O.; Kirner, S.; Klick, M.; Stannowski, B.; Schlatmann, R. Plasma monitoring and PECVD process control in thin film silicon-based solar cell manufacturing. *EPJ Photovolt.* **2014,** *5*, 55202.
21. Matsuda, A. Formation kinetics and control of microcrystallite in μc-Si:H from glow discharge plasma. *Journal of Non-Crystalline Solids* **1983,** *59-60*, 767-774.
22. van den Donker, M. N.; Rech, B.; Schmitz, R.; Klomfass, J.; Dingemans, G.; Finger, F.; Houben, L.; Kessels, W. M. M.; van de Sanden, M. C. M. Hidden parameters in the plasma deposition of microcrystalline silicon solar cells. *Journal of Materials Research* **2011,** *22* (7), 1767-1774.
23. Dingemans, G.; Donker, M. N. v. d.; Hrunski, D.; Gordijn, A.; Kessels, W. M. M.; Sanden, M. C. M. v. d. The atomic hydrogen flux to silicon growth flux ratio during microcrystalline silicon solar cell deposition. *Applied Physics Letters* **2008,** *93* (11), 111914.
24. Smirnov, V.; Lambertz, A.; Moll, S.; Bär, M.; Starr, D. E.; Wilks, R. G.; Gorgoi, M.; Heidt, A.; Luysberg, M.; Holländer, B.; Finger, F. Doped microcrystalline silicon oxide alloys for silicon-based photovoltaics: Optoelectronic properties, chemical composition, and structure studied by advanced characterization techniques. *physica status solidi (a)* **2016,** *213* (7), 1814-1820.
25. Li, Y.-F.; Feng, J.; Sun, H.-B. Perovskite quantum dots for light-emitting devices. *Nanoscale* **2019,** *11* (41), 19119-19139.
26. Zhao, Y.; Li, J.; Dong, Y.; Song, J. Synthesis of Colloidal Halide Perovskite Quantum Dots/Nanocrystals: Progresses and Advances. *Israel Journal of Chemistry* **2019,** *59* (8), 649-660.
27. Li, X.; Cao, F.; Yu, D.; Chen, J.; Sun, Z.; Shen, Y.; Zhu, Y.; Wang, L.; Wei, Y.; Wu, Y.; Zeng, H. All Inorganic Halide Perovskites Nanosystem: Synthesis, Structural Features, Optical Properties and Optoelectronic Applications. *Small* **2017,** *13* (9), 1603996.
28. Li, X.; Wu, Y.; Zhang, S.; Cai, B.; Gu, Y.; Song, J.; Zeng, H. $CsPbX_3$ Quantum Dots for Lighting and Displays: Room-Temperature Synthesis, Photoluminescence Superiorities, Underlying Origins and White Light-Emitting Diodes. *Advanced Functional Materials* **2016,** *26* (15), 2435-2445.
29. Deng, J.; Wang, H.; Xun, J.; Wang, J.; Yang, X.; Shen, W.; Li, M.; He, R. Room-temperature synthesis of excellent-performance $CsPb_{1-x}Sn_xBr_3$ perovskite quantum dots and application in light emitting diodes. *Materials & Design* **2020,** *185*, 108246.
30. Tien, C.-H.; Chen, L.-C.; Lee, K.-Y.; Tseng, Z.-L.; Dong, Y.-S.; Lin, Z.-J. High-Quality All-Inorganic Perovskite $CsPbBr_3$ Quantum Dots Emitter Prepared by a Simple Purified Method and Applications of Light-Emitting Diodes. *Energies* **2019,** *12* (18), 3507.
31. Yuan, S.; Chen, D.; Li, X.; Zhong, J.; Xu, X. In Situ Crystallization Synthesis of CsPbBr3 Perovskite Quantum Dot-Embedded Glasses with Improved Stability for Solid-State Lighting and Random Upconverted Lasing. *ACS Applied Materials & Interfaces* **2018,** *10* (22), 18918-18926.
32. Protesescu, L.; Yakunin, S.; Bodnarchuk, M. I.; Krieg, F.; Caputo, R.; Hendon, C. H.; Yang, R. X.; Walsh, A.; Kovalenko, M. V. Nanocrystals of Cesium Lead Halide Perovskites ($CsPbX_3$, X = Cl, Br, and I): Novel Optoelectronic Materials Showing Bright Emission with Wide Color Gamut. *Nano Letters* **2015,** *15* (6), 3692-3696.

33. Liu, F.; Ding, C.; Zhang, Y.; Ripolles, T. S.; Kamisaka, T.; Toyoda, T.; Hayase, S.; Minemoto, T.; Yoshino, K.; Dai, S.; Yanagida, M.; Noguchi, H.; Shen, Q. Colloidal Synthesis of Air-Stable Alloyed $CsSn_{1-x}Pb_xI_3$ Perovskite Nanocrystals for Use in Solar Cells. *Journal of the American Chemical Society* **2017,** *139* (46), 16708-16719.
34. Krieg, F.; Ochsenbein, S. T.; Yakunin, S.; ten Brinck, S.; Aellen, P.; Süess, A.; Clerc, B.; Guggisberg, D.; Nazarenko, O.; Shynkarenko, Y.; Kumar, S.; Shih, C.-J.; Infante, I.; Kovalenko, M. V. Colloidal $CsPbX_3$ (X = Cl, Br, I) Nanocrystals 2.0: Zwitterionic Capping Ligands for Improved Durability and Stability. *ACS Energy Letters* **2018,** *3* (3), 641-646.
35. Yang, D.; Li, X.; Zhou, W.; Zhang, S.; Meng, C.; Wu, Y.; Wang, Y.; Zeng, H. $CsPbBr_3$ Quantum Dots 2.0: Benzenesulfonic Acid Equivalent Ligand Awakens Complete Purification. *Advanced Materials* **2019,** *31* (30), 1900767.
36. Wu, L.; Zhong, Q.; Yang, D.; Chen, M.; Hu, H.; Pan, Q.; Liu, H.; Cao, M.; Xu, Y.; Sun, B.; Zhang, Q. Improving the Stability and Size Tunability of Cesium Lead Halide Perovskite Nanocrystals Using Trioctylphosphine Oxide as the Capping Ligand. *Langmuir* **2017,** *33* (44), 12689-12696.
37. Sanehira, E. M.; Marshall, A. R.; Christians, J. A.; Harvey, S. P.; Ciesielski, P. N.; Wheeler, L. M.; Schulz, P.; Lin, L. Y.; Beard, M. C.; Luther, J. M. Enhanced mobility $CsPbI_3$ quantum dot arrays for record-efficiency, high-voltage photovoltaic cells. *Science Advances* **2017,** *3* (10), eaao4204.
38. Inkson, B. J. 2 - Scanning electron microscopy (SEM) and transmission electron microscopy (TEM) for materials characterization. In *Materials Characterization Using Nondestructive Evaluation (NDE) Methods*, Hübschen, G.; Altpeter, I.; Tschuncky, R.; Herrmann, H.-G., Eds. Woodhead Publishing: 2016; pp 17-43.
39. Abd Mutalib, M.; Rahman, M. A.; Othman, M. H. D.; Ismail, A. F.; Jaafar, J. Chapter 9 - Scanning Electron Microscopy (SEM) and Energy-Dispersive X-Ray (EDX) Spectroscopy. In *Membrane Characterization*, Hilal, N.; Ismail, A. F.; Matsuura, T.; Oatley-Radcliffe, D., Eds. Elsevier: 2017; pp 161-179.
40. Jaegermann, W.; Kaiser, B.; Ziegler, J.; Klett, J. Interface Engineering of Semiconductor Electrodes for Photoelectrochemical Water Splitting: Application of Surface Characterization with Photoelectron Spectroscopy. In *Photoelectrochemical Solar Fuel Production: From Basic Principles to Advanced Devices*, Giménez, S.; Bisquert, J., Eds. Springer International Publishing: Cham, 2016; pp 199-280.
41. Williams, R. H.; Srivastava, G. P.; McGovern, I. T. Photoelectron spectroscopy of solids and their surfaces. *Reports on Progress in Physics* **1980,** *43* (12), 1357-1414.
42. Andrade, J. D. X-ray Photoelectron Spectroscopy (XPS). In *Surface and Interfacial Aspects of Biomedical Polymers: Volume 1 Surface Chemistry and Physics*, Andrade, J. D., Ed. Springer US: Boston, MA, 1985; pp 105-195.
43. Konno, H. Chapter 8 - X-ray Photoelectron Spectroscopy. In *Materials Science and Engineering of Carbon*, Inagaki, M.; Kang, F., Eds. Butterworth-Heinemann: 2016; pp 153-171.
44. Opilik, L.; Schmid, T.; Zenobi, R. Modern Raman Imaging: Vibrational Spectroscopy on the Micrometer and Nanometer Scales. *Annual Review of Analytical Chemistry* **2013,** *6* (1), 379-398.
45. Epp, J. 4 - X-ray diffraction (XRD) techniques for materials characterization. In *Materials Characterization Using Nondestructive Evaluation (NDE) Methods*, Hübschen, G.; Altpeter, I.; Tschuncky, R.; Herrmann, H.-G., Eds. Woodhead Publishing: 2016; pp 81-124.

46. Chatterjee, A. K. 8 - X-Ray Diffraction. In *Handbook of Analytical Techniques in Concrete Science and Technology*, Ramachandran, V. S.; Beaudoin, J. J., Eds. William Andrew Publishing: Norwich, NY, 2001; pp 275-332.
47. Cardenas-Morcoso, D.; Peiro-Franch, A.; Herraiz-Cardona, I.; Gimenez, S. Chromium doped copper vanadate photoanodes for water splitting. *Catalysis Today* **2017,** *290*, 65-72.
48. Bott, A. Practical problems in voltammetry 3: reference electrodes for voltammetry. *Current Separations* **1995,** *14*, 64-69.
49. Toma, F. M.; Cooper, J. K.; Kunzelmann, V.; McDowell, M. T.; Yu, J.; Larson, D. M.; Borys, N. J.; Abelyan, C.; Beeman, J. W.; Yu, K. M.; Yang, J.; Chen, L.; Shaner, M. R.; Spurgeon, J.; Houle, F. A.; Persson, K. A.; Sharp, I. D. Mechanistic insights into chemical and photochemical transformations of bismuth vanadate photoanodes. *Nature Communications* **2016,** *7* (1), 12012.
50. Samu, G. F.; Scheidt, R. A.; Kamat, P. V.; Janáky, C. Electrochemistry and Spectroelectrochemistry of Lead Halide Perovskite Films: Materials Science Aspects and Boundary Conditions. *Chemistry of Materials* **2018,** *30* (3), 561-569.
51. Dotan, H.; Sivula, K.; Grätzel, M.; Rothschild, A.; Warren, S. C. Probing the photoelectrochemical properties of hematite (α-Fe_2O_3) electrodes using hydrogen peroxide as a hole scavenger. *Energy & Environmental Science* **2011,** *4* (3), 958-964.
52. Haram, S. K.; Quinn, B. M.; Bard, A. J. Electrochemistry of CdS Nanoparticles: A Correlation between Optical and Electrochemical Band Gaps. *Journal of the American Chemical Society* **2001,** *123* (36), 8860-8861.
53. Inamdar, S. N.; Ingole, P. P.; Haram, S. K. Determination of Band Structure Parameters and the Quasi-Particle Gap of CdSe Quantum Dots by Cyclic Voltammetry. *ChemPhysChem* **2008,** *9* (17), 2574-2579.
54. Bertoluzzi, L.; Bisquert, J. Investigating the Consistency of Models for Water Splitting Systems by Light and Voltage Modulated Techniques. *The Journal of Physical Chemistry Letters* **2017,** *8* (1), 172-180.
55. Lopes, T.; Andrade, L.; Le Formal, F.; Gratzel, M.; Sivula, K.; Mendes, A. Hematite photoelectrodes for water splitting: evaluation of the role of film thickness by impedance spectroscopy. *Physical Chemistry Chemical Physics* **2014,** *16* (31), 16515-16523.
56. Randles, J. E. B. Kinetics of rapid electrode reactions. *Discussions of the Faraday Society* **1947,** *1* (0), 11-19.
57. Peter, L. M.; Wijayantha, K. G. U.; Tahir, A. A. Kinetics of light-driven oxygen evolution at α-Fe2O3 electrodes. *Faraday Discussions* **2012,** *155* (0), 309-322.
58. Dunn, H. K.; Feckl, J. M.; Müller, A.; Fattakhova-Rohlfing, D.; Morehead, S. G.; Roos, J.; Peter, L. M.; Scheu, C.; Bein, T. Tin doping speeds up hole transfer during light-driven water oxidation at hematite photoanodes. *Physical Chemistry Chemical Physics* **2014,** *16* (44), 24610-24620.
59. Thorne, J. E.; Jang, J.-W.; Liu, E. Y.; Wang, D. Understanding the origin of photoelectrode performance enhancement by probing surface kinetics. *Chemical Science* **2016,** *7* (5), 3347-3354.
60. Rodríguez-Pérez, M.; Rodríguez-Gutiérrez, I.; Vega-Poot, A.; García-Rodríguez, R.; Rodríguez-Gattorno, G.; Oskam, G. Charge transfer and recombination kinetics at WO3 for photoelectrochemical water oxidation. *Electrochimica Acta* **2017,** *258*, 900-908.
61. Thorne, J. E.; Zhao, Y.; He, D.; Fan, S.; Vanka, S.; Mi, Z.; Wang, D. Understanding the role of co-catalysts on silicon photocathodes using intensity modulated photocurrent spectroscopy. *Physical Chemistry Chemical Physics* **2017,** *19* (43), 29653-29659.

62. Zachäus, C.; Abdi, F. F.; Peter, L. M.; van de Krol, R. Photocurrent of $BiVO_4$ is limited by surface recombination, not surface catalysis. *Chemical Science* **2017,** *8* (5), 3712-3719.
63. Liu, Y.; Le Formal, F.; Boudoire, F.; Yao, L.; Sivula, K.; Guijarro, N. Insights into the interfacial carrier behaviour of copper ferrite ($CuFe_2O_4$) photoanodes for solar water oxidation. *Journal of Materials Chemistry A* **2019,** *7* (4), 1669-1677.
64. Rodríguez-Gutiérrez, I.; Djatoubai, E.; Rodríguez-Pérez, M.; Su, J.; Rodríguez-Gattorno, G.; Vayssieres, L.; Oskam, G. Photoelectrochemical water oxidation at FTO|WO_3@$CuWO_4$ and FTO|WO_3@$CuWO_4$|$BiVO_4$ heterojunction systems: An IMPS analysis. *Electrochimica Acta* **2019,** *308*, 317-327.
65. Ravishankar, S.; Aranda, C.; Boix, P. P.; Anta, J. A.; Bisquert, J.; Garcia-Belmonte, G. Effects of Frequency Dependence of the External Quantum Efficiency of Perovskite Solar Cells. *The Journal of Physical Chemistry Letters* **2018,** *9* (11), 3099-3104.
66. Khan, M. A.; Varadhan, P.; Ramalingam, V.; Fu, H.-C.; Idriss, H.; He, J.-H. Importance of Oxygen Measurements during Photoelectrochemical Water-Splitting Reactions. *ACS Energy Letters* **2019,** *4* (11), 2712-2718.
67. Polcari, D.; Dauphin-Ducharme, P.; Mauzeroll, J. Scanning Electrochemical Microscopy: A Comprehensive Review of Experimental Parameters from 1989 to 2015. *Chemical Reviews* **2016,** *116* (22), 13234-13278.
68. Fan, F.-R. F.; Liu, B.; Mauzeroll, J. 12 - Scanning Electrochemical Microscopy. In *Handbook of Electrochemistry*, Zoski, C. G., Ed. Elsevier: Amsterdam, 2007; pp 471-540.
69. Szunerits, S.; Thouin, L. 10 - Microelectrode Arrays. In *Handbook of Electrochemistry*, Zoski, C. G., Ed. Elsevier: Amsterdam, 2007; pp 391-428.

Chapter 3: Critical Overview

3.1 Problem statement and goals.

Nowadays, one of the greatest challenges that science and technology face relates to the development of alternatives energy sources to fossil fuel urgently needed to satisfy the increasing energy demand in a sustainable fashion.[1] In this context, solar energy, with a power generating capacity over 20 TW, is the only viable source with the potential to meet the world energy needs. On the other hand, a hydrogen-based economy from clean and renewable resources as sunlight and water offers an attractive alternative to current fuel production from fossil and other limited sources. Moreover, besides an outstanding energy vector, hydrogen also serves as an important precursor in the chemical industry and agriculture (fertilizers). Hydrogen production can be carried out by mimicking the natural photosynthesis scheme of plants, using adequate devices able to absorb light and produce charge carriers to drive the water splitting reactions, from which hydrogen is obtained as a product.[2] Therefore, the practical realization of artificial photosynthesis requires suitable semiconductor materials, where the fundamental processes leading to the effective harnessing of solar energy takes place. However, most of the identified materials suffer from important drawbacks including limited light harvesting, energy loss associated with fast recombination of photogenerated charge carriers, as well as electrode degradation. Consequently, enormous challenges are remaining to improve the efficiency and technological deployment of solar to chemical energy conversion systems.

In particular, efficient PEC water splitting for solar fuel production requires to significantly improve the efficiency of the kinetically-sluggish OER occurring at the photoanode. Among the semiconductor materials identified for that purpose, $BiVO_4$ has been extensively studied as a promising candidate as photoanode for PEC water splitting. This semiconductor has an indirect E_g of ~2.4 eV, which leads to a maximum theoretical photocurrent of ~7.5 mA cm^{-2} under 1 sun AM 1.5G illumination, and consequently, a 9.2% STH efficiency, which is close to the technological target for solar-driven water splitting (STH efficiency of 10%).[3] Nonetheless, this material exhibits several limitations related to the poor charge mobility within the bulk, concomitant to surface limitations evidenced by its low charge injection efficiency. Therefore, the use of surface co-catalyst that boosts the water oxidation kinetics at the semiconductor/liquid interface is imperative for the practical implementation of $BiVO_4$ photoelectrodes. However, the role of the co-catalyst is not necessarily related to improved water oxidation kinetics. Instead, other mechanisms, such as passivation of recombination centers at the $BiVO_4$ surface, have explained the improved PEC performance. Consequently, finding suitable surface co-catalysts that act by directly enhancing the OER on its active sites remains a key challenge for the development of efficient photoanodes.[4] Moreover, the investigation of the intrinsic and interface properties of this promising material requires a proper understanding and interpretation of the experimental techniques providing mechanistic information, that allows the deployment of further strategies to overcome its current limitations.

Another promising approach for solar energy conversion into added-value chemicals relies on solar-powered electrocatalytic processes. Herein, a PV device provides the electricity input as photogenerated charge carriers, which are transferred to the electrocatalyst to drive a chemical reaction. The combination of a suitable PV solar cell, –providing sufficient photovoltage to drive the water oxidation reaction, as well as high photocurrent for competitive efficiency–, with an Earth-abundant water oxidation

electrocatalyst, offers a very attractive alternative as an integrated PV–EC device acting as photoanode in a PEC water splitting cell. Despite the significant advances in both PV and EC individual technologies, from the technological point of view. integrated architectures where the PV and EC components are intimately connected offer a compact and less complex design for the realization of an "artificial leaf" for practical solar fuel production.[5]

Finally, the search for new materials, as well as the exploration of those already used in different fields but possessing attractive properties toward photo-electrocatalytic applications, constitute one of the main avenues for the development of semiconductor materials for solar energy conversion and storage. As an example, all-inorganic perovskite QDs have recently attracted great attention in the field of photoelectrochemistry, reflected on few seminal reports on photocatalytic applications.[6] Moreover, their successful implementation in solar PV conversion devices motivates harnessing their excellent optoelectronic properties for opening new opportunities in the next-generation of PEC systems. However, a systematic methodology that allows to accurately evaluate their potential for different PC and PEC applications has not been developed yet.

From these considerations, it is clear that there is an urgent need for novel and profitable semiconductor materials, and also detailed research on their fundamental properties that can be translated in the implementation of efficient modification strategies. In addition, to provide systematic methodologies that allow identifying and exploiting attractive semiconductor materials is essential in order to improve the current status of practical solar energy conversion and storage applications. In this context, this doctoral thesis addresses the **research of advanced semiconductor materials and their performance as photoelectrodes, in particular as photoanode, for solar fuel production** as the main goal. Therefore, the following objectives were set:

- To improve the PEC performance of $BiVO_4$ photoanodes with a MOF-converted co-catalyst and provide a mechanistic understanding of the improved performance.

- To reveal unexploited information in steady-state and small perturbation techniques used for the study of photoelectrodes, by explaining an anomalous feature observed in IMPS measurements.

- To develop a robust and stable integrated PV–EC photoanode from non-critical raw materials.

- To harness the outstanding optoelectronic properties all-inorganic perovskites QDs in PC and PEC applications.

For the development of this thesis, several characterization techniques –broadly described in **Chapter 2**– were used for the morphological, structural, optical, optoelectronic, and photoelectrochemical characterization of the developed materials and devices, together with their functional operation mechanism.

The achievement of the objectives listed above has led to the following contributions, as results of the studies developed in the present thesis:

- A novel application of MOFs-derived materials as efficient highly porous co-catalysts in a photoelectrode for the water oxidation reaction, leading to a significant improvement of the PEC performance of $BiVO_4$ photoanodes.

- Experimental demonstration of the meaning of the negative value of the IMPS transfer function. Moreover, such interpretation further established a new powerful method to provide insights on the specific operational mechanisms of the photoelectrodes.

- Achievement of robust and stable solar-assisted water splitting device, based on an integrated PV–EC photoanode, with an Earth-abundant electrocatalyst and thin-film silicon photovoltaics, with, with a remarkable 7.7.% STH efficiency.

- Assessment and practical demonstration of the high potential of all-inorganic perovskites QDs in PC and PEC applications, using the degradation of organic pollutants as a proof of concept. In addition, a systematic methodology applicable to the study of new materials with potential for photo-electrocatalytic applications was provided.

Those achievements represent significant steps forward in the development of new strategies for enhanced performance of semiconductor materials employed as photoanodes for solar energy conversion into fuels and chemicals. In the present chapter, a critical overview of each contribution is provided, considering their particular context in the field of solar energy conversion and storage. Particular attention is given to the semiconductor materials, as the heart of the solar conversion technologies.

3.2. Enhanced PEC performance of $BiVO_4$ photoanodes with a MOF-converted co-catalyst.

Among the several strategies explored to improve the PEC performance of $BiVO_4$ based photoanodes, the use of a suitable surface co-catalyst is imperative to overcome the limitations related to the sluggish water oxidation kinetics at the $BiVO_4$ surface. Additionally, the deposition of surface layers also protect against the partial dissolution suffered by the material under illumination conditions.[7] Moreover, the improved catalytic activity also requires highly porous architectures in order to expose a large concentration of catalytic active sites at the surface. Therefore, the identification of efficient and stable co-catalysts synthesized by low-cost and simple routes remains as a current challenge toward the practical realization of PEC solar fuel production using $BiVO_4$ photoanodes for OER.

In the recent years, metal–organic frameworks (MOFs) have aroused high interest for a wide range of applications including gas storage and separation, sensing, and chemical catalysis, due to their wide chemical diversity, exceptional porosity, and well-defined crystalline structure.[8-9] MOFs are a class of porous hybrid solids consisting of metal-containing nodes coordinated with multitopic organic linkers. The zeolitic imidazolate frameworks (ZIF), which constitute a sub-family of MOFs, consist of transition metal ions (Zn^{2+}, Co^{2+}) and imidazolate linkers forming a 3D tetrahedral framework.[10] **Figure 3.1** shows the structural representation of the cobalt-imidazole-based frameworks (ZIF-67), where Co^{2+} ions act as linkers of the methylimidazole groups forming coordinated clusters, which lead to a highly stable crystalline structure.[8]

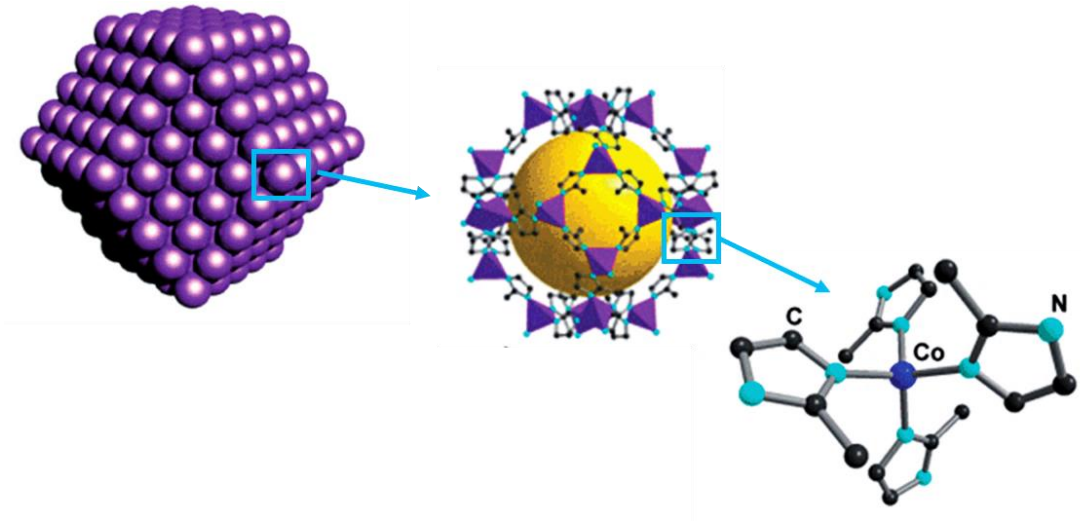

Figure 3.1. Structural representation of ZIF-67 crystals. Figures adapted with permission from reference [11].

Despite MOFs, and particularly ZIF-67, have been frequently used as precursor materials to synthesize high surface area electrocatalysts for OER, their utilization as co-catalysts on photoelectrodes for PEC applications has been unexplored. On the other hand, cobalt oxides, CoO_x, have shown high catalytic activity toward OER.[12] Therefore, the modification of $BiVO_4$ photoelectrodes with a highly porous CoO_x, co-catalyst derived from ZIF-67 could constitute an attractive strategy to exploit the beneficial features of the MOF-converted catalyst to partially overcome the intrinsic limitations of $BiVO_4$.

Consequently, ZIF-67 was directly grown on the surface of $BiVO_4$ photoelectrodes, –previously prepared by a reported synthesis method[13]–, where the ZIF-67 growth time was varied for the optimization of the resulting photoelectrode, finding the optimal condition at 6 h of growth time. The deposited MOF was thermally converted into porous cobalt oxide, via calcination in air, to get a heterostructured $CoO_x/BiVO_4$ photoelectrode, as depicted in **Figure 3.2a**. Such simple modification of the $BiVO_4$ photoelectrodes led to a remarkable enhancement of the extracted photocurrent, (j_e), at the water oxidation potential (1.23 V *vs* RHE), of around four-times compared to bare $BiVO_4$, as shown in **Figure 3.2b**, and a significant cathodic shift (~300 mV) of the onset potential of photocurrent, (V_{on}). Moreover, bare $BiVO_4$ photoelectrode shows a $j - V$ dependence characteristic of excessive surface losses, usually related to surface charge recombination. The shape of the curve is significantly enhanced with the MOF-converted CoO_x co-catalyst, indicating improved charge transfer kinetics, and hence, superior water oxidation activity of the photoanode.

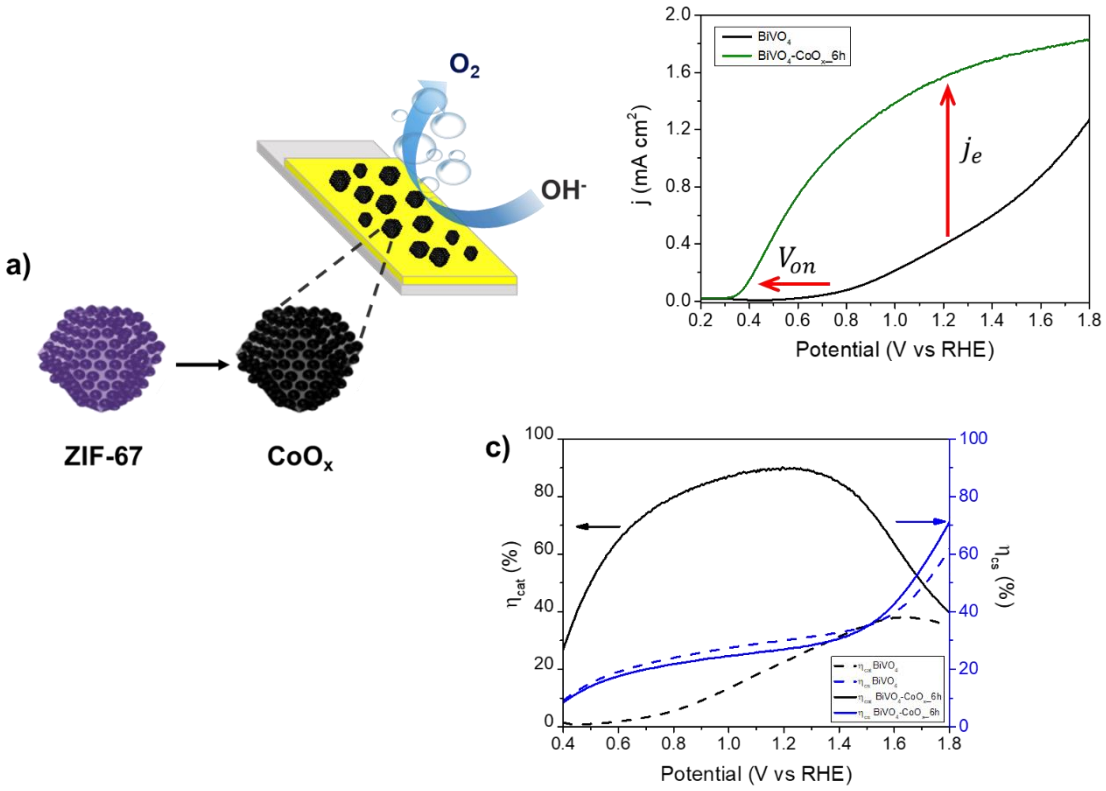

Figure 3.2. a) Schematic representation of modified $BiVO_4$ photoelectrode with a MOF-converted co-catalyst. **b)** $j-V$ plot of bare and MOF-converted co-catalyst modified $BiVO_4$ photoelectrodes, indicating the significant enhancement on both the j_e and the V_{on}. **c)** Charge injection and charge separation efficiency (η_{cat} and η_{cs}, respectively) as a function of the applied potential in $BiVO_4$ photoelectrodes, showing a remarkable enhancement of the η_{cat} after modification with the optimal MOF-converted catalyst. Figures adapted with permission from reference [14].

The nature of such PEC improvement was evaluated by using a sacrificial agent, acting as a fast hole scavenger, suggesting that the MOF-converted co-catalyst is responsible for the remarkable increase of the charge injection efficiency of the photoanode, as shown in **Figure 3.2c**. Conversely, the charge separation efficiency is not significantly affected by the presence of the MOF-converted co-catalyst, indicating that electronic bulk properties are still controlled by the $BiVO_4$.

Further mechanistic insights were extracted from IS measurements. **Figure 3.3a** shows representative Nyquist impedance plots of both bare and CoO_x-modified $BiVO_4$ photoanodes, showing the presence of a single arc. Therefore, a simple Randles' ECM, including a series resistance, (R_s), a charge transfer resistance at the photoelectrode/electrolyte interface (R_{ct}) and a capacitance, C, was used to fit the experimental data. The evolution of R_{ct} with the applied potential on a control and CoO_x-modified $BiVO_4$ photoelectrodes, both in the dark and under illumination conditions, is depicted in **Figure 3.3b.** In dark conditions, R_{ct} is not expected to change upon modification with the MOF-converted co-catalyst, since all minority carriers from $BiVO_4$ injected into the solution must be photogenerated. However, a decrease of this resistance was observed on the experimental results, which is explained by the enhanced direct dark water oxidation electrocatalysis from the FTO/CoO_x interface. Under illumination, a significant decrease in the R_{ct} takes place with both photoelectrodes, more remarkably for

the CoO_x-modified $BiVO_4$ photoanode, particularly at the region of 0.4–0.7 V *vs* RHE, in good agreement with the cathodic shift of V_{on} observed in the $j-V$ plot. Over this region, R_{ct} remains practically constant in a wide range of applied potentials (0.7–1.6 V *vs* RHE), suggesting a fast water oxidation kinetics arising due to the catalytic activity of the CoO_x co-catalyst. Interestingly, this behavior is similar to η_{cat} from the experiments in the presence of the hole scavenger, which also reaches maximum values at a similar applied potential range (see in **Figure 3.2c**). On the other hand, the decrease in R_{ct} upon increasing the applied potential in the control $BiVO_4$ sample is attributed to the suppression of surface recombination under the application of high anodic potentials. The lower R_{ct} at applied potentials more anodic than 1.6 V *vs* RHE is consistent with the higher slope of the $j-V$ curve of bare $BiVO_4$ photoelectrode in this region (see in **Figure 3.2c**).

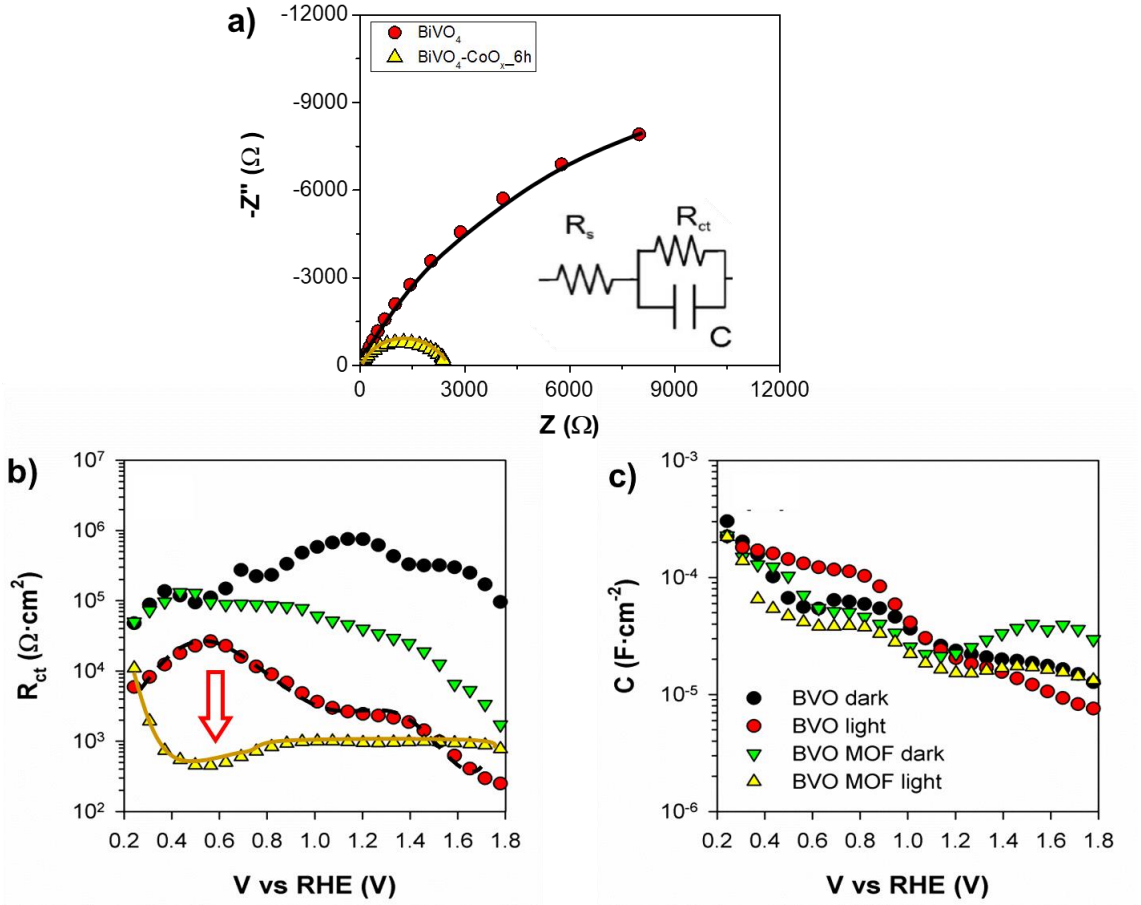

Figure 3.3. a) Nyquist plot of bare and CoO_x-modified $BiVO_4$ photoanodes, measured under illumination conditions, at 0.6 V *vs* RHE. As inset, a Randles' ECM used for fitting the experimental data. **b)** R_{ct} and **c)** C parameters extracted from fitting the IS data with the ECM model shown in a). In the figures, the lines are a guide to the view. Figures b) and c) are adapted with permission from reference [14].

Conversely, the dependence of C with the applied potential is similar in both control and modified photoelectrodes, indicating that the MOF-converted co-catalyst does not affect the energy band alignment of the $BiVO_4$ photoelectrodes, or acts as a surface state passivating layer, roles that have been assigned to others co-catalysts used on $BiVO_4$ surface. This suggests that the MOF-converted CoO_x in the heterostructured $CoO_x/BiVO_4$ photoelectrode acts as a "true" catalyst. Similar observations were found in Co-Fe PB

modified $BiVO_4$ photoanodes.[15] Electrochemical IS and hole scavenger studies suggested a more efficient hole transfer via the Co-Fe PB, further supported by DFT calculations. More recently, Durrant and co-workers carried out a deeper investigation on the role of Co-Fe PB in the improved PEC performance of $BiVO_4$.[4] They demonstrated, through optical spectroscopies, that holes from $BiVO_4$ are quickly and efficiently transferred to Co-Fe PB. This ability to separate charges, even at low applied potential, provides a favorable interface for efficient hole transfer that, coupled with effective catalytic functionality of Co-Fe PB, explains the remarkable PEC enhancement of the modified $BiVO_4$. In both cases, the MOF-derived CoO_x and Co-Fe PB, have shown a different role compared to Co-Pi co-catalyst, which was related to the suppression of surface recombination centers .[16]

The direct connection between the enhanced PEC activity of the $CoO_x/BiVO_4$ photoanode with accelerated catalytic oxygen evolution was further demonstrated with complementary PEC characterization techniques, including Scanning Electrochemical Microscope (SECM) and evolved gas detection by gas chromatography (more details are provided in **Chapter 4**). This research demonstrated the high value of MOF-converted materials as co-catalyst in PEC devices, a so far rarely explored application. Consequently, it was shown that with a simple modification, a significant PEC improvement in $BiVO_4$ photoanodes can be achieved. Additionally, mechanistic insight on the origin of such improvements is provided, significantly contributing to the future design of highly efficient photoanodes for solar energy conversion and storage.

3.3. The meaning of negative IMPS transfer function values observed in $BiVO_4$ photoanodes.

The detailed understanding of the optoelectronic properties on the PEC performance of the semiconductor material investigated as photoanode, is essential to further establish adequate strategies to overcome its limitations. Usually, this is a complex task, which involves the use of characterization methods delivering a set of results, which must be interpreted based on theoretical models. Small perturbation techniques (IS, IMPS, IMVS) are particularly useful to disentangle carrier dynamics in complex systems. Among them, IMPS technique has an important advantage for the study of PEC devices, by providing a small modulation of the minority carrier E_F with a modulated incident photon flux. Therefore, the IMPS response provides specific information on the minority carriers, which play the dominant role in the PEC performance. In contrast, IS can only modulate the majority carrier E_F from the semiconductor, through an external modulated voltage. Therefore, IS cannot provide direct information on the minority carriers in PEC systems.

Nevertheless, the interpretation of the obtained results with small perturbation techniques can be challenging, and many controls and iterative validations are needed for a sound mechanistic description. Moreover, the presence of "atypical" spectroscopic features makes interpretation even more complex. However, these anomalous features constitute a valuable source of information, which remains ignored in many occasions. Some relevant examples relate to the presence of negative capacitances[17] and resistances[18] during IS measurements of solar cell devices, and the observation of negative IMPS values during the measurements of photoelectrodes in PEC cells.[19-20]

In particular, a change of quadrant from positive to negative real part of the complex plane representation at low frequency has been observed during IMPS measurements in $BiVO_4$ photoelectrodes, usually at the region closer to the open circuit potential (OCP). This feature has been assigned to the switch of the photocurrent sign at this region (see in

Figure 3.4a and **b**).[20] To show that this feature is not related to the photocurrent sign, but it is directly connected to the variation of the steady-state extracted photocurrent (j_e) with the incident illumination intensity (j_ϕ), i.e. the differential EQE (EQE_{diff}), a specific experiment was designed (further details are provided in **Chapter 5**). Note that, the connection between the EQE_{diff} and the low frequency value of IMPS ($Q(0)$) has been previously described in perovskite solar cells,[21] finding that both values are directly linked to the dc component of the slope of $\overline{j_e}$ with $\overline{j_\phi}$, as depicted in Eq. 3.1. (The bar over the symbols denotes the steady-state condition.)

$$Q(0) = \frac{\widehat{j_e}(0)}{\widehat{j_\phi}(0)} = \frac{\partial \overline{j_e}}{\partial \overline{j_\phi}} = EQE_{diff} \tag{3.1}$$

However, such a connection had not been established to explain the change of sign of the low-frequency IMPS value observed in photoelectrodes used for PEC water splitting. In order to clearly show this relation, the $j_e - j_\phi$ steady-state curve of the $BiVO_4$ photoanode at an applied potential near to the OCP was recorded. Each point was measured during a sufficiently long time to reliably capture the steady-state condition of $j_e - j_\phi$, and to be compatible with the low-frequency domain of the IMPS measurements (~100 s). As shown in **Figure 3.4c**, at lower j_ϕ values there is a region where the extracted photocurrent is positive and its value decreases when increasing the light intensity, leading to a negative slope and, consequently to a negative EQE_{diff}. This observation was in good agreement with the measured negative Q transfer function at low frequency. Analogously, at higher j_ϕ, the negative EQE_{diff} is related to the decreasing $j_e - j_\phi$ slope, independently of the negative sign of the photocurrent, as shown in **Figure 3.4a** and **b**.[22]

This experimental proof of a particular operational point, where both the IMPS response and the EQE_{diff} are negative, while the photocurrent remains positive was critical for demonstrating that the negative value of the real part of the Q transfer function is associated with the derivative of the photocurrent with the illumination intensity, independently of the sign of the photocurrent. This is a significant contribution since this interpretation further establishes the measurement of $j_e - j_\phi$ curves, containing valuable information on specific recombination and trapping mechanisms during the operation of photoelectrochemical cells.

In the case of the $BiVO_4$ photoanodes, $EQE_{diff} = 0$ at voltages close to OCP indicates an invariant value of $\overline{j_e}$ with $\overline{j_\phi}$, indicating that $j - V$ plots at different light intensities will converge to the same OCP value. This can be indicative of Fermi level pinning on BVO_4. On the other hand, the observations of a negative EQE_{diff} at voltages close to or beyond the OCP, suggest that incident light intensity promotes the filling of a local density of shallow traps around the electron Fermi level, promoting the recombination of photogenerated holes with the trapped electrons. This leads to a decrease in j_e. At larger applied anodic bias, the shallow traps are filled with holes, allowing the photogenerated holes to be efficiently extracted and causing an increase of photocurrent with light intensity, and hence, a positive EQE_{diff}, as usually observed in water oxidation conditions.[22]

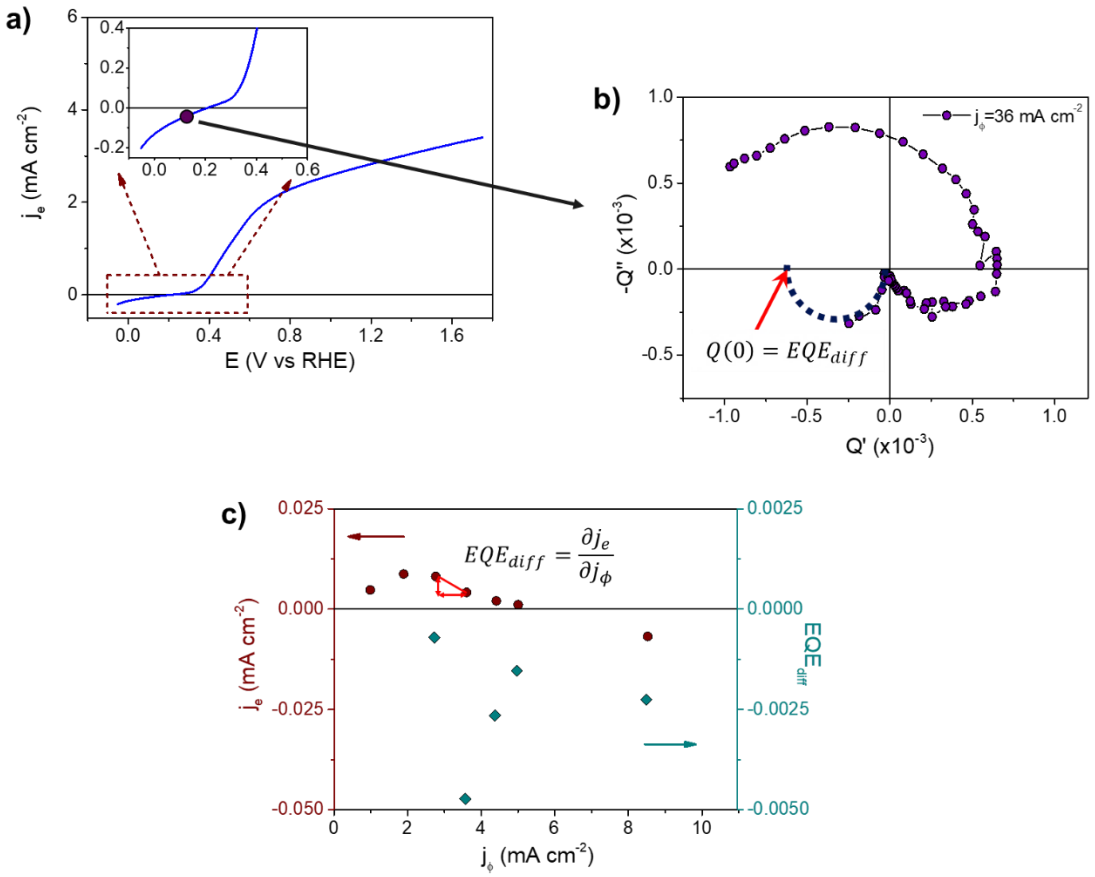

Figure 3.4. a) LSV for a $BiVO_4$ photoanode, under monochromatic dc illumination (λ=470 nm, 90 mW cm^{-2}). The inset shows the region closer to the OCP value. **b)** IMPS complex representation measured at j_ϕ=36 mA cm^{-2} (corresponding to 90 mW cm^{-2}), showing the low frequency IMPS value, $Q(0)$, at the intercept with the real axis. **c)** Measured $j_e - j_\phi$ steady-state curve in the $BiVO_4$ photoanode and the calculated EQE_{diff} from its slope. As an inset, the relation of the EQE_{diff} with the slope of the $j_e - j_\phi$ plot is depicted. Figures adapted with permission from reference [22].

These results provide a general optoelectrical method for mechanistic investigations of photoelectrodes, yielding valuable information on their operation and hence, paving the way for the search of successful strategies to improve their PEC performance. Usually, the treatment of IMPS measurements in PEC systems is carried out by using a rate constants model, which focuses on the evaluation of the competition of charge transfer and recombination process at the electrode surface.[23-24] However, the analysis of kinetic constants, which corresponds to the maximum ω of each arc observed in the Q complex plane, usually neglects the analysis of the value of the real part of the Q. This work, indeed, has demonstrated that the real part of Q actually contains significant physical information, allowing further understanding of operational mechanism of photoelectrodes. Moreover, this research provided a starting point for the validation of the mechanisms related to such unusual features observed with small perturbation techniques.

3.4. Robust and stable solar water splitting with an integrated PV–EC photoanode from non-critical raw materials.

Despite the significant advances for the optimization of photoanodes for PEC solar fuel production, the reported efficiencies on this approach are still far from competitive technological deployment. Even with the best-performance $BiVO_4$-based photoanode reported, the assistance of PV to reach an STH efficiency near to 10% was needed.[25] In this context, efficient and cost-effective "bias-free" water splitting with integrated PV–EC devices stands out as a promising strategy for the practical conversion of solar into chemical energy. Similar to PEC devices, this approach offers a compact and less complex design compared to externally connected PV+electrolyzer systems. Moreover, in PV–EC systems the power generated by the underlying solar cell is entirely available for the water electrolysis. Therefore, the obtained efficiencies are superior to other solar fuel production approaches (PC and PEC). However, its practical realization is hampered by the use of scarce and excessively expensive materials within the current high-performance devices, such as GaInP and GaAs as photo-absorbers, and noble-metal based oxides as electrocatalysts.

In this context, Ni-based catalysts offer the best alternatives owing to their high electrocatalytic activity and stability under alkaline conditions, together with the Earth-abundance and facile preparation routes. In fact, Ni-based electrocatalysts are currently the preferential anodes in large scale commercial alkaline electrolyzers. Moreover, the synergistic enhanced electrocatalytic activity towards OER reported for Ni-Fe alloys compared to the individual Ni or Fe components, has aroused a great interest in these materials. On the other hand, thin-film silicon multijunction architectures stand out as a reliable PV technology with applications in solar-driven processes, like water splitting. The main advantage of these devices is the high versatility to power any electrochemical reaction since the delivered photovoltage can be easily tuned by adjusting the solar cell layers stack.[26]

The advantages of the currently most promising PV and EC technologies were integrated into a PV–EC photoanode where both components are intimately connected, offering a compact design as well as high efficiency and stability toward PEC water splitting (**Figure 3.5a** and **b)**. An imperative requirement for integrated PV–EC devices is the sufficient protection of the PV component from possible chemical/electrochemical interaction with the solution, leading to its decomposition. Therefore, an important contribution was the direct growth of the EC component over a Ni substrate, which served as a precursor for the development of active OER catalysts. Additionally, this also offered a good contact to harness the photogenerated charge at the PV component, simultaneously preventing its interaction with the liquid medium (see **Figure 3.5a**).

The electrocatalyst was prepared by electrodeposition of Fe onto the Ni substrate, followed by thermal annealing. Such intentional Fe incorporation was reflected on the surface morphology of the electrocatalyst, as shown in **Figure 3.5c**. Additionally, the development of a high density of active sites for water oxidation was achieved, leading to enhanced electrocatalytic activity, compared to a Ni substrate subjected to the same thermal treatment. Determining the composition of Ni-Fe catalysts is usually a difficult task since single compositional analysis is not sufficient for this purpose. Therefore, combined structural and compositional characterization was key for further understanding the enhanced catalytic activity obtained with the Ni-Fe system. The detailed surface compositional characterization trough EDS, XRD, XPS, and confocal Raman microscopy revealed that NiO, α-Fe_2O_3, and $NiFe_2O_4$ were the main phases constituting the EC component. NiO and $NiFe_2O_4$ have been already reported as adequate water oxidation

electrocatalysts, after a subsequent CV treatment to develop (Ni, Fe)OOH as the active phase for OER (see **Chapter 1**, Sections 1.4.2.4 and 1.5.2). On the other hand, the role of α-Fe_2O_3 showing electrocatalytic activity for OER was recently reported for electrodeposited α-Fe_2O_3 particles.[27] Furthermore, the intentional Fe incorporation was also reflected in the electrochemical activation process needed in Ni-based compounds to maximize their catalytic activity towards OER. Further details are provided in **Chapter 6**.

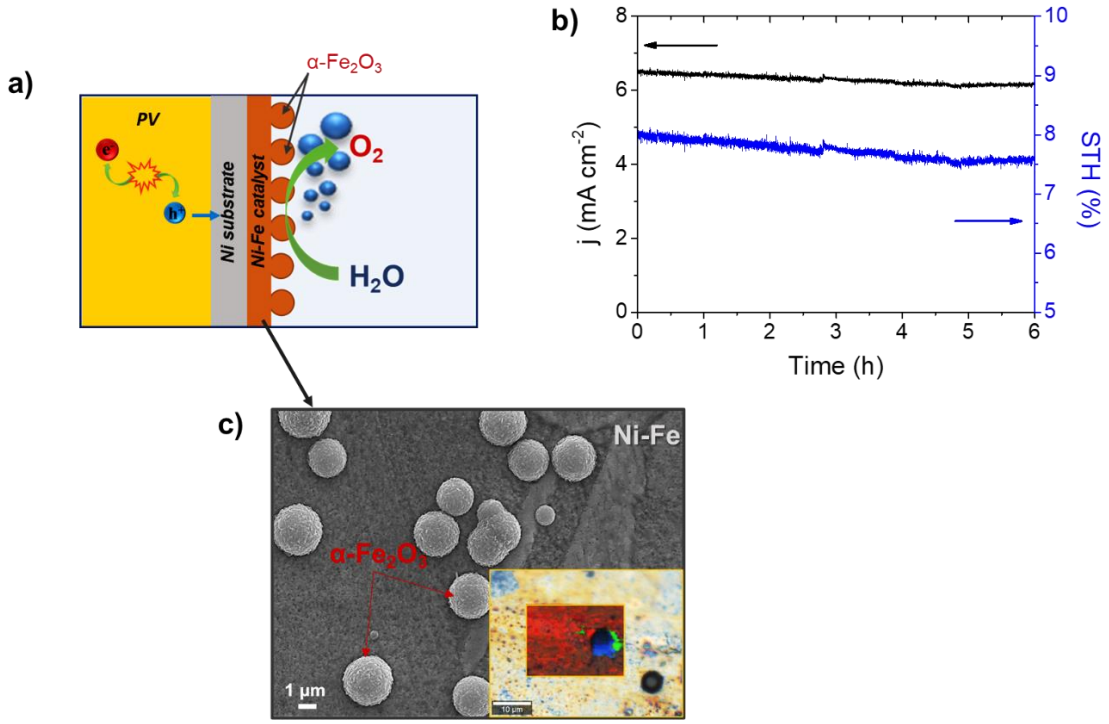

Figure 3.5. a) Schematic representation of the PV–EC integrated photoanode, obtained by the direct coupling of a Si-based PV device and a Ni-Fe optimized electrocatalyst. **b)** Chronoamperometry measurement at 0 V in a two-electrode cell with the integrated PV–EC device acting as photoanode. A *a-Si:H/a-Si:H/μc-Si:H* (triple junction) solar cell is used as PV component. The calculated STH efficiency from the extracted photocurrent is also represented. **c)** SEM micrography of the electrocatalyst, showing the electrodeposited α-Fe_2O_3 clusters over the Ni substrate. As an inset, the elemental mapping obtained with Raman microscopy, showing the heterogeneity of the Ni-Fe electrocatalyst composition.

On the other hand, two different PV devices were tested: *(i)* a triple junction solar cell, *a-Si:H/a-Si:H/μc-Si:H*, which provides a total 2.15 V OCP and *(ii)* a solar module consisting of two *a-Si:H/μc-Si:H* tandem solar cells connected in series. In this second device, each cell provides 1.3 V OCP, which is not sufficient to drive the OER, considering the unavoidable thermodynamic and kinetic overpotentials. The in-series connection of two *a-Si:H/μc-Si:H* tandem cells delivers a total 2.6 V OCP, exceeding the required voltage for water oxidation. However, the extracted photocurrent for this device was lower compared to that for the triple junction device. Therefore, the optimal PV–EC combination was realized with the *a-Si:H/a-Si:H/μc-Si:H* solar cell, reaching a 7.7% STH efficiency up to 20 h of stable operation, which is a remarkable milestone, considering the current state-of-the-art of PV–EC devices using noble-metal based materials.[5] Moreover, the obtained STH efficiency exceeds the latest reported one employing similar materials (5.1% in large-area device from NiMo/$NiFeO_x$ EC system and *a-Si:H/a-Si:H/μc-Si:H* triple-junction cell in cassette configuration)[28]. These results proved that PV–EC configurations based on non-

critical raw materials constitute a viable pathway for efficient and low-cost solar energy conversion schemes.

The design of the PV device is key for functional operation. As depicted in **Figure 3.6,** both "front" and "back contact" are placed outside the photo-active region, at the top side of the PV device. This design allows both electron and hole extraction to drive either reduction or oxidation reactions. Therefore, this configuration offers great versatility for the use of the PV devices either as photoanodes or photocathodes in PEC cells. Moreover, the intimate connection for both OER and HER ECs, in addition to adequate isolation of the monolithic device, allows the realization of a practical "artificial leaf" for solar-assisted fuel production.

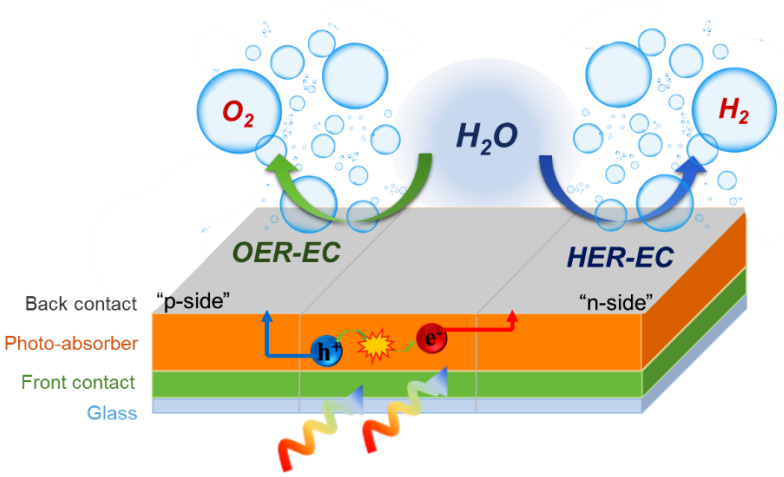

Figure 3.6. Schematic representation of the PV device design where both contacts are on the front side. The OER and HER electrocatalysts (OER-EC and HER-EC in the figure) can be integrated at the p-side and n-side of the solar cell, respectively.

3.5. The high potential of all-inorganic perovskites QDs in PC and PEC applications.

So far, we have devoted the attention to promising but extensively studied materials, by providing functional improvements for efficient solar fuel production. Despite the significant step forwards for their future implementation, the search for new semiconductor materials with potential interest in PC and PEC applications is still a great challenge. In this context, all-inorganic perovskite QDs, –which have shown outstanding optoelectronic properties already exploited in PV and LED applications– offer an attractive platform to be explored. Inspired by those amazing features, their potential towards the implementation of solar-driven catalytic strategies was assessed. For that purpose, it is essential to provide reliable testing conditions to ensure the stability of the material during the measurements. Additionally, the accurate determination of the band alignment is essential to understand the suitability of perovskite QDs materials toward PC and PEC applications.

The first step consisted of the assessment of the appropriate measuring conditions that assure the stability of the perovskite QDs during the PC and PEC experiments.[29] Therefore, different combinations of electrolytes and organic solvents were tested (see **Chapter 7** for details), finding the optimal environment with tetrabutylammonium hexafluorophosphate (Bu_4NPF_6) dissolved in dichloromethane, in good agreement with Kamat and co-workers report on hybrid halide perovskites.[30] The next step consists of the evaluation of the optoelectronic properties for application in solar-driven chemical reactions. Therefore, as a first contribution, the energy levels of different dispersions of perovskite QDs with different band gaps induced by the different ratios between halides (Br and I) and metallic

cations (Pb and Sn) were determined by electrochemical procedures. **Figure 3.7a** shows the CV of $CsPbI_3$ QDs dispersion, where the anodic (A_1) and cathodic (C_1) peaks reflect the charge transfer between the Pt working electrode and the perovskite QDs, which correspond to the E_{vb} and E_{cb} levels, respectively. The potential difference between the A_1 and C_1 peaks is referred to the quasiparticle (or electrochemical) band gap E_g^{qp}, and should be close to the optical band gap E_g^{op}, independently estimated from optical absorption and PL measurements.[31] In **Chapter 7**, further details about the structural, optical and optoelectronic analysis are provided. The band edges position for all the QDs dispersion tested, as well as the comparison between the E_g^{qp} and the E_g^{op}, is shown in **Figure 3.7b**.

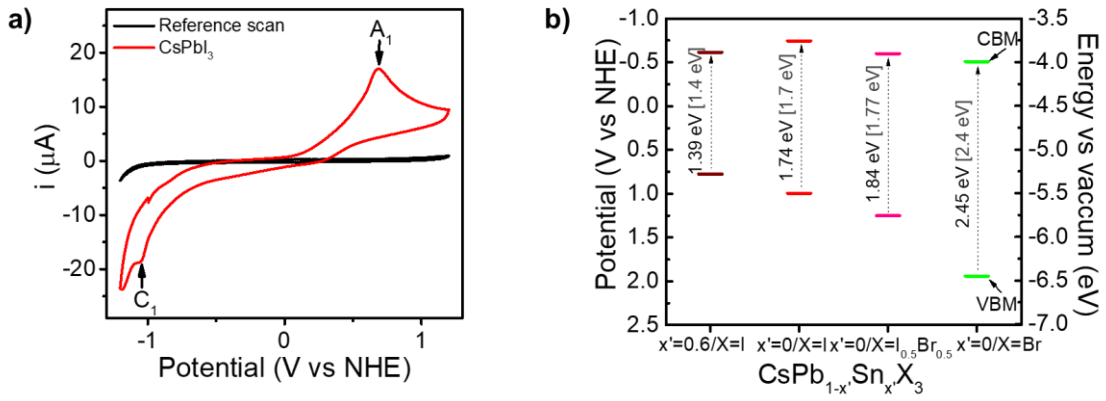

Figure 3.7. a) CV in an all-inorganic perovskite QDs dispersion ($CsPbI_3$ as an example), for the electrochemical determination of the energy levels. **b)** Energy diagram obtained from CV measurements. The E_g^{qp} is shown in black color, while the E_g^{op} is in grey, for comparison. Figures adapted with permission from reference [29].

The second important contribution was the experimental validation for the potential use of the perovskite QDs in PC and PEC applications, using as a proof-of-concept, the oxidation of 2-mercaptobenzothiazole (MBT) by $CsPbBr_3$ QDs. MBT is a well-known organic pollutant from industrial wastes. All the tested QDs were suitable for hole transfer to oxidize MBT. However, $CsPbBr_3$ QDs were selected, since their optical absorbance does not overlap with the characteristic band of MBT at 320 nm, monitored during the PC degradation experiments. **Figure 3.8a** shows the relative concentration of the MBT, as $\ln(C/C_0)$ versus time, as a result of the PC photodegradation in the presence of the $CsPbBr_3$ QDs, including control experiments without the QDs and with and without a UV filter during light irradiation, in order to unambiguously determine the role of the QDs. The photodegradation kinetics can be approximated by a pseudo-first-order rate law, with a rate constant *k*. The maximum value for *k* is reached in the presence of $CsPbBr_3$ QDs, under UV−Vis radiation. Furthermore, time-resolved photoluminescence (TRPL) and steady-state PL emission experiments confirmed the effective charge transfer from the $CsPbBr_3$ QDs to MBT, while electrospray mass-spectroscopy (ESI-MS) analysis also demonstrated the photodegradation of the MBT (see **Chapter 7** for details). [29] For PEC measurements, the QDs were confined on a transparent conductive substrate with a thin TiO_2 electron selective layer, resulting in a $CsPbBr_3/TiO_2$/FTO photoelectrode. As shown in **Figure 3.8b**, anodic photocurrent, characteristic of an n-type semiconductor photoanode injecting minority carriers (holes) into the solution, was obtained, which significantly increases in the presence of MBT. [29] Therefore, those results unambiguously confirm that hole injection from perovskite QDs to MBT takes place during the PC and PEC oxidation of MBT with

$CsPbBr_3$ QDs, as represented in the scheme of **Figure 3.8c**.

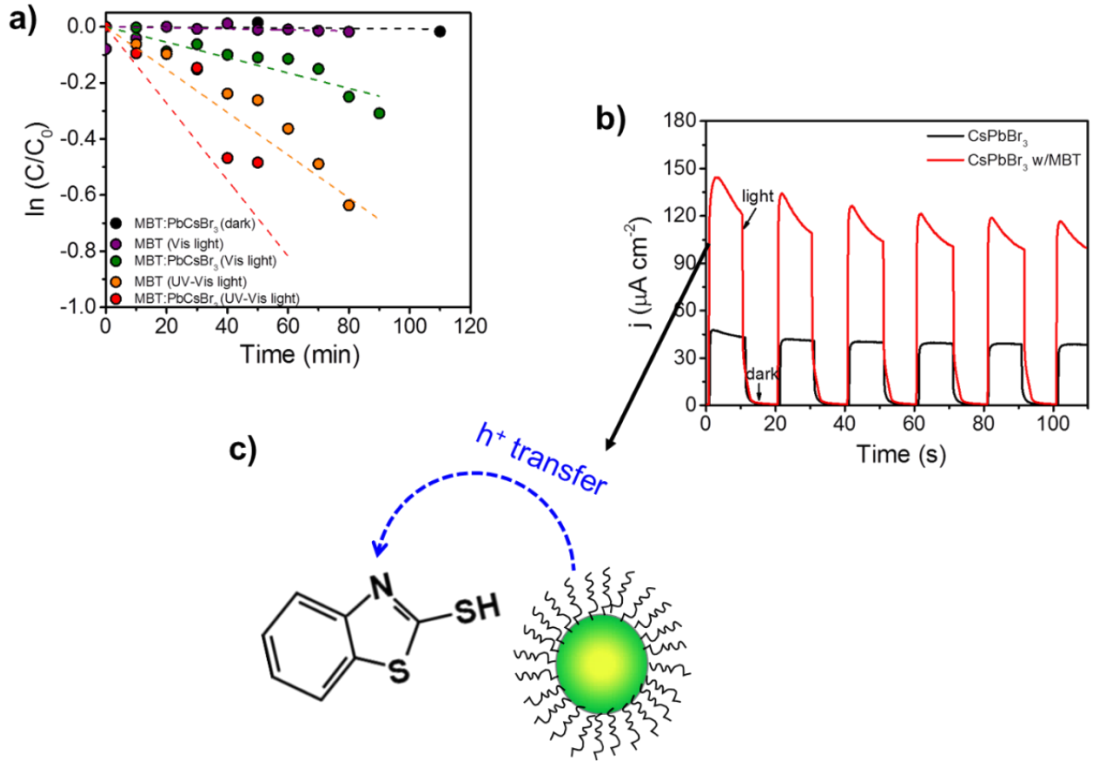

Figure 3.8. a) PC degradation of the MBT molecule with $CsPbBr_3$ QDs, shown as the relative change of the MBT concentration with time. Different conditions were tested for comparison. **b)** PEC degradation of the MBT molecule with $CsPbBr_3$ QDs, shown in a chronoamperometric measurement with chopped illumination. The positive extracted current also suggests the n-type behavior of the perovskite QDs. **c)** Proposed mechanism for degradation of the MBT with $CsPbBr_3$ QDs, based on the holes transfer to drive the PC and PEC degradation reactions. Figures a) and b) are adapted with permission from reference [29].

This investigation constitutes a significant step forward in the application of perovskite QDs for solar-driven catalytic processes and opens a promising avenue for the next generation of semiconductor materials for solar fuel production. Due to the novelty and interest of this study, the publication including these results was selected as *"ACS Editor's Choice"* of the respective journal edition (*JPCL, 2019, volume 10*). Moreover, it was ranked in the top-10 of the most downloaded/viewed articles of the journal in 2019.

3.6. Conclusions.

The results of the studies performed during the development of this doctoral thesis, crystallized in the following conclusions and achievements:

- A significant improvement to the PEC performance of $BiVO_4$ photoanodes by simple surface modification with a MOF-converted co-catalyst, was achieved. The conversion of the ZIF-67 led to highly porous CoO_x, a suitable water oxidation catalyst, which remarkably boosted the PEC performance of $BiVO_4$. The mechanistic studies revealed that the CoO_x co-catalyst significantly accelerates OER by acting like a "true" electrocatalyst, rather than serving as a passivating agent of surface states.

- It was demonstrated that the negative value of the IMPS transfer function is associated with the derivative of the photocurrent with the light intensity, rather than to the sign of the photocurrent. An operational condition where the low frequency IMPS response of a $BiVO_4$ photoanode and the EQE_{diff} are both negative, while the photocurrent remains positive, was experimentally showed. Moreover, $j_e - j_\phi$ measurements were established as a new source of valuable information about operational mechanisms in semiconductor photoelectrodes.

- A PV–EC photoanode was prepared integrating an Earth-abundant Ni-Fe based water oxidation electrocatalyst and a multijunction thin-film silicon device. A simple electrochemical deposition followed by thermal annealing leads to the development of OER-active NiO, α-Fe_2O_3, and $NiFe_2O_4$ electrocatalysts. Their adequate activity and stability, added to the suitability of the thin-film triple junction solar cells to provide the sufficient photovoltage and photocurrent, allowed the integrated device to show a robust performance toward water splitting, achieving a remarkable 7.7% STH efficiency.

- A systematic methodology for the assessment and practical demonstration of the high potential of all-inorganic perovskites QDs in PC and PEC applications was established. Their suitability for photo- and electrochemical applications was evaluated by the determination of the band alignment trough electrochemical and spectroscopic techniques. Furthermore, a demonstration of their potential for PC and PEC degradation of an organic pollutant was provided. This contribution opens promising perspectives for all-inorganic perovskite QDs in the field of solar energy conversion with PC and PEC approaches.

3.7 References.

1. Cook, T. R.; Dogutan, D. K.; Reece, S. Y.; Surendranath, Y.; Teets, T. S.; Nocera, D. G. Solar Energy Supply and Storage for the Legacy and Nonlegacy Worlds. *Chemical Reviews* **2010,** *110* (11), 6474-6502.
2. Fujishima, A.; Honda, K. Electrochemical Photolysis of Water at a Semiconductor Electrode. *Nature* **1972,** *238* (5358), 37-38.
3. García-Tecedor, M.; Cardenas-Morcoso, D.; Fernández-Climent, R.; Giménez, S. The Role of Underlayers and Overlayers in Thin Film $BiVO_4$ Photoanodes for Solar Water Splitting. *Advanced Materials Interfaces* **2019,** *6* (15), 1900299.
4. Moss, B.; Hegner, F. S.; Corby, S.; Selim, S.; Francàs, L.; López, N.; Giménez, S.; Galán-Mascarós, J.-R.; Durrant, J. R. Unraveling Charge Transfer in CoFe Prussian Blue Modified $BiVO_4$ Photoanodes. *ACS Energy Letters* **2019,** *4* (1), 337-342.
5. Kim, J. H.; Hansora, D.; Sharma, P.; Jang, J.-W.; Lee, J. S. Toward practical solar hydrogen production – an artificial photosynthetic leaf-to-farm challenge. *Chemical Society Reviews* **2019,** *48* (7), 1908-1971.
6. Zhang, Q.; Yin, Y. All-Inorganic Metal Halide Perovskite Nanocrystals: Opportunities and Challenges. *ACS central science* **2018,** *4* (6), 668-679.
7. Kim, T. W.; Choi, K.-S. Nanoporous $BiVO_4$ Photoanodes with Dual-Layer Oxygen Evolution Catalysts for Solar Water Splitting. *Science* **2014,** *343* (6174), 990-994.
8. Zhong, G.; Liu, D.; Zhang, J. The application of ZIF-67 and its derivatives: adsorption, separation, electrochemistry and catalysts. *Journal of Materials Chemistry A* **2018,** *6* (5), 1887-1899.
9. He, W.; Ifraemov, R.; Raslin, A.; Hod, I. Room-Temperature Electrochemical Conversion of Metal–Organic Frameworks into Porous Amorphous Metal Sulfides with Tailored Composition and Hydrogen Evolution Activity. *Advanced Functional Materials* **2018,** *28* (18), 1707244.
10. Aguado, S.; Quirós, J.; Canivet, J.; Farrusseng, D.; Boltes, K.; Rosal, R. Antimicrobial activity of cobalt imidazolate metal–organic frameworks. *Chemosphere* **2014,** *113*, 188-192.
11. Xia, W.; Zhu, J.; Guo, W.; An, L.; Xia, D.; Zou, R. Well-defined carbon polyhedrons prepared from nano metal–organic frameworks for oxygen reduction. *Journal of Materials Chemistry A* **2014,** *2* (30), 11606-11613.
12. Deng, X.; Tüysüz, H. Cobalt-Oxide-Based Materials as Water Oxidation Catalyst: Recent Progress and Challenges. *ACS Catalysis* **2014,** *4* (10), 3701-3714.
13. Kang, D.; Park, Y.; Hill, J. C.; Choi, K.-S. Preparation of Bi-Based Ternary Oxide Photoanodes $BiVO_4$, Bi_2WO_6, and $Bi_2Mo_3O_{12}$ Using Dendritic Bi Metal Electrodes. *The Journal of Physical Chemistry Letters* **2014,** *5* (17), 2994-2999.
14. Cardenas-Morcoso, D.; Ifraemov, R.; García-Tecedor, M.; Liberman, I.; Gimenez, S.; Hod, I. A metal–organic framework converted catalyst that boosts photo-electrochemical water splitting. *Journal of Materials Chemistry A* **2019,** *7* (18), 11143-11149.
15. Hegner, F. S.; Herraiz-Cardona, I.; Cardenas-Morcoso, D.; López, N.; Galán-Mascarós, J.-R.; Gimenez, S. Cobalt Hexacyanoferrate on $BiVO_4$ Photoanodes for Robust Water Splitting. *ACS Applied Materials & Interfaces* **2017,** *9* (43), 37671-37681.
16. Ma, Y.; Kafizas, A.; Pendlebury, S. R.; Le Formal, F.; Durrant, J. R. Photoinduced Absorption Spectroscopy of CoPi on $BiVO_4$: The Function of CoPi during Water Oxidation. *Advanced Functional Materials* **2016,** *26* (27), 4951-4960.

17. Klotz, D. Negative capacitance or inductive loop? – A general assessment of a common low frequency impedance feature. *Electrochemistry Communications* **2019,** *98*, 58-62.
18. Schneider, I. A.; Bayer, M. H.; Wokaun, A.; Scherer, G. G. Negative Resistance Values in Locally Resolved Impedance Spectra of Polymer Electrolyte Fuel Cells. *ECS Transactions* **2009,** *25* (1), 937-948.
19. Rodríguez-Gutiérrez, I.; García-Rodríguez, R.; Rodríguez-Pérez, M.; Vega-Poot, A.; Rodríguez Gattorno, G.; Parkinson, B. A.; Oskam, G. Charge Transfer and Recombination Dynamics at Inkjet-Printed $CuBi_2O_4$ Electrodes for Photoelectrochemical Water Splitting. *The Journal of Physical Chemistry C* **2018,** *122* (48), 27169-27179.
20. Antuch, M.; Millet, P.; Iwase, A.; Kudo, A. The role of surface states during photocurrent switching: Intensity modulated photocurrent spectroscopy analysis of $BiVO_4$ photoelectrodes. *Applied Catalysis B: Environmental* **2018,** *237*, 401-408.
21. Ravishankar, S.; Aranda, C.; Boix, P. P.; Anta, J. A.; Bisquert, J.; Garcia-Belmonte, G. Effects of Frequency Dependence of the External Quantum Efficiency of Perovskite Solar Cells. *The Journal of Physical Chemistry Letters* **2018,** *9* (11), 3099-3104.
22. Cardenas-Morcoso, D.; Bou, A.; Ravishankar, S.; García-Tecedor, M.; Gimenez, S.; Bisquert, J. Intensity-Modulated Photocurrent Spectroscopy for Solar Energy Conversion Devices: What Does a Negative Value Mean? *ACS Energy Letters* **2020,** *5* (1), 187-191.
23. Peter, L. M. Dynamic aspects of semiconductor photoelectrochemistry. *Chemical Reviews* **1990,** *90* (5), 753-769.
24. Ponomarev, E. A.; Peter, L. M. A generalized theory of intensity modulated photocurrent spectroscopy (IMPS). *Journal of Electroanalytical Chemistry* **1995,** *396* (1), 219-226.
25. Pihosh, Y.; Turkevych, I.; Mawatari, K.; Uemura, J.; Kazoe, Y.; Kosar, S.; Makita, K.; Sugaya, T.; Matsui, T.; Fujita, D.; Tosa, M.; Kondo, M.; Kitamori, T. Photocatalytic generation of hydrogen by core-shell $WO_3/BiVO_4$ nanorods with ultimate water splitting efficiency. *Scientific Reports* **2015,** *5* (1), 11141.
26. Urbain, F.; Smirnov, V.; Becker, J.-P.; Lambertz, A.; Yang, F.; Ziegler, J.; Kaiser, B.; Jaegermann, W.; Rau, U.; Finger, F. Multijunction Si photocathodes with tunable photovoltages from 2.0 V to 2.8 V for light induced water splitting. *Energy & Environmental Science* **2016,** *9* (1), 145-154.
27. Shaddad, M. N.; Ghanem, M. A.; Al-Mayouf, A. M.; Gimenez, S.; Bisquert, J.; Herraiz-Cardona, I. Cooperative Catalytic Effect of ZrO_2 and α-Fe_2O_3 Nanoparticles on $BiVO_4$ Photoanodes for Enhanced Photoelectrochemical Water Splitting. *ChemSusChem* **2016,** *9* (19), 2779-2783.
28. Welter, K.; Hamzelui, N.; Smirnov, V.; Becker, J. P.; Jaegermann, W.; Finger, F. Catalysts from earth abundant materials in a scalable, stand-alone photovoltaic-electrochemical module for solar water splitting. *Journal of Materials Chemistry A* **2018,** *6* (33), 15968-15976.
29. Cardenas-Morcoso, D.; Gualdrón-Reyes, A. F.; Ferreira Vitoreti, A. B.; García-Tecedor, M.; Yoon, S. J.; Solis de la Fuente, M.; Mora-Seró, I.; Gimenez, S. Photocatalytic and Photoelectrochemical Degradation of Organic Compounds with All-Inorganic Metal Halide Perovskite Quantum Dots. *The Journal of Physical Chemistry Letters* **2019,** *10* (3), 630-636.
30. Samu, G.F.; Scheidt, R. A.; Kamat, P.V.; Janáky, C. Electrochemistry and Spectroelectrochemistry of Lead Halide Perovskite Films: Materials Science Aspects and Boundary Conditions. *Chemistry of Materials* **2018,** 30 (3), 561-569

Chapter 4: Publication 1

"A metal-organic framework converted catalyst that boosts photo-electrochemical water splitting."

Cardenas-Morcoso, D.; Ifraemov, R.; García-Tecedor, M.; Liberman, I.; Giménez, S.; Hod, I.

Journal of Materials Chemistry A, ***2019****, 7, 11143-11149.*

4.1 Candidate's contribution

Nature of contribution:	**Extent of contribution:**
• Preparation of the $BiVO_4$ photoelectrodes. • Design and execution of optical, morphological and photoelectrochemical measurements. • Contribution to the analysis of the results. • Contribution to the figures and manuscript preparation. • Corrections on the manuscript according to the reviewer's opinions.	40%

4.2 Published manuscript

A metal-organic framework converted catalyst that boosts photo-electrochemical water splitting.

Drialys Cardenas-Morcoso, [†a] Raya Ifraemov, [†b] Miguel García-Tecedor,[a] Itamar Liberman, [b] Sixto Gimenez,[*a] and Idan Hod,[*b]

[a.] *Institute of Advanced Materials (INAM), Universitat Jaume I, 12071 Castelló, Spain Address.*

[b.] *Department of Chemistry and Ilse Katz Institute for Nanoscale Science and Technology, Ben-Gurion University of the Negev, Beer-Sheva 8410501, Israel.*

[†] *D.C.-M. and R.I. have equally contributed to this work*

[*]**Email:** sjulia@uji.es, hodi@bgu.ac.il

Abstract

Realization of photo-electrochemical water splitting to generate H_2 alternative fuel requires the facilitation of the kinetically-sluggish oxygen evolution reaction (OER) occurring at the photoanode. To do so, there is a need to develop new methods to assemble suitable OER co-catalysts at the semiconductor-solution interface. Although Metal-Organic Frameworks (MOFs) are frequently used as precursor materials to synthesize high surface area, effective OER electrocatalysts, until now their utilization as co-catalysts in a working photo-electrochemical cell (PEC) remained underexplored. As a proof-of-concept, here we provide a simple route for modification of $BiVO_4$-based photoanodes with highly-active porous cobalt-oxide co-catalysts, converted from a cobalt-imidazolium MOF (ZIF-67). Photo-electrochemical and impedance spectroscopy analysis reveal that the co-catalyst significantly accelerates photoanodic OER (rather than serving as a surface passivation layer), and thus greatly improves the overall PEC performance. Hence, given the chemical flexibility of MOFs, this work provides a new tool-kit for designing efficient water splitting PECs.

Table of Content

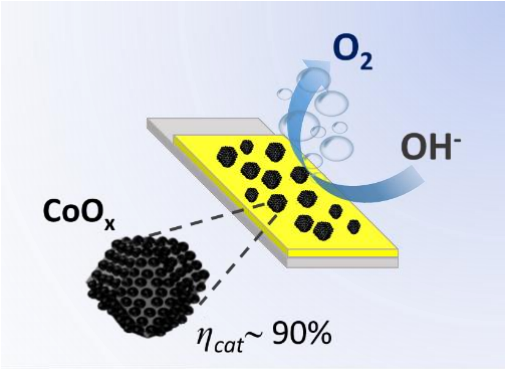

Introduction

Photo-electrochemical cells (PECs) are considered to be one of the most promising and economically feasible future technologies for producing alternative energy sources and could be used to directly convert sunlight into chemical fuels, for example by splitting water to form molecular hydrogen, H_2.[1] The water splitting process consists of two half reactions, namely oxygen evolution reaction (OER) occurring at the anode and hydrogen evolution reaction (HER) at the cathode.[2] Due to its four-electron four-proton coupled reaction, OER kinetics is relatively sluggish, and thus it is generally considered to be the kinetic bottle-neck for the total water splitting process. Consequently, in order to achieve a highly efficient water splitting device, the performance of the OER half reaction at the anode must be improved.

TiO_2,[3] WO_3,[4] α-Fe_2O_3[5] and $BiVO_4$[6] are among the most studied semiconductors for photo-electrochemical OER, since they possess a suitable band gap and adequate energy level alignments for efficient solar light absorption and water oxidation respectively. However, drawbacks as low charge separation efficiency, high recombination rates and slow water oxidation kinetics, impedes the development of efficient PECs based on these materials. In that regard, a promising route for accelerating the kinetics of water oxidation at the photoanode's surface is through the utilization of a suitable co-catalyst capable of rapid delivery of photo-generated redox equivalents, from the semiconductor toward the electrolyte solution. Co-catalysts based on Ni, Co and Fe (metal oxides such as NiOOH,[7] FeOOH[8] and Co_3O_4,[9] as well as CoPi[10] and Prussian-blue based Co-hexacyanoferrate)[11] are widely studied and used, since they exhibit high electrocatalytic activity for OER coupled with good stability during harsh reaction conditions. Nevertheless, in order to achieve further enhancement in the performance of water oxidation PECs, there is still a need to develop new types of highly efficient OER co-catalysts. A key requirement for such improvement in catalytic activity is to design a highly porous catalyst-architecture, in order to expose large surface-concentrations of electrolyte-accessible catalytically-active OER sites.

Knowing that, we have realized the great potential of using Metal-Organic Frameworks (MOFs) based materials for designing a new family of OER co-catalysts. MOFs are a subclass of coordination polymers consisting of metal clusters and organic linkers.[12] They attracted widespread attention, due to their high surface area, porosity and tuneable properties that can easily be controlled by a specific selection of metal nodes and organic linkers, resulting in diverse functionality. Therefore, they have been applied in fields such as gas storage and separation,[13, 14] chemical catalysis,[15-17] and sensing.[18, 19] Recently, increasing efforts have been put for utilizing MOFs in electrocatalytic applications.[20-26] However currently, the intrinsic low conductivity of most MOFs impedes their practical realization in electrochemical devices.[20, 27-29] To overcome this drawback, researchers have been using MOFs as a high surface area precursor material or templating agent to yield porous, conductive MOF-converted inorganic materials that possess unique electrocatalytic properties.[30-34] Hence, MOF-converted electrocatalysts contain all needed ingredients to construct highly efficient co-catalysts: high porosity, structural diversity and the desired intrinsic catalytic activity. Yet, despite the great progress in this field, to the best of our knowledge these MOF-converted materials have rarely been studied as co-catalysts in water splitting PECs.[35, 36]

Consequently, in this work we demonstrate that a great enhancement in the performance of a water splitting PEC could be achieved by a simple modification of the surface of a semiconducting photoanode with a MOF-derived, highly porous cobalt oxide (CoO_x) co-catalyst. As a proof-of-concept, we have chosen to focus our study on $BiVO_4$ based

photoanodes. In order to achieve a homogenous co-catalyst coverage on top of the $BiVO_4$ surface, the sample is first modified with the well-known cobalt-imidazole-based ZIF-67 MOF. Thereafter, the deposited MOF was thermally converted into porous cobalt oxide via calcination in air. Due to the high surface area of the MOF precursor, the resulting porous co-catalyst exposes a large amount of catalytically-active water oxidation sites, thus allowing significant acceleration of water oxidation kinetics and overall improvement in the performance of the whole $BiVO_4$-based water splitting PEC.

Results and discussion

Scheme 1 schematically illustrates the growth of CoO_x based co-catalysts on $BiVO_4$ electrodes. First, ZIF-67 was synthesized according to a previously reported solvothermal route (see Experimental section in **Supporting Information** for detailed procedure). To enable a uniform growth and robust attachment of ZIF-67 on top of $BiVO_4$, a monolayer of Benzene-1,3,5-tricarboxylic acid (H_3BTC) was used to modify the surface of $BiVO_4$. Hereafter, ZIF-67 was grown by simply mixing cobalt nitrate and 2-methylimidazole in methanol at room temperature, yielding homogeneous coverage of MOF particles at the semiconductor's surface (termed $BiVO_4$-ZIF-67). We have fabricated five types of $BiVO_4$-ZIF-67 electrodes by setting the growth duration of the ZIF-67 on top of the $BiVO_4$ to 1, 4, 6, 8.5 and 12 hours, termed $BiVO_4$-ZIF-67_1h, $BiVO_4$-ZIF-67_4h, $BiVO_4$-ZIF-67_6h, $BiVO_4$-ZIF-67_8.5h and $BiVO_4$-ZIF-67_12h respectively. Thereafter, the as synthesized $BiVO_4$-ZIF-67 samples were calcinated at 400 °C for 3 hours in air, in order to convert the deposited MOF particles into CoO_x co-catalysts (termed $BiVO_4$-CoOx). We note that for comparison, all control $BiVO_4$ films in this work were also subject to the same calcination process at 400 °C for 3 hours in air (termed $BiVO_4$ (400 °C)).

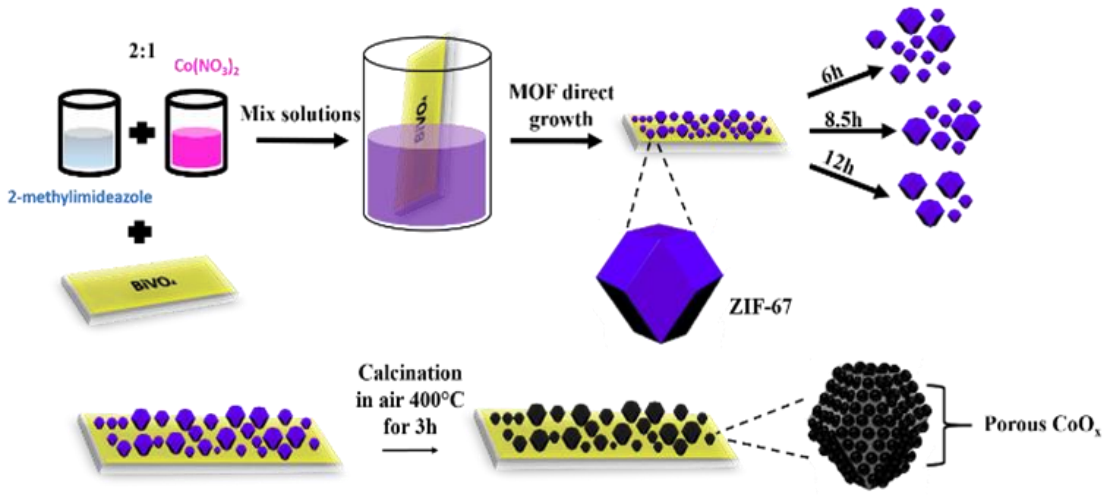

Scheme 1. Schematic illustration of the CoO_x co-catalyst growth procedure on $BiVO_4$ electrodes.

The growth of crystalline ZIF-67 on the surface of the $BiVO_4$ electrodes was confirmed by X-ray diffraction (XRD) and Raman spectroscopy. The XRD pattern contains sharp peaks positioned at 2θ angles: 7.3, 10.3, 12.7, 14.6 and 17.9°, as shown in **Figure 1a** which corresponds to the ZIF-67. Upon calcination at 400 °C in air, the corresponding ZIF-67 XRD peaks disappear and new peaks appeared in at 38.4, 44.6, 65.0, and 78.1, which correspond to the (222), (400), (440) and (533) planes of spinel cobalt oxide.[37] Importantly, the peaks corresponding to $BiVO_4$ remain unaffected, meaning that the photoactive

semiconductor preserves its crystallinity during the thermal treatment.

Moreover, characteristic Raman peaks of ZIF-67 were detected (**Figure 1b**).[30] In addition, the formation of cobalt oxide species after calcination was also confirmed by Raman spectroscopy, by clearly showing the appearance of additional peaks at 694, 529 and 485 cm^{-1} corresponding to the vibrational modes of cobalt oxide and the disappearance of the peaks related to ZIF-67.[38] We note that for the $BiVO_4$-ZIF-67_6 h sample an excitation laser beam of 633 nm was used (as opposed to 532 nm used for all other samples), since shorter excitation wavelengths caused significant light scattering from the $BiVO_4$ particles and thus prevented the detection of ZIF-67.

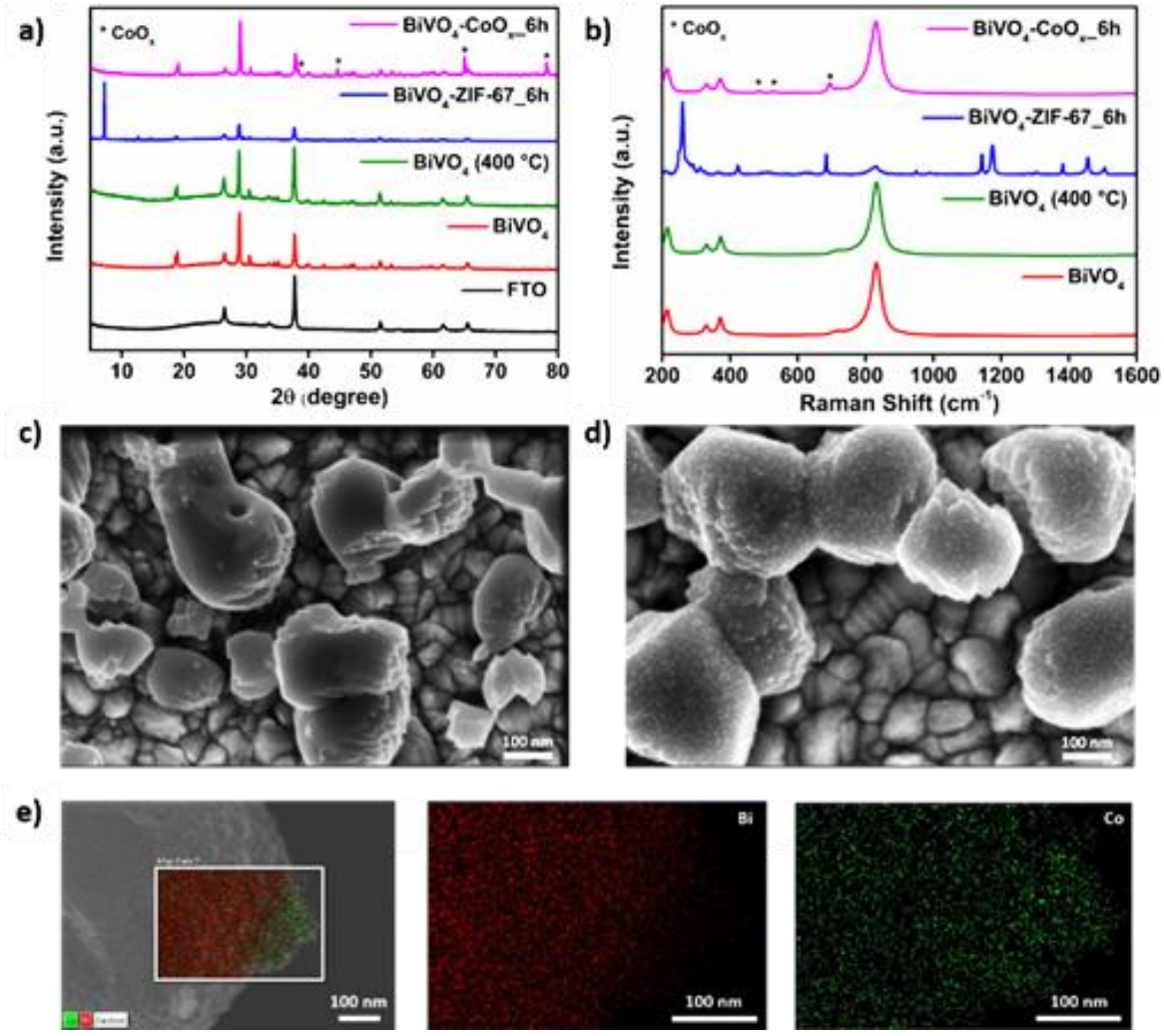

Figure 1. a) XRD patterns and **b)** Raman spectra of the bare $BiVO_4$ (red curve), $BiVO_4$ (400 °C) (green curve), $BiVO_4$-ZIF-67_6h (blue curve) and $BiVO_4$-CoO_x_6h (pink curve). The Raman spectra for the $BiVO_4$-ZIF-67_6h sample was obtained using a 633 nm excitation laser beam, while for all other samples 532 nm excitation was used. (we note that the Raman laser does not penetrate through the whole sample and thus no FTO related peaks are observed). **c)** SEM image of $BiVO_4$ film, d) SEM image of $BiVO_4$-CoO_x_6h film. **e)** Scanning Transmission Electron Microscopy (STEM) based EDS elemental mapping of $BiVO_4$-CoO_x_6h.

Scanning Electron Microscopy (SEM) images of $BiVO_4$-CoO_x electrodes reveal a homogeneous coverage of the crystalline $BiVO_4$ with nanoparticles of CoO_x having a size of a few tens of nanometres (**Figure 1c-d**). As seen in **Supporting Information, Table S1**,

ICP-OES measurements confirm that ZIF-67 surface-loading is increased with longer growth duration (though no clear differences in the either CoO_x particle's size or density was observed by the SEM images in **Supporting Information, Figure S1**). Nevertheless, looking at lower SEM magnifications, one can detect the presence of a few dodecahedral particles (preserving the typical crystal morphology of the pristine ZIF-67 precursor [39]) with the average size of 0.5 μm on top of the $BiVO_4$ surface (**Supporting Information, Figure S2**). EDS elemental mapping analysis of the samples was performed using Scanning Transmission Electron Microscopy (STEM), revealing that the deposited particles on the $BiVO_4$ surface nanoparticles are indeed composed of cobalt oxide (**Figure 1e**). In order to confirm that the origin of the CoO_x nanoparticles is indeed the grown ZIF-67 precursor, SEM images were taken for both $BiVO_4$-ZIF-67_6h and a control $BiVO_4$ sample immersed only in the MOF's cobalt precursor, $Co(NO_3)_2$ for 6 hours, without 2-methylimidazole ligands (termed $BiVO_4$-$Co(NO_3)_2$_6h). For $BiVO_4$-ZIF-67_6h sample, the SEM images and EDS characterization (**Supporting Information, Figure S3a-c**) revealed a uniform coverage of CoO_x nanoparticles on the surface of the $BiVO_4$ particles, while for the $BiVO_4$-$Co(NO_3)_2$_6h the BiVO4 particles remained unmodified (**Supporting Information, Figure S3d-f**).

Additionally, in order to further confirm the conversion of ZIF-67 into highly porous CoO_x, ZIF-67 was synthesized in a powder form, thus enabling us to characterize the structural and surface area changes resulting from the MOF calcination in air. As can be seen in **Supporting Information, Figure S4**, PXRD of the calcinated ZIF-67 reveal the typical crystalline structure of cubic-shaped Co_3O_4. Transmission electron microscopy (TEM) images clearly show the porous, dodecahedral particles formed during the ZIF-67 calcination in air appears (**Supporting Information, Figure S5a**). Selected area electron diffraction (SAED) was performed to determine whether the calcinated ZIF-67 product is a crystalline Co_3O_4. The resulting diffraction rings are indeed associated with the (111), (220), (311), (400), (422), (511) and (440) crystal planes of cubic Co_3O_4 (JCPDS 42-1467) (**Supporting Information, Figure S5b**). N_2 isotherm of the ZIF-67 converted CoO_x show a BET surface area of 63 m^2/gr, thus confirming that the resulting $BiVO_4$-mounted co-catalysts are indeed highly porous and expose high density of electrolyte-accessible catalytically-active sites (**Supporting Information, Figure S6**).

Surface characterization of the $BiVO_4$-ZIF-67_6h and $BiVO_4$-CoO_x_6h films was carried out by X-ray photoelectron spectroscopy (XPS). The global XPS spectra of the films (**Supporting Information, Figure S7a and S8a**) show the characteristic split signal corresponding to the Bi $4f_{5/2}$ and Bi $5f_{7/2}$ orbitals of Bi^{3+} state in $BiVO_4$, the V 2p and O 1s signals corresponding to V^{5+} and O^{2-} ions respectively and the characteristic Zr 3d and Zr 3p signals. Since the amount of Zr is at the detection limit of the equipment, the ratios between the Zr 3p1/2 and Zr 3p3/2 areas, could not be properly quantified with this technique. The presence of Sn in the XPS spectra arises from the underlying FTO substrate, which is exposed at some locations due to the porous nature of the specimens.

The $BiVO_4$-ZIF-67_6h films show a N1s signal with 2 distinct peaks at binding energies of 398.8 and 399.9 eV (**Supporting Information, Figure S8b**), corresponding to, which. The main peak located at 398.8 eV corresponds to N coordinated with Co^{2+} ions in ZIF-67, while the small peak at 399.9 eV corresponds to uncoordinated 2-methylimidazole (ZIF-67 surface defects).[30] The signal for Co 2p exhibits a single peak at 780.7 eV that corresponds to $Co2p_{3/2}$ and its satellite at 784.8 eV, attributed a Co-N species within the ZIF-67 MOF (**Supporting Information, Figure S8c**).[40]

For the calcinated $BiVO_4$-CoO_x_6h film, signals of N1s were not detected, which confirms the full conversion of ZIF-67 into porous CoO_x. As can be seen in **Figure S9**, the Co 2p signal of $BiVO_4$-CoO_x_6h exhibit 2 distinct peaks at binding energies of 783.1 and

780.6 eV, which are attributed to the co-existence of non-stoichiometric (CoO_x) and stoichiometric (Co_3O_4) cobalt oxide phases respectively at the surface of the electrode.[41, 42]

The optical properties of the control $BiVO_4$ (400 °C) films and upon deposition of different catalyst loadings (corresponding to 1, 4, 6, 8.5 and 12 hours) are showed in **Figure 2a**. $BiVO_4$ supra bandgap absorption takes place at wavelengths below 550 nm, in good agreement with previous reports.[43] It has been reported that nanostructured $BiVO_4$ prepared by electrochemical deposition induce light scattering,[44] as evidenced by the measured absorbance at wavelengths >550 nm. It is clear that the deposition of the MOF-converted co-catalyst significantly enhances both light scattering and $BiVO_4$ supra bandgap absorption, which is beneficial for light harvesting and solar energy conversion.

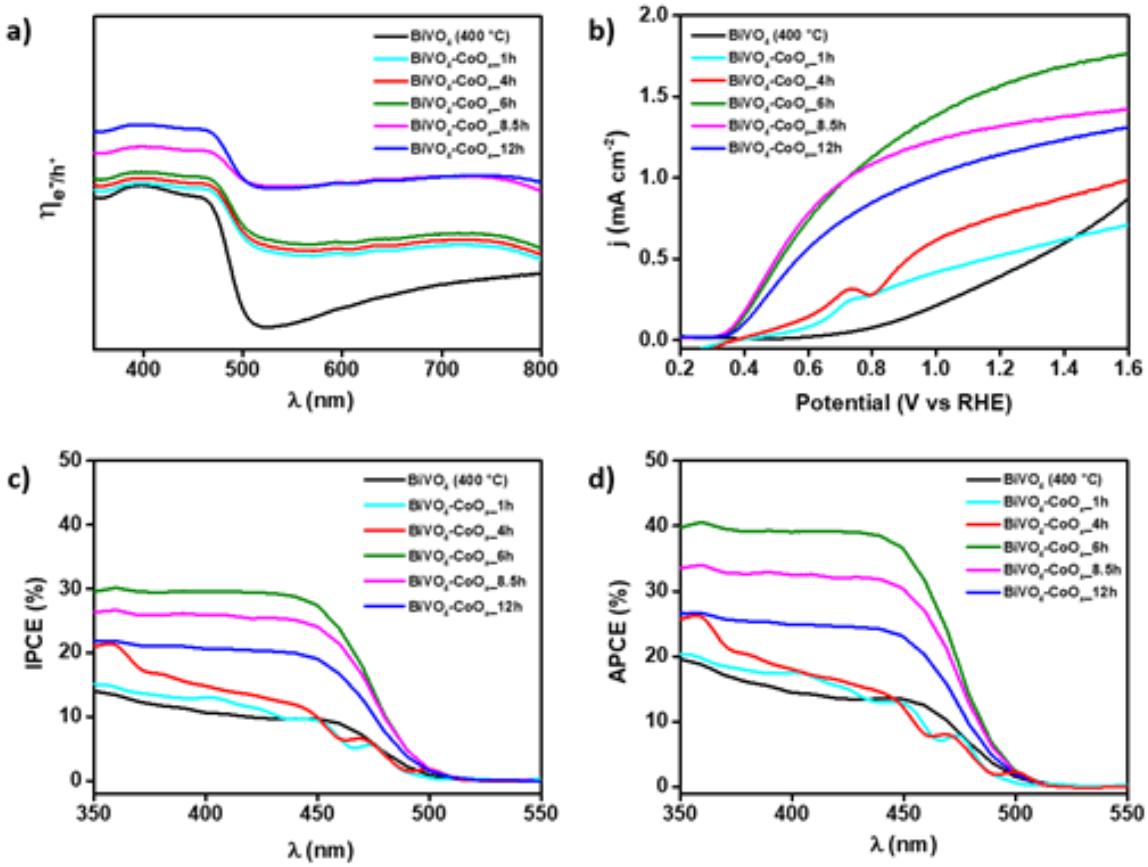

Figure 2. a) UV-Vis absorption spectra of $BiVO_4$ (400 °C) (control) and $BiVO_4$ with different loading of the MOF-converted CoO_x catalyst, **b)** j-V curves obtained with cyclic voltammetry c) IPCE and d) APCE spectra obtained from IPCE and absorbance measurements at 1.23 V vs RHE.

The photoelectrochemical behaviour of these films for water oxidation is summarized in **Figure 2b-d**. The photocurrent onset for the control sample takes place at 0.6 V vs RHE, which is around 300 mV more anodic than the flat band potential (vide infra). Moreover, the characteristic s-shape of the j-V curve is a clear indication of excessive surface losses,[45, 46] most probably related to surface recombination.[47, 48] A totally distinct behaviour is observed upon deposition of the MOF-converted co-catalyst, with photocurrent onsets very close to the flat band potential for $BiVO_4$ (vide infra) and a significant reduction of surface losses, as evidenced by the shape of the j-V curve. The highest photocurrents are obtained for the 6 hours CoO_x growth duration, clearly indicating that optical absorbance is not the main reason behind the increase of performance. Incident Photon to Current Efficiency

(IPCE) was evaluated to understand the spectral signature of the photocurrent, (**Figure 2c**). The photocurrent onset at λ = 525 nm clearly indicates that the absorbance measured at wavelengths >550 nm is not productive for photoinduced charge extraction. Additionally, the deposition of the MOF-converted co-catalyst does not modify the photocurrent onset, corroborating that the changes in the optical properties induced by the co-catalyst are not relevant for the operation of the photoanode. The total photocurrent was calculated from integration of IPCE with the solar spectrum, and the values are included in **Supporting Information, Table S2** showing perfect agreement with those obtained by voltammetry measurements (**Figure 2b**). The Absorbed Photon to Current Efficiency (APCE) was also estimated by integration of the absorptance spectra of the films with the IPCE (**Figure 2d**). $BiVO_4$-CoO_x_6h electrodes exhibit the highest Internal Quantum Efficiencies, confirming that 6 hours deposition time leads to the best photoelectrochemical performance. As can be seen in **Supporting Information, Figure S10**, the photoelectrochemical properties of the $BiVO_4$-$Co(NO_3)_2$_6h samples are very similar to those of $BiVO_4$ (400 °C control) films, thus confirming the fact that the ZIF-67 converted co-catalysts are the one responsible for the catalytic enhancement.

Figure 3a shows the j-V curves of the control and the $BiVO_4$-CoO_x samples under illumination with and without the presence of presence of a hole scavenger (0.1M Na_2SO_3). In the presence of the hole scavenger, the photocurrent onset is a good approximation of the flat band potential of the $BiVO_4$ photo-absorber.[49] The obtained value of ~0.3 V vs RHE is slightly more anodic than usually reported values.[43, 44, 50] Furthermore, from these measurements, the charge separation efficiency (η_{cs}) and the charge injection efficiency (η_{cat}) could be estimated (**Figure 3b**), clearly indicating that the MOF-converted co-catalyst is responsible for a remarkable increase of the charge injection efficiency of the photoanode, up to voltages close to 1.8 V vs RHE, where the high applied electric field vanishes surface recombination. Conversely, the charge separation efficiency is not affected by the presence of the MOF-converted catalyst and is controlled by the bulk of $BiVO_4$.

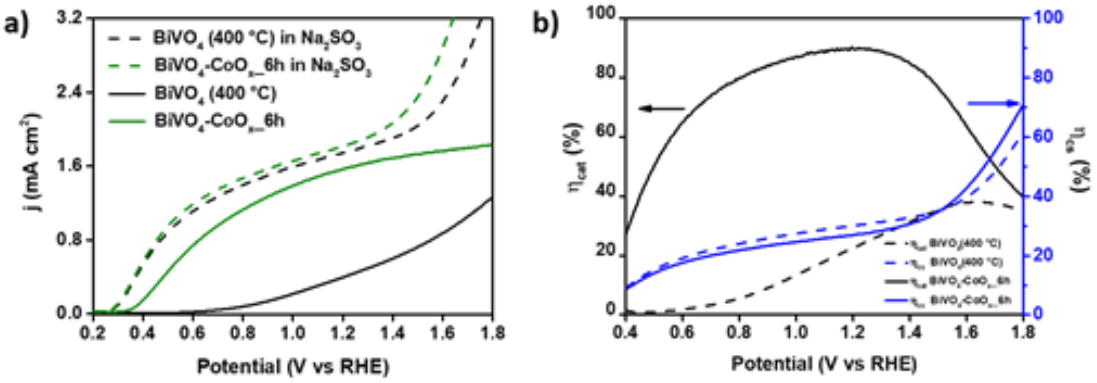

Figure 3. a) j-V curves of $BiVO_4$ (400 °C) and $BiVO_4$-CoO_x_6h electrodes with and without a sacrificial hole scavenger (0.1M Na_2SO_3) in the electrolyte solution. **b)** Charge injection (black lines) and charge separation (blue lines) efficiencies of $BiVO_4$ (400 °C) (dashed lines) and $BiVO_4$-CoO_x_6h (solid lines) electrodes.

Further mechanistic insights were extracted from impedance spectroscopy measurements in the dark and under illumination for both the control and the best performing $BiVO_4$-CoO_x electrode. The Nyquist impedance plots showed the presence of only one arc and consequently, a simple Randles' electrical equivalent circuit was

employed to fit the experimental data (see **Supporting Information, Figure S11**). This model includes a series resistance (R_s) accounting for the resistance of the solution and the contacts, the charge transfer resistance from the electrode to the electrolyte (R_{ct}) and a capacitance (C). Although this selected model oversimplifies the real operation of these complex electrodes, (e.g. direct charge transfer from the FTO to the solution is not considered here, and the MOF-converted catalyst is not explicitly considered in the analysis), the extracted results still provide useful information on the kinetics of the processes taking place and on the charge storage modes of this system. In all cases, the series resistance R_s spans between 20 - 60 $\Omega \cdot cm^2$ (**Supporting Information, Figure S12**). On the other hand, the charge transfer resistance at the $BiVO_4$/solution interface (R_{ct}) governs the water oxidation kinetics and decreases both upon addition of the MOF-converted catalyst and under illumination (**Figure 4a**). In the dark, this resistance is not expected to change upon addition of the MOF-converted catalyst, since all minority carriers from $BiVO_4$ injected into the solution must be photogenerated. However, the observed decrease of this resistance in our experimental results can be explained by the enhanced direct dark water oxidation electrocatalysis from the FTO/CoO_x substrate (see **Supporting Information, Figure S13**, SEM image of FTO/CoO_x sites). Under illumination, a significant decrease of R_{ct} takes place for both the control and $BiVO_4$-CoO_x electrodes. The control sample shows a decrease of charge-transfer resistance with applied anodic bias, which is attributed to the enhanced suppression of surface recombination in these conditions.[47, 48] However, in $BiVO_4$-CoO_x electrodes, a low R_{ct} value remains practically constant over a wide range of applied potentials (0.7V – 1.6V vs RHE), suggesting for fast water oxidation kinetics arising due to the catalytic activity of the CoO_x co-catalyst. It is interesting to note that this behaviour resembles the charge separation efficiency (η_{cs}) plot in **Figure3b**, which also reaches a constant maximum value at a similar potential range. We note that the lower R_{ct} obtained for the control $BiVO_4$ (400 °C) sample at potentials more anodic than 1.6 V vs RHE is consistent with the higher slope of the j-V curve at these potentials, as can clearly be observed in Figure 2b.The obtained capacitances (**Figure 4b**) do not significantly change for the different conditions tested and exhibit the expected behaviour for an n-type semiconductor (decreasing at more anodic applied potentials), although the complexity of the films does not allow obtaining a reliable Mott-Schottky behaviour. Indeed, the capacitance at the most negative potentials seems to be controlled by the FTO.[51] The fact that for all samples we observe similar potential dependent capacitance at the $BiVO_4$/electrolyte interface, serves as a good indication that the deposited MOF-converted co-catalyst does not affect the energy-band alignment of the $BiVO_4$ electrodes, as showed in a recent study[52] or passivate surface states[53], but rather acts as a true electrocatalyst. The total resistance extracted from impedance spectroscopy ($R_{total} = R_s + R_{ct}$) matched reasonably well that obtained by derivation of the j-V curve, $R_{total} = (dj/dV)^{-1}$ (see **Supporting Information, Figure S14**), validating the impedance analysis. Additionally, the j-V curves obtained from cyclic voltammetry before and after the impedance measurements were also in good correspondence with the j-V curves from impedance spectroscopy (**Supporting Information, Figure S15**).

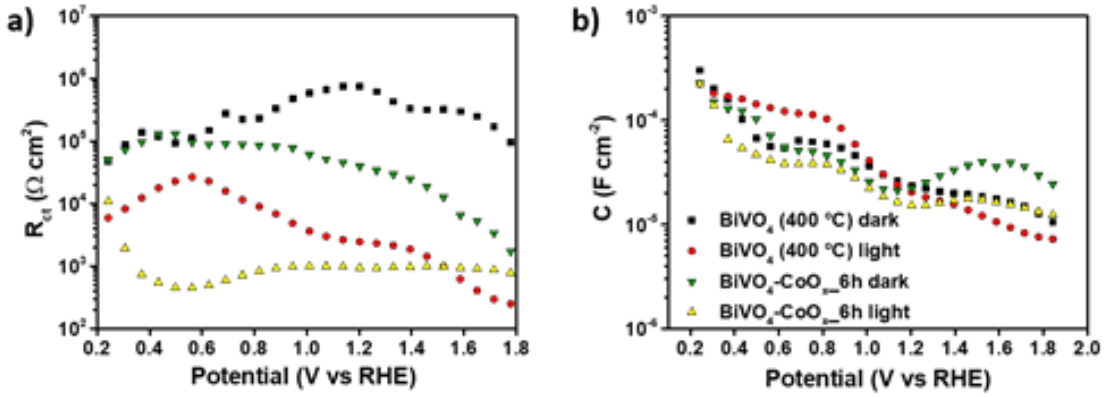

Figure 4. Parameters extracted from fitting the impedance spectroscopy data with the equivalent circuit model shown at **Supporting Information, Figure S7**. **a)** Charge transfer resistance (R_{ct}) **b)** Capacitance (C).

Next, we were interested in understanding whether the enhanced photoelectrochemical activity of $BiVO_4$-CoO_x_6h is directly correlated with accelerated catalytic oxygen evolution. As illustrated in **Figure 5a**, to do so, we have used a Scanning Electrochemical Microscope (SECM) setup to perform a substrate ($BiVO_4$-CoO_x_6h or control $BiVO_4$)-generation tip (10µm Pt-based ultramicroelectrode)-collection under illumination (using a 405nm LED with calibrated illumination intensity of 2mW/cm^2). First, the Pt tip was brought into close proximity of the photoanodes surface (10 µm, see approach curves in **Supporting Information, Figure S16**). Hereafter, light illumination was turned on and the substrate potential was scanned anodically to photoelectrochemically generate O_2. At the same time, direct O_2 detection was achieved by fixing the tip potential at 0.1V vs RHE to effectively reduce substrate-evolved O_2 at a mass-transport limited rate. As can be seen in **Figure 5b**, oxidative substrate photocurrent is followed by reductive tip current, thus providing a direct confirmation for the photo-electrocatalytic O_2 generation. Additionally, further evidence for the enhanced water oxidation kinetics of $BiVO_4$-CoO_x_6h compared to the control $BiVO_4$ is given by its significantly higher O_2 detection current measured at the tip.

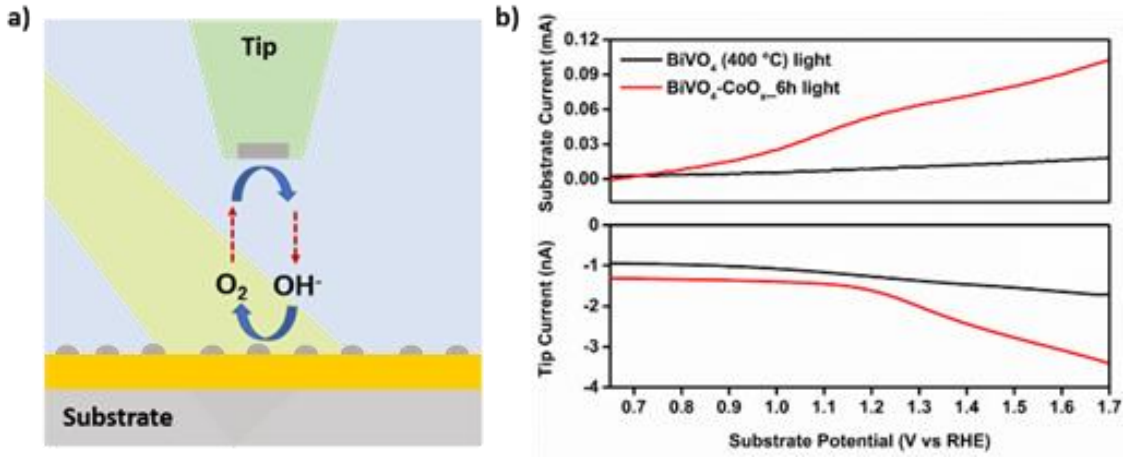

Figure 5. a) Schematic illustration of an SECM-based substrate-generation tip-collection experiment for direct detection of photoelectrochemical O_2 evolution. **b)** Substrate-generation tip-collection LSV curves of $BiVO_4$ (400 °C) (black lines) and $BiVO_4$-CoO_x_6h (red lines).

The stability of the best performing photoanode ($BiVO_4$-CoO_x_6h) was also evaluated through chronoamperometric measurements. During the first two hours of catalysis, the photocurrent remains practically constant, after a 20 min stabilization time (**Figure 6a**). Furthermore, connecting a gas chromatograph to the photoelectrochemical cell, we could confirm the oxygen evolution takes place with a faradaic efficiency of ~100%. The scattering of the faradaic efficiency during this period is due to flux control issues during the manual sampling process (**Figure 6b**).

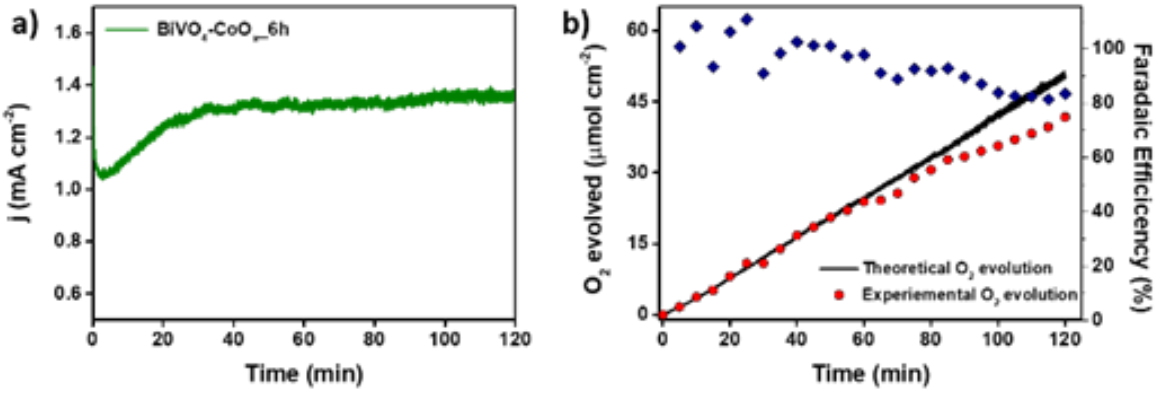

Figure 6. a) Chronoamperometric measurement at 1.23 V vs RHE in a $BiVO_4$-CoO_x_6h electrode, showing the first two hours in which gas chromatography measures were performed. **b)** O_2 evolution detection and faradaic efficiency extracted by gas chromatography.

After 2 hours of operation, the same electrode was subject to additional, long chronoamperometric test (24 hours) (**see Supporting Information, Figure S17**). At this point, one can see a rapid decline of the measured photocurrent occurring during the first 2 hours, significantly slowing down for the next 22 hours. Examination of post-mortem SEM micrographs and EDS analysis, (**Supporting Information, Figure S18**), suggests that the main factor for the performance loss can be ascribed to the degradation of both $BiVO_4$ and the MOF-converted co-catalyst, as evidenced by the decrease of Bi, V and Co concentrations**.** This conclusion is also supported by post-catalysis ICP-MS and XPS quantitative analysis of the supernatant electrolyte solution and the aged electrode surface respectively, which shows the presence of significant quantities of Co, Bi and V in the electrolyte solution and the decrease of the presence of these elements on the electrode surface (See **Supporting Information, Tables S3 and S4**). In addition, the reduced activity of the photoanode over time may also be ascribed to a chemical alteration of the cobalt oxide-based co-catalyst during photo-electrochemical water oxidation. As can be seen in **Supporting Information Figure S19**, Co 2p XPS signal analysis reveal that as opposed to the pristine films, the surface of the co-catalyst at the aged electrode contains only a stochiometric Co_3O_4 phase (as a result of the harsh oxidizing environment during catalytic operation).

Conclusions

In this work we demonstrate that a porous MOF-converted compound could be utilized as a highly efficient water oxidation co-catalyst in a photo-electrochemical cell. As a proof-of-concept, we have modified a $BiVO_4$-based photoanode with the well-known cobalt-based ZIF-67 MOF. Upon thermal treatment in air, the ZIF-67 was converted into highly porous CoO_x nanoparticles. Detailed photo-electrochemical characterization of the co-

catalyst modified photoanodes, reveal a substantial improvement in the catalytic performance compared to the bare $BiVO_4$ electrode (~4-times higher photocurrents coupled with a 300 mVs cathodic shift in catalytic onset potential). Furthermore, measurements with a fast hole scavenger as well as electrochemical impedance spectroscopy analysis point to the fact that the MOF-converted co-catalysts significantly accelerate the kinetics of water oxidation, rather than serving as a surface passivation layer. Hence, we believe that these results will pave the way for the future design of highly efficient photo-electrochemical cells, to be used in a variety of energy related applications.

Conflicts of interests

There are no conflicts to declare.

Acknowledgements

S.G thanks the support of the Spanish Ministerio de Ciencia, Innovación y Universidades through the project ENE2017-85087-C3-1-R. I.H thank the support of the Israel Science Foundation (ISF) (grant No. 306/18), and the Ilse Katz Institute for Nanoscale Science and Technology for the technical support in material characterization.

Conflicts of interest

There are no conflicts to declare.

Author contribution

† D.C.-M. and R.I. have equally contributed to this work

References

1. Li, Z. S.; Luo, W. J.; Zhang, M. L.; Feng, J. Y.; Zou, Z. G. Photoelectrochemical cells for solar hydrogen production: current state of promising photoelectrodes, methods to improve their properties, and outlook. *Energy & Environmental Science* **2013,** *6* (2), 347-370.
2. Walter, M. G.; Warren, E. L.; McKone, J. R.; Boettcher, S. W.; Mi, Q.; Santori, E. A.; Lewis, N. S. Solar Water Splitting Cells. *Chemical Reviews* **2010,** *110* (11), 6446-6473.
3. Ge, M.; Cai, J.; Iocozzia, J.; Cao, C.; Huang, J.; Zhang, X.; Shen, J.; Wang, S.; Zhang, S.; Zhang, K.-Q.; Lai, Y.; Lin, Z. A review of TiO_2 nanostructured catalysts for sustainable H_2 generation. *International Journal of Hydrogen Energy* **2017,** *42* (12), 8418-8449.
4. Dong, P.; Hou, G.; Xi, X.; Shao, R.; Dong, F. WO_3-based photocatalysts: morphology control, activity enhancement and multifunctional applications. *Environmental Science-Nano* **2017,** *4* (3), 539-557.
5. Sivula, K.; Le Formal, F.; Graetzel, M. Solar Water Splitting: Progress Using Hematite (α-Fe_2O_3) Photoelectrodes. *ChemSusChem* **2011,** *4* (4), 432-449.
6. Kim, T. W.; Choi, K.-S. Nanoporous BiVO4 Photoanodes with Dual-Layer Oxygen Evolution Catalysts for Solar Water Splitting. *Science* **2014,** *343* (6174), 990-994.
7. Trotochaud, L.; Young, S. L.; Ranney, J. K.; Boettcher, S. W. Nickel-Iron Oxyhydroxide Oxygen-Evolution Electrocatalysts: The Role of Intentional and Incidental Iron Incorporation. *Journal of the American Chemical Society* **2014,** *136* (18), 6744-6753.
8. Friebel, D.; Louie, M. W.; Bajdich, M.; Sanwald, K. E.; Cai, Y.; Wise, A. M.; Cheng, M.-J.; Sokaras, D.; Weng, T.-C.; Alonso-Mori, R.; Davis, R. C.; Bargar, J. R.; Norskov, J. K.; Nilsson, A.; Bell, A. T. Identification of Highly Active Fe Sites in (Ni,Fe)OOH for Electrocatalytic Water Splitting. *Journal of the American Chemical Society* **2015,** *137* (3), 1305-1313.
9. Jiao, F.; Frei, H. Nanostructured Cobalt Oxide Clusters in Mesoporous Silica as Efficient Oxygen-Evolving Catalysts. *Angewandte Chemie-International Edition* **2009,** *48* (10), 1841-1844.
10. Kanan, M. W.; Nocera, D. G. In situ formation of an oxygen-evolving catalyst in neutral water containing phosphate and Co^{2+}. *Science* **2008,** *321* (5892), 1072-1075.
11. Pintado, S.; Goberna-Ferron, S.; Escudero-Adan, E. C.; Ramon Galan-Mascaros, J. Fast and Persistent Electrocatalytic Water Oxidation by Co-Fe Prussian Blue Coordination Polymers. *Journal of the American Chemical Society* **2013,** *135* (36), 13270-13273.
12. Furukawa, H.; Cordova, K. E.; O'Keeffe, M.; Yaghi, O. M. The Chemistry and Applications of Metal-Organic Frameworks. *Science* **2013,** *341* (6149), 974.
13. Furlong, B. J.; Katz, M. J. Bistable Dithienylethene-Based Metal-Organic Framework Illustrating Optically Induced Changes in Chemical Separations. *J Am Chem Soc* **2017,** *139* (38), 13280-13283.
14. Rowsell, J. L. C.; Yaghi, O. M. Strategies for hydrogen storage in metal-organic frameworks. *Angew Chem Int Edit* **2005,** *44* (30), 4670-4679.
15. Lee, J.; Farha, O. K.; Roberts, J.; Scheidt, K. A.; Nguyen, S. T.; Hupp, J. T. Metal-organic framework materials as catalysts. *Chem Soc Rev* **2009,** *38* (5), 1450-1459.
16. Zhu, L.; Liu, X. Q.; Jiang, H. L.; Sun, L. B. Metal-Organic Frameworks for Heterogeneous Basic Catalysis. *Chem Rev* **2017,** *117* (12), 8129-8176.
17. Mondloch, J. E.; Katz, M. J.; Isley, W. C.; Ghosh, P.; Liao, P. L.; Bury, W.; Wagner, G.; Hall, M. G.; DeCoste, J. B.; Peterson, G. W.; Snurr, R. Q.; Cramer, C. J.; Hupp, J. T.; Farha, O. K. Destruction of chemical warfare agents using metal-organic frameworks. *Nat Mater* **2015,** *14* (5), 512-516.

18. Kreno, L. E.; Leong, K.; Farha, O. K.; Allendorf, M.; Van Duyne, R. P.; Hupp, J. T. Metal-Organic Framework Materials as Chemical Sensors. *Chem Rev* **2012,** *112* (2), 1105-1125.
19. Campbell, M. G.; Liu, S. F.; Swager, T. M.; Dinca, M. Chemiresistive Sensor Arrays from Conductive 2D Metal-Organic Frameworks. *J Am Chem Soc* **2015,** *137* (43), 13780-13783.
20. Hod, I.; Sampson, M. D.; Deria, P.; Kubiak, C. P.; Farha, O. K.; Hupp, J. T. Fe-Porphyrin-Based Metal-Organic Framework Films as High-Surface Concentration, Heterogeneous Catalysts for Electrochemical Reduction of CO_2. *Acs Catal* **2015,** *5* (11), 6302-6309.
21. Liu, J. X.; Woll, C. Surface-supported metal-organic framework thin films: fabrication methods, applications, and challenges. *Chem Soc Rev* **2017,** *46* (19), 5730-5770.
22. Usov, P. M.; Huffman, B.; Epley, C. C.; Kessinger, M. C.; Zhu, J.; Maza, W. A.; Morris, A. J. Study of Electrocatalytic Properties of Metal-Organic Framework PCN-223 for the Oxygen Reduction Reaction. *Acs Appl Mater Inter* **2017,** *9* (39), 33539-33543.
23. Kornienko, N.; Zhao, Y. B.; Kiley, C. S.; Zhu, C. H.; Kim, D.; Lin, S.; Chang, C. J.; Yaghi, O. M.; Yang, P. D. Metal-Organic Frameworks for Electrocatalytic Reduction of Carbon Dioxide. *J Am Chem Soc* **2015,** *137* (44), 14129-14135.
24. Miner, E. M.; Fukushima, T.; Sheberla, D.; Sun, L.; Surendranath, Y.; Dinca, M. Electrochemical oxygen reduction catalysed by Ni-3(hexaiminotriphenylene)(2). *Nat Commun* **2016,** *7*.
25. Hod, I.; Bury, W.; Karlin, D. M.; Deria, P.; Kung, C. W.; Katz, M. J.; So, M.; Klahr, B.; Jin, D. N.; Chung, Y. W.; Odom, T. W.; Farha, O. K.; Hupp, J. T. Directed Growth of Electroactive Metal-Organic Framework Thin Films Using Electrophoretic Deposition. *Adv Mater* **2014,** *26* (36), 6295-6300.
26. Hod, I.; Bury, W.; Gardner, D. M.; Deria, P.; Roznyatovskiy, V.; Wasielewski, M. R.; Farha, O. K.; Hupp, J. T. Bias-Switchable Permselectivity and Redox Catalytic Activity of a Ferrocene-Functionalized, Thin-Film Metal-Organic Framework Compound. *J Phys Chem Lett* **2015,** *6* (4), 586-591.
27. Hod, I.; Farha, O. K.; Hupp, J. T. Modulating the rate of charge transport in a metal-organic framework thin film using host: guest chemistry. *Chem Commun* **2016,** *52* (8), 1705-1708.
28. Lin, S. Y.; Usov, P. M.; Morris, A. J. The role of redox hopping in metal-organic framework electrocatalysis. *Chem Commun* **2018,** *54* (51), 6965-6974.
29. Ifraemov, R.; Shimoni, R.; He, W.; Peng, G.; Hod, I. A metal–organic framework film with a switchable anodic and cathodic behaviour in a photo-electrochemical cell. *J Mater Chem A* **2019**.
30. He, W.; Ifraemov, R.; Raslin, A.; Hod, I. Room-Temperature Electrochemical Conversion of Metal–Organic Frameworks into Porous Amorphous Metal Sulfides with Tailored Composition and Hydrogen Evolution Activity. *Advanced Functional Materials* **2018,** *28* (18), 1707244.
31. Cao, X. H.; Tan, C. L.; Sindoro, M.; Zhang, H. Hybrid micro-/nano-structures derived from metal-organic frameworks: preparation and applications in energy storage and conversion. *Chem Soc Rev* **2017,** *46* (10), 2660-2677.
32. Dang, S.; Zhu, Q. L.; Xu, Q. Nanomaterials derived from metal-organic frameworks. *Nat Rev Mater* **2018,** *3* (1).
33. Oar-Arteta, L.; Wezendonk, T.; Sun, X. H.; Kapteijn, F.; Gascon, J. Metal organic frameworks as precursors for the manufacture of advanced catalytic materials. *Mat Chem Front* **2017,** *1* (9), 1709-1745.

34. Yilmaz, G.; Yam, K. M.; Zhang, C.; Fan, H. J.; Ho, G. W. In Situ Transformation of MOFs into Layered Double Hydroxide Embedded Metal Sulfides for Improved Electrocatalytic and Supercapacitive Performance. *Adv Mater* **2017,** *29* (26).
35. Zhang, W.; Li, R.; Zhao, X.; Chen, Z.; Law, A. W.-K.; Zhou, K. A Cobalt-Based Metal–Organic Framework as Cocatalyst on $BiVO_4$ Photoanode for Enhanced Photoelectrochemical Water Oxidation. *ChemSusChem* **2018,** *11* (16), 2710-2716.
36. Jiao, Z.; Zheng, J.; Feng, C.; Wang, Z.; Wang, X.; Lu, G.; Bi, Y. Fe/W Co-Doped $BiVO_4$ Photoanodes with a Metal–Organic Framework Cocatalyst for Improved Photoelectrochemical Stability and Activity. *ChemSusChem* **2016,** *9* (19), 2824-2831.
37. Anh, L. T.; Rai, A. K.; Thi, T. V.; Gim, J.; Kim, S.; Mathew, V.; Kim, J. Enhanced electrochemical performance of novel K-doped Co_3O_4 as the anode material for secondary lithium-ion batteries. *J Mater Chem A* **2014,** *2* (19), 6966-6975.
38. Hadjiev, V. G.; Iliev, M. N.; Vergilov, I. V. The Raman-Spectra of Co_3O_4. *J Phys C Solid State* **1988,** *21* (7), L199-L201.
39. Zhong, G. H.; Liu, D. X.; Zhang, J. Y. The application of ZIF-67 and its derivatives: adsorption, separation, electrochemistry and catalysts. *J Mater Chem A* **2018,** *6* (5), 1887-1899.
40. Qin, J.; Wang, S.; Wang, X. Visible-light reduction CO_2 with dodecahedral zeolitic imidazolate framework ZIF-67 as an efficient co-catalyst. *Applied Catalysis B: Environmental* **2017,** *209*, 476-482.
41. Xia, Y. S.; Dai, H. X.; Jiang, H. Y.; Zhang, L. Three-dimensional ordered mesoporous cobalt oxides: Highly active catalysts for the oxidation of toluene and methanol. *Catal Commun* **2010,** *11* (15), 1171-1175.
42. Schenck, C. V.; Dillard, J. G.; Murray, J. W. Surface-Analysis and the Adsorption of Co(Ii) on Goethite. *J Colloid Interf Sci* **1983,** *95* (2), 398-409.
43. Shaddad, M. N.; Ghanem, M. A.; Al-Mayouf, A. M.; Gimenez, S.; Bisquert, J.; Herraiz-Cardona, I. Cooperative Catalytic Effect of ZrO_2 and α-Fe_2O_3 Nanoparticles on BiVO4 Photoanodes for Enhanced Photoelectrochemical Water Splitting. *ChemSusChem* **2016,** *9* (19), 2779-2783.
44. Shaddad, M. N.; Cardenas-Morcoso, D.; Arunachalam, P.; García-Tecedor, M.; Ghanem, M. A.; Bisquert, J.; Al-Mayouf, A.; Gimenez, S. Enhancing the Optical Absorption and Interfacial Properties of $BiVO_4$ with Ag_3PO_4 Nanoparticles for Efficient Water Splitting. *The Journal of Physical Chemistry C* **2018,** *122* (22), 11608-11615.
45. Shi, X.; Herraiz-Cardona, I.; Bertoluzzi, L.; Lopez-Varo, P.; Bisquert, J.; Park, J. H.; Gimenez, S. Understanding the synergistic effect of WO_3-$BiVO_4$ heterostructures by impedance spectroscopy. *Physical Chemistry Chemical Physics* **2016,** *18* (13), 9255-9261.
46. Bertoluzzi, L.; Lopez-Varo, P.; Jimenez Tejada, J. A.; Bisquert, J. Charge transfer processes at the semiconductor/electrolyte interface for solar fuel production: insight from impedance spectroscopy. *Journal of Materials Chemistry A* **2016,** *4* (8), 2873-2879.
47. Zachäus, C.; Abdi, F. F.; Peter, L. M.; van de Krol, R. Photocurrent of $BiVO_4$ is limited by surface recombination, not surface catalysis. *Chemical Science* **2017,** *8* (5), 3712-3719.
48. Yimeng, M.; Andreas, K.; R., P. S.; Florian, L. F.; R., D. J. Photoinduced Absorption Spectroscopy of CoPi on $BiVO_4$: The Function of CoPi during Water Oxidation. *Advanced Functional Materials* **2016,** *26* (27), 4951-4960.
49. Gimenez, S.; Bisquert, J. *Photoelectrochemical Solar Fuel Production: From Basic Principles to Advanced Devices*. Springer Customer Service Center Gmbh: 2018.
50. Trześniewski, B. J.; Digdaya, I. A.; Nagaki, T.; Ravishankar, S.; Herraiz-Cardona, I.; Vermaas, D. A.; Longo, A.; Gimenez, S.; Smith, W. A. Near-complete suppression of

surface losses and total internal quantum efficiency in $BiVO_4$ photoanodes. *Energy & Environmental Science* **2017,** *10* (6), 1517-1529.
51. Simone Hegner, F.; Herraiz-Cardona, I.; Cardenas-Morcoso, D.; Lopez, N.; Galan-Mascaros, J.-R.; Gimenez, S. Cobalt Hexacyanoferrate on $BiVO_4$ Photoanodes for Robust Water Splitting. *Acs Applied Materials & Interfaces* **2017,** *9* (43), 37671-37681.
52. Hermans, Y.; Murcia-López, S.: Klein, A.; van de Krol, R.; Andreu, T.; Morante, J. R.; Toupance T.; Jaegermann, W. Analysis of the interfacial characteristics of $BiVO_4$/metal oxide heterostructures and its implication on their junction properties. *Physical Chemistry Chemical Physics*, **2019**, 21, 5086–5096.
53. B. Lamm, B. J. Trześniewski, H. Döscher, W. A. Smith and M. Stefik, Emerging Postsynthetic Improvements of $BiVO_4$ Photoanodes for Solar Water Splitting *ACS Energy Letters*, **2018**, 3, 112–124

4.3 Supporting Information

Supporting Information for

A metal-organic framework converted catalyst that boosts photo-electrochemical water splitting.

Drialys Cardenas-Morcoso, [†a] Raya Ifraemov, [†b] Miguel García-Tecedor,[a] Itamar Liberman, [b] Sixto Gimenez,[*a] and Idan Hod,[*b]

[a.] *Institute of Advanced Materials (INAM), Universitat Jaume I, 12071 Castelló, Spain Address.*

[b.] *Department of Chemistry and Ilse Katz Institute for Nanoscale Science and Technology, Ben-Gurion University of the Negev, Beer-Sheva 8410501, Israel.*

[†] *D.C.-M. and R.I. have equally contributed to this work*

[*]**Email:** sjulia@uji.es, hodi@bgu.ac.il

Experimental

Materials.

The chemicals: Bismuth(III) nitrate ($Bi(NO_3)_3 \cdot 5H_2O \geq 98.0\%$), Vanadyl acetylacetonate ($VO(acac)_2 \geq 97.0\%$), potassium phosphate monobasic and dibasic ($KH_2PO_4 \geq 99.0\%$ and $K_2HPO_4 \geq 98.0\%$), zirconyl chloride octahydrate ($ZrOCl_2 \cdot 8H_2O$), Benzene-1,3,5-tricarboxylic acid ($H_3BTC \geq 95\%$), 2-methylimidazole ($C_4H_6N_2 \geq 99\%$), and cobalt nitrate hexahydrate ($Co(NO_3)_2 \cdot 6H_2O \geq 98\%$) were purchased from Sigma-Aldrich, Na_2SO_3 from J.T. Baker, potassium ferri(III)cyanide ($K_3[Fe(CN)_6] \geq 99.5\%$) from fluorochem and potassium chloride ($KCl \geq 99.0\%$)from Frutarom LTD. The Solvents; dimethyl sulfoxide ($DMSO \geq 99.9\%$), ethylene glycol (ethane-1,2-diol $\geq 99.0\%$) were obtained from Sigma-Aldrich and Methanol (absolute) from Bio-Lab Ltd.

Synthesis of FTO-$BiVO_4$ electrodes.

Zr doped $BiVO_4$ films were prepared through a previously reported method[1] based on the electrodeposition of metallic Bi on fluorine doped tin oxide (FTO) coated glass, followed by a reaction with a vanadium precursor, $VO(acac)_2$ (Sigma-Aldrich) in DMSO, at 450 ºC for 2h. Zr was added as 2.5 mol.% of $ZrCl_2O \cdot 8H_2O$ (Sigma-Aldrich) to the Bi^{3+} plating bath, according to a previous optimization process.[2]

Modification of $BiVO_4$ electrodes with a ZIF-67.

$BiVO_4$ modified FTO slides (FTO-$BiVO_4$) were immersed (with the conductive side upwards) in a 20 ml methanol solution of H_3BTC (21.01 mg, 5 mM) for 12 hours at room temperature for a surface modification with a monolayer of H_3BTC. The H_3BTC-modified $BiVO_4$ slides were carefully rinsed in methanol and dried in room temperature. Direct growth of ZIF-67 thin films on $BiVO_4$ slides was achieved by immersing the modified slides in a mixture of the two following solutions: 10 ml of $Co(NO_3)_2 \cdot 6H_2O$ (58.21 mg, 20 mM) and 10 ml of 2-methylimidazole (32.84 mg, 40 mM) both in methanol, for different periods of time: 1, 4, 6, 8.5 and 12 hours at room temperature. Thereafter, samples were rinsed gently in methanol for several times and dried in room temperature.

Preparation of $BiVO_4$-CoO_x electrodes.

ZIF-67 modified FTO-$BiVO_4$ samples (1, 4, 6, 8.5 and 12 hours of the MOF synthesis) were heated to 400 ºC in air, at a heating rate of 5 ºC /min. Upon reaching 400 ºC, the temperature was kept constant for 3 hours, and then the samples were cooled-down to room temperature.

Materials Characterization.

The crystalline structure of FTO- $BiVO_4$, $BiVO_4$-ZIF-67 and $BiVO_4$-CoO_x samples before and after calcination in air was confirmed by X-ray diffraction (XRD) measurements on a PANalytical's Empyrean multi-purpose diffractometer, using Cu-Ka (0.15405 nm) radiation. The vibrational modes of the samples were studied by Raman spectroscopy, using a Jobin-Yvon LabRam HR-high resolution analytical Raman instrument equipped with an Argon laser at 514.5 nm as excitation sources, in order to confirm the formation of the metal oxide composite on top of the $BiVO_4$ surface after calcination. Scanning electron microscopy (SEM) images were recorded using a JSM-7499F ultrahigh resolution cold FEG-SEM scanning electron microscope, operating at an acceleration voltage of 3 V with an INCA 400 Oxford EDS analyzer (Oxford, U.K.) in order to observe the morphology, particle size and chemical composition of the samples. EDS-scanning transmission electron microscope (STEM) was utilized for element mapping using annular dark-field imaging method.

N_2 physisorption isotherms for the calcinated ZIF-67 MOF powder were taken at 77 K using a Quantachrome Novatouch porosimeter. The sample was degassed at 120 °C in vacuum for 17 hours prior to isotherm measurement. The surface area of the sample was calculated by applying the Brunauer-Emmett-Teller (BET) model to the isotherm data points (adsorption branch). In order to obtain information about surface structure and possible changes of electronic coordination before and after electrochemical treatment the samples were analyzed by X-ray Photoelectron Spectroscopy (XPS). XPS data were collected by using an X-ray photoelectron spectrometer ESCALAB 250 ultrahigh vacuum (1×10-9 bar) apparatus with an AlKα X-ray source and a monochromator. The X-ray beam size was 500 μm and survey spectra was recorded with a pass energy (PE) of 150 eV and high energy resolution spectra were recorded with a PE of 20 eV. To correct for charging effects, all spectra were calibrated relative to a carbon C 1s peak, positioned at 284.8 eV. XPS results were processed by using the AVANTGE software.

The optical properties of the prepared films were determined through UV-Vis spectrophotometry, using a Cary 300 Bio spectrophotometer. The absorbance (A) was estimated from transmittance (T) and diffuse reflectance (R) measurements as: $A = -\log(T + R)$. The direct optical bandgap of $BiVO_4$ (E_g) was estimated by Tauc plots as: $(h\upsilon\alpha)^{1/n} = A(h\upsilon - E_g)$, where n=1/2 for direct transitions, h is the Planck's constant and υ the frequency.

Photo-electrochemical Characterization.

The photoelectrochemical performance of the electrodes was evaluated in a three-electrode cell consisting of a working electrode, an Ag/AgCl (3 M KCl) reference electrode, a Pt wire as a counter electrode and a 0.1 M potassium phosphate (K-Pi) buffer solution of pH 7.5 as electrolyte. Alternatively, a 0.1M Na_2SO_3 solution was added to the electrolyte as hole scavenger. The measurements were carried out by using an Autolab potentiostat/galvanostat PGSTAT302, and a 300 W Xe lamp was used for those experiments under illumination conditions. The light intensity was adjusted to 100 mW/cm^2 using a thermopile and illumination was carried out through the FTO substrate. All the potentials were referred to the Reversible Hydrogen Electrode (RHE) through the Nernst equation: $V_{RHE} = V_{Ag/AgCl} + V^0_{Ag/AgCl} + 0.059 \cdot pH$. Electrochemical Impedance Spectroscopy (EIS) measurements were performed between 0.1 Hz and 40 kHz with 20 mV of amplitude perturbation, with a step potential of 64 mV in the anodic direction. The EIS data were analyzed with ZView software (Scribner associates). Incident Photon to Current Efficiency (IPCE) measurements were performed with a 300 W Xe lamp coupled with a monochromator and an optical power meter. The photocurrent was measured at 1.23 V vs RHE, with 10 nm spectral step. IPCE was calculated through the expression: $IPCE\ \% = \frac{I_{ph}(A)}{P(W)} \times \frac{1239.8}{\lambda\ (nm)} \times 100$, where I_{ph} is the photocurrent measured at a wavelength λ and P is the power of the monochromatic light at the same wavelength. The Absorbed Photon to Current Efficiency (APCE) was also calculated as: $APCE\ \% = \frac{IPCE}{\eta_{e^-/h^+}} \times 100$, where η_{e^-/h^+} is the absorptance, defined as the fraction of electron–hole pairs generated per incident photon flux and was obtained from the absorbance (A) as $\eta_{e^-/h^+} = 1 - 10^{-A}$. From measurements in the presence of a Na_2SO_3 sacrificial hole scavenger and the theoretical maximum photocurrent estimated from the absorbance measurements, ($j_{abs} = \frac{e}{hc}\int \lambda \cdot I(\lambda) \cdot (1 - 10^{-A})d\lambda$, with *I(λ)*as the spectral irradiance, e the elemental charge, h the Planck constant and c the light speed), the charge separation efficiency (η_{cs}) and the charge injection efficiency (η_{cat}) were calculated as: $\eta_{cat} = \frac{j_{H_2O}}{j_{HS}}$ and $\eta_{cs} = \frac{j_{HS}}{j_{abs}}$. The

faradaic efficiency for O_2 evolution at the electrode surface was estimated through the relation between the amount of evolved O_2 monitored every 5 min during a measurement at 1.23 V vs RHE in phosphate buffer (pH 7.5), in a sealed cell coupled to an Agilent Micro-GC gas chromatograph, and the theoretical O_2 evolution calculated with the Faraday´s Law.

Scanning electrochemical microscopy (SECM) measurements were performed on the $BiVO_4$ (400 °C) and the $BiVO_4$-CoO_x_6h electrodes, utilizing a BIOLOGIC SECM-150 workstation. The measurements were performed in a phosphate buffer solution (pH=7.5), were the $BiVO_4$-based films function as the substrate, a Pt ultramicroelectrode (UME) with radius of 5 μm utilized as the SECM tip, while Ag/AgCl (St.) and Pt wire were served as the reference and the counter electrode, respectively. In the SECM substrate-generation tip-collection measurements, the potential on the tip was kept constant at 0.1 V_{RHE} while the potential on substrate was swept from 0.65 V_{RHE} to 1.7 V_{RHE} with a scan rate of 5 mV/sec. The measurements were performed under light illumination using a 2 mW/cm^2 405 nm LED lamp. Prior to the measurement the gap spacing (Z), between the tip and a substrate was determined by monitoring the tip position, using an aqueous solution containing 5 mM ferricyanide and 0.1 M KCl, while keeping the tip and substrate in a constant potential of 0.4 V and 1.2 V vs RHE. The obtained approach curves where fitted with using a MIRA SECM simulation software to accurately extract the substrate-to-tip distance.

Supplementary Results.

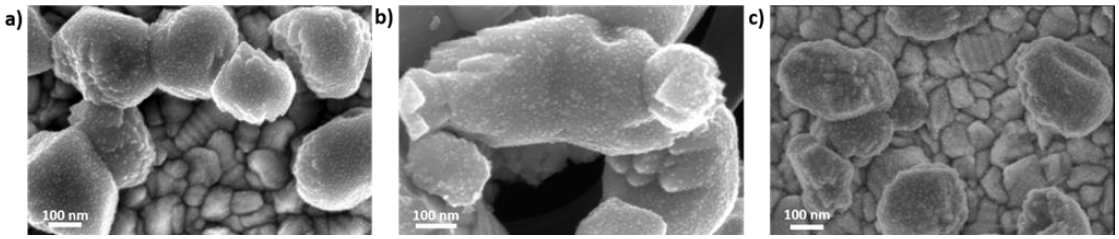

Figure S1. SEM images of **a)** $BiVO_4$-CoO_x_6h, **b)** $BiVO_4$-CoO_x_8.5h, and **c)** $BiVO_4$-CoO_x_12h.

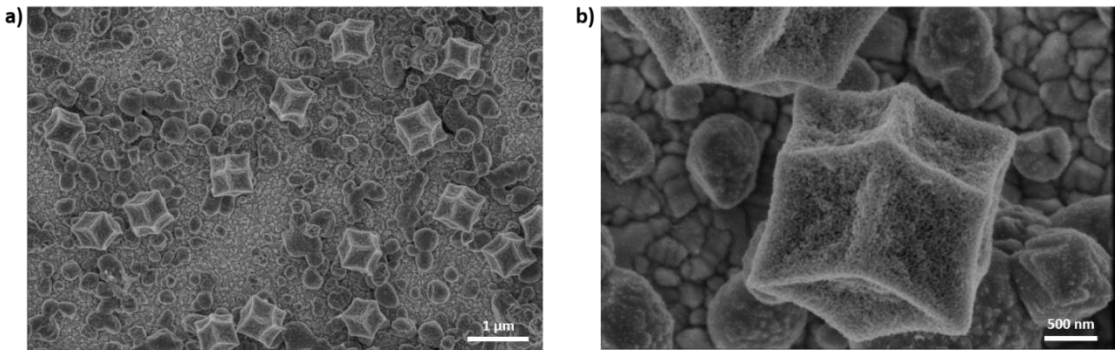

Figure S2. SEM image of dodecahedral ZIF-67-converted CoO_x particles in $BiVO_4$-CoO_x_6h films.

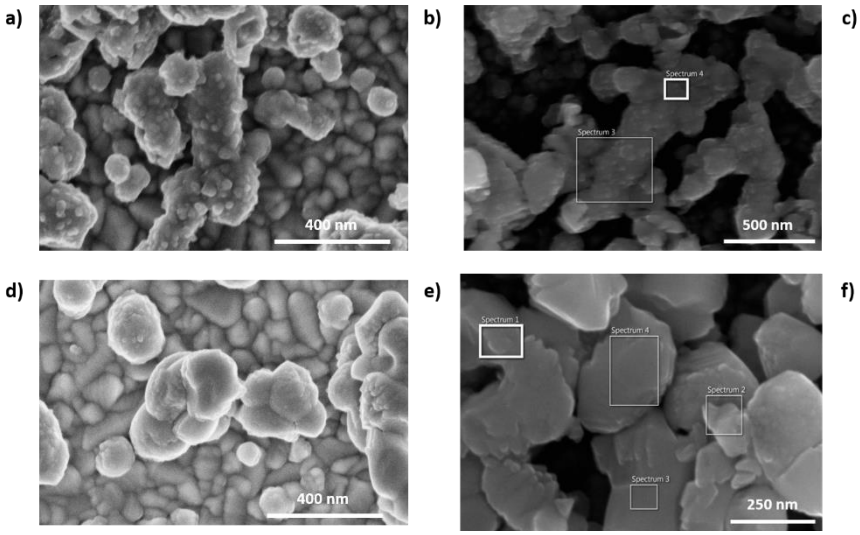

c)

Spectrum	Element At (%)		
	Bi	V	Co
3	48.1	47.2	4.7
4	46.7	46.4	6.9

f)

Spectrum	Element At (%)		
	Bi	V	Co
1	45.7	53.8	0.5
2	46.3	53.7	0.0
3	45.2	54.7	0.0
4	46.4	53.1	0.5

Figure S3. SEM images, EDS atomic percentage of the selected elements and their corresponding regions in SEM of the $BiVO_4$-ZIF-67_6h **(a-c)** and $BiVO_4$-$Co(NO_3)_2$_6h **(d-f).**

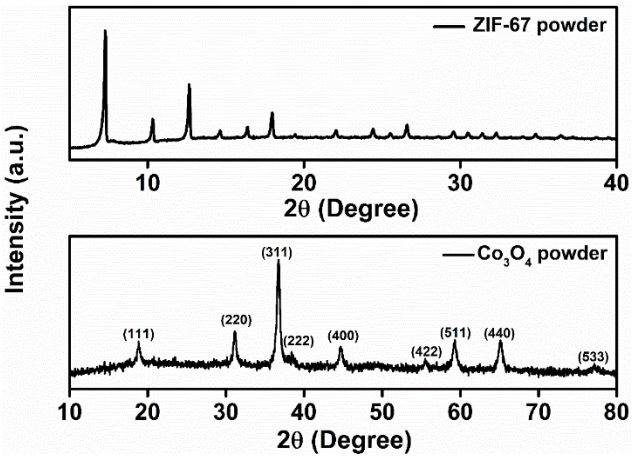

Figure S4. XRD patterns of as synthesized ZIF-67 powder (top) and ZIF-67 converted Co_3O_4 (bottom).

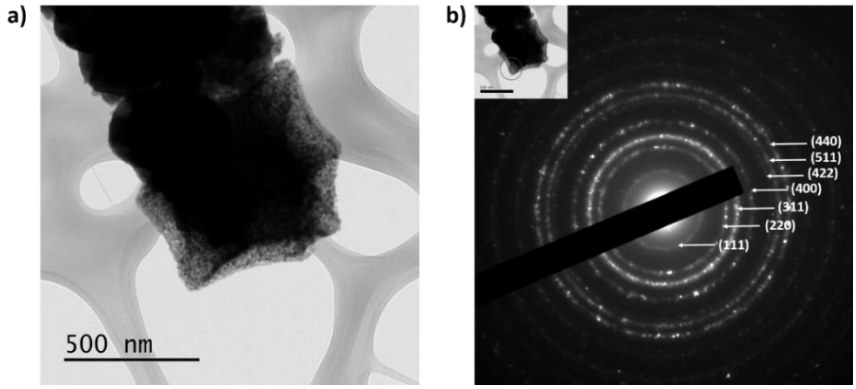

Figure S5. a) Transmission electron microscopy (TEM) images of ZIF-67 converted porous CoO_x, **b)** Selected area electron diffraction (SAED) of CoO_x exhibiting diffraction rings corresponding to a cubic Co_3O_4 crystal phase.

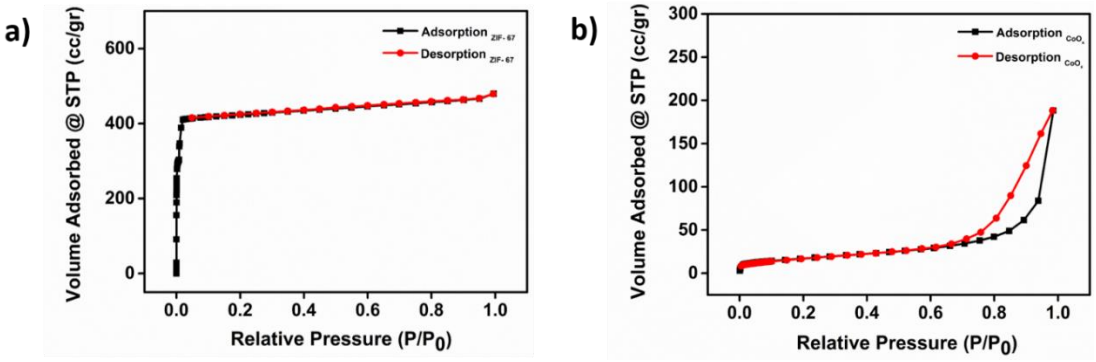

Figure S6. N_2 isotherm analysis of **a)** as-synthesized ZIF-67 (BET surface area of 1340 m^2/g), and **b)** air calcinated ZIF-67 (CoO_x) powder (BET surface area of 63 m^2/g).

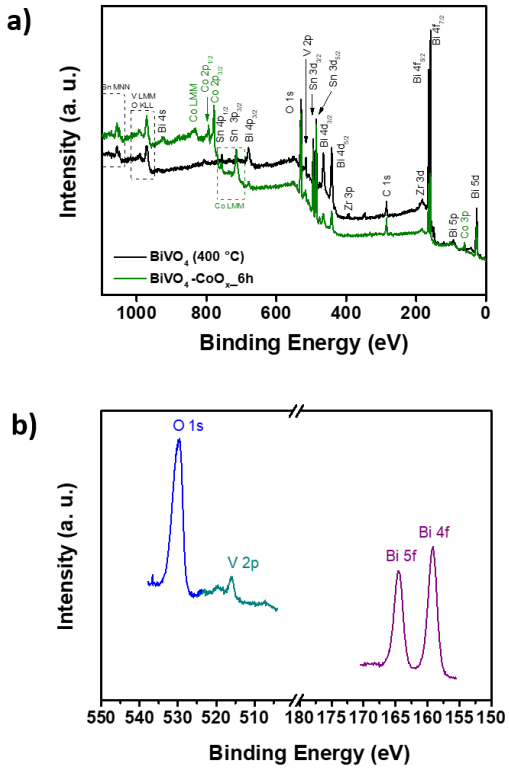

Figure S7. a) Global XPS spectra of $BiVO_4$ (400 ºC, control) and $BiVO_4$-CoOx_6h electrodes surface. **b)** XPS spectra of specific O 1s, V 2p and Bi 4f orbitals in $BiVO_4$-CoOx_6h electrode surface.

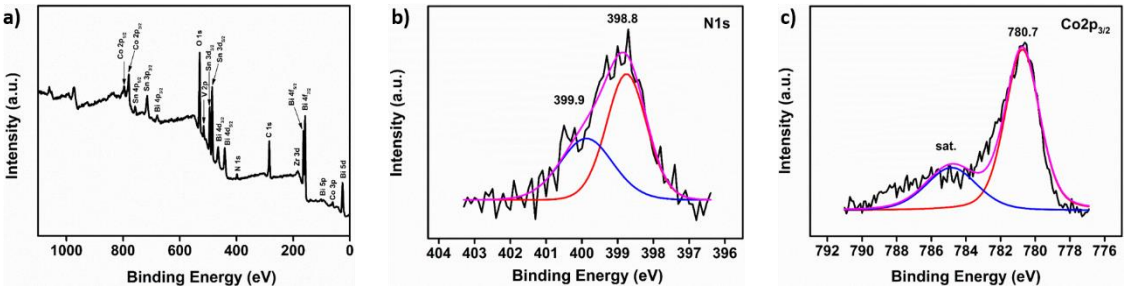

Figure S8. a) Global, **b)** N1s and **c)** Co2p XPS spectra of $BiVO_4$-ZIF-67_6h sample

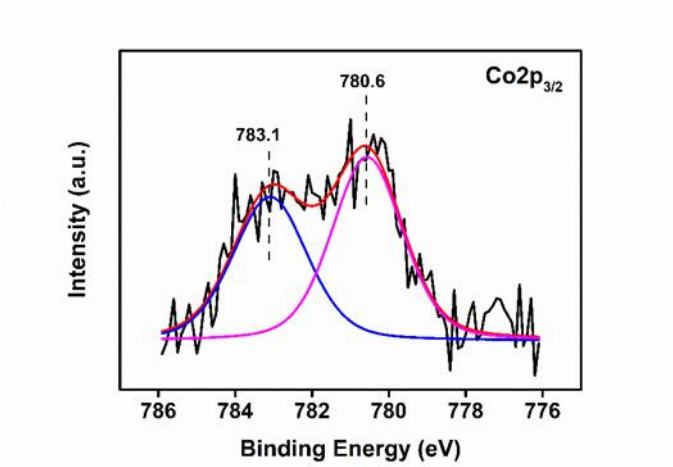

Figure S9. XPS Spectra analysis of the signals of Co 2p orbitals in $BiVO_4$-CoO_x_6h films, showing the presence of both CoO_x and Co_3O_4 surface-residing phases.

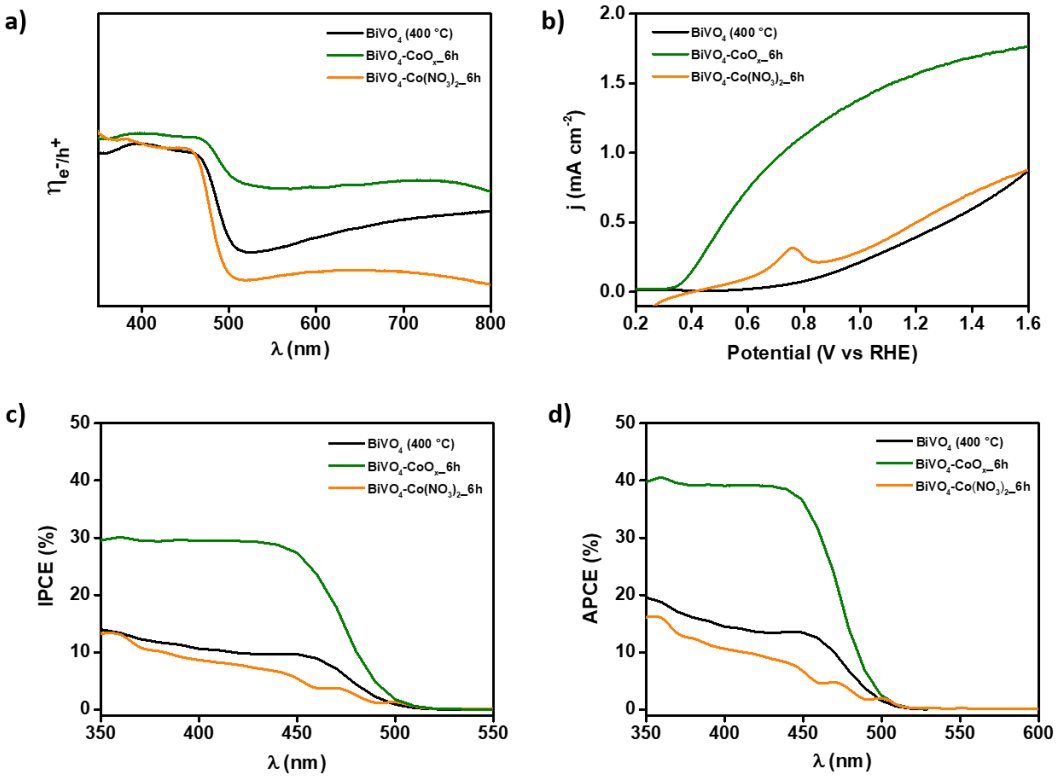

Figure S10. a) UV-Vis absorption spectra of the two control sample: $BiVO_4$ (400 °C), $BiVO_4$_$Co(NO_3)_2$ and the $BiVO_4$-CoO_x_6h, **b)** j-V curves obtained with cyclic voltammetry **c)** IPCE and **d)** APCE spectra obtained from IPCE and absorbance measurements at 1.23 V vs RHE

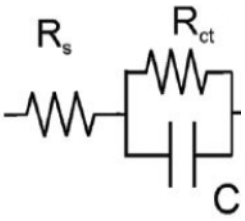

Figure S11. Equivalent circuit model used to fit the experimental EIS data. The circuit includes a series resistance (R_s) accounting for the solution resistance and the resistance at the contacts, a charge transfer resistance (R_{ct}) accounting for the injection of carriers (holes) into the solution, and a capacitance (C).

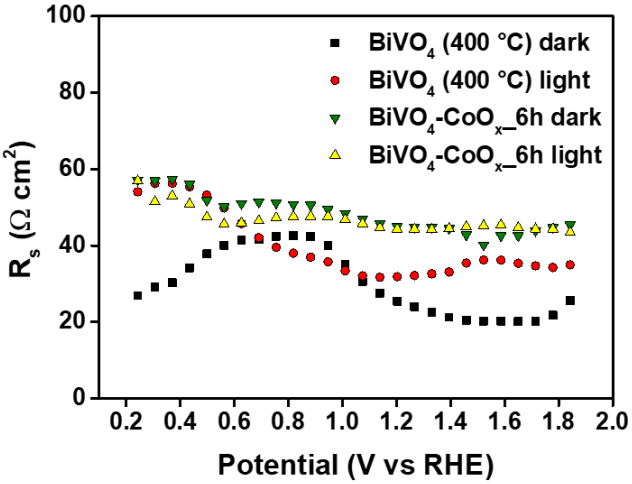

Figure S12. Series resistance (R_s) of the $BiVO_4$ (400 °C) and best performing $BiVO_4$-CoO_x_6h electrode in the dark and under illumination at 100 $mW \cdot cm^{-2}$.

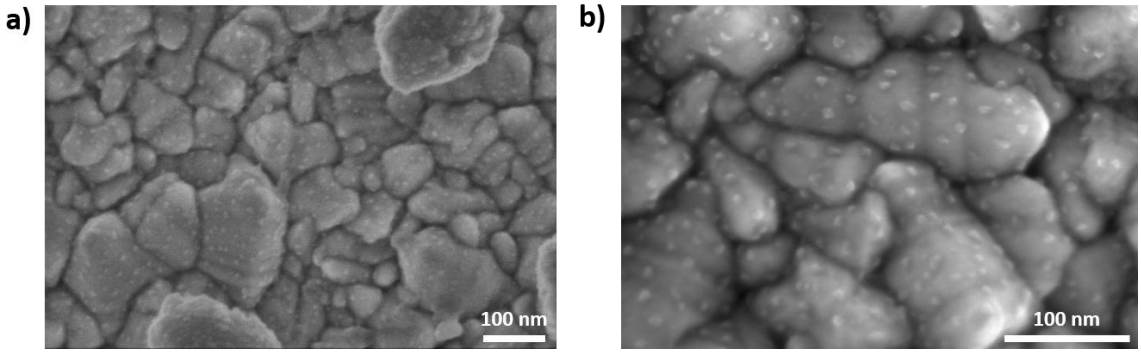

Figure S13. SEM images of the FTO/CoO_x interface at an $BiVO_4$-CoO_x_6h electrode.

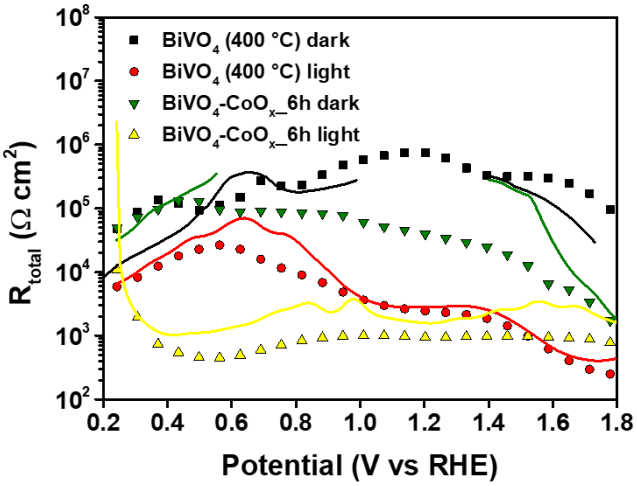

Figure S14. Comparison between the total resistance (R_{total}) extracted from impedance spectroscopy and from derivation of the j-V curves obtained by cyclic voltammetry.

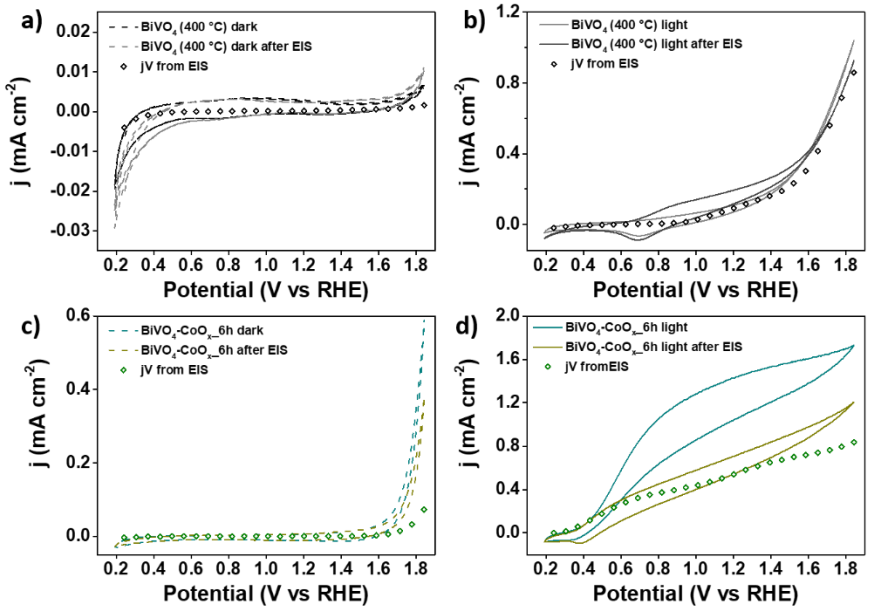

Figure S15. Cyclic voltammetry j-V curves before and after the impedance spectroscopy measurements (lines) together with j-V curves directly extracted from impedance measurements.

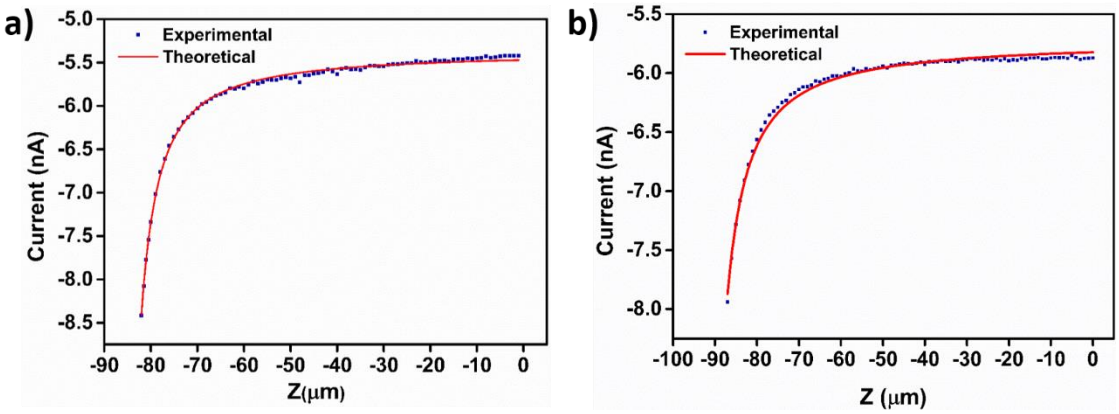

Figure S16. SECM approach curves for the **a)** $BiVO_4$ (400 °C) and, **b)** $BiVO_4$-CoO_x_6h electrodes. The measurement was performed in an aqueous solution containing 5 mM ferricyanide, 0.1 M KCl, while the potential on the tip and substrate held at 0.4 V and 1.2 V vs RHE, respectively. The experimental results (blue dots) are compared to the theoretical approach curves obtained from MIRA Simulation software (red line).

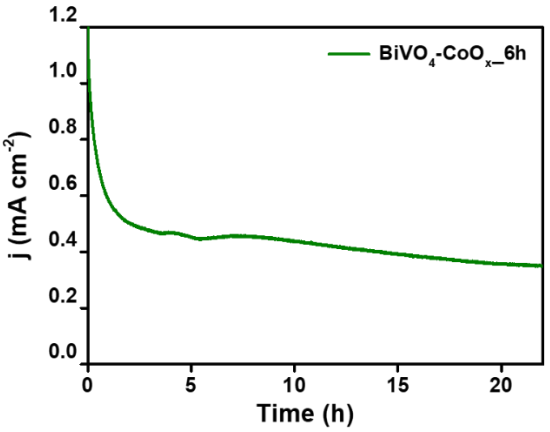

Figure S17. Long term stability in $BiVO_4$-CoO_x_6h electrode.

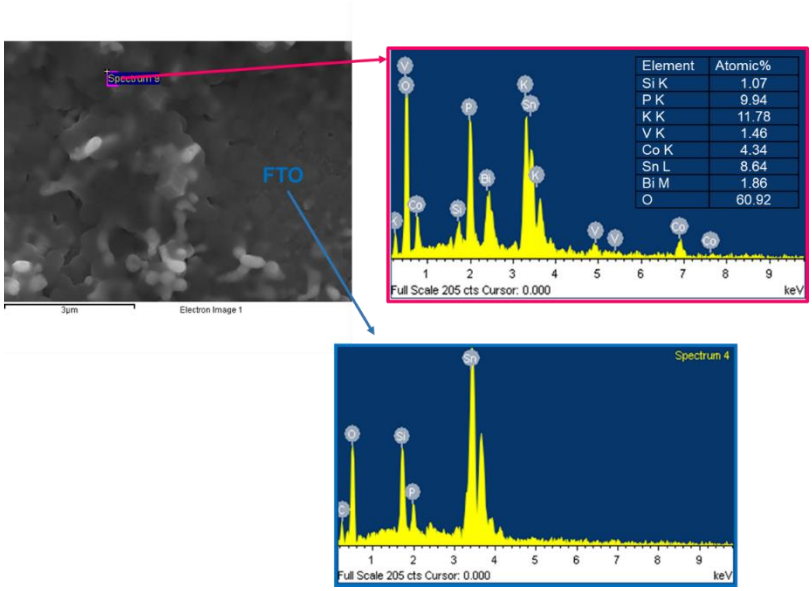

Figure S18. Post-mortem **a)** SEM and **b)** XPS analysis on $BiVO_4$-CoO_x_6h electrode surface after long term stability test.

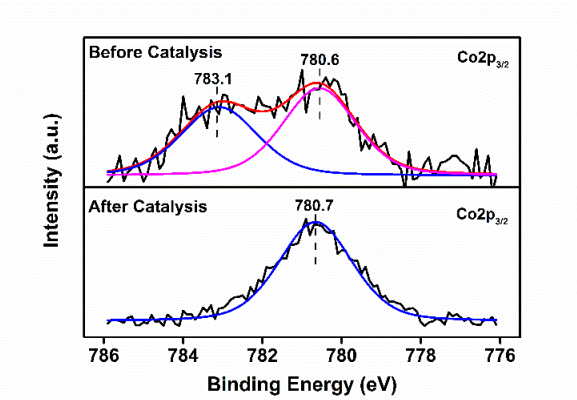

Figure S19. XPS spectra of $BiVO_4$-CoO_x_6h before and after long term stability measurement.

Table S1: ICP analysis for Co surface loading for the 6, 8.5, 12 hours ZIF-67 growth duration.

Sample	Co (µg/cm²)	Co (µmol/cm²)
ZIF-67_6h	9.778	0.166
ZIF-67_8.5h	16.60	0.282
ZIF-67_12h	35.85	0.608

Table S2. Comparison of current density values extracted from j-V curves and calculated from IPCE measurements at 1.23 V vs RHE.

Sample	***j @1.23 V vs RHE from jV (mA cm^{-2})***	***j from IPCE (mA cm^{-2}) [300 nm-540 nm]***
$BiVO_4$ 400ºC (control)	0.428	0.666
$BiVO_4$-CoO_x_6h	1.59	1.654
$BiVO_4$-CoO_x_1h	0.538	0.523
$BiVO_4$-CoO_x_4h	0.781	0.704
$BiVO_4$-CoO_x_8.5h	1.33	1.468
$BiVO_4$-CoO_x_12h	1.16	1.179

Table S3. ICP-MS elemental analysis of the electrolyte after long term stability test of $BiVO_4$-CoO_x_6h electrode. (Analysis performed in an Agilent 7500cx quadrupole analyzer equipped with collision cell)

Element	**Pristine [X] in ppb (µg/L)**	**Aged [X] in ppb (µg/L)**
V	0.94	16.9
Co	0.06	19.5
Bi	0.43	7.68

Table S4. Elemental quantification for XPS analysis on $BiVO_4$-CoO_x_6h electrode surface before and after long term stability test.

	Atomic %	
Element	**$BiVO_4$/ZIF-67, 6h**	**$BiVO_4$/ZIF-67, 6h Aged**
O	48.2	41.7
Sn	7.7	-
N	3.1	-
Ca	-	-
C	23.3	20.5
Bi	4.3	0.3
V	2.7	-
Co	10.6	1.2
K	-	23.6
P	-	12.7

References

1. Kang, D.; Park, Y.; Hill, J. C.; Choi, K.-S. Preparation of Bi-Based Ternary Oxide Photoanodes $BiVO_4$, Bi_2WO_6, and $Bi_2Mo_3O_{12}$ Using Dendritic Bi Metal Electrodes. *The Journal of Physical Chemistry Letters* **2014,** *5* (17), 2994-2999.
2. Kim, T. W.; Choi, K.-S. Nanoporous $BiVO_4$ Photoanodes with Dual-Layer Oxygen Evolution Catalysts for Solar Water Splitting. *Science* **2014,** *343* (6174), 990-994.

Chapter 5: Publication 2

"Intensity Modulated Photocurrent Spectroscopy for solar energy conversion devices. What does negative value mean?"

Cardenas-Morcoso, D.; Bou, A.; Ravishankar, S.; García-Tecedor, M.; Giménez, S.; Bisquert, J.

ACS Energy Letters, ***2020***, *5*, *187-191*

5.1 Candidate's contribution

Nature of contribution:	**Extent of contribution:**
• Preparation of the $BiVO_4$ photoelectrodes. • Execution of the photoelectrochemical and IMPS measurements. • Contribution to the analysis of results. • Contribution to the manuscript preparation.	60%

5.2 Published manuscript

Intensity Modulated Photocurrent Spectroscopy for solar energy conversion devices. What does negative value mean?

Drialys Cardenas-Morcoso, Agustín Bou, Sandheep Ravishankar, Miguel García-Tecedor, Sixto Gimenez*, Juan Bisquert*

Institute of Advanced Materials (INAM), Universitat Jaume I, 12071 Castelló, Spain Address.

***Email:** sjulia@uji.es, bisquert@uji.es

Small perturbation techniques constitute a wide family of tools for the characterization of solar energy conversion devices such as photovoltaic cells and photoelectrochemical (PEC) cells for solar fuel production. Two main small perturbation methods frequently used in the area of solar energy conversion materials are Impedance Spectroscopy (IS) and Intensity Modulated Photocurrent Spectroscopy (IMPS). The first one consists of applying a small voltage perturbation and measuring modulated extracted current. The second one consists of applying the perturbation to the illumination and measuring the modulated extracted current.

It is well known that we can get the resistances and the capacitances of the system from the real and the imaginary part of the IS spectra respectively, and recently we have demonstrated that the differential External Quantum Efficiency (EQE_{diff}) can be obtained from the real part of the IMPS spectra.[1] However, researchers working on solar cell characterization such as the IS of metal halide perovskite solar cells are well aware that spectral responses are often not straightforward to interpret. There appear frequently experimental responses that display exotic behaviours that do not correspond to usual quantities or phenomena. For example, in the case of IS, there have been reports about *negative* values of the real part of the impedance, which are associated to negative resistances.[2] Negative values of the IS imaginary part or negative capacitances have been also reported, particularly in recent results on perovskite solar cells.[3-7] Those unexpected results, as compared to ordinary physical-chemical behaviour, are difficult to explain and their origins are still under debate, with different interpretations found in the literature.[6-9]

Recently, IMPS has become increasingly popular for understanding the charge transfer/transport/recombination dynamics and its connection to performance limitations of semiconductor materials in PECs.[10-17] One such material is $BiVO_4$, which has become an attractive candidate as a photoanode for water oxidation in PEC water splitting cells, due to its suitable band gap and valence band position for light absorption and hole injection, respectively.[18-20] Despite these desirable properties, this material also exhibits several limitations related to the charge mobility within the bulk, concomitant to surface limitations evidenced as a low charge injection efficiency.[19] In particular, the origin of these surface limitations has been extensively discussed, leading to divergent interpretations on whether the bare surface of $BiVO_4$ is catalytically active or not, and hence, about the true role of the co-catalysts used to improve the photoelectrode performance.[15, 21-22] This context motivates the investigation of the intrinsic and surface properties of this promising material in order to overcome its current limitations and, furthermore, to properly understand and interpret the results obtained from small perturbation experimental techniques.

In this Viewpoint we handle a puzzling result that is frequently obtained in IMPS measurements, particularly when measuring photoanodes for water splitting applications. It has been observed that at the region of applied potential close to the open-circuit potential (OCP), the IMPS response goes to the *negative* real part of the complex plane representation at low frequency. This phenomenon is usually accompanied by a photocurrent sign switching, observed in linear sweep voltammetry (LSV) measurements. This feature has been reported in $BiVO_4$ photoanodes,[23] for inject-printed $CuBi_2O_4$ photocathodes[24] and in Gold-decorated Cadmium chalcogenide nanorods.[25]

While the switch of the sign of the low frequency value of the IMPS response, $Q(0)$, that reaches *negative* values under different conditions, has been associated to the sign of the photocurrent in many papers,[23-25] here we show that such interpretation is not consistent with the experimental measurements. A physical model based on the general features of IMPS[1] will be presented to explain negative $Q(0)$, that sheds new light into

the interpretation of quantum efficiency and charge extraction in solar energy conversion devices.

The two techniques of IS and IMPS can be summarized in a general expression that relates the photocurrent, $\hat{j}_e$, arising from a small perturbation of light, $\hat{j}_\phi$, or voltage, $\hat{V}$, at any frequency as a linear combination of the IMPS (Q) and IS (Z) transfer functions expressed as coefficients:[26]

$$\hat{j}_e = Q(\omega)\hat{j}_\phi + Z^{-1}(\omega)\hat{V} \quad (1)$$

From this general constraint, the IS response is obtained in the absence of modulated illumination ($\hat{j_\phi} = 0$) and otherwise IMPS when $\hat{V} = 0$. IS combines current and voltage, and consequently, the real part of the transfer function is related to a resistance and the imaginary part conveys information about capacitance. Therefore, IS enables distinguishing between loss processes (resistive) and polarizing processes (capacitive) and it provides an estimation of the time-scale for these processes. Moreover, the low frequency intercept corresponds to the DC resistance:

$$Z(0) = \frac{\hat{V}(0)}{\hat{j_e}(0)} = \frac{\partial \bar{V}}{\partial \bar{j_e}} = R_{DC} \quad (2)$$

where $\bar{V}$ and $\bar{j_e}$ are the DC voltage and steady state extracted current respectively. On the other hand, IMPS relate the extracted photocurrent and the illumination, as shown in the scheme of **Figure 1a.** Therefore, the real part of its transfer function is related to the variation of the EQE.

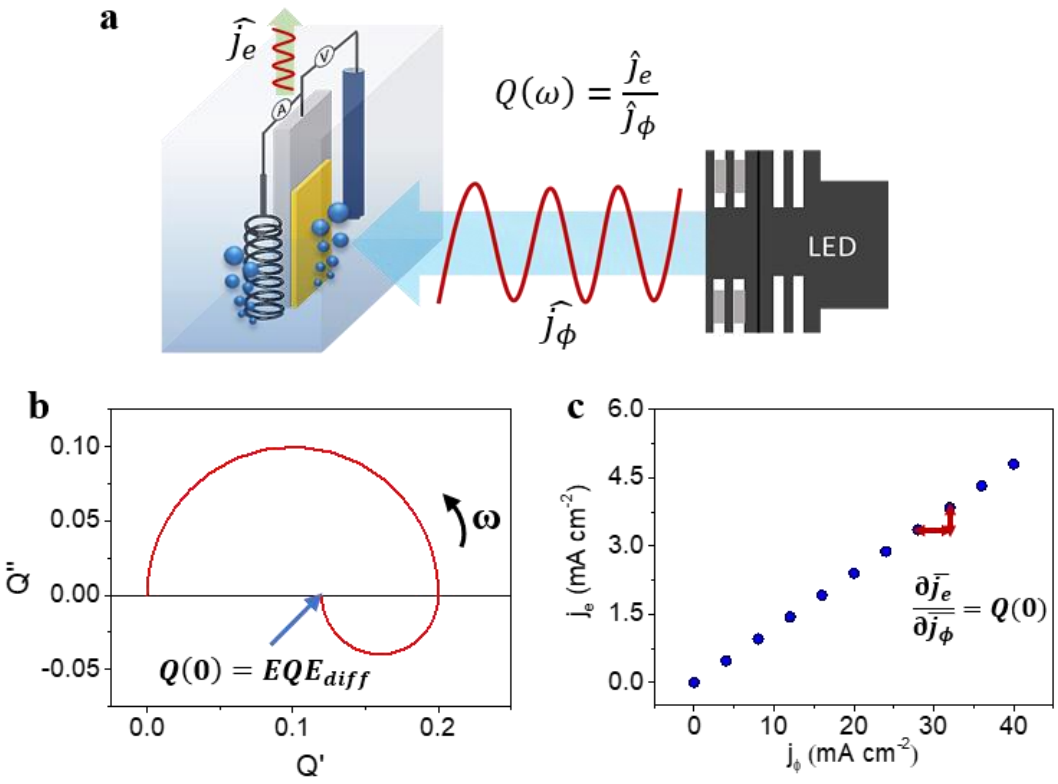

Figure 1. a Schematic representation of IMPS measurement setup in solar conversion photoelectrodes; **b** IMPS complex representation, where Q' and $-Q''$ are the real and imaginary components, respectively, of the transfer function Q (ω); **c** Representative $j_e - j_\phi$ plot showing that the slope in this graph is directly linked whit the $Q(0)$ intercept from IMPS measurements.

Similarly to IS and the R_{DC}, the low frequency value of the IMPS is directly linked with the DC component of the slope of $\overline{J_e}$ with $\overline{J_\phi}$, as depicted in **Figure 1c**.[27]

$$Q(0) = \frac{\widehat{J_e}(0)}{\widehat{J_\phi}(0)} = \frac{\partial \overline{J_e}}{\partial \overline{J_\phi}} \tag{3}$$

This expression has a connection with the external quantum efficiency (EQE), which is a key parameter for the evaluation of solar conversion devices, including PECs, since it gives the ratio of the incident photons that are converted into electron-hole pairs further extracted, as function of the wavelength. Usually, in photoelectrochemical characterization, the EQE is referred as the Incident Photon-to-Current Efficiency (IPCE) which is calculated by measuring the extracted steady state photocurrent $\overline{J_e}$ under a monochromatic light source of DC spectral photon flux, $\overline{\phi}(\lambda)$. We will refer to this quantity as EQE_{SS}, defined as:

$$EQE_{SS} = \frac{j_{ph}}{q\phi_{ph}} = \frac{\bar{J}_e}{\bar{J}_\phi} \tag{4}$$

Here, q is the elementary charge. However, another method widely employed in solar conversion device characterization involves the measurement of the differential spectral response, EQE_{diff}.[28] In this method, the sample is illuminated by a DC white light intensity, and the extracted photocurrent is measured under a small low frequency perturbation of monochromatic light. Usually, an optical chopper is employed to provide the AC perturbation. At infinitely slow perturbation, i.e. $\omega \to 0$, the EQE_{diff} can be written as:

$$EQE_{diff} = \frac{\hat{J}_e}{\hat{J}_\phi}(\omega \to 0) \approx \frac{\partial \overline{J_e}}{\partial \overline{J_\phi}} \tag{5}$$

Comparing equations (3) and (5) we get that:

$$Q(0) = EQE_{diff} \tag{6}$$

Hence, the IMPS measurements constitute an alternative method to obtain the EQE_{diff}, and it must match the slope of the extracted photocurrent with changing the illumination, as already shown by Ravishankar et al.[28]

Based on these definitions, we show that the IMPS transfer function negative value is associated to the derivative of the photocurrent with the illumination independently whether the photocurrent is positive or negative. To demonstrate this statement, we show an example of negative $Q(0)$ and negative EQE_{diff}, and simultaneously, positive value of its photocurrent. Moreover, we demonstrate experimentally the match of values of $Q(0)$ and EQE_{diff} as predicted by Eq. (6).

Figure 2a shows a linear sweep voltammetry (LSV) curve performed on a $BiVO_4$ photoanode, at monochromatic DC illumination (λ =470 nm; 90 mW cm^{-2}) and scan rate of 50 mV s^{-1}. The complete details about the photoelectrode preparation and the experimental setup can be found in the **Supporting Information** file. The inset in **Figure 2a** shows the region closer to the OCP, which is around 0.25 V vs RHE. Below this value, negative photocurrent is obtained, leading to a photocurrent switching point, and such photocurrent is strongly dependent on the incident light intensity. Similar behaviour has been previously reported on $BiVO_4$ photoanodes.[23]

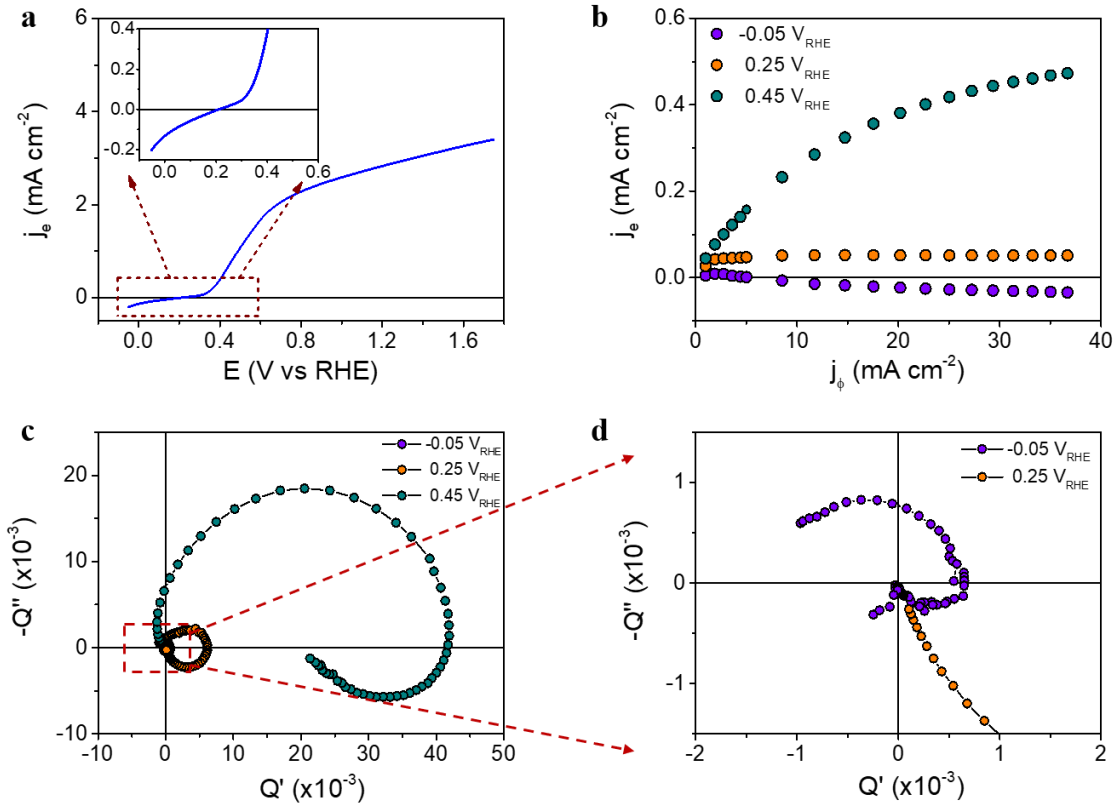

Figure 2. a Linear sweep voltammetry for a $BiVO_4$ photoanode, recorded at 50 mV s^{-1} under monochromatic DC illumination (λ=470 nm, 90 mW cm^{-2}). The inset shows the region closer to the OCP value; **b** $j_e - j_\phi$ plot at representative applied potentials closer to the OCP value; **c** Q complex representation measured at j_ϕ=36 mA cm^{-2} (corresponding to 90 mW cm^{-2}) at different applied potentials; **d** Magnification of region of **c**. All the measurements were performed in potassium phosphate buffer, at pH 7.5.

In **Figure 2b**, we show the relationship between the steady state extracted photocurrent and the incident light intensity at representative applied potentials. At applied potentials above the OCP, the extracted photocurrent tends to increase with increased photon flux, however this trend is nonlinear, and the slope tends to decrease with increasing light intensity. This means that the EQE_{diff} decreases with light intensity. At closer values to the OCP, the extracted current does not significantly change with light intensity, then the EQE_{diff} is zero. This situation changes at potentials below the OCP, where the extracted photocurrent becomes more negative when increasing the photon flux, meaning that the differential EQE value is negative. It is worth noting that when measuring the extracted photocurrent at a certain applied potential and different light intensities, a stable record of the extracted photocurrent was obtained after 60 seconds of chronoamperometric measurement. However, for intensities below 10 mW cm^{-2}, and especially at the region below the OCP, the time needed to reach a stable photocurrent value was around 120 s.

First, we carried out IMPS measurements at three different applied potentials and maximum illumination. In **Figure 2c**, at 0.45 V vs RHE, the IMPS signal at low frequency is clearly located at the positive real axis of the spectrum. At 0.25 V vs RHE, the IMPS response tends to zero at low frequency as shown in the zoom from **Figure 2d**, in good agreement with the evolution of the $\overline{J_e} - \overline{J_\phi}$ plot shown in **Figure 2b**, where a constant photocurrent is shown. Thus, we have

$$Q(0) = EQE_{diff} = 0 \quad (7)$$

Finally, at -0.05 V vs RHE, at the lowest frequency values, the IMPS transfer function moves to the negative part of the real axis, resulting in a negative $Q(0)$.

However, these measurements at maximum illumination, (i.e. at the points on the right side of **Figure 2b**) are not able to discriminate whether the IMPS sign switching is due to the photocurrent sign switching or to the EQE_{diff} one. Nevertheless, from the points at -0.05 V vs RHE in **Figure 2b**, we can differentiate two regions, one with negative photocurrent and negative slope (right side) and one with positive photocurrent and negative slope (left side), at lower illumination intensities. At this second region, the slope is negative and consequently, the differential EQE is also negative, even when the photocurrent is positive. This point allows clearly discriminating whether the IMPS sign is related to photocurrent sign, or to the sign of the slope of $\overline{J_e} - \overline{J_\phi}$ plot, i.e., the EQE_{diff}. If the IMPS switching is only related to the photocurrent switching, this point will give a positive $Q(0)$, whereas if IMPS is related to the EQE_{diff}, $Q(0)$ will be negative.

To better illustrate this, **Figure 3a** represents both the extracted photocurrent and the EQE_{diff} calculated from the slope of **Figure 2b**. Here it is shown unequivocally that, at the low illumination intensity region, the net extracted current is positive, while the slope is negative. At this point (same illumination intensity and applied voltage) we carried out IMPS measurements and found out that the IMPS transfer function at low frequency is also negative (**Figure 3b**), discarding the hypothesis that IMPS sign switching is related to photocurrent sign switching. At higher illumination intensities, the photocurrent is negative and, as shown before, the IMPS spectrum at the lowest frequency region is also negative (**Figure 3c**). Here, the negative IMPS is not related to the negative sign of the photocurrent, but its negative slope with increasing illumination.

Finally, we compared the values of the EQE_{diff} calculated from the slope of the data at -0.05 V vs RHE in **Figure 2b** with the values of $Q(0)$ extracted from IMPS spectra by extrapolating the final arc. As we expected, the values are in the same order of magnitude. The values are shown in **Table S1, in the Supporting Information**.

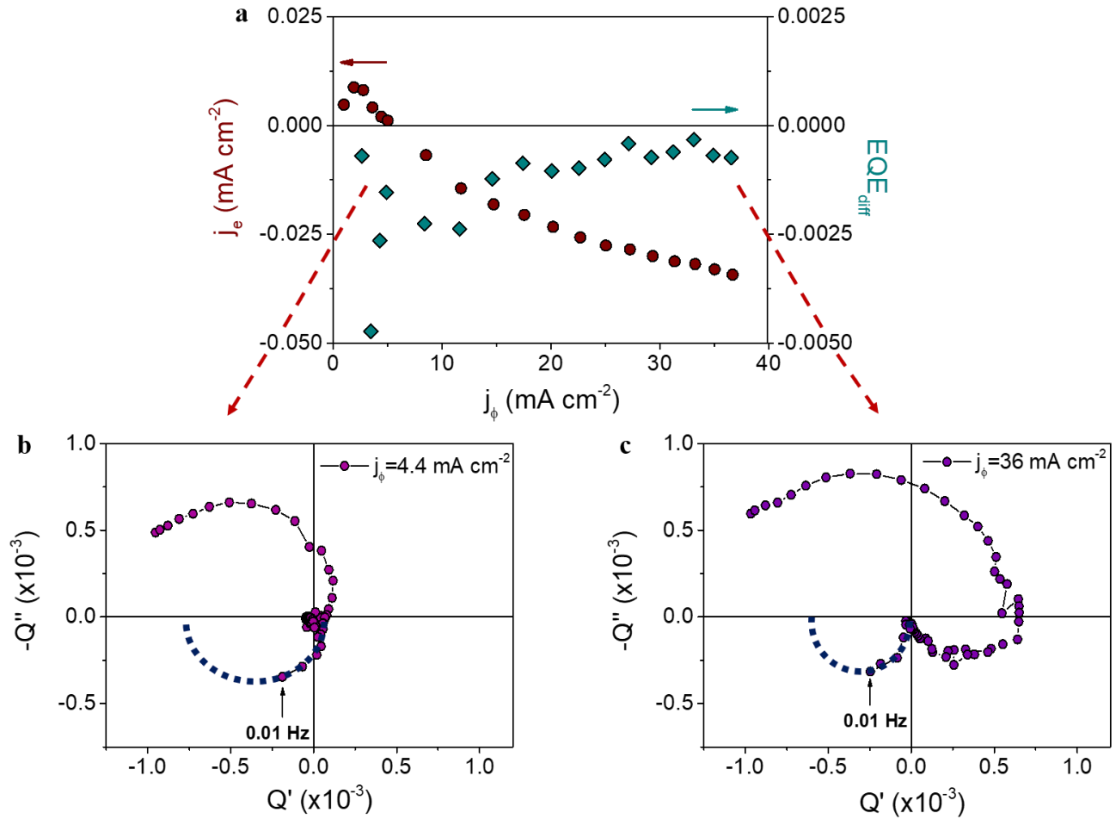

Figure 3. a Extracted photocurrent measured at -0.05 V vs RHE and EQE_{diff} calculated from the slope of steady-state values as function of the illumination intensity; **b** and **c** Q complex representation recorded under 4.4 mA cm^{-2} and 36 mA cm^{-2} photon current density, respectively, showing the tendency to negative values of the real part of Q at low frequency. We have included an extrapolation of the last arc to estimate the value of $Q(0)$.

The results discussed so far provide a general opto-electrical method of investigation of PEC cells that can yield a rich amount of information regarding its operation. The evolution of the steady state photocurrent with light intensity can provide direct intuition regarding specific recombination mechanisms, such as changes in ideality factors, trapping effects and injection barriers. For example, an EQE_{diff} value of 0 at voltages close to OCP as seen in Figure 1b (0.25 V vs RHE) indicates an invariant value of photocurrent for different light intensities, indicating that LSV measurements at different light intensities will converge to the same or very similar OCP value. This can indicate the occurrence of Fermi level pinning in the BVO_4 (as has been suggested from IS measurements in ref. [29]), where the applied potential is absorbed by a dipole at the interface, as has also been observed for crystal-deficient rutile TiO_2 nanowires[30]. For observations of a negative EQE_{diff} at voltages close to or beyond the OCP, it is likely that the applied light intensity promotes the filling of a local density of shallow traps around the electron Fermi level. This promotes recombination of the photogenerated holes with the trapped electrons which, coupled with the poor transport properties of the $BiVO_4$, creates a reduction in the extracted photocurrent. Finally, for large reverse biases, the shallow traps are filled with holes, allowing the photogenerated holes to be extracted efficiently and causing a rise in photocurrent with light intensity.[31] Detailed validation of these mechanisms related to the negative EQE_{diff} is currently in progress but beyond the

scope of the present Viewpoint.

In summary, we have experimentally demonstrated that the negative value of the real part of the transfer function observed in IMPS measurements is not a consequence of a current sign switching but indicating the change in the extracted photocurrent with a change in the incident photon flux intensity. We confirm this in $BiVO_4$ photoanodes by identifying a region beyond the OCP that shows a positive photocurrent while yielding a negative EQE_{diff} value. We also establish the study of photocurrent-light intensity spectra at different voltages as a powerful method to provide extra insight regarding specific mechanisms of operation such as trapping and recombination, and Fermi level pinning in PEC devices.

Associated content

Supporting Information

The Supporting Information is available free of charge at https://pubs.acs.org/doi/10.1021/acsenergylett.9b02555. Experimental details of photoelectrode preparation, as well as equipment and conditions used for photoelectrochemical measurements; table with differential quantum efficiency values extracted from IMPS and steady-state measurements (PDF).

Author information

Corresponding Authors
*E-mail: sjulia@uji.es (S.G.).
*E-mail: bisquert@uji.es (J.B.).

ORCID
Sandheep Ravishankar: 0000-0002-8118-0159
Sixto Gimenez: 0000-0002-4522-3174
Juan Bisquert: 0000-0003-4987-4887

Notes

Views expressed in this Viewpoint are those of the authors and not necessarily the views of the ACS.

The authors declare no competing financial interest.

Acknowledgments

We would like to acknowledge financial support from the Ministerio de Ciencia, Innovación y Universidades of Spain (ENE2017-85087-C3-1-R).

References

1. Ravishankar, S.; Riquelme, A.; Sarkar, S. K.; Garcia-Batlle, M.; Garcia-Belmonte, G.; Bisquert, J. Intensity-Modulated Photocurrent Spectroscopy and Its Application to Perovskite Solar Cells. *The Journal of Physical Chemistry C* **2019,** *123* (41), 24995-25014.
2. Schneider, I. A.; Bayer, M. H.; Wokaun, A.; Scherer, G. G. Negative Resistance Values in Locally Resolved Impedance Spectra of Polymer Electrolyte Fuel Cells. *ECS Transactions* **2009,** *25* (1), 937-948.
3. Mora-Seró, I.; Bisquert, J.; Fabregat-Santiago, F.; Garcia-Belmonte, G.; Zoppi, G.; Durose, K.; Proskuryakov, Y. Y.; Oja, I.; Belaidi, A.; Dittrich, T.; Tena-Zaera, R.; Katty, A.; Lévy-Clement, C.; Barrioz, V.; Irvine, S. J. C. Implications of the negative capacitance observed at forward bias in nanocomposite and polycrystalline solar cells. *Nano Letters* **2006,** *6*, 640-650.
4. Fabregat-Santiago, F.; Kulbak, M.; Zohar, A.; Vallés-Pelarda, M.; Hodes, G.; Cahen, D.; Mora-Seró, I. Deleterious Effect of Negative Capacitance on the Performance of Halide Perovskite Solar Cells. *ACS Energy Letters* **2017,** *2* (9), 2007-2013.
5. Guerrero, A.; Garcia-Belmonte, G.; Mora-Sero, I.; Bisquert, J.; Kang, Y. S.; Jacobsson, T. J.; Correa-Baena, J.-P.; Hagfeldt, A. Properties of Contact and Bulk Impedances in Hybrid Lead Halide Perovskite Solar Cells Including Inductive Loop Elements. *The Journal of Physical Chemistry C* **2016,** *120* (15), 8023-8032.
6. Moia, D.; Gelmetti, I.; Calado, P.; Fisher, W.; Stringer, M.; Game, O.; Hu, Y.; Docampo, P.; Lidzey, D.; Palomares, E.; Nelson, J.; Barnes, P. R. F. Ionic-to-electronic current amplification in hybrid perovskite solar cells: ionically gated transistor-interface circuit model explains hysteresis and impedance of mixed conducting devices. *Energy & Environmental Science* **2019,** *12* (4), 1296-1308.
7. Ebadi, F.; Taghavinia, N.; Mohammadpour, R.; Hagfeldt, A.; Tress, W. Origin of apparent light-enhanced and negative capacitance in perovskite solar cells. *Nature Communications* **2019,** *10* (1), 1574.
8. Ghahremanirad, E.; Bou, A.; Olyaee, S.; Bisquert, J. Inductive Loop in the Impedance Response of Perovskite Solar Cells Explained by Surface Polarization Model. *The Journal of Physical Chemistry Letters* **2017,** *8* (7), 1402-1406.
9. Klotz, D. Negative capacitance or inductive loop? – A general assessment of a common low frequency impedance feature. *Electrochemistry Communications* **2019,** *98*, 58-62.
10. Peter, L. M.; Wijayantha, K. G. U.; Tahir, A. A. Kinetics of light-driven oxygen evolution at α-Fe2O3 electrodes. *Faraday Discussions* **2012,** *155* (0), 309-322.
11. Dunn, H. K.; Feckl, J. M.; Müller, A.; Fattakhova-Rohlfing, D.; Morehead, S. G.; Roos, J.; Peter, L. M.; Scheu, C.; Bein, T. Tin doping speeds up hole transfer during light-driven water oxidation at hematite photoanodes. *Physical Chemistry Chemical Physics* **2014,** *16* (44), 24610-24620.
12. Thorne, J. E.; Jang, J.-W.; Liu, E. Y.; Wang, D. Understanding the origin of photoelectrode performance enhancement by probing surface kinetics. *Chemical Science* **2016,** *7* (5), 3347-3354.
13. Rodríguez-Pérez, M.; Rodríguez-Gutiérrez, I.; Vega-Poot, A.; García-Rodríguez, R.; Rodríguez-Gattorno, G.; Oskam, G. Charge transfer and recombination kinetics at WO3 for photoelectrochemical water oxidation. *Electrochimica Acta* **2017,** *258*, 900-908.
14. Thorne, J. E.; Zhao, Y.; He, D.; Fan, S.; Vanka, S.; Mi, Z.; Wang, D. Understanding the role of co-catalysts on silicon photocathodes using intensity modulated

photocurrent spectroscopy. *Physical Chemistry Chemical Physics* **2017,** *19* (43), 29653-29659.
15. Zachäus, C.; Abdi, F. F.; Peter, L. M.; van de Krol, R. Photocurrent of BiVO4 is limited by surface recombination, not surface catalysis. *Chemical Science* **2017,** *8* (5), 3712-3719.
16. Liu, Y.; Le Formal, F.; Boudoire, F.; Yao, L.; Sivula, K.; Guijarro, N. Insights into the interfacial carrier behaviour of copper ferrite ($CuFe_2O_4$) photoanodes for solar water oxidation. *Journal of Materials Chemistry A* **2019,** *7* (4), 1669-1677.
17. Rodríguez-Gutiérrez, I.; Djatoubai, E.; Rodríguez-Pérez, M.; Su, J.; Rodríguez-Gattorno, G.; Vayssieres, L.; Oskam, G. Photoelectrochemical water oxidation at FTO|WO_3@$CuWO_4$ and FTO|WO_3@$CuWO_4$|$BiVO_4$ heterojunction systems: An IMPS analysis. *Electrochimica Acta* **2019,** *308*, 317-327.
18. García-Tecedor, M.; Cardenas-Morcoso, D.; Fernández-Climent, R.; Giménez, S. The Role of Underlayers and Overlayers in Thin Film $BiVO_4$ Photoanodes for Solar Water Splitting. *Advanced Materials Interfaces* **2019,** *6* (15), 1900299.
19. Kim, J. H.; Lee, J. S. Elaborately Modified $BiVO_4$ Photoanodes for Solar Water Splitting. *Advanced Materials* **2019,** *31* (20), 1806938.
20. Tayebi, M.; Lee, B.-K. Recent advances in $BiVO_4$ semiconductor materials for hydrogen production using photoelectrochemical water splitting. *Renewable and Sustainable Energy Reviews* **2019,** *111*, 332-343.
21. Zhong, D. K.; Choi, S.; Gamelin, D. R. Near-Complete Suppression of Surface Recombination in Solar Photoelectrolysis by "Co-Pi" Catalyst-Modified W:$BiVO_4$. *Journal of the American Chemical Society* **2011,** *133* (45), 18370-18377.
22. Nellist, M. R.; Qiu, J.; Laskowski, F. A. L.; Toma, F. M.; Boettcher, S. W. Potential-Sensing Electrochemical AFM Shows CoPi as a Hole Collector and Oxygen Evolution Catalyst on $BiVO_4$ Water-Splitting Photoanodes. *ACS Energy Letters* **2018,** *3* (9), 2286-2291.
23. Antuch, M.; Millet, P.; Iwase, A.; Kudo, A. The role of surface states during photocurrent switching: Intensity modulated photocurrent spectroscopy analysis of BiVO4 photoelectrodes. *Applied Catalysis B: Environmental* **2018,** *237*, 401-408.
24. Rodríguez-Gutiérrez, I.; García-Rodríguez, R.; Rodríguez-Pérez, M.; Vega-Poot, A.; Rodríguez Gattorno, G.; Parkinson, B. A.; Oskam, G. Charge Transfer and Recombination Dynamics at Inkjet-Printed $CuBi_2O_4$ Electrodes for Photoelectrochemical Water Splitting. *The Journal of Physical Chemistry C* **2018,** *122* (48), 27169-27179.
25. Miethe, J. F.; Lübkemann, F.; Poppe, J.; Steinbach, F.; Dorfs, D.; Bigall, N. C. Spectroelectrochemical Investigation of the Charge Carrier Kinetics of Gold-Decorated Cadmium Chalcogenide Nanorods. *ChemElectroChem* **2018,** *5* (1), 175-186.
26. Bertoluzzi, L.; Bisquert, J. Investigating the Consistency of Models for Water Splitting Systems by Light and Voltage Modulated Techniques. *The Journal of Physical Chemistry Letters* **2017,** *8* (1), 172-180.
27. Klotz, D.; Ellis, D. S.; Dotan, H.; Rothschild, A. Empirical in operando analysis of the charge carrier dynamics in hematite photoanodes by PEIS, IMPS and IMVS. *Physical Chemistry Chemical Physics* **2016,** *18* (34), 23438-23457.
28. Ravishankar, S.; Aranda, C.; Boix, P. P.; Anta, J. A.; Bisquert, J.; Garcia-Belmonte, G. Effects of Frequency Dependence of the External Quantum Efficiency of Perovskite Solar Cells. *The Journal of Physical Chemistry Letters* **2018,** *9* (11), 3099-3104.
29. Trześniewski, B. J.; Digdaya, I. A.; Nagaki, T.; Ravishankar, S.; Herraiz-Cardona, I.; Vermaas, D. A.; Longo, A.; Gimenez, S.; Smith, W. A. Near-complete suppression of

surface losses and total internal quantum efficiency in $BiVO_4$ photoanodes. *Energy & Environmental Science* **2017,** *10* (6), 1517-1529.
30. Zhang, K.; Ravishankar, S.; Ma, M.; Veerappan, G.; Bisquert, J.; Fabregat-Santiago, F.; Park, J. H. Overcoming Charge Collection Limitation at Solid/Liquid Interface by a Controllable Crystal Deficient Overlayer. *Advanced Energy Materials* **2017,** *7* (3), 1600923.
31. Kelly, J. J.; Memming, R. The Influence of Surface Recombination and Trapping on the Cathodic Photocurrent at p-Type III-V Electrodes. *Journal of The Electrochemical Society* **1982,** *129* (4), 730-738.

5.3 Supporting Information

Supporting Information for

Intensity Modulated Photocurrent Spectroscopy for solar energy conversion devices. What does negative value mean?

Drialys Cardenas-Morcoso, Agustín Bou, Sandheep Ravishankar, Miguel García-Tecedor, Sixto Gimenez*, Juan Bisquert*

Institute of Advanced Materials (INAM), Universitat Jaume I, 12071 Castelló, Spain Address.

***Email:** sjulia@uji.es, bisquert@uji.es

Experimental details:

$BiVO_4$ photoelectrodes synthesis

$BiVO_4$ photoanodes were prepared by a two-step method previously reported in Ref.[1], consisting in the electrodeposition on fluorine doped tin oxide (FTO) coated glass of metallic Bi from a Bi^{3+} plating bath (20 mM $Bi(NO_3)_3 \cdot 5H_2O$ (Sigma-Aldrich) in ethylene glycol), followed by deposition by drop casting of $VO(acac)_2$ (Sigma-Aldrich) in DMSO as vanadium precursor. The electrodeposition was carried out by passing a total charge of 0.32 C cm^{-2}. The samples were annealed at 500ºC for 2h and finally, the electrode was cleaned by soaking in a 1M NaOH solution for 30 min under vigorous stirring.

Photoelectrochemical measurements:

The photoelectrochemical measurements was performed on a three-electrode cell connected to a Autolab Potentiostat/Galvanostat PGSTAT302; were the $BiVO_4$/FTO was the working electrode, an Ag/AgCl in 3 M KCl electrode and a Pt wire were used as reference and counter electrode respectively, and a 0.1 M potassium phosphate buffer at pH 7.5 was used as electrolyte. The applied potentials were referred to the Reversible Hydrogen Electrode (RHE) using the Nernst equation: $V_{RHE} = V_{Ag/AgCl} + V^0_{Ag/AgCl} + 0.059 \cdot pH$. For measurements with constant and modulated illumination, a monochromatic LED (λ=470 nm) from Philips LUMILEDS and controlled by a LED driver module coupled to the potentiostat, was used. The extracted photocurrent, j_e, was recorded from chronopotentiometry measurements for 60 seconds for each dc light illumination, j_ϕ. For light intensities below 10 mA cm^{-2}, the measurement was extended to 120 s. A Si photodiode was used to calibrate the range of dc light intensities, as well as the ac perturbation for modulated measurements, which in all cases was the 10% of the dc light intensity. IMPS measurements were carried out between 20 kHz and 0.01 Hz.

Table S1. EQE_{diff} values extracted from IMPS measurements at -0.05 V vs RHE and from the slope of steady-state values at the same voltage.

j_ϕ	**4.4 mA cm^{-2}**	**36 mA cm^{-2}**
$EQE_{diff\text{-}IMPS}$	-0.00075	-0.00065
EQE_{diff}	-0.0015	-0.00073

References

1. Safshekan, S.; Herraiz-Cardona, I.; Cardenas-Morcoso, D.; Ojani, R.; Haro, M.; Gimenez, S. Solar Energy Storage by a Heterostructured $BiVO_4$–PbO_x Photocapacitive Device. *ACS Energy Letters* **2017,** *2* (2), 469-475.

Chapter 6: Publication 3

"An Integrated Photoanode Based on Non-Critical Raw Materials for Robust Solar Water Splitting."

Cardenas-Morcoso, D., García Tecedor, M., Merdzhanova, T., Smirnov, V., Finger, F., Kaiser, B., Jaegermann, W., Gimenez, S.*

Submitted

6.1 Candidate's contribution.

Nature of contribution:	Extent of contribution:
• Design and preparation of the PV-EC device. • Execution of morphological, structural and compositional characterizations. • Execution of photo- and electrochemical measurements. • Analysis of results. • Preparation of figures. • Writing of the manuscript	80%

6.2 Submitted manuscript.

An Integrated Photoanode Based on Non-Critical Raw Materials for Robust Solar Water Splitting

Drialys Cardenas-Morcoso,[a] Miguel García Tecedor,[a] Tsvetelina Merdzhanova,[b] Vladimir Smirnov,[b] Friedhelm Finger,[b] Bernhard Kaiser,[c] Wolfram Jaegermann,[c] Sixto Gimenez[a*]

[a] *Institute of Advanced Materials (INAM), Universitat Jaume I, Avenida de Vicent Sos Baynat, s/n, 12006 Castelló de la Plana, Castellón, Spain.*
[b] *IEK-5 Photovoltaik, Forschungszentrum Jülich, Jülich, 52425, Germany.*
[c] *Institute of Materials Science, TU Darmstadt, Darmstadt, 64287, Germany.*

[*]**Email:** sjulia@uji.es

Abstract

Herein, we have developed an integrated photoanode for solar water splitting based on an "Earth-abundant" Ni-Fe based electrocatalyst combined with a versatile multijunction Si-based photovoltaic device, designed in such a way to allow a direct coupling with the electrocatalyst with minimal losses. The water oxidation catalyst was prepared by electrochemical deposition of iron on a nickel foil, followed by thermal annealing, leading to the formation of NiO, α-Fe_2O_3, and $NiFe_2O_4$ phases. Detailed structural and surface characterization revealed the effect of the addition of different Fe contents and the subsequent implications on the electrocatalytic performance. The optimized integrated photoanode delivered a maximum photocurrent density of 6.2 mA cm^{-2} at 0 V applied bias, which corresponds to a 7.7 % of Solar-To-Hydrogen conversion efficiency, which remained stable for more than 20 hours. These results pave the way towards large-scale, efficient and low-cost solar energy conversion solutions based on non-critical raw materials

Table of Content

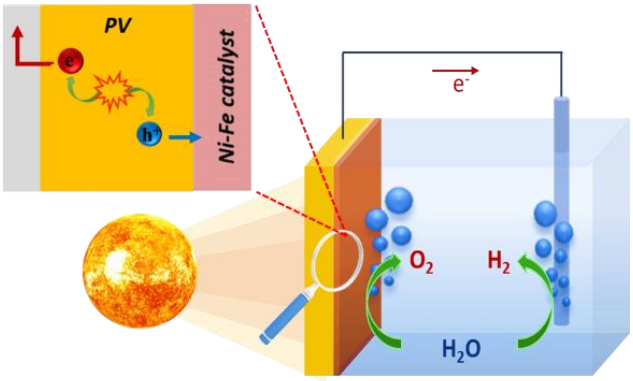

Introduction

The development of sustainable, fossil-free strategies to synthesize fuels and added-value chemicals has raised enormous interest in the last years, in order to provide reliable energy vectors as well as the feedstocks needed for the chemical industry at a global scale.[1-3] One of the most promising alternatives involves the use of renewable electricity (wind, solar, hydropower, etc…) to power electrochemical conversion processes, which convert abundant molecules (e.g., water, carbon dioxide, and nitrogen) into higher-value products (e.g., hydrogen, hydrocarbons, oxygenates, and ammonia). In all these processes, water oxidation stands out as the preferred reaction to provide the protons and electrons needed for the target reduction reactions, although this process is considered a kinetic bottleneck and consequently, the development of electrocatalytic materials that effectively oxidise water is essential for improving the efficiency of the overall electrochemical conversion process.[4]

Currently, the most efficient water oxidation catalysts are based on scarce and excessively expensive materials as iridium and ruthenium oxides, IrO_2 and RuO_2.[5-6] Consequently, an intensive search for catalytic materials based on earth-abundant elements and low-cost synthetic processes has been carried out in order to find sustainable and cost-effective alternatives to minimize the use of these critical raw materials. Among them, Ni-based catalysts constitute one of the best alternatives due to their high electrocatalytic activity and stability under alkaline conditions, as a consequence of their high electrical conductivity and corrosion resistance.[7-8] Indeed, large scale commercial alkaline electrolyzers, preferentially use nickel-based anodes.[9-10] Furthermore, several Oxygen Evolution Reaction (OER) electrocatalysts, which combine Ni with other transition metals exhibit low overpotentials and high stability under alkaline conditions.[11-12] Specifically, Ni-Fe alloys have been reported as synergistic catalysts towards OER, significantly more active compared to the individual Ni or Fe components.[13] In this context, the beneficial interaction between Fe and Ni towards water oxidation was firstly observed by the unintentional incorporation of Fe into the structure of the Ni-based materials during electrochemical testing.[14] Once this effect was reported, several studies focused on understanding the catalytic role of Fe ions incorporated by several methods, particularly on Ni/Fe oxides and oxyhydroxides,[15-19] becoming a controversial topic among the scientific community in the recent years. At present, there are basically two different views about the role of Fe ions on Ni-based catalysts: some authors claim that Fe atoms provide true active sites for catalysis of the OER,[15] while others support that Fe ions synergistically enhance the catalytic activity of Ni.[14, 19-20]

A further step towards the exploitation of efficient water oxidation catalysts (WOC) involves their integration in more complex energy conversion devices fed by renewable electricity, in order to minimize the balance of system components, which is essential for large scale applications.[21] The paradigmatic example of robust and cost-effective 'bias-free' photoelectrochemical water splitting devices resulting from the combination of different WOC with thin film photo-absorbers, stands out as a promising strategy for conversion of solar energy into chemical energy, stored in solar fuels or added-value chemicals.[22-23] This approach is based on an adapted photovoltaic device providing the electricity input as photogenerated charge carries, which are transferred to the electrocatalyst, to drive the water oxidation reaction. Indeed, similar configurations can be employed for other more complex electrochemical reactions leading to the production of added value chemicals such as hydrogen peroxide (H_2O_2), hypochlorous acid (HClO), persulfates ($H_2S_2O_8$), IO_4^-, Ce^{4+}, hydrocarbons and oxygenates.[3, 24] Consequently, several

approaches of photo- and electrocatalyst/photovoltaic devices combinations have been designed and tested, demonstrating that photovoltaic-electrocatalyst (PV-EC) integrated systems lead to higher Solar-To-Fuel (STF) efficiencies, compared to their photoelectrochemical (PEC) counterparts based on photoactive electrodes, where the photovoltage is generated at the semiconductor-liquid junction (SCLJ).[25]

From the technological point of view, integrated architectures where the photovoltaic cell and the electrocatalyst are intimately, connected offer a compact and less complex design for realization of an "artificial leaf" for practical solar fuel production.[26-27] The highest reported efficiencies in PV-EC systems have been achieved with scarce and expensive materials as GaInP and GaAs as photo-absorbers, and noble metal based oxides as IrO_x or RuO_x for the electrocatalyst.[1, 27-28] However, the use of critical raw materials jeopardizes the future technological deployment of this technology and consequently, the use of Earth-abundant and low-cost materials is imperative for further development of these systems. In this context, silicon thin films, particularly as multijunction architectures, are at the forefront of photovoltaic technologies with application in the production of solar hydrogen.[22, 29-31] In particular, record Solar-To-Hydrogen (STH) efficiencies of 10% using crystalline silicon photovoltaic[26] and 14% with silicon heterojunction cells,[32] have been reported. More recently, some of us developed triple and quadruple junction solar cells based on amorphous (*a-Si:H*) and microcrystalline (*μc-Si:H*) silicon thin films, providing higher STH efficiencies, up to 9.5%, with an integrated photocathode using the *a-Si:H/a-Si:H/μc-Si:H* triple junction as photo-absorber.[33] One of the major advantages of these systems consists of the versatility to power any electrochemical reaction, since the delivered photovoltage can be conveniently tuned by adjusting the solar cell layers stack, providing higher flexibility to choose the electrocatalytic systems depending on the overpotential requirements. [30, 33] On the other hand, stability issues remain a key parameter when considering up-scaling of integrated PV-EC devices, which in several cases is limited to few hours.[34] As solid-liquid junction type devices, integrated PV-EC electrodes require tailored strategies to prevent performance losses, mostly induced by the partial dissolution of the photovoltaic component layers. Those strategies include the encapsulation of the electrode and the use of conductive materials acting as a barrier between the PV component and the electrocatalyst. [13, 20] On the other hand, PV-EC integration as photoanodes is a rarely explored application of multijunction silicon thin-film solar cells. The main reason is the conventional architecture of the Si solar cells, where the hole selective contact is placed ed at the bottom of the device, limiting the connection of the electrocatalyst to the external wiring.

In the present study, we have designed and fabricated an integrated PV-EC photoanode from an Earth-abundant water oxidation electrocatalyst and a multijunction Silicon thin-film solar cell. A mixed Ni-Fe oxide electrocatalyst was prepared by a simple method based on direct electrochemical deposition of Fe on the surface of a Ni foil, followed by thermal annealing. The resulting electrocatalyst shows enhanced performance compared to the reference nickel oxide, decreasing the overpotential by more than 50 mV. Furthermore, we have explored the integration of the electrocatalyst on two different PV devices such as thin-film silicon triple-junction solar cell and a solar module based on two tandem junction solar cells connected in series. The PV-EC integration was possible due to the flexible design of the photovoltaic component, were both front and back contacts are placed at the top side of the device. The optimized configuration provided bias-free water splitting with a 7.7 % STH efficiency, stable for more than 20 hours.

Experimental methods

Preparation of Ni-Fe based electrocatalyst: Prior to deposition, a nickel sheet (99.2% purity, from Metall Jobst, Germany) used as substrate was cut into 1.5 × 1.5 cm^2 samples, which were first cleaned by ultrasonicating in acetone (AnalaR NORMAPUR) for 30 min, followed by rinsing with deionized water (Millipore), and then in 3M HCl solution prepared from HCl (25%, Emsure) and deionized water. Finally, the samples were rinsed with deionized water and ethanol (GPR rectapur, 99.5% denaturated with 1% MEK) and dried with compressed air. The overall process for the synthesis of the electrocatalyst is showed in **Supporting Information, Figure SI1**. Fe incorporation on the Ni samples was carried out by electrodeposition from a 20 mM $FeCl_2 \cdot 4H_2O$ (Emsure) solution using dimethyl sulfoxide, (DMSO) as solvent, by applying a constant potential of -2 V vs Ag/AgCl with a Gamry Instruments Reference 600 potentiostat, in a three-electrode cell configuration. An Ag/AgCl (3M KCl) electrode and a Pt mesh were used as reference and counter electrode, respectively. The total deposited charge was varied as 2, 5, 12, 25 and 36 mC cm^{-2}, on a geometrical area of 0.5 cm^{-2}, defined by an O-ring sealing aperture. After Fe deposition, the samples were rinsed with ethanol to remove the solvent and dried with compressed air. Finally, the substrates were annealed at 450^{o}C for 1h in air atmosphere, with a heating rate of 2^{o}C /min, to promote the conversion of Fe^0 to Fe^{3+}.

Morphological characterization and chemical composition of the Ni-Fe electrocatalyst: Field Emission Scanning Electron Microscopy (SEM) performed with a JSM-7000F JEOL FEG-SEM system (Tokyo, Japan) equipped with an INCA 400 Oxford EDS analyzer (Oxford, U.K.) and operating at 15 kV, was used for the morphological characterization of the samples. Their crystalline structure was assessed by X-ray diffraction (XRD) collected on a Rigaku Miniflex 600, (Rigaku corporation, Tokyo, Japan) with copper K_α radiation (λ = 1.5418 Å) operating at a grazing incidence of 1º, at a scan rate of $3° \cdot min^{-1}$. The chemical composition of the resulting electrocatalytic electrodes was investigated by Confocal Multi-Spectral Imaging (CMSI) Raman Spectroscopy and X-ray Photoelectron Spectroscopy (XPS). CMSI Raman spectroscopy was carried out with a WiTec *apyron* system, equipped with a 300 mm focal length UHTS 300 spectrometer system. Measurements were performed with an excitation wavelength of 532.165 nm and 24.737 mW laser power. Raman imaging was obtained from the simultaneous treatment of Raman spectra recorded every 0.5 μm in a selected area (28 x 30 μm^2) of the sample surface. The software is able to transform the multispectral maps into images, showing the heterogeneity of the surface composition. The data were analyzed with the WiTec software Project FIVE. XPS measurements were performed in the Daisy-Fun laboratory, at a pressure of 5 × 10^{-10} mbar using a Specs Phoibos 150 setup.[35] A monochromatized Al Kα line of 1486.64 eV was used as X-ray excitation source. Survey measurements were obtained with a pass energy of 20 eV, while all detailed spectra were measured with a pass energy of 10 eV. The obtained data were evaluated using the CasaXPS software package.

Electrochemical characterization of the electrocatalysts: Linear sweep voltammetry (LSV) and cyclic voltammetry (CV) were performed with a Gamry Instruments Reference 600 potentiostat, at 10 mV/s^{-1} scan rate, in a three-electrode configuration cell, using a Pt mesh as counter electrode, and an Ag/AgCl (3M KCl) electrode as reference. A 1M KOH solution at pH 13.6 was used as electrolyte. The potentials were referred to the Reversible Hydrogen Electrode (RHE) through the Nernst equation: $V_{RHE} =$

$V_{Ag/AgCl} + V^0_{Ag/AgCl} + 0.059 \cdot pH$. Measurements in two-electrode configurations were also performed for further calculations in combination with the photovoltaic devices. The electrode/electrolyte contact area was defined as 0.5 cm^2 by an O-ring sealing aperture. The turnover frequency (TOF) was calculated as: $TOF = \frac{j_{geo}}{nq}$, where j_{geo} is the geometrical current density at an overpotential of 350 mV (selected for comparison), n is the number of electrons transferred during the reaction (for water oxidation, $n = 4$), and q is the integrated area under the cathodic redox wave, divided by the scan rate. The O_2 evolution at the electrocatalyst surface was determined by gas chromatography measurements using a sealed cell coupled to an Agilent Micro-GC gas chromatograph, during a chronoamperometric measurement at 1.6 V vs RHE, in 1M KOH solution. The faradaic efficiency (FE) was estimated through the relation: $FE\ (\%) = \frac{O_2\ (exp)}{O_2(theo)} \cdot 100$, were $O_2\ (exp)$ is the amount of evolved O_2 in mol, monitored every 5 min, and $O_2(theo)$ is the theoretical O_2 evolution calculated with the Faraday´s Law: $n\ (mol) = \frac{j_{O2}\ t}{nF}$, where j_{O2} is the current density recorded in the chronoamperometry measurement, t is the time in seconds, n is the number of electrons transferred in the reaction and F is the Faraday constant, 96 485.33 C mol^{-1}.

Preparation and characterization of Si-based multijunction photovoltaic devices: In this work two types of PV devices were investigated in terms of their potential application as integrated photoanodes for solar water splitting. The first device is a solar cell based on *a-Si:H/a-Si:H/µc-SiH* triple junction prepared on fluorine-doped tin oxide (F:SnO_2) coated glass substrates that serves as a front contact The (p-i-n) *a-Si:H* top and middle sub-cells and (p-i-n) *µc-Si:H* bottom sub-cell were deposited by a Plasma Enhanced Chemical Vapor Deposition (PECVD) technique at excitation frequency of 13.56 MHz and substrate temperature of about 180°C. The intrinsic absorber layers were prepared with a mixture of silane (SiH_4) and hydrogen (H_2) gases. The n- and p-type layers, were prepared using phosphine (PH_3), trimethylborane (TMB) and methane (CH_4) gases, added to the silane-hydrogen mixture. A zinc oxide/silver (ZnO:Al/Ag) reflecting layer was sputtered as a back contact. The size of the solar cell is defined from the metal contact area of 1cm^2. Laser scribing process was used to prepare the solar cell in a design where the front and back contacts were placed outside of the 'photo-active area', at the top sides of the device, which allows an easy coupling with the electrocatalyst. The second device is a solar module consisting of two *a-Si:H/µc-Si:H* tandem solar cells connected in series via laser scribing. Detailed description of the laser scribing process is given elsewhere.[36] In order to simplify the reference to the PV devices along the text, the *a-Si:H/a-Si:H/uc-Si:H* triple junction solar cell and the module of two *a-Si:H/uc-Si:H* tandem cells connected in series will be referred as "PV-1" and "PV-2", respectively.

The solar cells and modules were characterized by current -voltage measurements at standard test conditions (100 mW cm^{-2}, 25°C) using a double source (Class A) AM 1.5G sun simulator. The spectral response measurements to determine the external quantum efficiency (EQE), were conducted using a monochromator at a wavelength range between 300 nm and 1100 nm.

Photoelectrochemical characterization of the integrated PV-EC photoanode: In the integrated PV-EC device, the Ni foil used as substrate for catalyst deposition, was mechanically attached to the "p-side" (or "front-contact") of the photovoltaic component, also acting as protective barrier against corrosion. Kapton tape was used for additional

protection of the device against possible contact with the electrolyte during the cell assembly. The contribution of the contact resistance on the device performance was found negligible, as evidenced in the unaltered open circuit potential and extracted photocurrent of the integrated device. Linear sweep voltammetry (LSV) and chronoamperometric measurements were recorded with a Gamry Instruments potentiostat, in a two-electrode configuration cell, with a Pt mesh as counter electrode. A 1M KOH solution was used as electrolyte. The electrode-electrolyte contact area was defined by an O-ring sealing aperture of 0.5 cm^2. Measurements under illumination conditions were carried out using simulated AM 1.5 solar illumination (100 mW cm^{-2}), provided by an Oriel LCS-100 solar simulator.

Results and discussion

Ni-Fe based water oxidation electrocatalyst: The Ni-Fe based water oxidation electrocatalyst was prepared by electrodeposition of metallic Fe on previously cleaned Ni foil surface, followed by thermal annealing for conversion of Fe^0 to Fe^{3+}. We previously showed that electrochemical deposition of Fe under specific conditions led to the formation of catalytically active α-Fe_2O_3 nanoparticles on the surface of water splitting photoanode.[37] Although α-Fe_2O_3 has been widely studied as a water oxidation photoanode, [38-42] it has been suggested that electrodeposited α-Fe_2O_3 particles provide cooperative electrocatalytic behaviour on $BiVO_4$ photoanodes for water oxidation.[37] Consequently, we have explored the electrocatalytic activity of Ni-Fe based materials, using a Ni foil as conductive substrate. Three different deposition charges of Fe were tested: 5, 12 and 25 mC·cm-2, corresponding to 0.49, 1.06 and 6.27 at-% of Fe detected by EDS analysis on Ni foil (Supporting Information, **Figure SI2** and **Table SI1**). Additionally, 36 mC·cm-2 of Fe charge (14.65 at-%) was used to prepare α-Fe_2O_3 thin films, as reported earlier[37, 40] After thermal annealing at 450ºC, according to the Fe-O,[43] and Ni-O[44] phase diagrams, it is expected that phase transition from metallic iron to iron (III) oxide takes place, concomitant to phase transition on the Ni foil surface, due to the formation of nickel oxide (II) above 400ºC.[45] Furthermore, the formation of the $FeNi_3$ intermetallic phase is expected at temperatures higher than 200 ºC according to the Ni-Fe phase diagram.[46] This $FeNi_3$ can react with oxygen according to the reaction $4FeNi_3 + 9O_2 \rightarrow 2NiFe_2O_4 + 10NiO$,[47] after the subsequent increase of the temperature. A reference Ni foil sample thermally treated in the same conditions was used for comparison with the Fe-containing samples.

In order to evaluate the electrocatalytic behaviour of the prepared materials for water oxidation, cyclic voltammetry measurements in a 1M KOH electrolyte were performed. **Figure 1a** summarizes the evolution of catalytic performance versus Fe content. This performance is expressed as the overpotential (η, mV) required for water oxidation and the turnover frequency (TOF) at 400 mV overpotential, versus the Fe content in **Figure 1b**. The optimal performance was obtained at a Fe content of 1.06 at-%, (corresponding to 12 mC cm^{-2} load) with a reduction of the overpotential of about 50 mV, as compared to the reference Ni foil (after annealing), as showed in Figure 1b. Moreover, the calculated TOF value, which is related to the amount of oxygen evolved per mole of the catalyst per second, also shows to be strongly dependent on the Fe content, reaching the highest value (0.5 s^{-1}) at 1.06 at-%. On the other hand, it is accepted that Ni-based electrocatalysts need an electrochemical activation process (several cyclic voltammetry scans) to maximize their catalytic activity towards water oxidation, since water from the electrolyte percolates within the structure of the catalyst introducing Fe impurities and increasing the exposed

surface area.[14] Consequently, electrochemical activation was carried out on both reference and record Ni-Fe sample for comparison. The cyclic voltammograms before and after electrochemical activation (50 cycles), at scan rate of 10 mV s^{-1}, are represented in **Figure 1c**. The observed anodic and cathodic peaks, A_1 and C_1 respectively, are associated to the α-$Ni(OH)_2$/γ-NiOOH transformation, while the secondary A_2 and C_2 peaks are related to the β-$Ni(OH)_2$/β-NiOOH conversion.[13, 48-49] The complete set of cyclic voltammograms is showed as **Supporting Information, Figure SI3**. Furthermore, the Faradaic efficiency for oxygen evolution was determined (blue diamonds) on the optimal electrocatalyst under operation from gas chromatography measurements (red circles) and catalytic current, (black line), see **Figure 1d**. The obtained values increased with time, reaching the 100% efficiency after 100 min of operation.

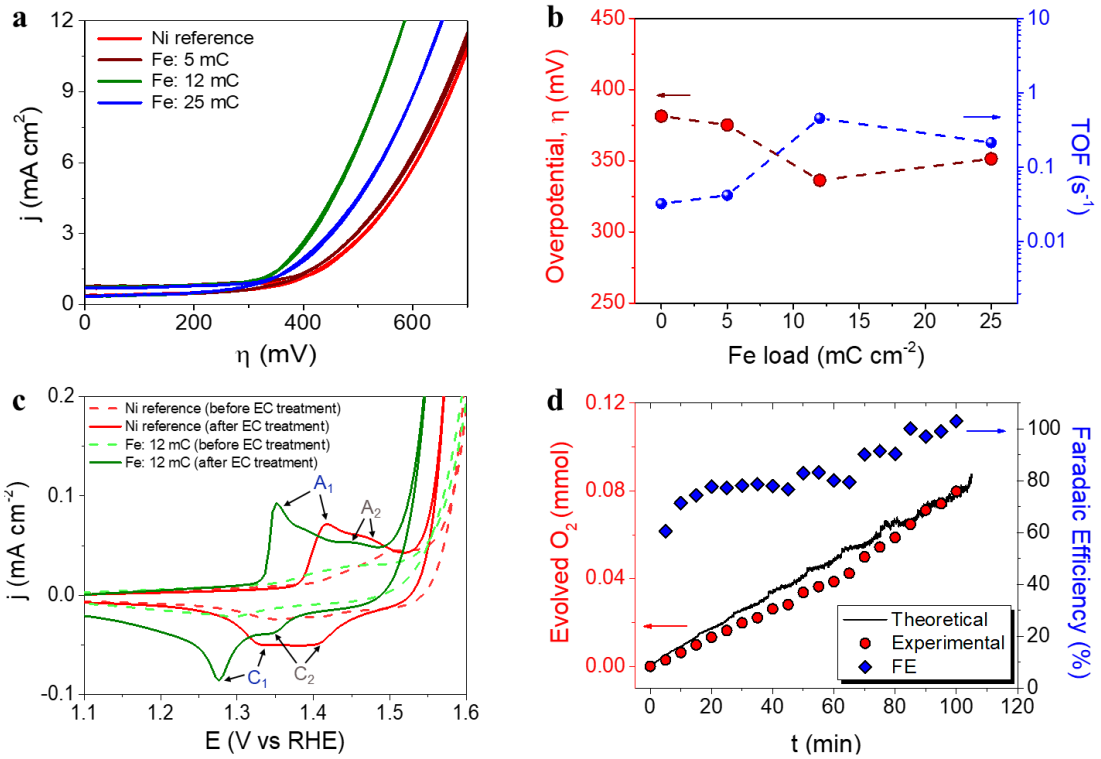

Figure 1. a. Cyclic voltammetry measurements, recorded with scan rate of 10 mV s^{-1}, for the different samples prepared with different electrodeposited Fe charges. **b.** Overpotential (η) for the water oxidation onset and turn-over frequency (TOF), calculated at an overpotential of 400 mV, as a function of the Fe content on the Ni-based electrocatalysts. **c**. Effect of electrochemical activation on reference Ni foil thermally treated and optimal Ni-Fe electrocatalyst before (dashed lines) and after (solid lines) electrochemical activation (50 cycles). **d.** Oxygen evolution measurement and Faradaic efficiency (FE), performed with the optimal Ni-Fe catalyst (Fe load: 12 mC cm^{-2} leading to 1.06 at-% Fe content) after activation at 1.6 V vs RHE.

To understand the observed electrocatalytic performance, we have combined structural and compositional characterization tools, to determine the structure and composition of the Ni-Fe electrocatalyst. First, morphological and structural characterization of the as-prepared samples was carried by SEM and XRD. **Figure 2a** shows the top-view of the reference Ni foil used as substrate, after thermal annealing. 1.06 at-% Fe content led to distributed clusters of particles (3-5 μm) at the surface (**Figures 2b** and **2c**). It is expected

that this dispersion will increase the surface density of catalytic active sites and subsequently, the electrocatalytic performance. EDS analysis at different locations reveals that Fe is mainly confined at these dispersed clusters, as shown in **Figure 2c** (see **Supporting Information, Figure SI4** for the EDS spectra). Then, it is expected that Ni-Fe active phases are formed in the vicinity of such clusters, providing a higher density of active sites for water oxidation. A detailed compilation of SEM micrographs at all the different Fe charges tested is showed as **Supporting Information Figure SI2.** From those images, the electrodeposited Fe charge clearly had a significant impact on the morphology of the samples. Furthermore, the highest Fe content (14.65 at-%), led to the formation of an iron oxide film covering the Ni foil surface, as showed in **Supporting Information, Figure SI2d**.

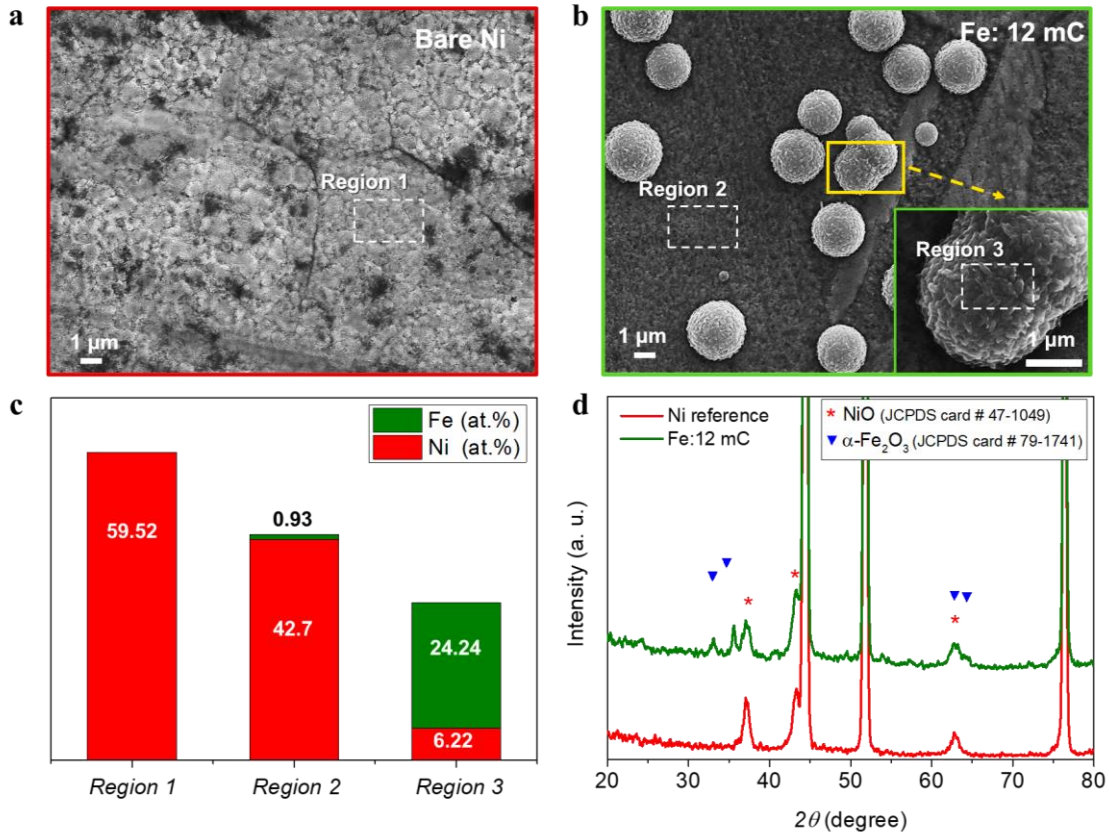

Figure 2. Surface morphological and structural characterization of Ni-based electrocatalyst by SEM and XRD: **a.** SEM image of reference Ni substrate after thermal annealing; **b.** SEM image of the Ni substrate with optimal Fe content (1.06 at-%), showing the clusters formed after Fe loading and thermal annealing; the inset shows a magnification of one of the Ni-Fe clusters. **c.** Bars chart with the atomic percentage (at.%) of nickel and iron at the different selected regions. **d.** X-ray diffractograms of reference Ni substrate, and Ni substrate with optimal Fe content (1.06 at-%). The reference peaks of NiO and α-Fe_2O_3 phases are included for comparison (symbols).

Figure 2d shows the X-ray diffractograms of the reference Ni substrate after thermal annealing and the Ni substrate with the optimal Fe content (1.06 at-%). Both diffractograms show sharp peaks at 2θ values of 44.52º, 51.88º and 76.4º (see **Supporting Information SI5**), which can be indexed as the (111), (200) and (220) planes of the face-centred cubic (fcc) nickel according to the JCPDS card number 04-0850. Both samples

show diffraction peaks at 37.08º, 43.28º and 62.72º, indexed as the (111), (200) and (220) planes of the fcc nickel (II) oxide, NiO, (JCPDS card number 47-1049). Furthermore, the diffractogram of the optimal Fe charge sample shows additional peaks at 33.04º, 35.64º, 63.12º and 64.36º corresponding to the (104), (110), (214) and (300) planes of the monoclinic structure of iron oxide, α-Fe_2O_3, (JCPDS card number 79-1741). Note that the position of the symbols conveys the relative intensity of the peaks in the reference patterns.

The chemical composition was further investigated through Confocal Multi-Spectral Imaging (CMSI) Raman spectroscopy and X-ray Photoelectron Spectroscopy (XPS). **Figure 3a** and **3b** show the chemical mapping and the Raman spectra of a selected area of the optimal Ni-Fe catalyst surface, where three different compositions were detected. The Raman spectrum of the component at the region *(i)* shows a sharp signal at 550 cm^{-1}, which can be assigned to the Ni-O stretching mode of the nickel (II) oxide, NiO.[50-51] The slight shift with respect to the characteristic value for this vibrational mode (~536 cm^{-1}) is attributed to different crystal orientations. The Raman spectrum in region *(ii)*, which is directly related to the clusters observed in **Figure 2b**, shows the characteristic phonon modes at 210 cm^{-1} (A_{1g}), 270 cm^{-1} (E_g) and less intense 380 cm^{-1} (E_g) and 580 cm^{-1} (E_g), corresponding to the metal-oxide vibrations of hematite, α-Fe_2O_3.[52-53] These observations are in excellent agreement with the SEM and EDS analyses discussed above, where it was found that the deposited Fe is preferably confined at the clusters. Finally, the Raman spectrum corresponding to the region *(iii)*, which is related to the interface between the Fe-rich aggregates and the nickel oxide on the substrate surface, shows the phonon modes at 200 cm^{-1} (F_{2g}), 290 cm^{-1} (E_g) and 460 cm^{-1} (F_{2g}), characteristic of oxygen atom bending in M−O bond at octahedral voids of the spinel $NiFe_2O_4$, and the band at 675 cm^{-1} (A_{1g}), related to a stretching mode of the oxygen atom with respect to metal−ion in the tetrahedral void, confirming the formation of the mixed oxide $NiFe_2O_4$.[54-55] The Raman spectrum of the Ni foil sample after the thermal treatment taken as reference is provided in **Supporting Information SI6**, showing a principal signal around 536 cm^{-1}, characteristic of the Ni-O stretching mode of the NiO phase.

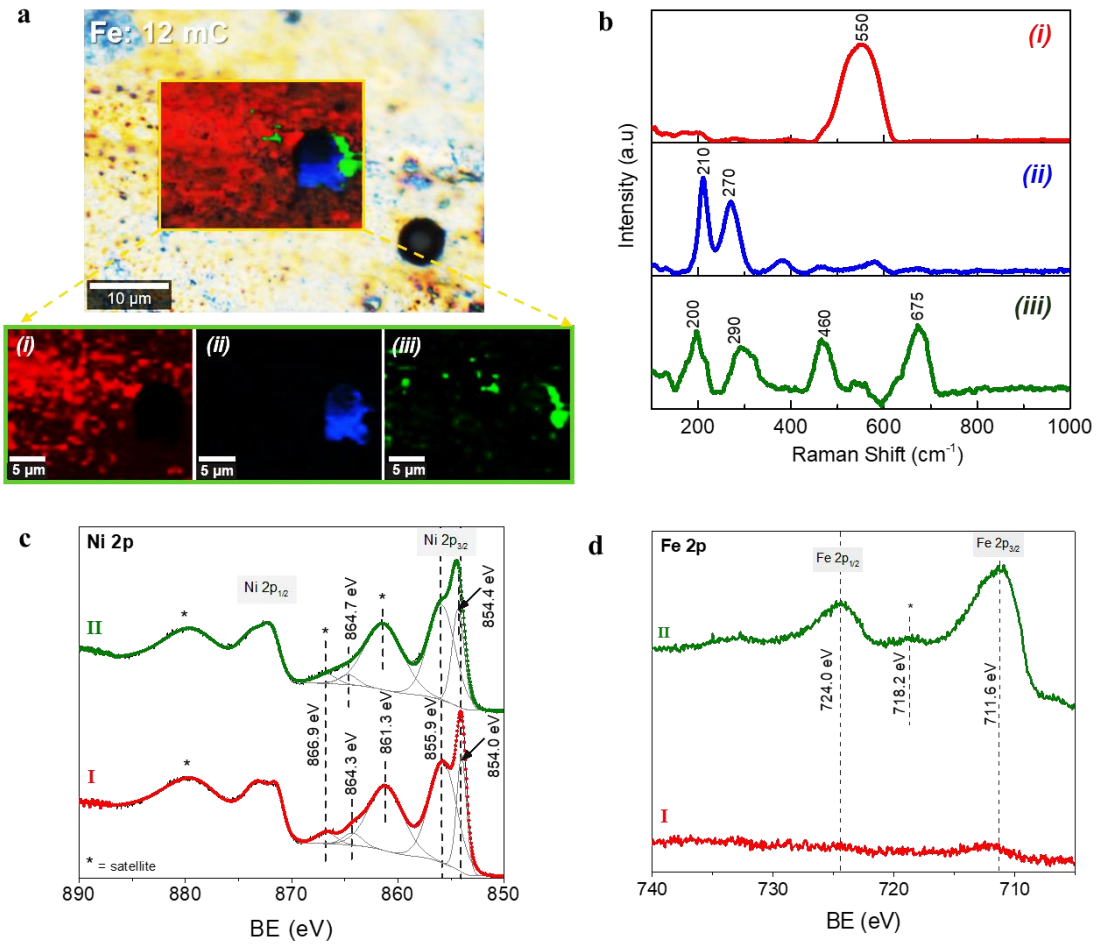

Figure 3. Compositional characterization of Ni-based electrocatalyst by Raman spectroscopy and XPS: **a.** Optical image of the of the Ni-Fe electrocatalyst with the optimal Fe content (1.06 at-%) surface; as an inset, the Confocal Multi-Spectral Imaging (CMSI) maps in a selected area and individual regions from the CMSI mapping, **b.** Raman shift spectra corresponding to the different regions from (**a.**). **c.** XPS Ni 2p spectra and **d.** XPS Fe 2p spectra of Ni reference (**I**) and optimal Ni-Fe electrocatalyst (**II**).

More detailed surface characterization was carried out by XPS analysis. It has been reported that Fe and Ni species with high spin in Ni-Fe phases lead to multiple splitting of the 2p signals, as well as peak asymmetries and overlapping of binding energies. Consequently, the identification of specific chemical states on oxides and hydroxide compounds of such elements is extremely challenging.[56-57] The Ni 2p signals of reference and optimal Ni-Fe samples (labeled as **I** and **II** respectively) are showed in **Figure 3c** and the survey spectra can be found in **Supporting Information SI7a**. After fitting the Ni $2p_{3/2}$ signal on each sample, the peak positions show the presence of Ni^{2+} as the dominant species at the surface of both materials. Comparing to specific literature related to identification of Ni and Fe compound through XPS, the Ni 2p spectra obtained here for reference and Fe loaded samples are characteristic fingerprints for NiO and $NiFe_2O_4$ respectively.[56-57] The Fe 2p spectrum of the optimal Ni-Fe catalyst, depicted in **Figure 3c**, shows the characteristic binding energies of Fe^{3+} species, confirming the successful conversion from metallic Fe during thermal annealing. As expected, no Fe-related signals were found on the reference Ni substrate. The O 2s signal also offers further information about the surface composition (see **Supporting Information SI7b**). The characteristic

peaks related to hydroxides and water (531.2 eV and 532.4 eV respectively) are clearly observed on the reference Ni sample, together with a peak at 529.6 eV, related to oxygen linked to a metal, particularly characteristic of Ni-O. Consequently, we can conclude that nickel (II) oxide, NiO, is the dominant phase at the surface of the reference Ni sample after thermal annealing, in perfect agreement with the SEM, XRD and CMSI analyses. On the other hand, after optimal Fe loading, an intense signal 530.2 eV relates to metal-oxygen bond, characteristic for α-Fe_2O_3, in excellent agreement with the information provided by XRD and Raman spectroscopy. The Ni-O related signal is still clearly visible but less intense. These results confirm the presence of mixed phases of Ni-Fe compounds in the optimal electrocatalyst, as showed in **Figure 3a**. The XPS-VB spectra are shown in **Supporting Information SI7c** for both samples. The spectrum of the reference Ni substrate also shows a higher energy emission at around 2 eV and a shoulder close to 3.5 eV related to Ni 3d states in NiO.[58] However, both features are shifted to higher binding energies at the Ni-Fe sample, while the shoulder is less defined, in good agreement with the features associated to $NiFe_2O_4$.[59] The position of the Fermi level is closer to the valence band maximum (VBM) for the reference Ni sample compared to the Ni-Fe sample, as shown in **Supporting Information SI7c**. The effect of the different Fe charges tested on the XPS spectra is illustrated as **Supporting Information, Figure SI8.** The Ni 2p signal reveals that only with the optimal 1.06 at-% Fe content, the formation of $NiFe_2O_4$ is favoured, and the Fe 2p signal clearly reflects the increase of Fe species at the electrode surface with the Fe load, concomitant to the decrease of the Ni signal. Furthermore, compared to the highest Fe content (14.65 at-%), (see **Supporting Information, Figure SI8**) the Ni 2p signal is negligible, since the surface is mainly covered by Fe species, (as shown in **Supporting Information, Figure SI2d**) and the density of exposed Ni sites is negligible. All the identified compounds: NiO, α-Fe_2O_3 and $NiFe_2O_4$, constitute efficient water oxidation electrocatalysts, and the best performance has been reported for α-Fe_2O_3 and $NiFe_2O_4$,[60-61] which nicely agrees with the functional characterization showed in **Figure 1**. NiO and $NiFe_2O_4$ have been reported as active water oxidation electrocatalysts,[11] after the subsequent CV treatment to develop (Ni, Fe)OOH as the active phase for OER.[62] On the other hand, the electrocatalytic activity of α-Fe_2O_3 towards OER has been reported for electrodeposited α-Fe_2O_3 nanoparticles.[37] Nonetheless, we observe that the activity of the optimal electrocatalyst prepared herein is moderate, compared to the state-of-the-art of Ni-Fe based materials studied as water oxidation catalysts.[63] Further optimization, including nanostructuring to increase the surface area and pre/post-synthetic treatments,[62, 64, 65] can be addressed to improve the electrocatalytic activity. However, such optimization is out of the scope of this study, since the final performance of the integrated device, for which the electrocatalyst is aimed, is limited by the photovoltaic component. Consequently, we have focused on the facile modification of the Ni foil used for both contact and protective barrier to the photovoltaic component, to reach a competitive electrocatalytic activity toward water oxidation, and high stability, with the integrated photoanode.

A relevant insight related to the effect of Fe content on the Ni foil surface stems from the redox peaks related to the reversible reaction $Ni(OH)_2 + OH^- \leftrightarrow NiOOH + H_2O + e$, characteristic of the Ni-based electrocatalysts.[66] It has already been reported that the accumulation of active sites, reflected on the size of the redox wave correlates to the catalytic activity.[14,67] The sample with 1.06 at-% of Fe content shows both the highest catalytic activity and the largest redox wave (**Figure 1c**). Increasing the number of cycles during the electrochemical activation process leads to a significant enhancement of the

Ni^{2+}/Ni^{3+} redox wave (**Supporting Information, Figure SI2)**, suggesting the increase of Ni oxo-hydroxide species as actives sites for water oxidation catalysis and hence, a cathodic shift of 50 mV of the onset potential for water oxidation. The presence of Ni oxo-hydroxides was further confirmed by XPS measurements, as shown in **Supporting Information Figure SI9.**

Both the method to incorporate Fe ions and their concentration play a crucial role on the final electrocatalytic performance of the Ni-based electrocatalysts.[19] When Fe is incorporated as an impurity in the host Ni lattice, it improves the activity towards OER by providing active sites or favouring the Ni centres, modifying the local Ni environment. On the other hand, when the Fe content exceeds a certain limit, a less active phase is formed.[13, 15] Two different effects related to Fe incorporation can be observed in **Figure 1c**: the intentional addition of Fe to the catalytic system (red and green lines) and the unintentional incorporation of Fe traces from the electrolyte (dashed and solid lines), both increasing the catalytic activity.

The photovoltaic device: The photovoltaic devices employed in the present study were prepared with a design where both "front" and "back contact" were placed outside the photo-active region, at the top side of the device, as represented in **Figure 4a,** allowing both electron and hole extraction to drive either reduction or oxidation reactions. This configuration offers great versatility for the use of the photovoltaic devices either as photoanodes or photocathodes in PEC cells. On the other hand, integrated amorphous (*a-Si*) and microcrystalline (*µc-Si*) silicon layers provide high versatility for photo-electrocatalytic applications, due to the tunable photovoltage (Open Circuit Potential, OCP), which depends on the specific multijunction Si-based device architecture. Current devices provide OCP values ranging from 1.5 V up to 2.8 V.[31, 68] A detailed description of multijunction Si architectures for water splitting applications can be found elsewhere.[30, 33] In the present study, two different multijunction Si cells have been tested as photo-absorber in combination with the Ni-Fe water oxidation electrocatalyst developed: *(i)* a triple junction solar cell, *a-Si:H/a-Si:H/µc-Si:H*, (PV-1) (**Figure 4b**) which provides a total 2.15 V OCP and *(ii)* a solar module with two a-*Si:H/µc-Si:H* tandem solar cells connected in series (PV-2) (**Figure 4c**). In this second device, each cell provides 1.3 V OCP, which is not sufficient to drive the water oxidation reaction, considering the unavoidable thermodynamic and kinetic overpotentials. However, the in-series connection of two *a-Si:H/µc-Si:H* tandem cells delivers a total 2.6 V OCP, exceeding the required voltage for water oxidation.

Figure 4d shows the characteristic current-voltage curves of the two types of multijunction thin film solar devices described, and the photovoltaic parameters extracted from these curves are summarized in **Table 1**. The External Quantum Efficiency (EQE), including individual spectra for each sub-cell of the photovoltaic devices is provided as **Supporting Information, Figure SI10**. The theoretical operation point of an integrated PV-EC device for water splitting, at 1.23 V, is also represented in **Figure 4d**. Since practical electrochemical water oxidation requires voltages >1.8 V, considering the overpotentials, both configurations can provide a sufficient photovoltage to drive the water oxidation reaction. However, enhanced performance is expected for PV-1 combined with the Ni-Fe electrocatalyst due to its higher photocurrent. Conversely, the higher photovoltage of PV-2 can be more efficiently exploited in photoelectrochemical applications where higher voltages are required, as e.g. CO_2 reduction or synthesis of added values products.[3, 24]

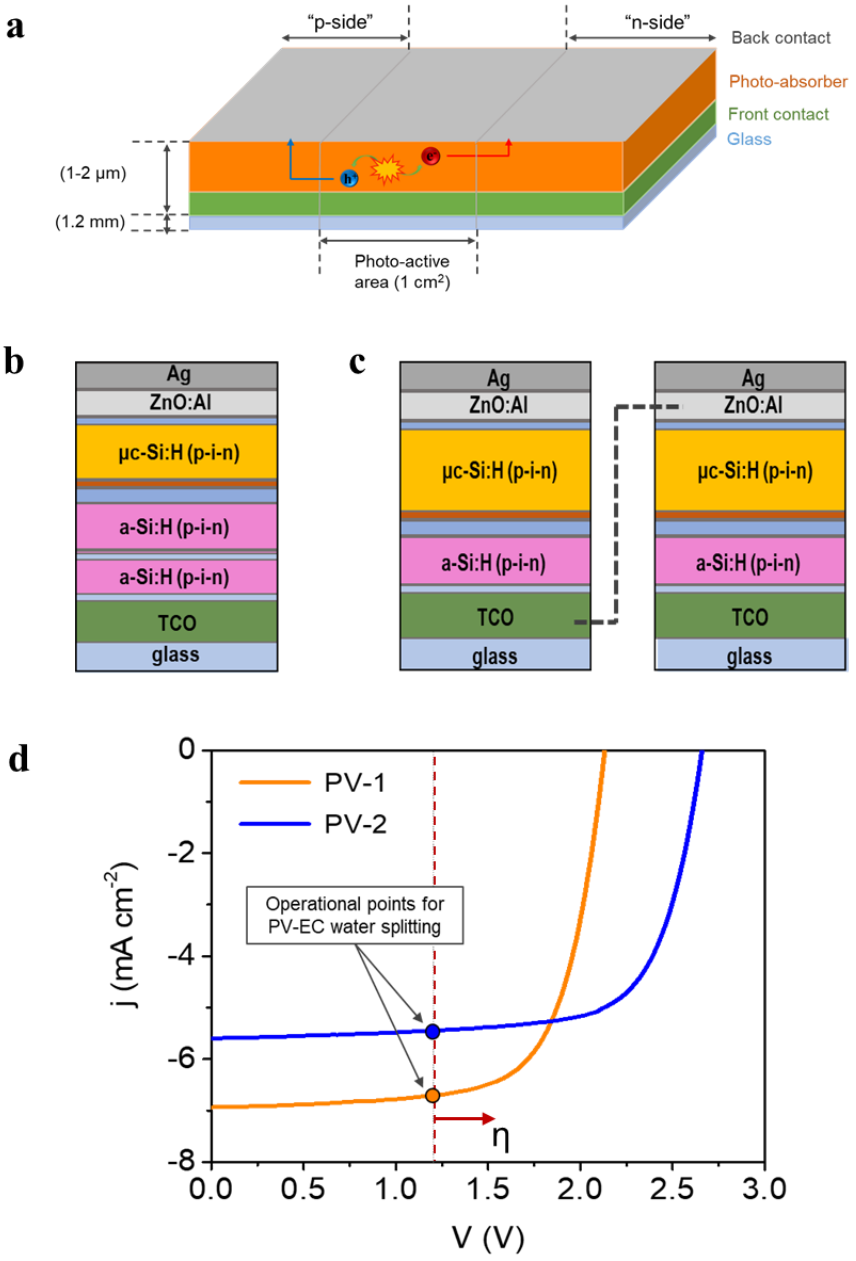

Figure 4. a. Schematic representation of the photovoltaic device design, where the Ag contacts are outside of the 'photo-active area', and serve to transport the photogenerated charge carries to the electrocatalyst. The photo-active region, with a size of 1cm^2, consists in a Si-based device. Architecture of the two different devices employed: **b.** A *a-Si:H/a-Si:H/μc-Si:H* triple junction solar cell (PV-1) and **c.** A module of two *a-Si:H/μc-Si:H* tandem cells connected in series (PV-2). **d.** Characteristic current-voltage curves of PV-1 and PV-2 devices. The theoretical operational points of the integrated PV-EC water splitting devices are represented (the dashed line indicates the water splitting thermodynamic potential at 1.23 V). The red arrow indicates that "practical" operating point is shifted due to overpotentials (η).

Table 1. Photovoltaic parameters from the characteristic current-voltage curves of the employed photovoltaic devices.

Device parameters	PV-1	PV-2
η (%)	10.3	10.7
j_{sc} (mA cm^{-2})	6.9	5.6
V_{oc} (V)	2.13	2.66
FF (%)	69.6	71.1
P_{mpp} (mW)	10.3	10.7

The PV-EC integrated photoanode: **Figure 5a** schematically represents the combination of a Si photovoltaic device, with the optimal Ni-Fe water oxidation electrocatalyst in the integrated water splitting photoanode. Note that, due to the design of the photovoltaic component (**Figure 4a**), it is possible to prepare either a photoanode, placing the catalyst on the "p-side", or a photocathode, if it is placed on the "n-side", even when using a Si-based cell with p-i-n configuration, as those employed here. The integrated photoanode and the experimental setup of the photoelectrochemical cell in operation is showed as **Supporting Information, Figure SI11**. The performance of the PV-EC integrated device can be predicted by the estimation of the theoretical operation point, obtained as the intersection of the current–voltage plot of the photovoltaic device with the linear voltammogram of the electrocatalyst in two-electrode configuration,[31] as illustrated in **Figure 5b.** Hence, the expected STH efficiency, or η_{STH}, can be calculated as:

$$\eta_{STH} = \frac{\Delta E \cdot \eta_F \cdot J_{op}}{\Phi_{in}} \quad (1)$$

where ΔE is the thermodynamic potential for water splitting (ΔE_{H2O}=1.23 V); η_F is the Faradaic efficiency, assumed to be unity for a Pt cathode; J_{op} is the current density at the operation point and Φ_{in} is the total integrated power input density. It is worth noting that the operational photocurrent of the integrated PV-EC device is limited by the performance of the multijunction thin-film solar cells. While single and double junction Si photovoltaic cells deliver higher photocurrent densities,[69] the multijunction cells provide higher photovoltages (over 1.7 V) for bias-free water splitting,[70] which intrinsically lead to lower delivered photocurrent. The estimated current densities at the operation point and the STH efficiency obtained from eq. (1) for the PV-EC integrated devices showed in **Figure 5b**, are summarized as **Supporting Information, Table SI1.** A 7.7% STH efficiency is predicted for the combination of the optimal Ni-Fe electrocatalyst with the PV-1 device. Moreover, the values predicted by **Figure 5b** highlight the importance of the rational selection of the photovoltaic component, which strongly impacts on the performance of the integrated photoanode, as discussed above. Using the PV-2, the effect of Fe incorporation on the Ni-based electrocatalyst appears to be irrelevant for the final STH efficiency of the photoanode, since the current density at the operation point is limited by the photocurrent delivered by the photovoltaic component, independently of the enhanced

performance of the electrocatalyst, as showed in **Figure 5b** (blue dots). However, when the electrocatalyst is coupled to the PV-1 system, delivering a higher photocurrent, a clear effect of the electrodeposited Fe charge on the performance of the integrated device is expected from **Figure 5b** (orange dots). Furthermore, both, the current density at the operation point and the STH efficiency, as a function of the Fe load on the electrocatalyst coupled to the PV-1 device, are shown in **Supporting Information, Figure SI12**.

The measured performance of the integrated photoanodes in a two-electrode configuration cell is showed in **Figure 5c**. Both photovoltaic devices PV-1 and PV-2 were tested for comparison. As expected, higher current density at zero applied bias is obtained for PV-1, in spite of the detrimental shift of the onset potential compared to the solar module, due to the lower photovoltage. The 7.7 % STH efficiency measured for the optimal architecture, nicely agrees with that predicted from **Figure 5b** and is comparable to recent reports.[27, 29, 71] As an example, using a NiMo/$NiFeO_x$ catalyst system and *a-Si:H/a-Si:H/μc-Si:H* triple-junction cell in cassette configuration, a 5.1% STH efficiency was reported for a larger area device (A_{EC}=50.3 cm^2; A_{PV}=64 cm^2) device.[68] Finally, the stability of the best integrated device (from the assemble of the optimal Ni-Fe electrocatalyst and the PV-1 device) was tested by a chronoamperometric test running for 20 h, as shown in **Figure 5d**. Ni-Fe mixed electrocatalyst are highly stable and corrosion resistant in alkaline media, particularly at the operating current density of the integrated PV-EC device under study.[72] This is evidenced by the long-term stable behaviour of the PV-EC device under operation in Figure 5d, where there is not a significant decrease of the photocurrent density. SEM and EDS analysis after the long-term stability test, provided as **Supporting Information, Figure SI13**, showed minor changes on both the morphology and the composition on the electrocatalyst surface. The small decrease of the photocurrent is due to the formation of oxygen bubbles at the electrode surface, decreasing the active area and, hence, the extracted current density. However, the initial photocurrent is restored after switching-off the light, and releasing the formed bubbles, showing a stable behaviour of the integrated device. It is worth noting, that stability tests on integrated PV-EC electrodes in direct contact with the electrolyte are usually carried out for few minutes, mainly because of the partial dissolution of the photovoltaic component.[23, 34] Here, since the Ni substrate of the Ni-Fe electrocatalyst acts as a protective barrier, and the photovoltaic component design allows a good electrical contact with the electrocatalyst, the device can run under operating conditions without current losses for more than 20 hours.

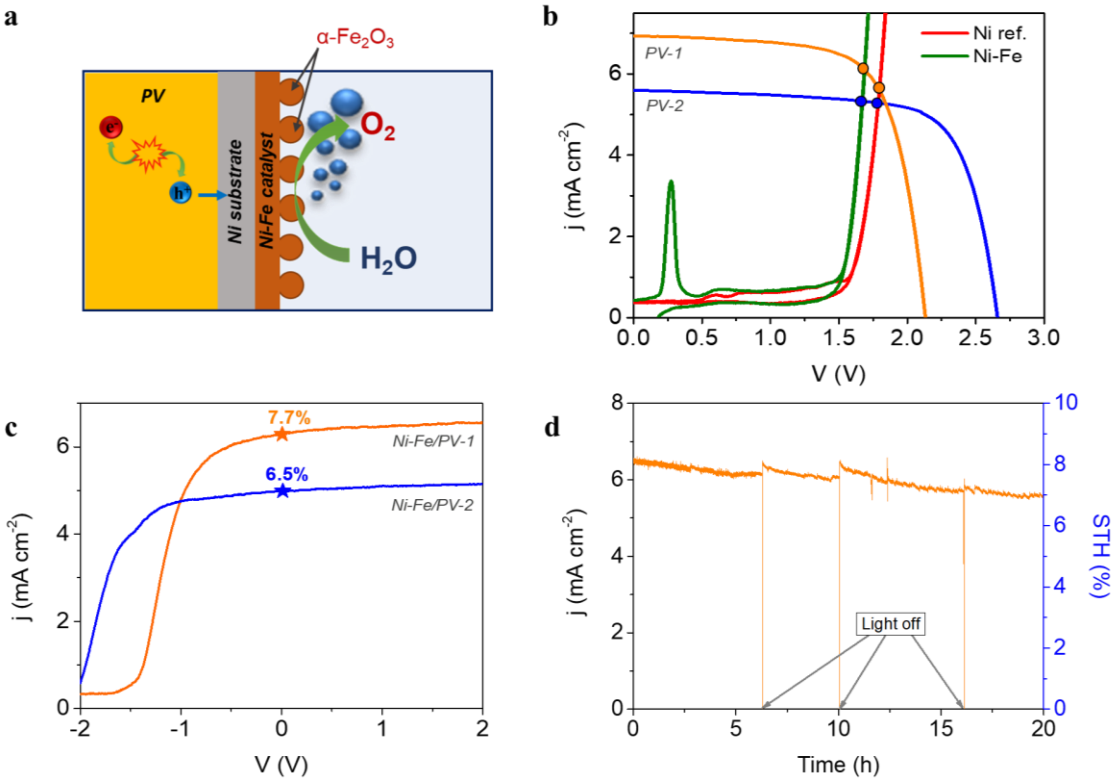

Figure 5. a. Schematic representation of general operation of the integrated PV-EC photoanode, obtained by the direct coupling of the Si-based solar device and the Ni-Fe optimized catalyst. **b.** Estimation of the theoretical operation point from the characteristic current-voltage curve of the photovoltaic devices and LSV of the reference Ni sample and the optimal electrocatalyst (Ni-Fe), measured in two-electrode configuration. **c.** LSV recorded in two-electrode configuration at 50 mV s^{-1}, of the integrated PV-EC devices as photoanodes and STH efficiencies. **d.** Stability test of the integrated photoanode combining the optimal Ni-Fe electrocatalyst and the PV-1 showing promising stability for more than 20 hours under continuous operation. The left y-axis shows the recorded photocurrent density, while the right y-axis represents the calculated STH efficiency.

Conclusions

We have shown that the combination of an optimized Ni-Fe based electrocatalyst (mixed NiO, α-Fe_2O_3 and $NiFe_2O_4$ phases) for water oxidation, with a Si-based multijunction photovoltaic device leads to an efficient and stable integrated photoanode. The concept has been applied here for solar water splitting, although more challenging reactions can be addressed, given the tunability of the accessible photovoltage delivered by the photovoltaic component, and the versatility for driving either oxidation or reduction process, inherent to the device design. The intentional incorporation of Fe by electrodeposition is reflected on the surface morphology of the electrocatalyst, as well as on the development of a high density of active sites for water oxidation during the electrochemical treatment, leading to a 50 mV decreased overpotential compared to the reference Ni substrate. Furthermore, the rational selection of the photovoltaic component is highlighted, targeting the enhancement of the device performance when an optimal electrocatalyst is used. The resulting integrated photoanode shows a competitive 7.7%

STH efficiency and promising stability (20 hours test) at zero applied bias. These results demonstrate that PV-EC configurations based on non-critical raw materials constitute a viable pathway for efficient and low-cost solar energy conversion schemes.

Acknowledgments

This work was financially supported by the European Union's Horizon 2020 project A-LEAF (Grant Agreement No. 732840). The authors would like to thank to J. Kirchhoff and G. Schöpe for their support with solar cell fabrication, and C. Zahren for his support in solar cell characterization.

References

1. Kim, J. H.; Hansora, D.; Sharma, P.; Jang, J.-W.; Lee, J. S. Toward practical solar hydrogen production - an artificial photosynthetic leaf-to-farm challenge. *Chemical Society Reviews* **2019,** *48* (7), 1908-1971.
2. De Luna, P.; Hahn, C.; Higgins, D.; Jaffer, S. A.; Jaramillo, T. F.; Sargent, E. H. What would it take for renewably powered electrosynthesis to displace petrochemical processes? *Science* **2019,** *364* (6438), 350.
3. Sayama, K. Production of High-Value-Added Chemicals on Oxide Semiconductor Photoanodes under Visible Light for Solar Chemical-Conversion Processes. *Acs Energy Letters* **2018,** *3* (5), 1093-1101.
4. You, B.; Sun, Y. Innovative Strategies for Electrocatalytic Water Splitting. *Accounts of Chemical Research* **2018,** *51* (7), 1571-1580.
5. Trasatti, S. Electrocatalysis by oxides — Attempt at a unifying approach. *Journal of Electroanalytical Chemistry and Interfacial Electrochemistry* **1980,** *111* (1), 125-131.
6. Lee, Y.; Suntivich, J.; May, K. J.; Perry, E. E.; Shao-Horn, Y. Synthesis and Activities of Rutile IrO_2 and RuO_2 Nanoparticles for Oxygen Evolution in Acid and Alkaline Solutions. *The Journal of Physical Chemistry Letters* **2012,** *3* (3), 399-404.
7. Vij, V.; Sultan, S.; Harzandi, A. M.; Meena, A.; Tiwari, J. N.; Lee, W.-G.; Yoon, T.; Kim, K. S. Nickel-Based Electrocatalysts for Energy-Related Applications: Oxygen Reduction, Oxygen Evolution, and Hydrogen Evolution Reactions. *ACS Catalysis* **2017,** *7* (10), 7196-7225.
8. De Silva, U.; Masud, J.; Zhang, N.; Hong, Y.; Liyanage, W. P. R.; Asle Zaeem, M.; Nath, M. Nickel telluride as a bifunctional electrocatalyst for efficient water splitting in alkaline medium. *Journal of Materials Chemistry A* **2018,** *6* (17), 7608-7622.
9. Trześniewski, B. J.; Diaz-Morales, O.; Vermaas, D. A.; Longo, A.; Bras, W.; Koper, M. T. M.; Smith, W. A. In Situ Observation of Active Oxygen Species in Fe-Containing Ni-Based Oxygen Evolution Catalysts: The Effect of pH on Electrochemical Activity. *Journal of the American Chemical Society* **2015,** *137* (48), 15112-15121.
10. Fabbri, E.; Habereder, A.; Waltar, K.; Kotz, R.; Schmidt, T. J. Developments and perspectives of oxide-based catalysts for the oxygen evolution reaction. *Catal. Sci. Technol.* **2014,** *4* (11), 3800-3821.
11. McCrory, C. C. L.; Jung, S.; Peters, J. C.; Jaramillo, T. F. Benchmarking Heterogeneous Electrocatalysts for the Oxygen Evolution Reaction. *Journal of the American Chemical Society* **2013,** *135* (45), 16977-16987.
12. Ju, H.; Li, Z.; Xu, Y. Electro-catalytic activity of Ni–Co-based catalysts for oxygen evolution reaction. *Materials Research Bulletin* **2015,** *64*, 171-174.
13. Louie, M. W.; Bell, A. T. An Investigation of Thin-Film Ni–Fe Oxide Catalysts for the Electrochemical Evolution of Oxygen. *Journal of the American Chemical Society* **2013,** *135* (33), 12329-12337.
14. Trotochaud, L.; Young, S. L.; Ranney, J. K.; Boettcher, S. W. Nickel–Iron Oxyhydroxide Oxygen-Evolution Electrocatalysts: The Role of Intentional and Incidental Iron Incorporation. *Journal of the American Chemical Society* **2014,** *136* (18), 6744-6753.
15. Klaus, S.; Cai, Y.; Louie, M. W.; Trotochaud, L.; Bell, A. T. Effects of Fe Electrolyte Impurities on $Ni(OH)_2$/NiOOH Structure and Oxygen Evolution Activity. *The Journal of Physical Chemistry C* **2015,** *119* (13), 7243-7254.
16. Zaffran, J.; Stevens, M. B.; Trang, C. D. M.; Nagli, M.; Shehadeh, M.; Boettcher, S. W.; Caspary Toroker, M. Influence of Electrolyte Cations on Ni(Fe)OOH Catalyzed Oxygen Evolution Reaction. *Chemistry of Materials* **2017,** *29* (11), 4761-4767.

17. Fidelsky, V.; Toroker, M. C. The secret behind the success of doping nickel oxyhydroxide with iron. *Physical Chemistry Chemical Physics* **2017,** *19* (11), 7491-7497.
18. Song, F.; Busch, M. M.; Lassalle-Kaiser, B.; Hsu, C.-S.; Petkucheva, E.; Bensimon, M.; Chen, H. M.; Corminboeuf, C.; Hu, X. An Unconventional Iron Nickel Catalyst for the Oxygen Evolution Reaction. *ACS Central Science* **2019,** *5* (3), 558-568.
19. Francàs, L.; Corby, S.; Selim, S.; Lee, D.; Mesa, C. A.; Godin, R.; Pastor, E.; Stephens, I. E. L.; Choi, K.-S.; Durrant, J. R. Spectroelectrochemical study of water oxidation on nickel and iron oxyhydroxide electrocatalysts. *Nature Communications* **2019,** *10* (1), 5208.
20. Görlin, M.; Chernev, P.; Ferreira de Araújo, J.; Reier, T.; Dresp, S.; Paul, B.; Krähnert, R.; Dau, H.; Strasser, P. Oxygen Evolution Reaction Dynamics, Faradaic Charge Efficiency, and the Active Metal Redox States of Ni–Fe Oxide Water Splitting Electrocatalysts. *Journal of the American Chemical Society* **2016,** *138* (17), 5603-5614.
21. Kim, W.; McClure, B. A.; Edri, E.; Frei, H. Coupling carbon dioxide reduction with water oxidation in nanoscale photocatalytic assemblies. *Chemical Society Reviews* **2016,** *45* (11), 3221-3243.
22. Urbain, F.; Becker, J. P.; Smirnov, V.; Ziegler, J.; Yang, F.; Kaiser, B.; Jaegermann, W.; Hoch, S.; Maljusch, A.; Rau, U.; Finger, F. Influence of the operating temperature on the performance of silicon based photoelectrochemical devices for water splitting. *Mater. Sci. Semicond. Process* **2016,** *42*, 142-146.
23. Reece, S. Y.; Hamel, J. A.; Sung, K.; Jarvi, T. D.; Esswein, A. J.; Pijpers, J. J. H.; Nocera, D. G. Wireless Solar Water Splitting Using Silicon-Based Semiconductors and Earth-Abundant Catalysts. *Science* **2011,** *334* (6056), 645-648.
24. Zhang, W.; Hu, Y.; Ma, L.; Zhu, G.; Wang, Y.; Xue, X.; Chen, R.; Yang, S.; Jin, Z. Progress and Perspective of Electrocatalytic CO_2 Reduction for Renewable Carbonaceous Fuels and Chemicals. *Advanced Science* **2018,** *5* (1).
25. Ronge, J.; Bosserez, T.; Huguenin, L.; Dumortier, M.; Haussener, S.; Martens, J. A. Solar Hydrogen Reaching Maturity. *Oil & Gas Science and Technology-Revue D Ifp Energies Nouvelles* **2015,** *70* (5), 863-876.
26. Cox, C. R.; Lee, J. Z.; Nocera, D. G.; Buonassisi, T. Ten-percent solar-to-fuel conversion with nonprecious materials. *Proceedings of the National Academy of Sciences* **2014,** *111* (39), 14057.
27. Kim, J. H.; Hansora, D.; Sharma, P.; Jang, J.-W.; Lee, J. S. Toward practical solar hydrogen production – an artificial photosynthetic leaf-to-farm challenge. *Chemical Society Reviews* **2019,** *48* (7), 1908-1971.
28. Chang, W. J.; Lee, K.-H.; Ha, H.; Jin, K.; Kim, G.; Hwang, S.-T.; Lee, H.-m.; Ahn, S.-W.; Yoon, W.; Seo, H.; Hong, J. S.; Go, Y. K.; Ha, J.-I.; Nam, K. T. Design Principle and Loss Engineering for Photovoltaic–Electrolysis Cell System. *ACS Omega* **2017,** *2* (3), 1009-1018.
29. Tan, C. S.; Kemp, K. W.; Braun, M. R.; Meng, A. C.; Tan, W.; Chidsey, C. E. D.; Ma, W.; Moghadam, F.; McIntyre, P. C. >10% solar-to-hydrogen efficiency unassisted water splitting on ALD-protected silicon heterojunction solar cells. *Sustainable Energy & Fuels* **2019,** *3* (6), 1490-1500.
30. Urbain, F.; Wilken, K.; Smirnov, V.; Astakhov, O.; Lambertz, A.; Becker, J.-P.; Rau, U.; Ziegler, J.; Kaiser, B.; Jaegermann, W.; Finger, F. Development of Thin Film Amorphous Silicon Tandem Junction Based Photocathodes Providing High Open-Circuit Voltages for Hydrogen Production. *International Journal of Photoenergy* **2014,** *2014*, 10.

31. Becker, J. P.; Turan, B.; Smirnov, V.; Welter, K.; Urbain, F.; Wolff, J.; Haas, S.; Finger, F. A modular device for large area integrated photoelectrochemical water-splitting as a versatile tool to evaluate photoabsorbers and catalysts. *Journal of Materials Chemistry A* **2017,** *5* (10), 4818-4826.
32. Schüttauf, J.-W.; Modestino, M. A.; Chinello, E.; Lambelet, D.; Delfino, A.; Dominé, D.; Faes, A.; Despeisse, M.; Bailat, J.; Psaltis, D.; Moser, C.; Ballif, C. Solar-to-Hydrogen Production at 14.2% Efficiency with Silicon Photovoltaics and Earth-Abundant Electrocatalysts. *Journal of The Electrochemical Society* **2016,** *163* (10), F1177-F1181.
33. Urbain, F.; Smirnov, V.; Becker, J.-P.; Lambertz, A.; Yang, F.; Ziegler, J.; Kaiser, B.; Jaegermann, W.; Rau, U.; Finger, F. Multijunction Si photocathodes with tunable photovoltages from 2.0 V to 2.8 V for light induced water splitting. *Energy & Environmental Science* **2016,** *9* (1), 145-154.
34. Ager, J. W.; Shaner, M. R.; Walczak, K. A.; Sharp, I. D.; Ardo, S. Experimental demonstrations of spontaneous, solar-driven photoelectrochemical water splitting. *Energy & Environmental Science* **2015,** *8* (10), 2811-2824.
35. Jaegermann, W.; Kaiser, B.; Ziegler, J.; Klett, J. Interface Engineering of Semiconductor Electrodes for Photoelectrochemical Water Splitting: Application of Surface Characterization with Photoelectron Spectroscopy. In *Photoelectrochemical Solar Fuel Production: From Basic Principles to Advanced Devices*, Giménez, S.; Bisquert, J., Eds. Springer International Publishing: Cham, **2016**; pp 199-280.
36. Haas, S.; Gordijn, A.; Stiebig, H. High speed laser processing for monolithical series connection of silicon thin-film modules. *Progress in Photovoltaics: Research and Applications* **2008,** *16* (3), 195-203.
37. Shaddad, M. N.; Ghanem, M. A.; Al-Mayouf, A. M.; Gimenez, S.; Bisquert, J.; Herraiz-Cardona, I. Cooperative Catalytic Effect of ZrO_2 and α-Fe_2O_3 Nanoparticles on $BiVO_4$ Photoanodes for Enhanced Photoelectrochemical Water Splitting. *ChemSusChem* **2016,** *9* (19), 2779-2783.
38. Steier, L.; Herraiz-Cardona, I.; Gimenez, S.; Fabregat-Santiago, F.; Bisquert, J.; Tilley, S. D.; Grätzel, M. Understanding the Role of Underlayers and Overlayers in Thin Film Hematite Photoanodes. *Advanced Functional Materials* **2014,** *24* (48), 7681-7688.
39. Klahr, B.; Gimenez, S.; Fabregat-Santiago, F.; Hamann, T.; Bisquert, J. Water Oxidation at Hematite Photoelectrodes: The Role of Surface States. *Journal of the American Chemical Society* **2012,** *134* (9), 4294-4302.
40. Hegner, F. S.; Cardenas-Morcoso, D.; Giménez, S.; López, N.; Galan-Mascaros, J. R. Level Alignment as Descriptor for Semiconductor/Catalyst Systems in Water Splitting: The Case of Hematite/Cobalt Hexacyanoferrate Photoanodes. *ChemSusChem* **2017,** *10* (22), 4552-4560.
41. Badia-Bou, L.; Mas-Marza, E.; Rodenas, P.; Barea, E. M.; Fabregat-Santiago, F.; Gimenez, S.; Peris, E.; Bisquert, J. Water Oxidation at Hematite Photoelectrodes with an Iridium-Based Catalyst. *The Journal of Physical Chemistry C* **2013,** *117* (8), 3826-3833.
42. Sharma, P.; Jang, J.-W.; Lee, J. S. Key Strategies to Advance the Photoelectrochemical Water Splitting Performance of α-Fe_2O_3 Photoanode. *ChemCatChem* **2019,** *11* (1), 157-179.
43. Wriedt, H. A. The Fe-O (Iron-Oxygen) System. *Journal of Phase Equilibria* **1991,** *12* (2), 170-200.
44. Neumann, J. P.; Zhong, T.; Chang, Y. A. The Ni−O (Nickel-Oxygen) system. *Bulletin of Alloy Phase Diagrams* **1984,** *5*, 141-144.

45. Wu, Y.; He, Y.; Wu, T.; Chen, T.; Weng, W.; Wan, H. Influence of some parameters on the synthesis of nanosized NiO material by modified sol–gel method. *Materials Letters* **2007,** *61* (14), 3174-3178.
46. Swartzendruber, L. J.; Itkin, V. P.; Alcock, C. B. Erratum to: The Fe-Ni (iron-nickel) system. *Journal of Phase Equilibria* **1992,** *13* (6), 585-585.
47. Zhu, J.; Xiao, D.; Li, J.; Yang, X.; Wu, Y. Characterization of FeNi3 alloy in Fe–Ni–O system synthesized by citric acid combustion method. *Scripta Materialia* **2006,** *54* (1), 109-113.
48. Mellsop, S. R.; Gardiner, A.; Johannessen, B.; Marshall, A. T. Structure and transformation of oxy-hydroxide films on Ni anodes below and above the oxygen evolution potential in alkaline electrolytes. *Electrochimica Acta* **2015,** *168*, 356-364.
49. Lyons, M. E. G.; Doyle, R. L.; Godwin, I.; O'Brien, M.; Russell, L. Hydrous Nickel Oxide: Redox Switching and the Oxygen Evolution Reaction in Aqueous Alkaline Solution. *Journal of the Electrochemical Society* **2012,** *159* (12), H932-H944.
50. Neale, A. R.; Jin, Y.; Ouyang, J.; Hughes, S.; Hesp, D.; Dhanak, V.; Dearden, G.; Edwardson, S.; Hardwick, L. J. Electrochemical performance of laser micro-structured nickel oxyhydroxide cathodes. *Journal of Power Sources* **2014,** *271*, 42-47.
51. Luo, C.; Li, D.; Wu, W.; Zhang, Y.; Pan, C. Preparation of porous micro–nano-structure NiO/ZnO heterojunction and its photocatalytic property. *RSC Advances* **2014,** *4* (6), 3090-3095.
52. Chourpa, I.; Douziech-Eyrolles, L.; Ngaboni-Okassa, L.; Fouquenet, J.-F.; Cohen-Jonathan, S.; Soucé, M.; Marchais, H.; Dubois, P. Molecular composition of iron oxide nanoparticles, precursors for magnetic drug targeting, as characterized by confocal Raman microspectroscopy. *Analyst* **2005,** *130* (10), 1395-1403.
53. de Faria, D. L. A.; Venâncio Silva, S.; de Oliveira, M. T. Raman microspectroscopy of some iron oxides and oxyhydroxides. *Journal of Raman Spectroscopy* **1997,** *28* (11), 873-878.
54. Ortiz-Quiñonez, J.-L.; Pal, U.; Villanueva, M. S. Structural, Magnetic, and Catalytic Evaluation of Spinel Co, Ni, and Co–Ni Ferrite Nanoparticles Fabricated by Low-Temperature Solution Combustion Process. *ACS Omega* **2018,** *3* (11), 14986-15001.
55. Salazar-Tamayo, H.; García, K. E.; Barrero, C. A. New method to calculate Mössbauer recoilless f-factors in $NiFe_2O_4$. Magnetic, morphological and structural properties. *Journal of Magnetism and Magnetic Materials* **2019,** *471*, 242-249.
56. Biesinger, M. C.; Payne, B. P.; Grosvenor, A. P.; Lau, L. W. M.; Gerson, A. R.; Smart, R. S. C. Resolving surface chemical states in XPS analysis of first row transition metals, oxides and hydroxides: Cr, Mn, Fe, Co and Ni. *Applied Surface Science* **2011,** *257*, 2717-2730.
57. Biesinger, M. C.; Payne, B. P.; Lau, L. W. M.; Gerson, A.; Smart, R. S. C. X-ray photoelectron spectroscopic chemical state quantification of mixed nickel metal, oxide and hydroxide systems. *Surface and Interface Analysis* **2009,** *41* (4), 324-332.
58. Krasnikov, S. A.; Preobrajenski, A. B.; Chasse, T.; Szargan, R. Thickness dependence of photoemission and X-ray fluorescence spectra in epitaxial NiO layers on Ag(100). *Thin Solid Films* **2003,** *428* (1-2), 201-205.
59. Chen, D.; Zhang, F.; Wang, W.; Yang, Y.; Qian, G. Synergistic effect of PANI and $NiFe_2O_4$ for photocatalytic hydrogen evolution under visible light. *International Journal of Hydrogen Energy* **2018,** *43* (4), 2121-2129.

60. Liu, J.; Zhu, D.; Ling, T.; Vasileff, A.; Qiao, S.-Z. S-$NiFe_2O_4$ ultra-small nanoparticle built nanosheets for efficient water splitting in alkaline and neutral pH. *Nano Energy* **2017,** *40*, 264-273.
61. Liu, G.; Wang, K.; Gao, X.; He, D.; Li, J. Fabrication of mesoporous $NiFe_2O_4$ nanorods as efficient oxygen evolution catalyst for water splitting. *Electrochimica Acta* **2016,** *211*, 871-878.
62. L.-A. Stern and X. Hu. Enhanced oxygen evolution activity by NiO_x and $Ni(OH)_2$ nanoparticles *Faraday Discussions*, **2014**, *176*, 363-379.
63. R. Gao and D. Yan. Recent Development of Ni/Fe-Based Micro/Nanostructures toward Photo/Electrochemical Water Oxidation. *Advanced Energy Materials*, **2020**, *10*, 1900954.
64. X. Li, X. Hao, Z. Wang, A. Abudula and G. Guan. In-situ intercalation of NiFe LDH materials: An efficient approach to improve electrocatalytic activity and stability for water splitting *Journal of Power Sources*, **2017**, *347*, 193-200.
65. M. Yu, G. Moon, E. Bill and H. Tüysüz. Optimizing Ni–Fe Oxide Electrocatalysts for Oxygen Evolution Reaction by Using Hard Templating as a Toolbox. *ACS Applied Energy Materials*, **2019**, *2*, 1199-1209.
66. Lyons, M. E.; Brandon, M. P. The Oxygen Evolution Reaction on Passive Oxide Covered Transition Metal Electrodes in Aqueous Alkaline Solution. Part 1-Nickel *Int. J. Electrochem. Sci* **2018,** *3* (12), 1386-1424.
67. Corby, S.; Garcia-Tecedor, M.; Tengeler, S.; Steinert, C.; Moss, B.; Mesa, C. A.; Kaiser, B.; Jaegermann, W.; Francas, L.; Gimenez, S.; Durrant, J. R. Bulk and Surface Processes in NiO_x Electrocatalysts for Water Oxidation. *Journal of Materials Chemistry A* **2020,** *In press*.
68. Welter, K.; Hamzelui, N.; Smirnov, V.; Becker, J. P.; Jaegermann, W.; Finger, F. Catalysts from earth abundant materials in a scalable, stand-alone photovoltaic-electrochemical module for solar water splitting. *Journal of Materials Chemistry A* **2018,** *6* (33), 15968-15976.
69. N. Wang, M. Liu, J. Liang, T. Li, H. Tan, B. Liu, Q. Zhang, C. Wei, Y. Zhao and X. Zhang. Fabrication, characterization, and stability of supported single-atom catalysts. *Catal. Sci. Technol.*, **2017**, *7*, 5608-5613.
70. F. Friedhelm, W. Katharina, U. Félix, S. Vladimir, K. Bernhard and J. Wolfram. Photoelectrochemical Water Splitting using Adapted Silicon Based Multi-Junction Solar Cell Structures: Development of Solar Cells and Catalysts, Upscaling of Combined Photovoltaic-Electrochemical Devices and Performance Stability. *Zeitschrift für Physikalische Chemie*, **2019**, 20191453.
71. Zhou, X.; Zhou, J.; Huang, G.; Fan, R.; Ju, S.; Mi, Z.; Shen, M. A bifunctional and stable Ni–Co–S/Ni–Co–P bistratal electrocatalyst for 10.8%-efficient overall solar water splitting. *Journal of Materials Chemistry A* **2018,** *6* (41), 20297-20303.
72. J. Mohammed-Ibrahim. A review on NiFe-based electrocatalysts for efficient alkaline oxygen evolution reaction. *Journal of Power Sources*, **2020**, *448*, 227375.

6.3 Supporting Information

Supporting Information for

An Integrated Photoanode Based on Non-Critical Raw Materials for Robust Solar Water Splitting

Drialys Cardenas-Morcoso,[a] Miguel García Tecedor,[a] Tsvetelina Merdzhanova,[b] Vladimir Smirnov,[b] Friedhelm Finger,[b] Bernhard Kaiser,[c] Wolfram Jaegermann,[c] Sixto Gimenez[a*]

[a] *Institute of Advanced Materials (INAM), Universitat Jaume I, Avenida de Vicent Sos Baynat, s/n, 12006 Castelló de la Plana, Castellón, Spain.*
[b] *IEK-5 Photovoltaik, Forschungszentrum Jülich, Jülich, 52425, Germany.*
[c] *Institute of Materials Science, TU Darmstadt, Darmstadt, 64287, Germany.*

[*]**Email:** sjulia@uji.es

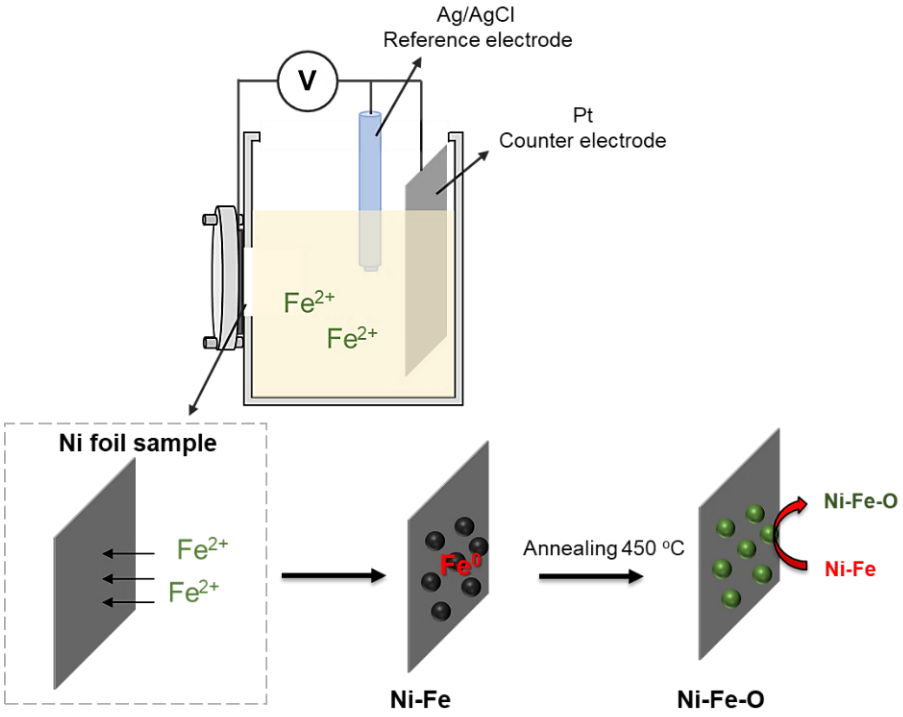

Figure SI1. Preparation of the Ni-Fe electrocatalyst by electrodeposition of metallic Fe on Ni foil, followed by thermal annealing to form the mixed Ni-Fe oxide.

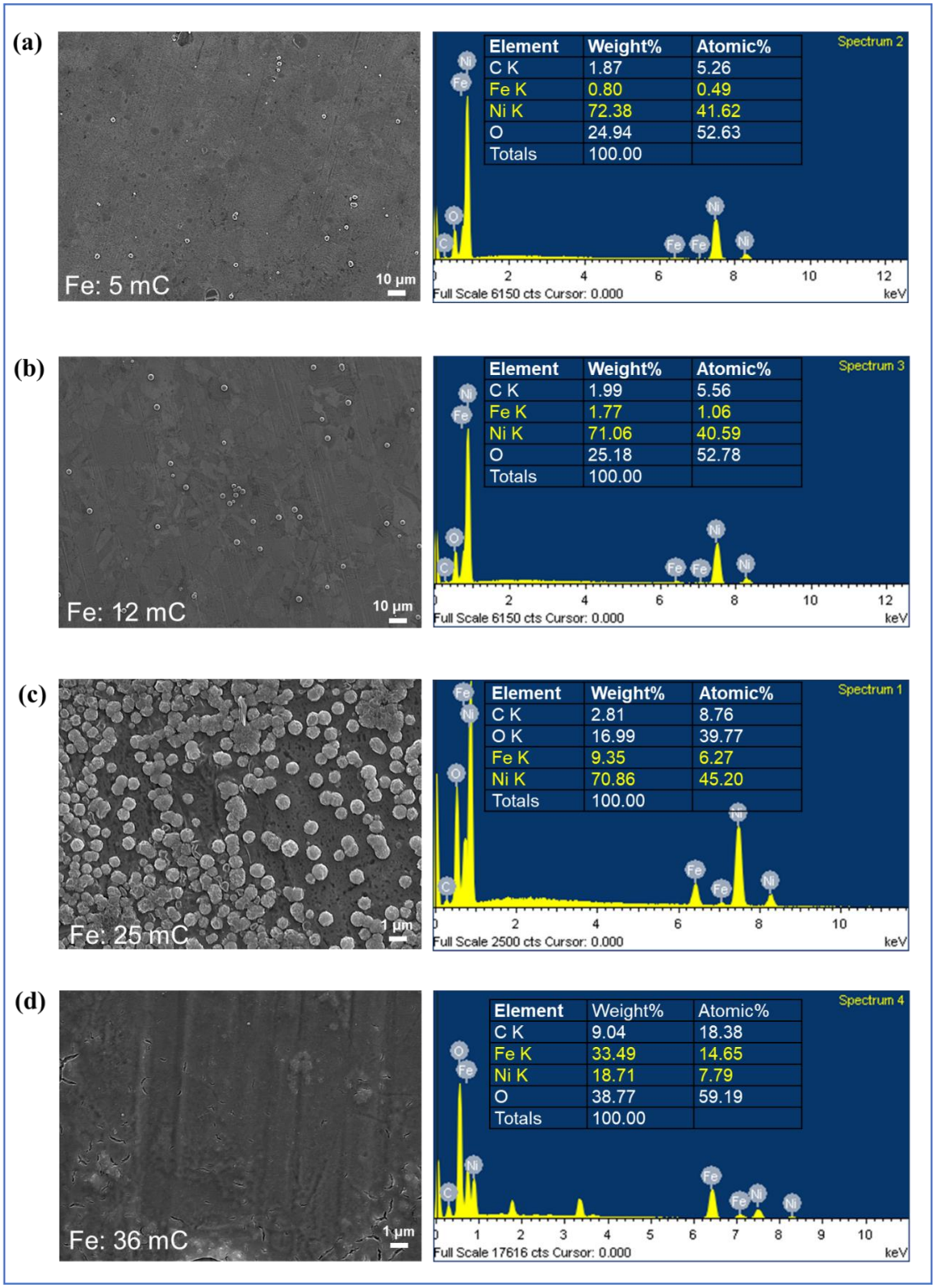

Figure SI2. SEM micrography and EDS analysis of thermally treated Ni substrate surfaces with **a.** 5 mC cm^{-2}, **b.** 12 mC cm^{-2}, **c.** 25 mC cm^{-2} **d.** 36 mC cm^{-2} Fe load.

Table SI1.- EDS analysis of the Ni films after different Fe electrodeposited charges.

	5 mC cm^{-2}	**12 mC cm^{-2}**	**25 mC cm^{-2}**	**36 mC cm^{-2}**
Element	**at.-%**	**at.-%**	**at.-%**	**at.-%**
C K	5.26	5.56	8.76	18.38
Fe K	**0.49**	**1.06**	**6.27**	**14.65**
Ni K	41.62	40.59	45.20	7.79
O	52.63	52.78	39.77	59.19

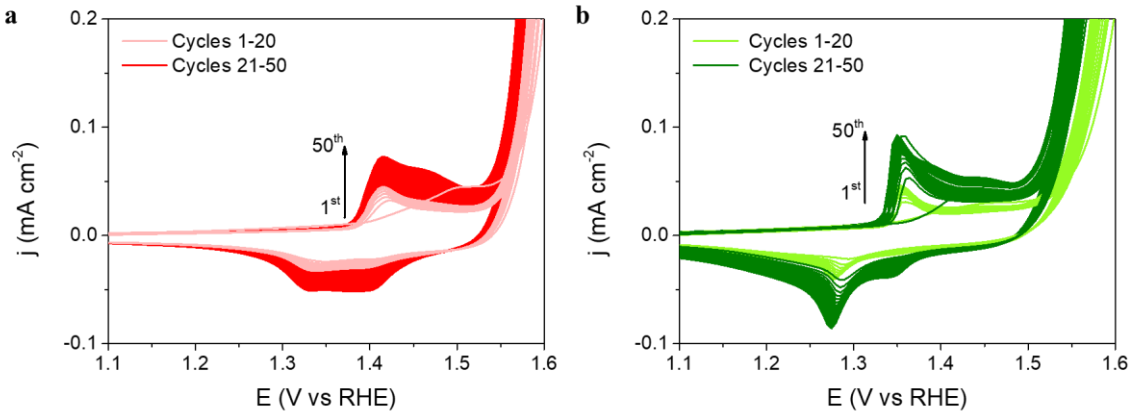

Figure SI3. Full cyclic voltammetry treatment performed on **a** bare Ni foil (thermally treated) and **b** Ni foil with 12 mC cm^{-2} Fe load.

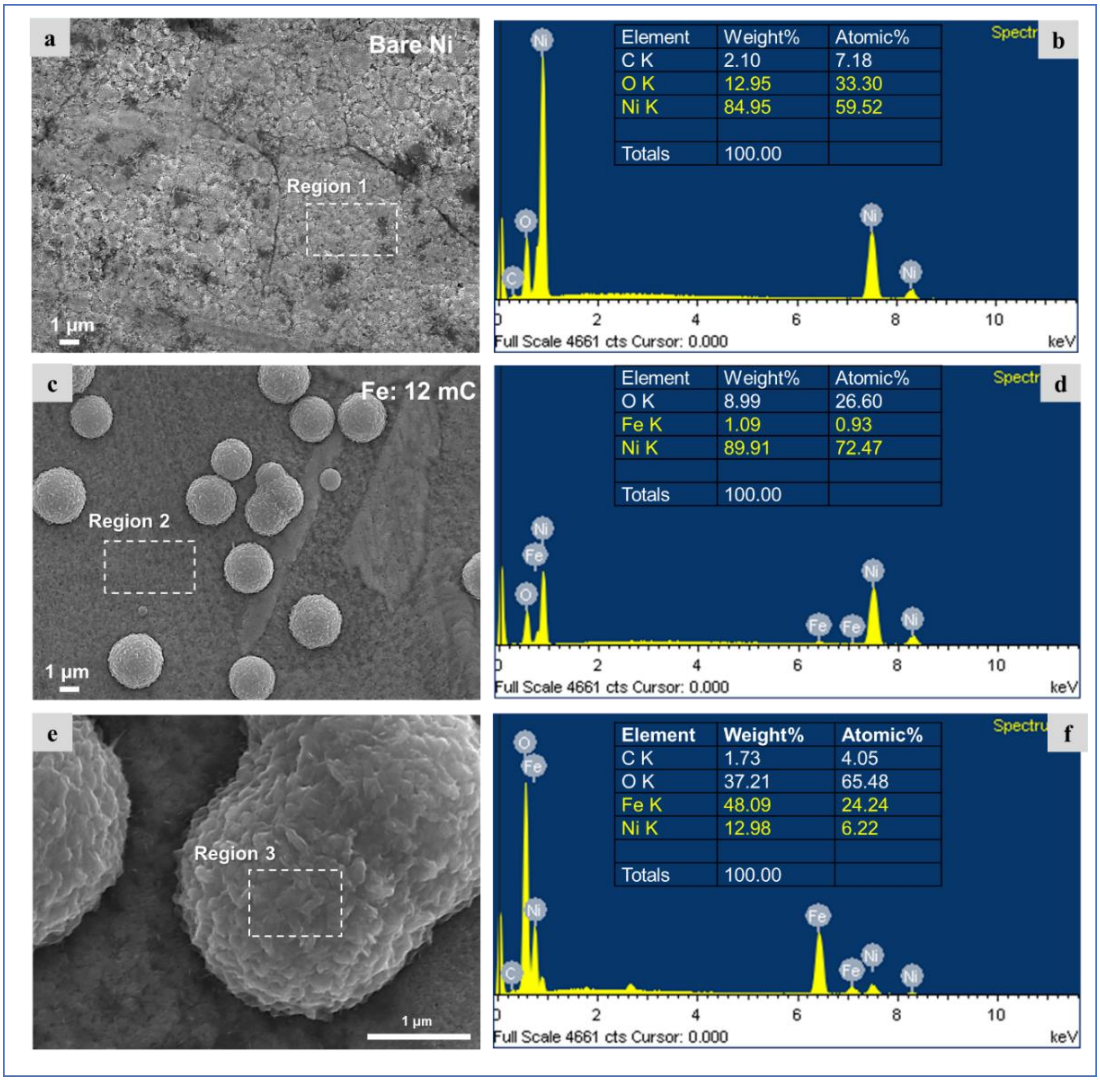

Figure SI4. SEM micrographs and EDS analyses of: **a** and **b:** reference Ni substrate after thermal annealing; **b, c, d** and **f:** two different regions of the Ni -Fe catalyst (12 mC cm^{-2} of Fe charge).

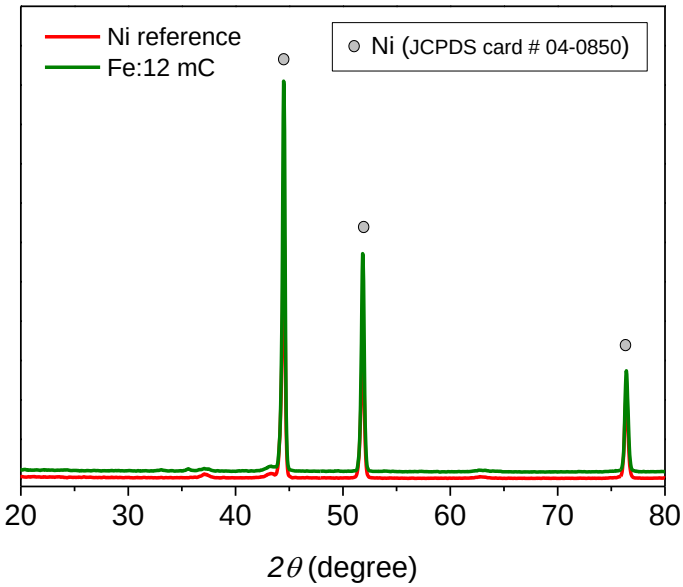

Figure SI5. XRD pattern of optimal Ni-Fe catalyst and reference Ni foil annealed.

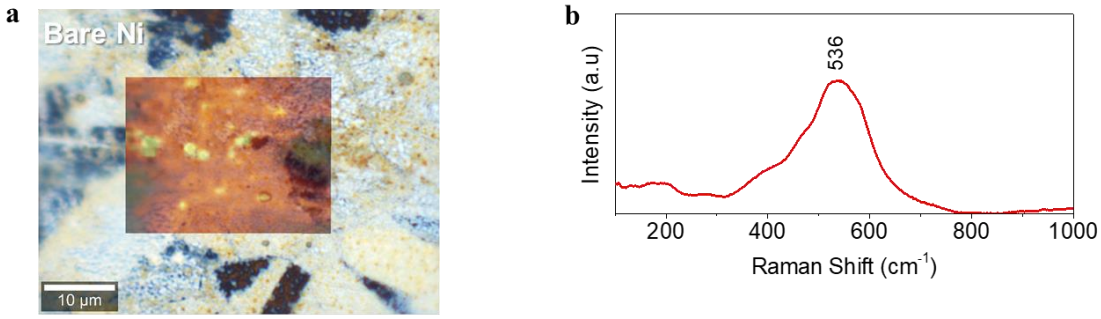

Figure SI6. Optical image of the Ni foil surface after annealing, taken as reference and Confocal Multi-Spectral Imaging (CMSI) maps in a selected area. **b.** Raman shift spectra corresponding to the selected area.

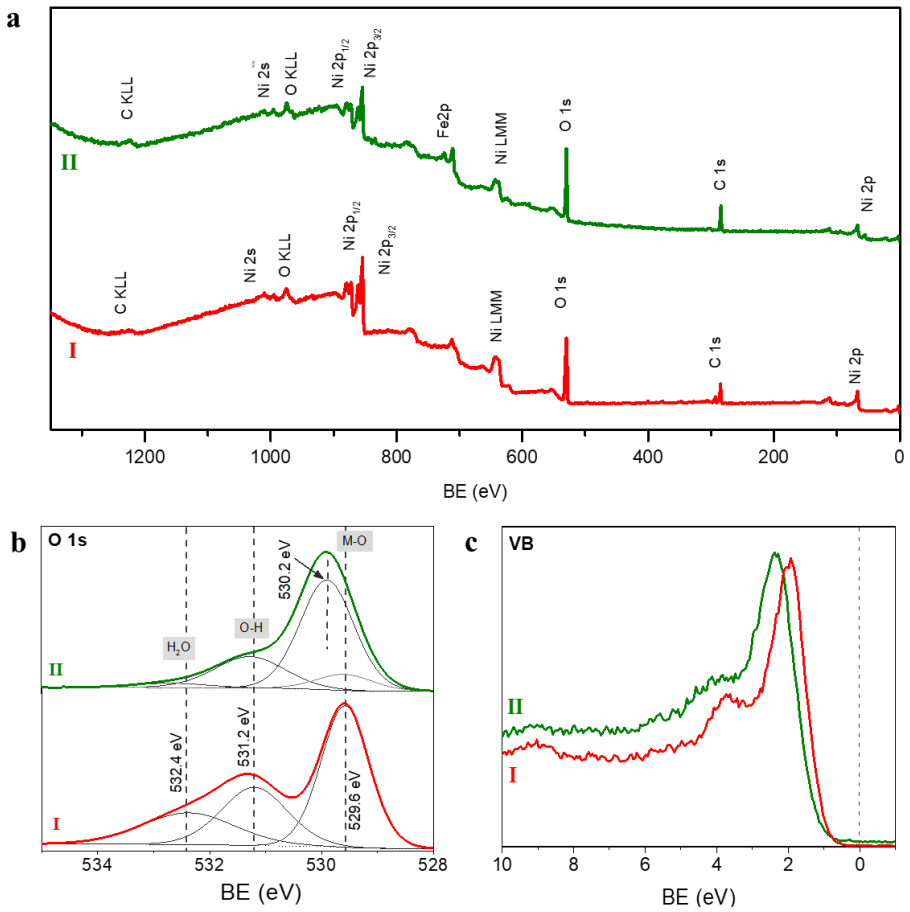

Figure SI7. XPS survey spectra of **I** bare, and **II** optimal Fe loaded Ni foil after annealing.

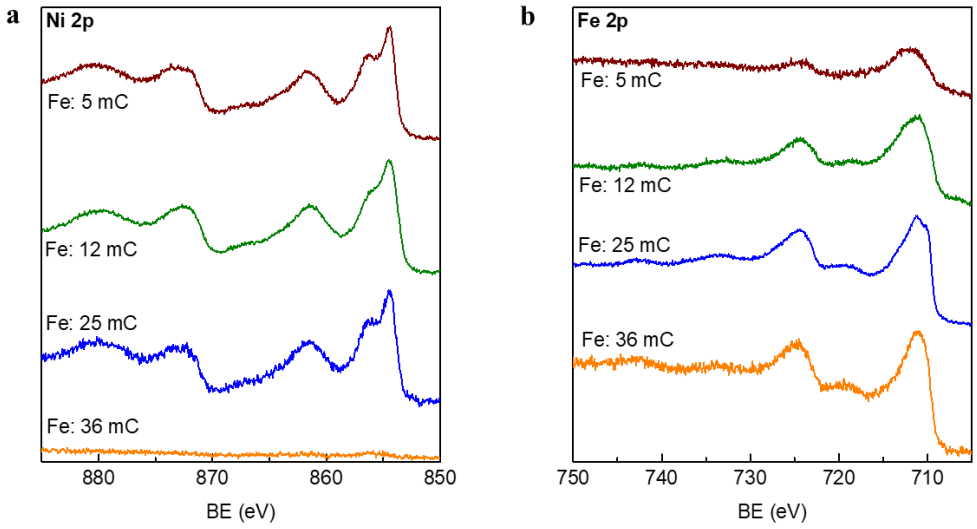

Figure SI8. a Ni 2p signal and **b** Fe 2p signal in XPS spectra of different samples prepared varying the Fe charge during the electrochemical deposition.

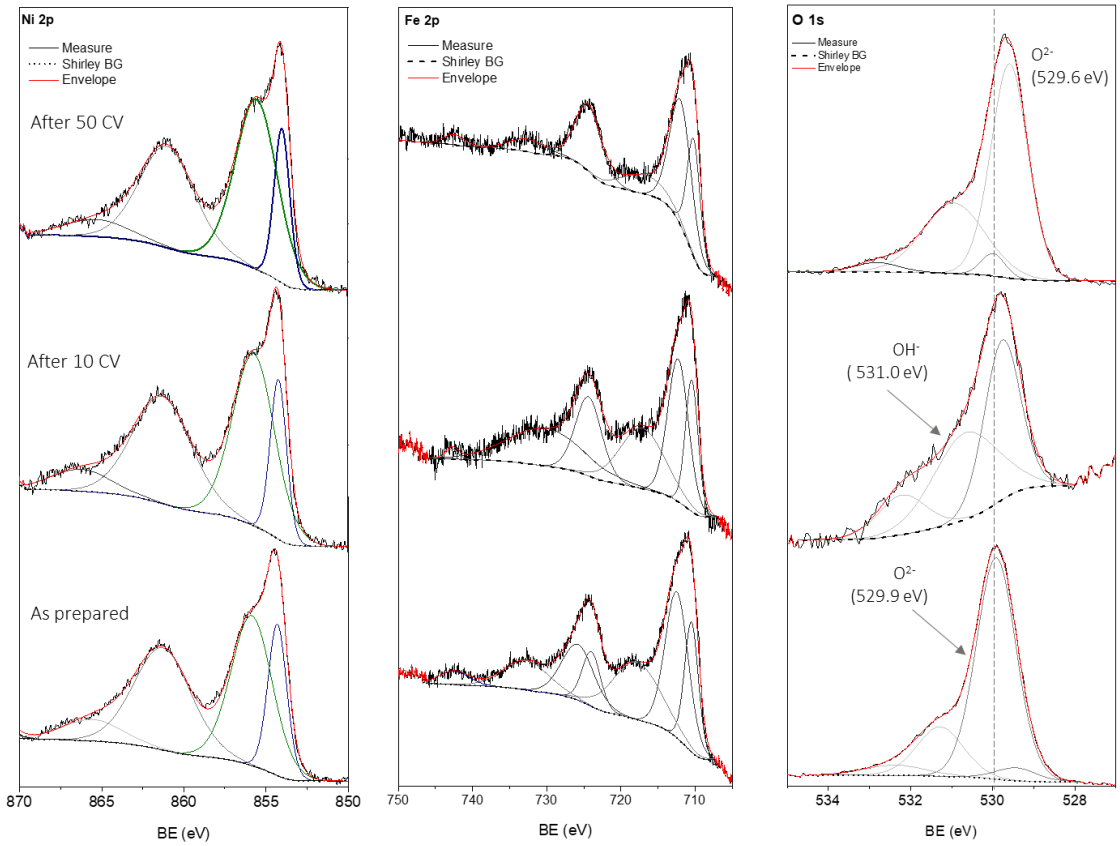

Figure SI9. XPS spectra at different stages of the electrochemical activation process for the optimal Ni-Fe electrocatalyst.

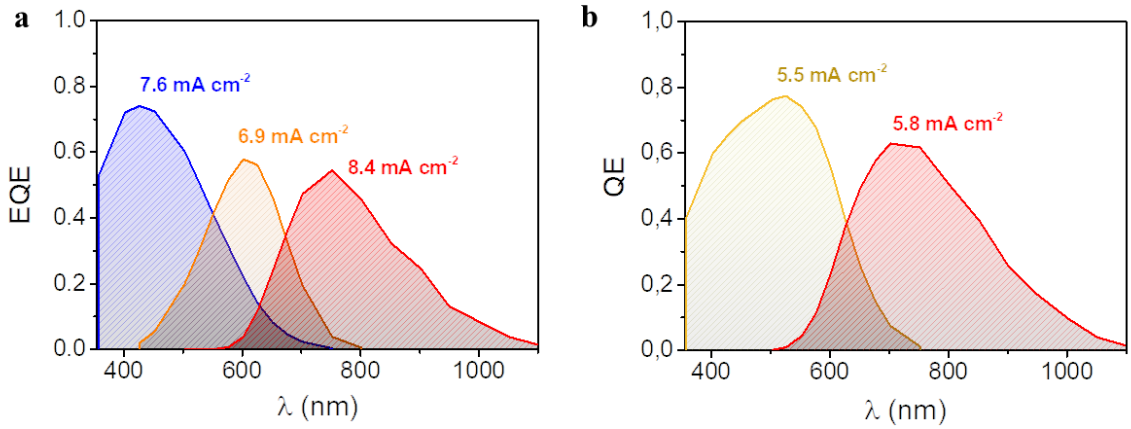

Figure SI10. Spectral response (external quantum efficiency, EQE), including individual spectra for each sub-cell, of the photovoltaic devices: **(a)** PV-1 **(b)** PV-2. The integrated current density value from the EQE spectrum for each sub-cell is placed in the respective measurement.

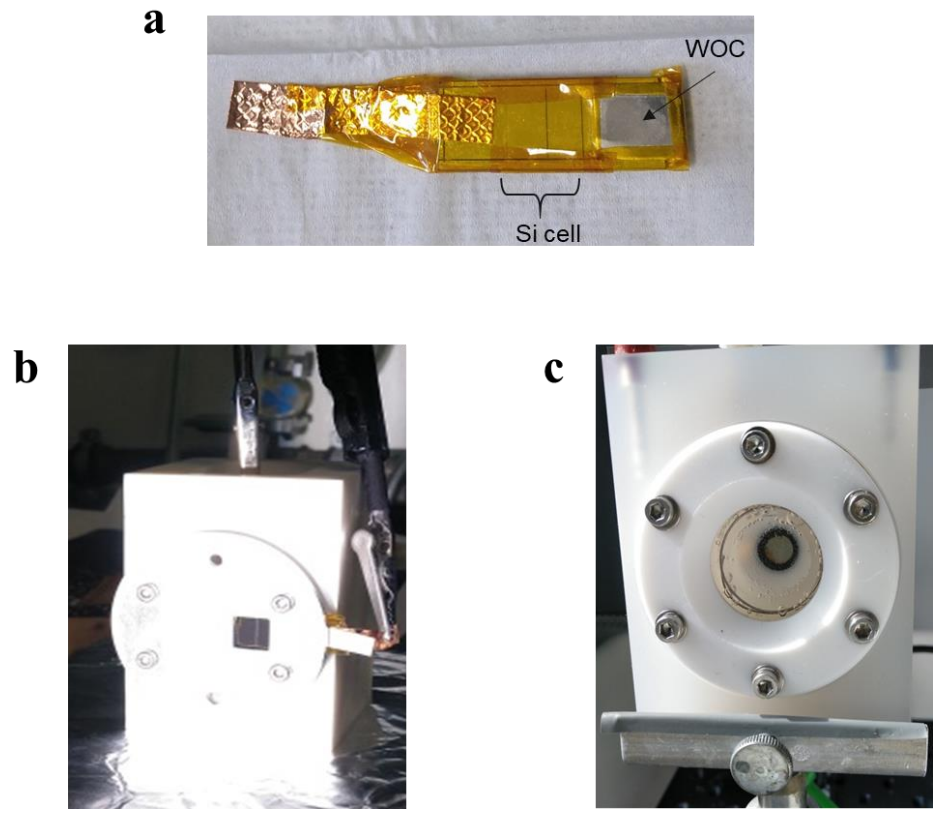

Figure SI11. a. Integrated PV-EC photoanode. The water oxidation electrocatalyst (WOC) is coupled to the Si multijunction PV device on the "p-side", whereas a Cu foil is used to transport the holes from the "n-side" to the counter electrode. The photoelectrochemical setup for characterization of the integrated device: **b.** View from the "back side" of the PV-EC device, showing the photoactive part, **c.** View from the "front side", showing the gas bubbles produced at the electrode surface.

Table SI2. Current density at the theoretical operation point and estimated STH efficiency.

	NiO		**$NiFeO_x$**	
Photovoltaic device	j_{op}	η_{STH}	j_{op} $(mA\ cm)^{-2}$	η_{STH}
PV-1	5.62	6.9%	6.09	7.5%
PV-2	5.28	6.5%	5.33	6.5%

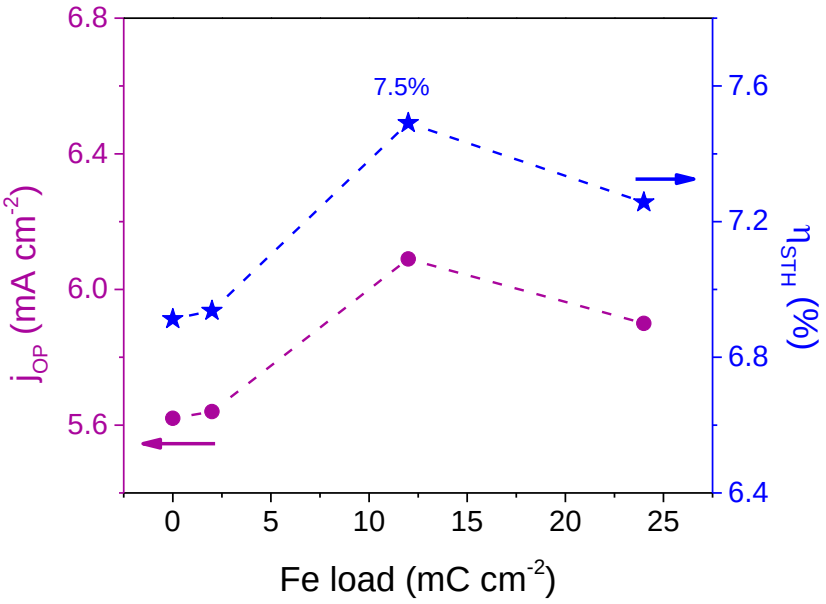

Figure SI12. Current density at the operation point (light blue circles) and STH efficiency (dark blue stars), as function of the Fe load on the electrocatalyst, in combination with the PV-1 device.

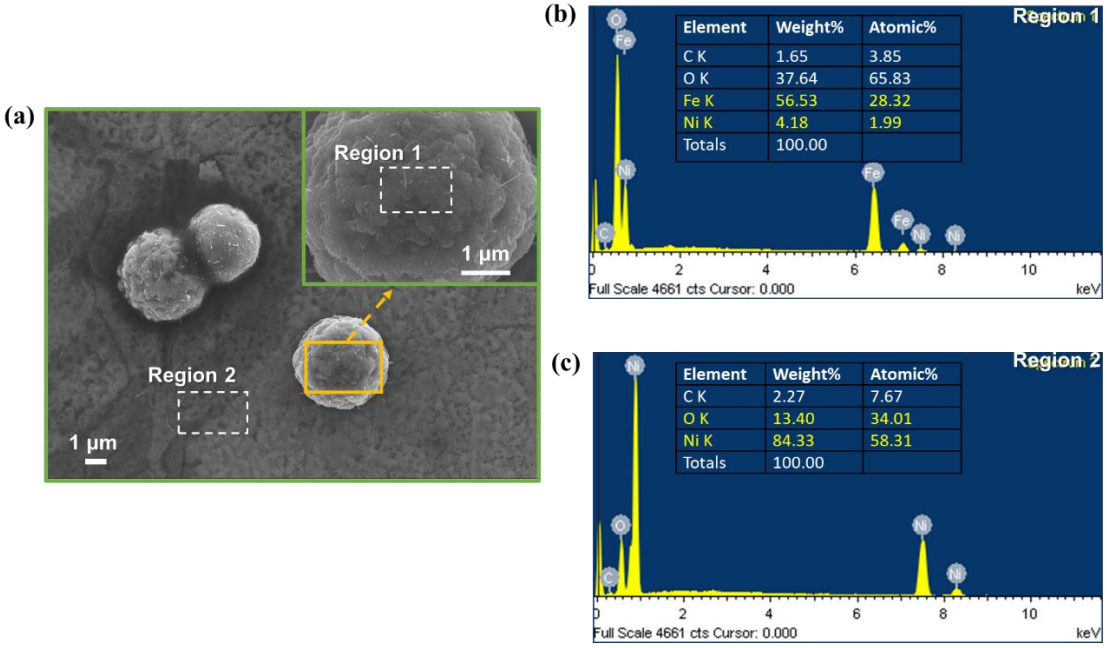

Figure SI13. Top view SEM micrograph and EDS analysis of the Ni-Fe electrocatalyst after the long-term (20 h) stability test.

Chapter 7: Publication 4

"Photocatalytic and photoelectrochemical degradation of organic compounds with all-inorganic metal halide perovskite quantum dots."

Cardenas-Morcoso, D.; Gualdrón-Reyes, A. F.; Vittoreti, A. B.; García-Tecedor, M.; Yoon Joon, S.; Solís de la Fuente, M.; Mora-Seró, I.; Giménez, S.

*The Journal of Physical Chemistry Letters, **2019**, 10, 630-636.*

7.1 Candidate's contribution.

Nature of contribution:	**Extent of contribution:**
• Assessment of the environmental conditions for measurements. • Design of the photocatalytic and photoelectrochemical experiments. • Execution of optical, photocatalytic and (photo-)electrochemical measurements. • Contribution to the analysis of the results. • Contribution to the figures and manuscript preparation. • Corrections on the manuscript according to the reviewers' comments.	60%

7.2 Published manuscript.

Photocatalytic and photoelectrochemical degradation of organic compounds with all-inorganic metal halide perovskite quantum dots.

Drialys Cardenas-Morcoso, [†] Andrés F. Gualdrón-Reyes, [†, ‡, §] Ana Beatriz Ferreira-Vitoreti, [†, §, ǂ] Miguel García-Tecedor, [†] Seog Joon Yoon, [†] Mauricio Solis de la Fuente, [‖] Iván Mora-Seró, * [†] Sixto Gimenez * [†]

[†] *Institute of Advanced Materials (INAM), Universitat Jaume I, 12071 Castelló, Spain*
[‡] *Centro de Investigaciones en Catálisis (CICAT), Universidad Industrial de Santander, Sede UIS Guatiguará, Piedecuesta, Santander, Colombia. C.P. 681011.*
[§] *Centro de Investigación Científica y Tecnológica en Materiales y Nanociencias (CMN), Universidad Industrial de Santander, Piedecuesta, Santander, Colombia. C.P. 681011.*
[δ] *Department of Natural Science, Federal University of São João del-Rei, 36301-160 São João del-Rei, Brazil*
[ǂ] *CAPES Foundation, Ministry of Education of Brazil, Brasília, 70040-020, Brazil*
[‖] *Lawrence Berkeley National Laboratory, Energy Technologies Area, 1 Cyclotron Road, Berkeley, California 94720, United States of America*

[*]**Email:** sero@uji.es, sjulia@uji.es

Abstract

Inspired by the outstanding optoelectronic properties reported for all-inorganic halide perovskite quantum dots (QDs), we have evaluated the potential of these materials toward the photocatalytic and photoelectrochemical degradation of organic compounds, taking the oxidation of 2-mercaptobenzothiazole (MBT) as a proof-of-concept. First, we determined electrochemically the energy levels of dispersions of perovskite QDs with different band gaps induced by the different ratios between halides (Br and I) and metallic cations (Pb and Sn). Then, we selected CsPbBr3 QDs to demonstrate the photocatalytic and photoelectrochemical oxidation of MBT, confirming that hole injection takes place from CsPbBr3 QDs to MBT, resulting in the total degradation of MBT as evidenced by electrospray mass spectrometry analyses. Although the stability and toxicity of these QDs are major issues to address in the near future, the results obtained in the present study open promising perspectives for the implementation of solar-driven catalytic strategies based on these fascinating materials.

Table of Content

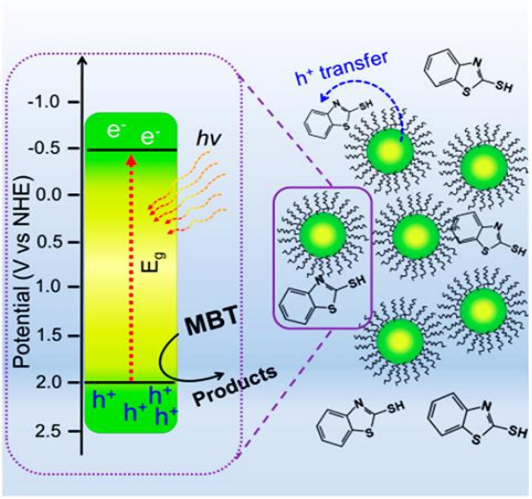

All-Inorganic Halide Perovskite Quantum Dots (QDs) have emerged in the last three years with outstanding optoelectronic properties and promising stability.[1-2] The high photoluminescence quantum yield (PLQY) of core nanoparticles with narrow PL spectra and reduced PL blinking,[3] together with low lasing threshold,[4] enables these materials as excellent candidates for applications in photovoltaics, stimulated and light emission.[5] The outstanding PLQY of perovskite QDs is a clear evidence of the significant reduction of non-radiative recombination pathways. Consequently, after photoexcitation these systems present a pool of photoexcited carriers, whose extra energy can be used in an efficient radiative emission or take advantage of them in different ways such as providing work in solar cells or drive diverse chemical reactions. These remarkable optoelectronic properties have been demonstrated in few seminal studies of these materials for photocatalysis, with interesting examples for the degradation of organic dyes,[6] functionalization of C−H bonds in alkanes[7] and CO_2 conversion into added value products.[8-10] In this context, it is essential to provide a systematic approach to understand the suitability of perovskite QDs toward photoelectrochemical and photocatalytic applications. As a first step, careful assessment of the environmental and experimental conditions for photoelectrochemical tests is needed to control any chemical and photochemical interaction which can take place with perovskite QDs during operation. Next, the energy levels in the selected electrolyte must be determined, i.e. conduction band (CB) minimum and valence band (VB) maximum, to assess the potential of these materials to inject photogenerated carriers into an electrolytic or molecular acceptor under illumination, which is essential for photoelectrochemical and photocatalytic applications. Since the pioneering work from Bard and coworkers,[11] who reported the correlation between the optical and electrochemical bandgap in dispersions of CdS QDs, cyclic voltammetry (CV) measurements have been successfully employed to determine the band structure and quantum confinement effects in CdSe[12-13] and CdTe[14-15] QDs. More recently, Nag and co-workers studied the effect of halide composition in $CsPbX_3$ (X= Cl, Br, I) nanoparticles on the VB and CB position and the effect on optical transition probabilities across these edges.[16] On the other hand, CV has been also employed as a relevant interrogating tool on hybrid organic-inorganic perovskite films,[17] where the main difference with nanoparticle dispersions is that the electrochemical reactions are kinetically controlled, instead of diffusion controlled.[12]

Herein, we have selected four different perovskite QDs solutions with different band gaps, covering the whole visible spectrum by the variation of the nominal compositions: $CsPbBr_3$, $CsPbI_3$, $CsPb_{0.4}Sn_{0.6}I_3$ and $CsPb(Br_{0.5}I_{0.5})_3$. **Figure 1** shows the typical structural and photophysical properties of the $CsPbX_3$ (X= Br, I) and mixed $CsPbBr_{1.5}I_{1.5}$ and $CsPb_{0.4}Sn_{0.6}I_3$ QDs perovskites, prepared by hot-injection method (see **Supporting Information** to further details of experimental methods**).** Under UV light, highly luminescent nanocrystals were obtained (**Figure 1a**), featuring a wide variety of colors as a consequence of the increase of iodine/bromine ratio,[1] or to the cation interchange in the B-position of the ABX_3 type-structure,[18] inducing the band gap narrowing. The same trend is also reflected on the photoluminescence (PL) and absorbance spectra (**Figure 1b and Supporting Information, Figure S2**) obtained for each tested material, where a red-shift of both the emission peak and the absorption band edge is observed. In the case of the $CsPb_{0.4}Sn_{0.6}I_3$ QDs, the partial substitution of Pb by Sn strengthens the B-X bond into the perovskite, increasing/lowering the VB/CB energy position.[18] On the other hand, as $CsPbX_3$ (X= Br, I) QDs, the mixed $CsPb(Br_{0.5}I_{0.5})_3$ and $CsPb_{0.4}Sn_{0.6}I_3$ QDs exhibited a symmetric emission feature at 683 nm and 893 nm, respectively, characteristic from homogeneous solid solutions.[1]

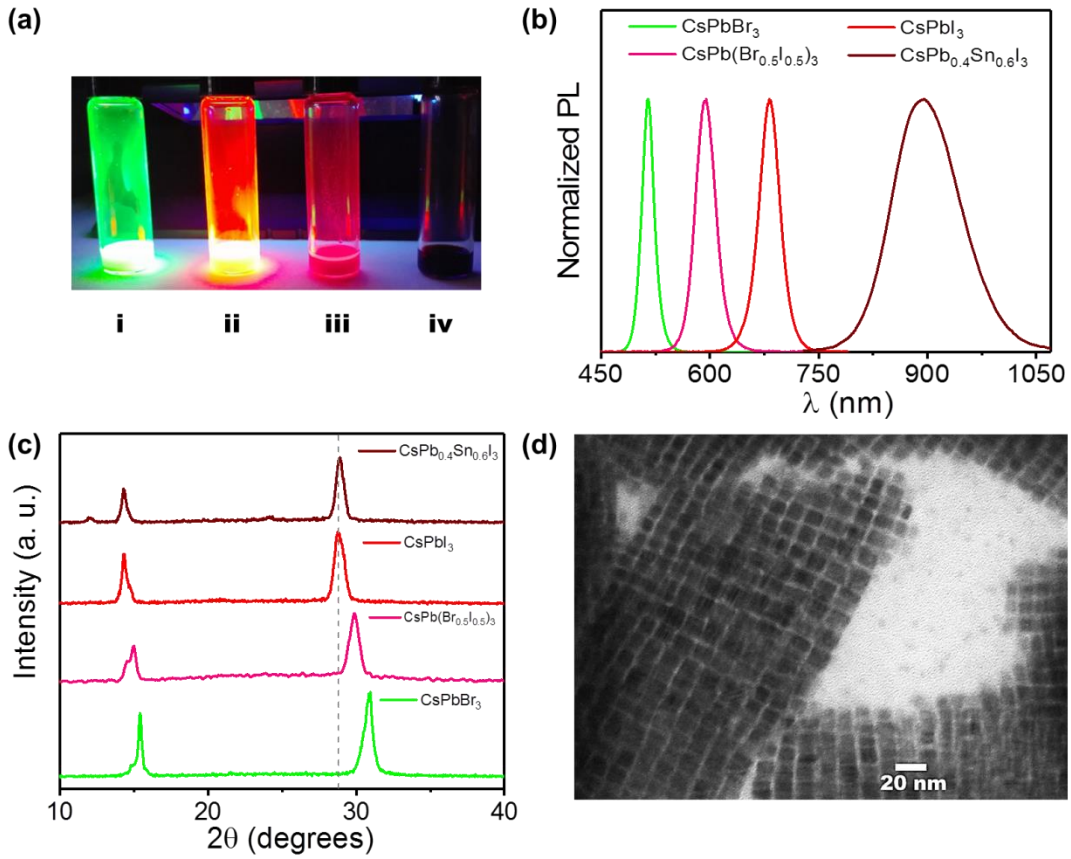

Figure 1. Optical and structural characterization of the different perovskite QDs studied: **(a)** Digital photograph of perovskite QDs solutions under UV light: **i** $CsPbBr_3$, **ii** $CsPbI_3$, **iii** $CsPb(I_{0.5}Br_{0.5})_3$ and **iv** $CsPb_{0.4}Sn_{0.6}I_3$; **(b)** Normalized PL spectra; **(c)** XRD diffractograms, the dashed vertical line is centred at $CsPbI_3$ peak to provide a direct visualization of the peak shifts due to the partial cation substitution and partial/total anion substitution. **(d)** Representative TEM picture of the $CsPbBr_3$ QDs.

The crystalline structure of the QDs was characterized by XRD as shown in **Figure 1c**. Two representative peaks are associated to the (100) and (200) planes from the perovskite structure with cubic phase (JCPDS card # 00-054-0752).[19] Furthermore, the increase of Br content is reflected on a shift of the peak positions to higher Bragg angles. This is due to the decrease of ionic radius of the halide into the material, reducing the Pb-X bond length into the lattice.[20-21] The incorporation of Sn into $CsPbI_3$ to obtain the mixed cation $CsPb_{0.4}Sn_{0.6}I_3$ QDs led to a slight shift of the perovskite peak position compared to $CsPbI_3$. However, a small peak around 12 degrees appeared, ascribed to trace amounts of impurities as SnI_2/SnI_4, or their mixtures.[22] A representative TEM image of the $CsPbBr_3$ QDs is showed in **Figure 1d,** revealing a particle size between 10 and 15 nm with and the characteristic cubic morphology of the perovskite crystalline structure; which is identical for all the systems tested (see **Supporting Information, Figure S3**, where the size distribution is also indicated).

As a fundamental preliminary step in our study, we conducted a detailed survey of different electrolyte/solvent combinations in order to ascertain the stability of the perovskite QDs solutions during the different photocatalytic/photoelectrochemical tests (see **Supporting Information, Table S1**). We found that the tetrabutylammonium

hexafluorophosphate dissolved in dichloromethane (Bu_4NPF_6/DCM) was the most stable environment, in good agreement with a recent report on hybrid halide perovskites.[23]

In the electrochemical measurements with QDs dispersions, charge transfer between the Pt working electrode and the perovskite QDs is reflected as anodic (A_1) and cathodic peaks (C_1) in the cyclic voltammograms, corresponding to the band edge positions, i.e. VB and CB respectively. The potential difference between A_1 and C_1 peaks is referred as the quasi-particle bandgap (E_g^{qp})[12] and should be close to the optical bandgap (E_g^{op}), determined through optical absorption and photoluminescence (PL) measurements. **Figure 2a** shows a representative cyclic voltammogram of a Pt working electrode in a $CsPbI_3$ QDs solution at 100 mV s^{-1}. The irreversible peaks at -1 V vs NHE and at 0.74 V vs NHE correspond to C_1 and A_1, respectively. This irreversibility has been attributed to partial QDs degradation after the charge transfer.[11-12] The potential difference (E_g^{qp}) between C_1 and A_1 (1.74 V) is in excellent agreement with the E_g^{op} value, obtained by absorbance and PL measurements (**Supporting Information, Table S2)**. Identical measurements were performed on $CsPb_{0.4}Sn_{0.6}I_3$, $CsPb(I_{0.5}Br_{0.5})_3$ and $CsPbBr_3$ QDs and **Figure 2b** shows the voltammograms corresponding to all tested samples, recorded at 100 mV s^{-1}. The corresponding A_1 and C_1 peaks are indicated in all cases and, from these values, E_g^{qp} was calculated. **Supporting Information Figure S4** displays the cyclic voltammograms recorded for the same dispersion of $CsPb_{0.4}Sn_{0.6}I_3$ QDs at different scan rates (ν). The linear dependence between the peak current value of A_1 and C_1 versus $\nu^{1/2}$ confirms the diffusion-controlled process, validating the treatment of the perovskite QDs as isolated quasi-particles.[12] It is worth mentioning that some additional peaks have been identified as C_2 and A_2 in the reported voltammograms for $CsPb_{0.4}Sn_{0.6}I_3$ QDs, which have been ascribed to trap-to-bands transitions.[22] All the results are included in the energy diagram of **Figure 2c** and **Supporting Information, Table S2**, also including E_g^{op} calculated from optical measurements. In all cases, the correspondence between both electrochemical and optical bandgaps is excellent. Furthermore, Ultraviolet Photoelectron Spectroscopy (UPS) was also employed to corroborate the trend of the band positions of the perovskite QDs, by the determination of the VB (**Supporting Information Figure S5**) and the obtained values are summarized in **Figure 2d**, also showing very good agreement with both electrochemical and optical measurements. Indeed, the values obtained in this work are also in reasonably good agreement with those reported with electrochemical measurements of perovskites nanocrystals,[16] UPS of films,[24] and Photoelectron Yield Spectroscopy (PYS) of colloidal QDs,[22] as showed in **Figure 2d**. Note that although identical energy positions should not be expected from electrochemistry and UPS, due to the sensitivity of E_g^{qp} to the QDs environment, a similar trend is obtained. To further validate the energetic alignment of the different QDs tested, steady-state PL measurements were carried out to monitor the change in emission properties of the QDs, upon addition of a second chromophore, to demonstrate straddling gap (type-I) or staggered gap (type-II) alignment between different QDs combination (further details in **Supporting Information**). From these experiments, it was confirmed type-I alignment between $CsPbI_3$ and $CsPb_{0.4}Sn_{0.6}I_3$, meanwhile type-II alignment was observed between $CsPb_{0.4}Sn_{0.6}I_3$/$CsPbBr_3$ and $CsPbBr_3$/$CsPbI_3$ combinations (**Supporting Information Figure S6**).

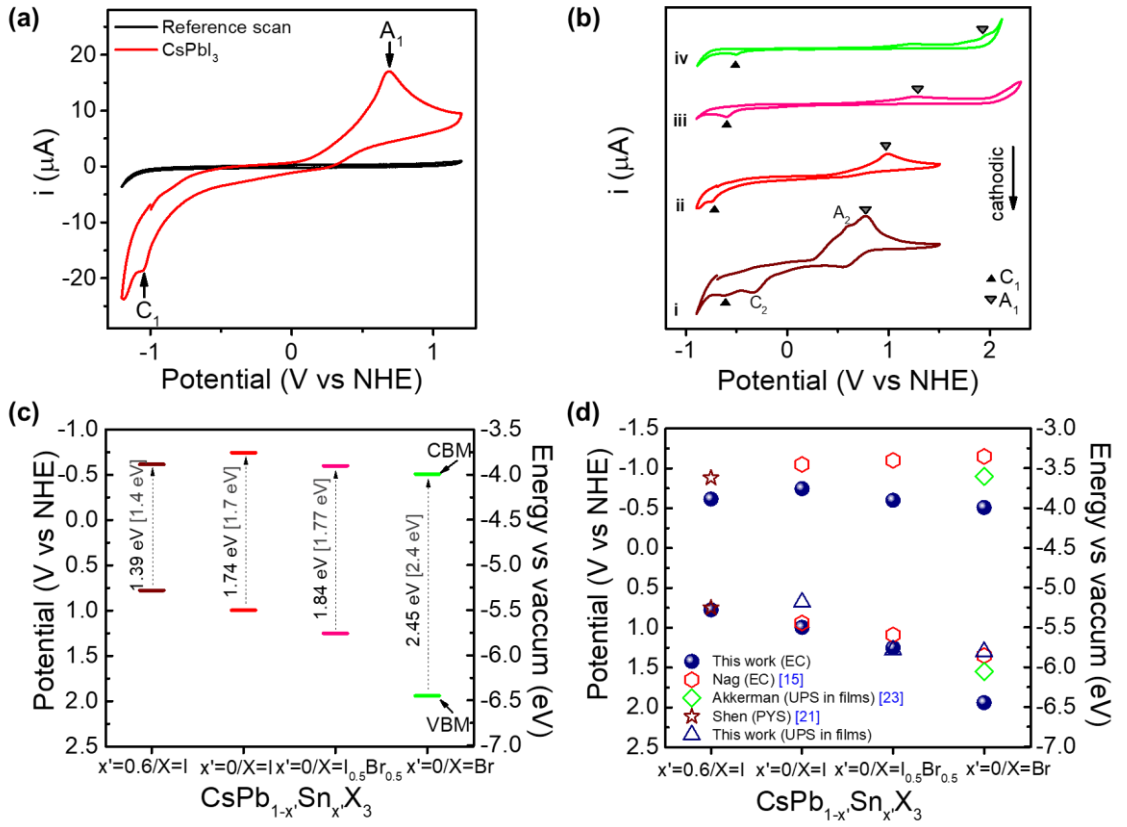

Figure 2. Cyclic voltammetry of the perovskite QDs investigated, recorded at 100 mV s^{-1} **(a)** $CsPbI_3$ (Reference scan on a 100 mM Bu_4NPF_6 in DCM solution is also shown) **(b)** **i** $CsPb_{0.4}Sn_{0.6}I_3$, **ii** $CsPbI_3$, **iii** $CsPb(I_{0.5}Br_{0.5})_3$ and **iv** $CsPbBr_3$. A_1 and C_1 peaks are indicated in each case (A_2 and C_2 also indicated for $CsPb_{0.4}Sn_{0.6}I_3$). **(c)** Energy diagram obtained with the A_1 and C_1 values from (**b**). The electrochemical bandgap (E_g^{qp}) is showed in black color and the optical bandgap (E_g^{op}) in grey color for comparison. **(d)** Comparison between the values obtained in the present study trough CV and UPS and previous reports.

The detailed information on the alignment of perovskite QDs energy levels allows a reliable evaluation of the suitability of these systems to promote the photocatalytic and photoelectrochemical degradation of different organic compounds. Accordingly, as a proof-of-concept, we selected 2-mercaptobenzothiazole (MBT). The oxidation of this compound has been reported between 0.47 and 1 V vs NHE (depending on the working electrode, MBT conditions, etc…).[25] This organic pollutant is expected to be degraded by photo-excited holes generated in the perovskite QDs upon illumination. This compound is an important member of the benzothiazole group of heterocyclic aromatic compounds. It is widely used in rubber additive production, particularly as accelerator of sulphur polymerization (vulcanization). It has been also employed as bio-corrosion inhibitor in industrial cooling systems, in the galvanic industry and also as fungicide, herbicide and anti-algal agent.[26-27] It is poorly biodegradable and exhibits aquatic toxicity, induce tumours to aquatic organisms and stands as one of the most frequent allergens and a human carcinogen.[28] All the tested QDs have suitable band positions for hole transfer to MBT, as showed in **Supporting Information S9a**. However, we specifically focused on $CsPbBr_3$ QDs, since the optical absorbance of these QDs does not overlap with the

characteristic band of MBT at 320 nm, which is monitored during photocatalytic degradation (see **Supporting Information, Figure S9b**).

Consequently, we have tracked the photocatalytic degradation of MBT in the presence of $CsPbBr_3$ QDs by following the evolution of this characteristic absorbance band, as showed in **Figure 3a**. In order to unambiguously determine the role of the perovskite QDs during the photodegradation of MBT, control experiments were carried out without the QDs in the solution and with and without a UV filter during light irradiation **(Supporting Information, Figure S10a-c).** The results are summarized in **Figure 3b** as the relative concentration of the pollutant as $\ln(C/C_0)$ versus time. Without the presence of $CsPbBr_3$ QDs, only UV light is effective towards the degradation of MBT, while no degradation takes place in the dark or under visible illumination in good correspondence with previous reports.[29] Upon addition of the $CsPbBr_3$ QDs, significantly faster degradation rates are observed under both UV and visible illumination. The linear trend of the photodegradation kinetics can be approximated by a pseudo-first-order rate law, from which the rate constant (k) can be calculated as $\ln\left(\frac{C}{C_0}\right) = kt$, where t is the irradiation time. The obtained values are showed in **Table 1**. Additional control experiments with QDs and MBT in the dark were carried out **(Supporting Information, Figure S10d)** to rule out any possible competing chemical degradation mechanism. Remarkably, upon addition of the perovskite QDs in the MBT solution, the degradation rate is doubled for experiments with UV-Vis irradiation and multiplied by a factor six for experiments with visible illumination.

Effective charge transfer from the $CsPbBr_3$ QDs to MBT was confirmed through time-resolved photoluminescence (TRPL) and steady-state PL emission carried out at different times; see **Figure 3c-d**, respectively. The solution was saturated with MBT for these experiments in order to avoid mass transfer limitations. Surprisingly, the emission quenching took place over 45 min, and the PL average lifetime (τ_{avg}) changed from 26.3 ns to 11 ns over 45 min. Note that after 45 min, there was no emission or τ_{avg} difference **(Supporting Information, Table S4)**. This slow quenching process suggests that the interaction between $CsPbBr_3$ QDs and MBT needs some time to proceed. In contrast, the charge transfer process between QDs and acceptor molecules generally takes place in less than 1 μs.[30] Since the perovskite QDs were covered by long-carbon chain (C-18) ligands, *i.e.*, oleic amine and oleic acid, which are in dynamic equilibrium between adsorption and desorption in the solution,[31] we speculate that even in saturated MBT solution, MBT can progressively replace these ligands with time (tens of minutes) binding to the surface of $CsPbBr_3$ QDs. Therefore, the photocatalytic degradation of MBT occurred more significantly after 20 min under UV-Vis illumination. It is also worth noting the slight blue-shift observed in the PL spectra of **Figure 3d** with time, which can be related to $CsPbBr_3$ instabilities under ambient conditions, as previously described in pure $CsPbBr_3$ nanocrystal-based films.[32]

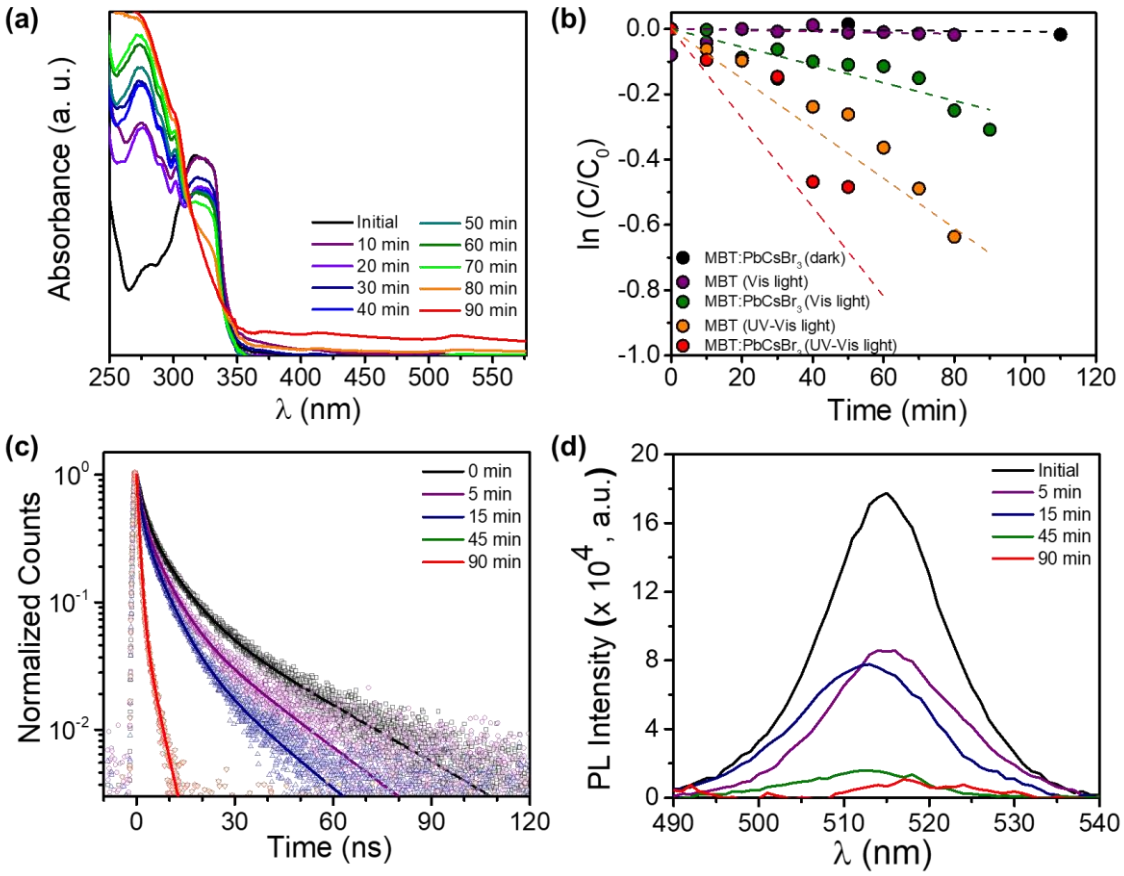

Figure 3. (a) Absorbance spectra for MBT photodegradation in presence of $CsPbBr_3$ QDs under 100 mW cm^{-2} irradiation with UV filter (for better appreciation, the absorbance spectra of $CsPbBr_3$ QDs was subtracted from the global spectra), **(b)** Relative change of the MBT concentration with time in different conditions, (**c)** Time-resolved PL decays (scatter symbols; lines are fitted curves through tri-exponential decay) and **(d)** PL emission before addition of MBT (0 min) and after, under 100 mW cm^{-2} irradiation with UV filter.

Additional confirmation of the degradation of MBT was provided by Electrospray Mass Spectroscopy (ESI-MS) analysis **(Supporting Information, Figure S11)**. The experiments were performed with a control sample (only containing MBT dissolved in hexane) and with an MBT solution with $CsPbBr_3$ QDs before and after illumination at 100 mW cm^{-2} for 100 minutes with a UV filter. The initial m/z (167.9937) characteristic peak of MBT clearly disappears after 100 min of irradiation, confirming the total degradation of the organic compound.

Table 1. Rate constants of MBT photodegradation with or without $CsPbBr_3$ QDs under different illumination conditions, obtained through optical absorbance measurements in **Figure 3b**.

Condition	$\|k\|\ h^{-1}$
MBT (UV-Vis light)	0.5346
MBT:$CsPbBr_3$ (UV-Vis light)	1.0188
MBT (Vis light)	0.0303
MBT:$CsPbBr_3$ (Vis light)	0.1812
MBT:$CsPbBr_3$ (dark)	0.0099

In order to further understand the carrier dynamics of the $CsPbBr_3$ QDs/MBT system, we deposited a 300 nm thick layer of perovskite QDs on a transparent conductive substrate with a thin electron selective layer (FTO/TiO_2), confining the QDs onto the electrode surface. The photoelectrochemical behavior of the tested photoelectrodes was characterized in a three-electrode configuration using a 100 mM Bu_4NPF_6 in DCM with and without MBT. Linear sweep voltammograms (LSV) in the optimized potential range for the $CsPbBr_3$/TiO_2/FTO electrode (see **Supporting Information, Figure S12a**) with and without the addition of MBT are showed in **Figure 4**. In the dark, no current is extracted (**Figure 4a**), while under 100 mW cm^{-2} illumination, an anodic photocurrent is measured, characteristic of an n-type semiconductor photoanode injecting minority carriers (holes) into the solution. When MBT is present in the solution, this anodic photocurrent significantly increases to a maximum of 140 μA cm^{-2}, confirming hole transfer from the $CsPbBr_3$ to the MBT. The photoelectrochemical behavior is stable at least for the timescale of the photoelectrochemical tests carried out, as evidenced from chopped-light chronoamperometric tests showed in **Figure 4b**. The n-type behavior of the films is also confirmed by the cathodic shift of the open circuit potential (OCP) under illumination (see **Supporting Information, Figure S12b**). Mott-Schottky analysis revealed a donor density of $6.77x10^{19}$ cm^{-3} and a flat band potential of -0.109 V vs NHE (**Supporting Information, Figure S13**) also in good correspondence with the CB of the perovskite QDs suspensions extracted by CV and UPS (**Figure 1**).

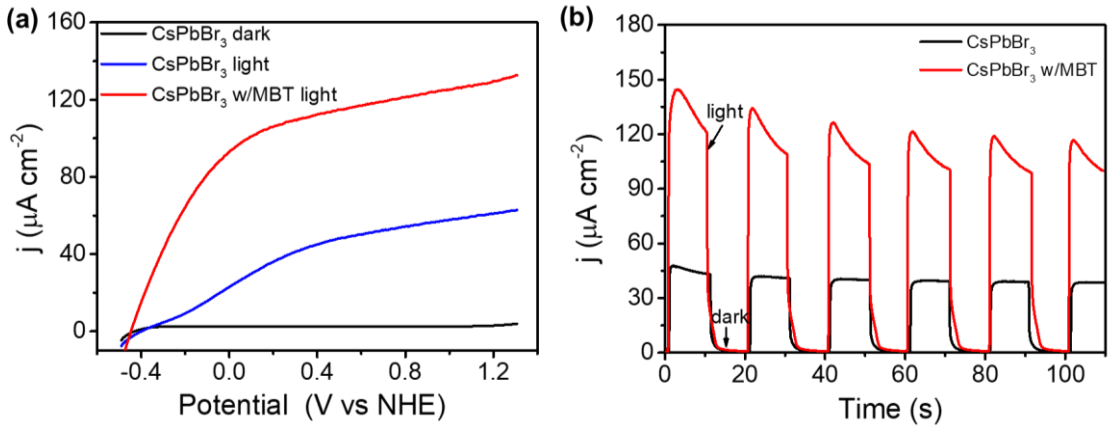

Figure 4. (a) LSV of $CsPbBr_3$/c-TiO_2/FTO film in 100 mM Bu_4NPF_6 in DCM solution, with and without MBT added to the electrolyte. **(b)** Chronoamperometry measurement in $CsPbBr_3$/c-TiO_2/FTO film under chopped 100 mW cm^{-2} illumination with and without MBT added to the electrolyte solution, at constant potential of 1V vs NHE.

The stability of the $CsPbBr_3$/c-TiO_2/FTO films during the PEC measurements was evaluated trough absorbance and photoluminescence measurements (**Supporting Information, Figure S14-15**) after photoelectrochemical testing. Remarkably, the QDs films maintain their mechanical integrity, although the photoluminescence is less intense after the PEC treatment, evidencing the interaction between MBT and the $CsPbBr_3$ surface. In any case, we recognize that the stability of these systems must be significantly improved to target real technological applications. Some promising strategies to stabilize these QDs by conformal coating with metal oxide layers have been reported.[33] Toxicity of lead is also a significant limitation for environmental applications, and although the photoelectrochemical route confines Pb onto the electrode surface alleviating this toxicity problem, the total replacement of this element by other more benign constituent must be urgently addressed in near future.[34-35] Indeed, very promising results have been reported on Pb-free perovskite systems, like Cs_2TiBr_6,[36-37] featuring good stability, although performance still lag behind that of their Pb-containing counterparts. It is expected that the achievements developed for the nanoparticles employed in the present study can be easily extrapolated to other systems in the near future.

In summary, we have showed that the outstanding optoelectronic properties of perovskite QDs can be harnessed for both the photocatalytic (as dispersed nanoparticles) and photoelectrochemical (as thin films) degradation of organic compounds, using MBT as a proof-of-concept. The systematic evaluation of the environmental conditions needed for stable operation of these systems along with the determination of the energy levels by spectroscopic (absorbance, PL, UPS) and electrochemical (CV) methods is key to understand the potential electrochemical reactions accessible for these systems. The obtained results unambiguously confirm that hole injection from perovskite QDs to MBT takes place during the photocatalytic and photoelectrochemical (photocurrent at 1V vs NHE, j_{ph} = 150 $\mu A \cdot cm^{-2}$) oxidation of MBT with $CsPbBr_3$ QDs, confirming the effective degradation of the molecule by ESI-MS. These results constitute a significant step forward in the application of perovskite QDs for solar-driven catalytic processes, opening promising perspectives in the fields of solar synthesis, photocatalysis and photoelectrochemistry. This study could have important implications not only for the family of perovskite QDs reported here but also for the increased number of new perovskite and perovskite related compounds that are appearing in the recent times.

Associated content

Supporting Information

The Supporting Information is available free of charge on the ACS Publications website at DOI: 10.1021/acs.jpclett.8b03849.Experimental details, further optical and microscopic characterization of the as-prepared perovskite QDs, electrochemical tests to demonstrate the diffusion controlled electrochemical process of perovskite QDs, ultraviolet photon spectroscopy (UPS) measurements, PL measurements to validate discussion of the dilution effect, photocatalytic measurements for the degradation of MBT, ESI-MS measurements, electrochemical measurements in perovskite QDs films, Mott−Schottky plot of a perovskite QD film, and characterization of the stability of QD films under photoelectrochemical oxidation of MBT (PDF).

Author information

Corresponding Authors
*E-mail: sero@uji.es (I.M.-S.).
*E-mail: sjulia@uji.es (S.G.).

ORCID
Miguel García-Tecedor: 0000-0002-9664-4665
Iván Mora-Seró: 0000-0003-2508-0994
Sixto Gimenez: 0000-0002-4522-3174

Notes

The authors declare no competing financial interest.

Acknowledgements

We would like to acknowledge financial support from the European Commission via ERC Consolidator Grant (724424 - No-LIMIT), Ministerio de Ciencia, Innovación y Universidades of Spain (ENE2017-85087-C3-1-R), University Jaume I (SOLENPE UJI-B2016-05) and to the Generalitat Valenciana through the Santiago Grisolia Program, grant 2015-031. Serveis Centrals at UJI (SCIC) are also acknowledged for the assistance with TEM and XRD characterization and Molecular Foundry of Lawrence Berkeley National Laboratory USA by UPS measurements and CONACyT-SENER -2015-07 Project 269386.

References

1. Protesescu, L.; Yakunin, S.; Bodnarchuk, M. I.; Krieg, F.; Caputo, R.; Hendon, C. H.; Yang, R. X.; Walsh, A.; Kovalenko, M. V. Nanocrystals of Cesium Lead Halide Perovskites ($CsPbX_3$, X = Cl, Br, and I): Novel Optoelectronic Materials Showing Bright Emission with Wide Color Gamut. *Nano Letters* **2015,** *15* (6), 3692-3696.
2. Jizhong, S.; Jianhai, L.; Xiaoming, L.; Leimeng, X.; Yuhui, D.; Haibo, Z. Quantum Dot Light-Emitting Diodes Based on Inorganic Perovskite Cesium Lead Halides ($CsPbX_3$). *Advanced Materials* **2015,** *27* (44), 7162-7167.
3. Abhishek, S.; Ramya, C.; Kumar, R. V.; Mir, I.; Arindam, C.; Angshuman, N. Colloidal CsPbBr3 Perovskite Nanocrystals: Luminescence beyond Traditional Quantum Dots. *Angewandte Chemie International Edition* **2015,** *54* (51), 15424-15428.
4. Yakunin, S.; Protesescu, L.; Krieg, F.; Bodnarchuk, M. I.; Nedelcu, G.; Humer, M.; De Luca, G.; Fiebig, M.; Heiss, W.; Kovalenko, M. V. Low-threshold amplified spontaneous emission and lasing from colloidal nanocrystals of caesium lead halide perovskites. *Nature Communications* **2015,** *6*, 8056.
5. Buin, A.; Comin, R.; Xu, J.; Ip, A. H.; Sargent, E. H. Halide-Dependent Electronic Structure of Organolead Perovskite Materials. *Chemistry of Materials* **2015,** *27* (12), 4405-4412.
6. Gao, G.; Xi, Q.; Zhou, H.; Zhao, Y.; Wu, C.; Wang, L.; Guo, P.; Xu, J. Novel inorganic perovskite quantum dots for photocatalysis. *Nanoscale* **2017,** *9* (33), 12032-12038.
7. Huang, H.; Yuan, H.; Zhao, J.; Solís-Fernández, G.; Zhou, C.; Seo, J. W.; Hendrix, J.; Debroye, E.; Steele, J. A.; Hofkens, J.; Long, J.; Roeffaers, M. B. J. C(sp3)–H Bond Activation by Perovskite Solar Photocatalyst Cell. *ACS Energy Letters* **2018**, 203-208.
8. Jungang, H.; Shuyan, C.; Yunzhen, W.; Zhanming, G.; Fei, L.; Yiqing, S.; Zheshuai, L.; Licheng, S. Inorganic Colloidal Perovskite Quantum Dots for Robust Solar CO_2 Reduction. *Chemistry – A European Journal* **2017,** *23* (40), 9481-9485.
9. Xu, Y.-F.; Yang, M.-Z.; Chen, B.-X.; Wang, X.-D.; Chen, H.-Y.; Kuang, D.-B.; Su, C.-Y. A CsPbBr3 Perovskite Quantum Dot/Graphene Oxide Composite for Photocatalytic CO_2 Reduction. *Journal of the American Chemical Society* **2017,** *139* (16), 5660-5663.
10. Lei, Z.; Yang-Fan, X.; Bai-Xue, C.; Dai-Bin, K.; Cheng-Yong, S. Synthesis and Photocatalytic Application of Stable Lead-Free Cs2AgBiBr6 Perovskite Nanocrystals. *Small* **2018,** *14* (11), 1703762.
11. Haram, S. K.; Quinn, B. M.; Bard, A. J. Electrochemistry of CdS Nanoparticles: A Correlation between Optical and Electrochemical Band Gaps. *Journal of the American Chemical Society* **2001,** *123* (36), 8860-8861.
12. N., I. S.; P., I. P.; K., H. S. Determination of Band Structure Parameters and the Quasi-Particle Gap of CdSe Quantum Dots by Cyclic Voltammetry. *ChemPhysChem* **2008,** *9* (17), 2574-2579.
13. Kucur, E.; Riegler, J.; Urban, G. A.; Nann, T. Determination of quantum confinement in CdSe nanocrystals by cyclic voltammetry. *Journal of Chemical Physics* **2003,** *119* (4), 2333-2337.
14. Markad, G. B.; Battu, S.; Kapoor, S.; Haram, S. K. Interaction between Quantum Dots of CdTe and Reduced Graphene Oxide: Investigation through Cyclic Voltammetry and Spectroscopy. *The Journal of Physical Chemistry C* **2013,** *117* (40), 20944-20950.
15. Haram, S. K.; Kshirsagar, A.; Gujarathi, Y. D.; Ingole, P. P.; Nene, O. A.; Markad, G. B.; Nanavati, S. P. Quantum Confinement in CdTe Quantum Dots: Investigation

through Cyclic Voltammetry Supported by Density Functional Theory (DFT). *The Journal of Physical Chemistry C* **2011,** *115* (14), 6243-6249.
16. Ravi, V. K.; Markad, G. B.; Nag, A. Band Edge Energies and Excitonic Transition Probabilities of Colloidal $CsPbX_3$ (X = Cl, Br, I) Perovskite Nanocrystals. *ACS Energy Letters* **2016,** *1* (4), 665-671.
17. Samu, G. F.; Scheidt, R. A.; Kamat, P. V.; Janáky, C. Electrochemistry and Spectroelectrochemistry of Lead Halide Perovskite Films: Materials Science Aspects and Boundary Conditions. *Chemistry of Materials* **2018,** *30* (3), 561-569.
18. Grånäs, O.; Vinichenko, D.; Kaxiras, E. Establishing the limits of efficiency of perovskite solar cells from first principles modeling. *Scientific Reports* **2016,** *6*, 36108.
19. Vitoreti, A. B. F.; Agouram, S.; Solis de la Fuente, M.; Muñoz-Sanjosé, V.; Schiavon, M. A.; Mora-Seró, I. Study of the Partial Substitution of Pb by Sn in Cs–Pb–Sn–Br Nanocrystals Owing to Obtaining Stable Nanoparticles with Excellent Optical Properties. *The Journal of Physical Chemistry C* **2018,** *122* (25), 14222-14231.
20. Eperon, G. E.; Paterno, G. M.; Sutton, R. J.; Zampetti, A.; Haghighirad, A. A.; Cacialli, F.; Snaith, H. J. Inorganic caesium lead iodide perovskite solar cells. *Journal of Materials Chemistry A* **2015,** *3* (39), 19688-19695.
21. Min, C.; Yatao, Z.; Linzhong, W.; Qi, P.; Di, Y.; Huicheng, H.; Yeshu, T.; Qixuan, Z.; Yong, X.; Haiyu, L.; Baoquan, S.; Qiao, Z. Solvothermal Synthesis of High-Quality All-Inorganic Cesium Lead Halide Perovskite Nanocrystals: From Nanocube to Ultrathin Nanowire. *Advanced Functional Materials* **2017,** *27* (23), 1701121.
22. Liu, F.; Ding, C.; Zhang, Y.; Ripolles, T. S.; Kamisaka, T.; Toyoda, T.; Hayase, S.; Minemoto, T.; Yoshino, K.; Dai, S.; Yanagida, M.; Noguchi, H.; Shen, Q. Colloidal Synthesis of Air-Stable Alloyed $CsSn_{1-x}Pb_xI_3$ Perovskite Nanocrystals for Use in Solar Cells. *Journal of the American Chemical Society* **2017,** *139* (46), 16708-16719.
23. Serdechnova, M.; Ivanov, V. L.; Domingues, M. R. M.; Evtuguin, D. V.; Ferreira, M. G. S.; Zheludkevich, M. L. Photodegradation of 2-mercaptobenzothiazole and 1,2,3-benzotriazole corrosion inhibitors in aqueous solutions and organic solvents. *Phys. Chem. Chem. Phys.* **2014,** *16* (45), 25152-25160.
24. Akkerman, Q. A.; Gandini, M.; Di Stasio, F.; Rastogi, P.; Palazon, F.; Bertoni, G.; Ball, J. M.; Prato, M.; Petrozza, A.; Manna, L. Strongly emissive perovskite nanocrystal inks for high-voltage solar cells. *Nature Energy* **2016,** *2*, 16194.
25. Shahrokhian, S.; Amini, M. K.; Mohammadpoor-Baltork, I.; Tangestaninejad, S. Potentiometric Detection of 2-Mercaptobenzimidazole and 2-Mercaptobenzothiazole at Cobalt Phthalocyanine Modified Carbon-Paste Electrode. *Electroanalysis* **2000,** *12* (11), 863-867.
26. Clarke, B. O.; Smith, S. R. Review of 'emerging' organic contaminants in biosolids and assessment of international research priorities for the agricultural use of biosolids. *Environment international* **2011,** *37* (1), 226-47.
27. De Wever, H.; Verachtert, H. Biodegradation and toxicity of benzothiazoles. *Water Research* **1997,** *31* (11), 2673-2684.
28. Sorahan, T. Cancer risks in chemical production workers exposed to 2-mercaptobenzothiazole. *Occupational and Environmental Medicine* **2009,** *66* (4), 269-273.
29. Li, F. B.; Li, X. Z.; Hou, M. F.; Cheah, K. W.; Choy, W. C. H. Enhanced photocatalytic activity of Ce^{3+}–TiO_2 for 2-mercaptobenzothiazole degradation in aqueous suspension for odour control. *Applied Catalysis A: General* **2005,** *285* (1), 181-189.

30. Hines, D. A.; Kamat, P. V. Quantum Dot Surface Chemistry: Ligand Effects and Electron Transfer Reactions. *The Journal of Physical Chemistry C* **2013,** *117* (27), 14418-14426.
31. Roberto, G.; Doriana, D.; Paolo, S. G.; Giuseppe, G.; Carlo, G. The Dynamic Organic/Inorganic Interface of Colloidal PbS Quantum Dots. *Angewandte Chemie International Edition* **2016,** *55* (23), 6628-6633.
32. Draguta, S.; Sharia, O.; Yoon, S. J.; Brennan, M. C.; Morozov, Y. V.; Manser, J. M.; Kamat, P. V.; Schneider, W. F.; Kuno, M. Rationalizing the light-induced phase separation of mixed halide organic-inorganic perovskites. *Nature Communications* **2017,** *8*.
33. Loiudice, A.; Saris, S.; Oveisi, E.; Alexander, D. T. L.; Buonsanti, R. $CsPbBr_3$ QD/AlO_x Inorganic Nanocomposites with Exceptional Stability in Water, Light, and Heat. *Angewandte Chemie International Edition* **2017,** *56* (36), 10696-10701.
34. Zhang, Q.; Hao, F.; Li, J.; Zhou, Y.; Wei, Y.; Lin, H. Perovskite solar cells: must lead be replaced – and can it be done? *Science and Technology of Advanced Materials* **2018,** *19* (1), 425-442.
35. Pazoki, M.; Jacobsson, T. J.; Hagfeldt, A.; Boschloo, G.; Edvinsson, T. Effect of metal cation replacement on the electronic structure of metalorganic halide perovskites: Replacement of lead with alkaline-earth metals. *Physical Review B* **2016,** *93* (14), 144105.
36. Volonakis, G.; Filip, M. R.; Haghighirad, A. A.; Sakai, N.; Wenger, B.; Snaith, H. J.; Giustino, F. Lead-Free Halide Double Perovskites via Heterovalent Substitution of Noble Metals. *The Journal of Physical Chemistry Letters* **2016,** *7* (7), 1254-1259.
37. Ju, M.-G.; Chen, M.; Zhou, Y.; Garces, H. F.; Dai, J.; Ma, L.; Padture, N. P.; Zeng, X. C. Earth-Abundant Nontoxic Titanium(IV)-based Vacancy-Ordered Double Perovskite Halides with Tunable 1.0 to 1.8 eV Bandgaps for Photovoltaic Applications. *ACS Energy Letters* **2018,** *3* (2), 297-304.

7.3 Supporting Information

Supporting Information for

Photocatalytic and photoelectrochemical degradation of organic compounds with all-inorganic metal halide perovskite quantum dots.

Drialys Cardenas-Morcoso, [†] Andrés F. Gualdrón-Reyes, [†, ‡, §] Ana Beatriz Ferreira-Vitoreti, [†, δ, ǂ] Miguel García-Tecedor, [†] Seog Joon Yoon, [†] Mauricio Solis de la Fuente, [‖] Iván Mora-Seró, * [†] Sixto Gimenez * [†]

[†] *Institute of Advanced Materials (INAM), Universitat Jaume I, 12071 Castelló, Spain*
[‡] *Centro de Investigaciones en Catálisis (CICAT), Universidad Industrial de Santander, Sede UIS Guatiguará, Piedecuesta, Santander, Colombia. C.P. 681011.*
[§] *Centro de Investigación Científica y Tecnológica en Materiales y Nanociencias (CMN), Universidad Industrial de Santander, Piedecuesta, Santander, Colombia. C.P. 681011.*
[δ] *Department of Natural Science, Federal University of São João del-Rei, 36301-160 São João del-Rei, Brazil*
[ǂ] *CAPES Foundation, Ministry of Education of Brazil, Brasília, 70040-020, Brazil*
[‖] *Lawrence Berkeley National Laboratory, Energy Technologies Area, 1 Cyclotron Road, Berkeley, California 94720, United States of America*

[*]**Email:** sero@uji.es, sjulia@uji.es

Experimental methods

Materials and Reagents: All chemicals used for all synthesis were purchased from Sigma-Aldrich, unless otherwise specified. Cesium carbonate (Cs_2CO_3, 99.9 %), lead iodide (PbI_2, ABCR, 99.999 %), lead bromide ($PbBr_2$, TCI, 99.99 %), tin iodide (SnI_2, 99.99 %), oleic acid (OA; technical grade, 90 %), oleylamine (OLA; primary amine, 98 %), trioctylphosphine (TOP; technical grade, 90 %), 1-octadecene (ODE; technical grade, 90 %) and hexane (CHROMASOLV, 95 %), anhydrous methyl acetate (MeOAC, 99,5 %), anhydrous octane (99 %), lead nitrate ($Pb(NO_3)_2$, 99.99 %), acetone (Panreac, 99.5 %) and ethanol (Panreac, 96 %).

Synthesis of $CsPbX_3$ (X = Br, I) and $CsPbBr_{1.5}I_{1.5}$ QDs: The synthesis of $CsPbX_3$ and $CsPbBr_{1.5}I_{1.5}$ QDs was performed following the procedure described by Kovalenko and coworkers.[1] First, Cs-oleate solution was prepared dissolving 0.61 g of Cs_2CO_3, 1.88 mL of OA and 30 mL of ODE in a 50 mL-three neck flask at 120°C, under vacuum for 1 h, under stirring. Then, the flask was purged with N_2 and heated at 150°C, until the solution became clear. The Cs-oleate solution was cooled and stored under N_2 to carry out the QDs preparation.

To prepare $CsPbX_3$ (X = Br, I) and $CsPbBr_{1.5}I_{1.5}$ QDs, the corresponding halide precursor (0.69 g of $PbBr_2$ or 0.87 g of PbI_2) or the mixture and 50 mL of ODE were loaded into a 100 mL-three neck flask and degassed for 1 h at 120°C, under stirring. Then, the flask was purged with N_2, and OA and subsequently OLA (5 mL of each one) were injected at 120°C. The reaction flask was degassed for 1 min until the total dissolution of halide precursor was completed. The flask was again purged with N_2 and quickly heated to 170°C. Once the reaction temperature was reached, 4 mL of preheated Cs-oleate was rapidly added to the reaction flask and after 5 s, the reaction was quenched by cooling in an ice bath.

Synthesis of $CsPb_{0.4}Sn_{0.6}I_3$ QDs: $CsPb_{0.4}Sn_{0.6}I_3$ QDs were synthetized according with the reported method of Shen and coworkers.[2] Briefly, 0.74 g SnI_2 and 0.35 g PbI_2 were mixed in 2.5 mL TOP, to prepare the SnI_2-PbI_2 precursor solution. The solution was heated at 90°C for 5 h. On the other hand, 0.12 g of Cs_2CO_3, 0.4 mL of OA and 0.4 mL OLA were added to a 12 mL of ODE, in a 50 mL-three neck flask. The reaction mixture was degassed at 100°C for 3 h under stirring, and purged with N_2 at 120°C, to achieve a clear solution. The reaction temperature was increased to 170°C, followed by the fast injection of SnI_2-PbI_2 precursor solution. The reaction quenching was carried out by cooling in ice bath for 5 s. The as-synthetized $CsPbBr_3$, $CsPbI_3$, $CsPbBr_{1.5}I_{1.5}$ and $CsPb_{0.4}Sn_{0.6}I_3$ QDs were centrifuged at 4700 rpm for 5 min to separate the aggregated nanoparticles. After centrifugation, the supernatant was discarded and the QDs pellets were re-dispersed in hexane to prepare long-term stable colloidal solutions.

Purification of $CsPbBr_3$ QD: To isolate the $CsPbBr_3$ QDs, two-step purification was achieved. For the first step, 70 mL of MeOAc were added to 32 mL of colloidal QDs solution and then centrifuged at 4700 rpm for 10 min. After discarding the supernatant, the QDs solid was dispersed in 8 mL of hexane. In the second purification step, 10 mL of MeAOc was loaded to the dispersion of QDs, and then centrifuged at 4700 rpm for 5 min. After discarding the supernatant, the purified QDs were dispersed in 10 mL of hexane and stored at low temperature at least for 48 h, to decant residual products as Cs and Pb oleates. The colloidal QDs solution was dried with a N_2 flow and the final QDs precipitate was concentrated at 50 $mgmL^{-1}$ with hexane.

Preparation of $CsPbBr_3$ QD films: Prior to film preparation FTO substrates

(Pilkington, TEC-15) were rinsed with soap/Milli-Q water, acetone and ethanol, each one for 15 min. After drying the substrates under air flow, the conducting surface was cleaned under UV-O_3 for 15 min. Then, TiO_2 compact layer was deposited on FTO by spin-casting 80 µL of a Ti-alkoxide solution (ShareChem, SC-BT060) at a spin rate of 4000 rpm for 30 s. The as-deposited TiO_2 layer was dried at 150°C for 10 min, and then annealed at 500°C for 30 min. The purified $CsPbBr_3$ QDs solution in octane was deposited by spin-coating on TiO_2 compact layer at 1000 rpm for 20 s. The as-prepared films were dipped into a solution composed by 10 mg mL^{-1} of $Pb(NO_3)_2$ in MeOAc and rinsed with neat MeOAc. The procedure to prepare the $Pb(NO_3)_2$/MeOAc solution is reported elsewhere.[3] The QDs deposition and dipping into $Pb(NO_3)_2$/MeOAc solution was repeated 4 times.

Structural and optical characterization of perovskite QDs: XRD diffraction data was collected on a Rigaku Miniflex 600, (Rigaku corporation, Tokyo, Japan) with copper K_α radiation (λ = 1.5418 Å) at a scan speed of $3°\cdot min^{-1}$. Transmission electron microscopy (TEM) was performed in a JEM-2100 JEOL transmission electron microscope operating at 100 kV. The absorbance of the colloidal QDs solutions was measured on a Varian Cary 300 Bio spectrophotometer. Photoluminescence (PL) measurements were done through home-built optical setup with 405 nm continuous (CW) laser (10 mW/cm^2, Thorlabs) as excitation source and charged coupled device (CCD) camera (Andor Monochromator system, DV420A-OE) as detector in visible region. To remove scattered light from the excitation source, 435 nm long pass filter was applied in front of the CCD detector. Ultraviolet Photoelectron Spectroscopy (UPS) was measured in halide perovskite quantum dots (1mg/ml) deposited on corning glass substrates by spin coating (1000rpm). K-Alpha Plus XPS/UPS equipment was used, He I as source gun, analyzer mode pass energy 2.0 eV and energy step size 0.050 eV.

CV measurements of perovskite QDs dispersions: CV measurements were performed on a three-electrode cell and using an Autolab Potentiostat/Galvanostat. A non-aqueous $Ag/AgNO_3$ electrode (ALS, Japan), a Platinum electrode (CHI Instruments, USA, 2 mm of diameter) and a Platinum wire was used as reference, working and counter electrode, respectively. A 100 mM tetrabutylammonium hexafluorophosphate (Bu_4NPF_6; Signa-Aldrich) solution in dichloromethane (DCM; anhydrous, Sigma-Aldrich) was used as supporting electrolyte.[4] The net concentration of QDs was kept as 4 mg mL^{-1} in all the experiments, in a total volume of 10 ml. Before each measurement, the Pt working electrode was polished with 0.3 µm alumina paste, rinsed with deionized water and finally dried with compressed air. All the glassware and solid reactants were dried at 80 ºC for three hours before use. To calibrate the system to the Normal Hydrogen Electrode (NHE) scale, the Ferrocene/Ferrocenium (Fc/Fc^+) couple was used as internal standard,[5] by adding 1.9 mM of ferrocene after the electrochemical tests (see below in **Figure S1**).

Steady-state/time resolved photoluminescence measurements: Steady-state photoluminescence measurements were carried out to validate the band alignment as determined by CV. In all the experiments, a concentration of 0.04 mg/mL of QDs dispersed in hexane was used. Prior to measurements, we monitored the emission change with time after adding pure solvent in order to characterize the dilution effect when mixing two solutions. When checking type-II alignment, in order to differentiate between fast (emission quenching, in few seconds) and slow (halide exchange) processes, continuous spectra were recorded. Time-resolved photoluminescence (TRPL) was measured through photoluminescence spectrophotometer (Fluorolog 3-11, Horiba). 405 nm pulsed laser (1 MHz frequency, NanoLED-405L, <100 ps of pulse width) was used to excite QDs. All measurements for the TRPL were performed under inert environment with N_2 purged

solution to prevent extra excitation quenching.

Photocatalytic degradation of MBT: The photodegradation of MBT was monitored through the optical absorbance at 320 nm, which is the characteristic band for this compound,[6] using a Cary 300 Bio spectrophotometer. The working solution consisted of a mix of 0.08 mg mL^{-1} QDs and 0.03 mM MBT in hexane. This solution was placed inside a quartz cuvette and irradiated at 100 mW cm^{-2} with an Oriel 300 W Xenon lamp. 1 ml aliquots of this solution were extracted every 10 min to monitor the evolution of the absorbance at 320 nm. Electrospray Mass Spectra (ESI-MS) were obtained with a QTOF Premier instrument with an orthogonal Z-spray-electrospray interface (Waters, Manchester, UK). The drying and cone gas was nitrogen set to flow rates of 300 and 30 L/h, respectively. A capillary voltage of 3.5 kV or 2.5 kV was used in the positive ESI(+) and negative ESI(-) scan mode, respectively. The cone voltage was adjusted in both ESI(+) or ESI(-) scan modes to a low value (typically U_c = 10 V) to control the extent of fragmentation in the source region. Sample solutions dissolved in methanol were introduced through a fused-silica capillary to the ESI source via syringe pump at a flow rate of 10 μL/min.

Photoelectrochemical (PEC) measurements in QDs films: cyclic voltammetry, linear sweep voltammetry and chronoamperometric measurements were performed on a three-electrode cell and using an Autolab Potentiostat/Galvanostat were a non-aqueous $Ag/AgNO_3$ electrode (ALS, Japan) and a Platinum wire was used as reference and counter electrode, respectively. A $CsPbBr_3/TiO_2$/FTO electrode was used as the working electrode. A 0.1 M Bu_4NPF_6; solution in DCM was used as supporting electrolyte. The formal potential of the $Ag/AgNO_3$ electrode was estimated using the Fc/Fc^+ couple as standard. Single Frequency Impedance Spectroscopy measurements (100 Hz) were performed for the determination of the space charge capacitance of the electrodes, by Mott-Schottky analysis through the relation: $C_{SC}^{-2} = \frac{2}{q\varepsilon\varepsilon_0 N_D}\left(V + V_{fb} - \frac{k_B T}{q}\right)$, where q is the elemental charge, ε is the relative dielectric constant of the $CsPbBr_3$ QDs (4.96 [1]), ε_0 the vacuum permittivity, N_D is the donor density, V is the applied potential and $k_B T$ the Boltzmann constant times the temperature.

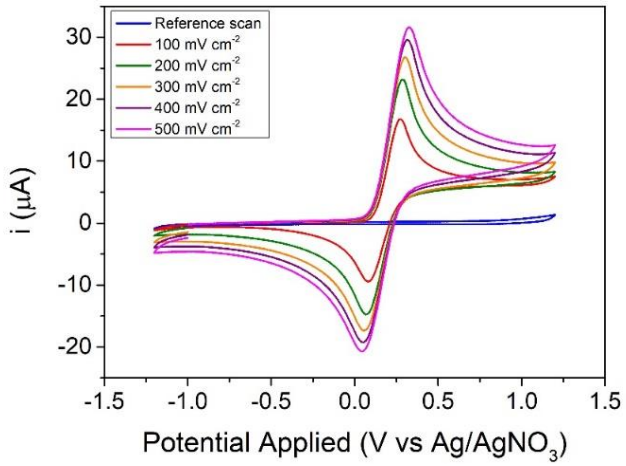

Figure S1. CV measurement at different scan rate of the $Fc^{+/0}$ couple with which the system was calibrated. The molar concentration of ferrocene was 1.9 mM. Reference scan was performed in 0.1 M Bu_4NPF_6 in dichloromethane electrolyte.

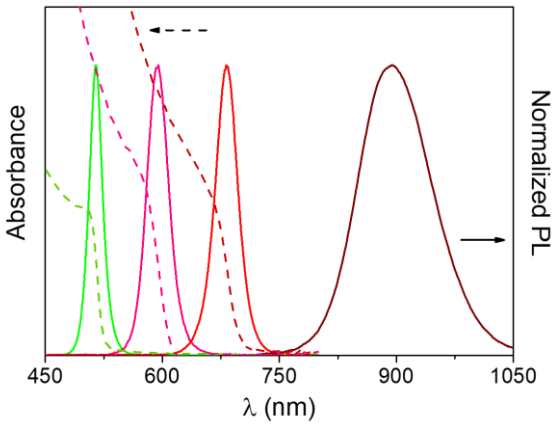

Figure S2. Absorbance (dashed lines) and PL spectra (straight lines) of $CsPbBr_3$ (green), $CsPb(Br_{0.5}I_{0.5})_3$ (pink), $CsPbI_3$ (red) and $CsPb_{0.4}Sn_{0.6}I_3$ (dark red) QDs.

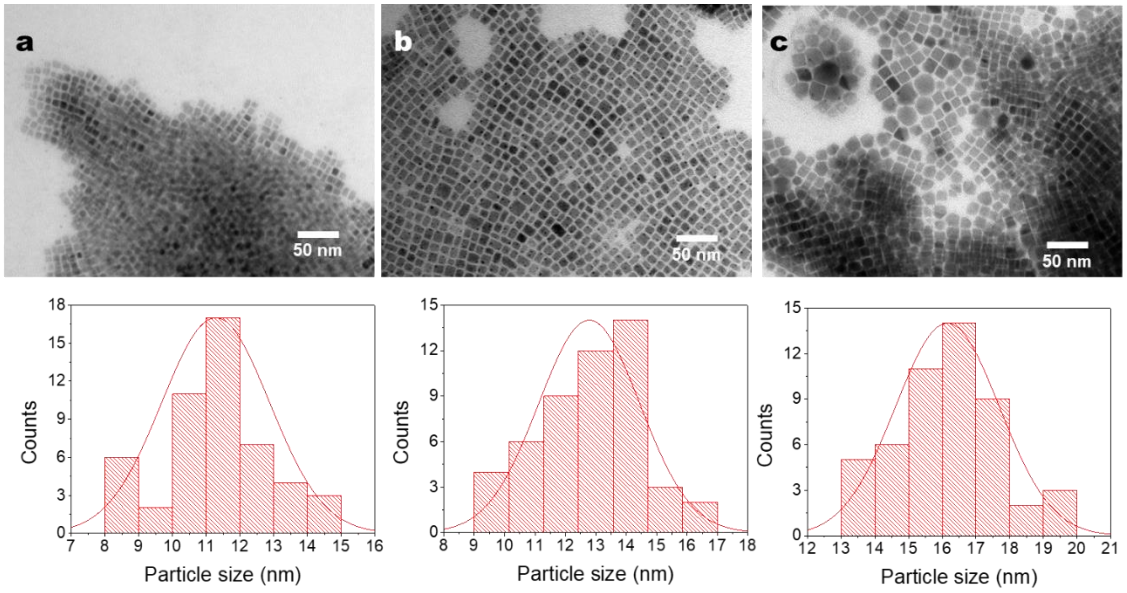

Figure S3. TEM micrographies and histograms with the particles size distribution of the $CsPbBr_3$, $CsPb(Br_{0.5}I_{0.5})_3$ and $CsPbI_3$.

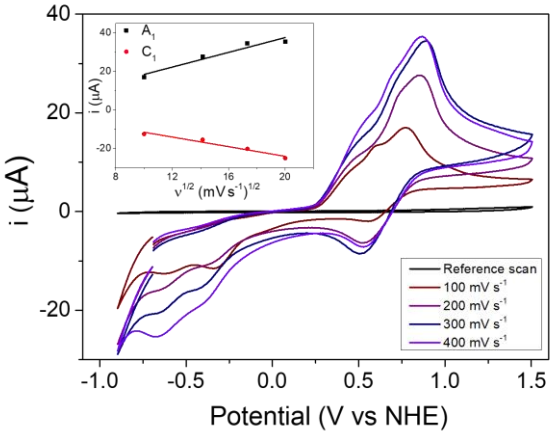

Figure S4. CV in a $CsPb_{0.4}Sn_{0.6}I_3$ QDs dispersion at different scan rates. As inset, linear fitting of A_1 and C_1 peak currents vs $v^{1/2}$, confirming the diffusion-controlled process.

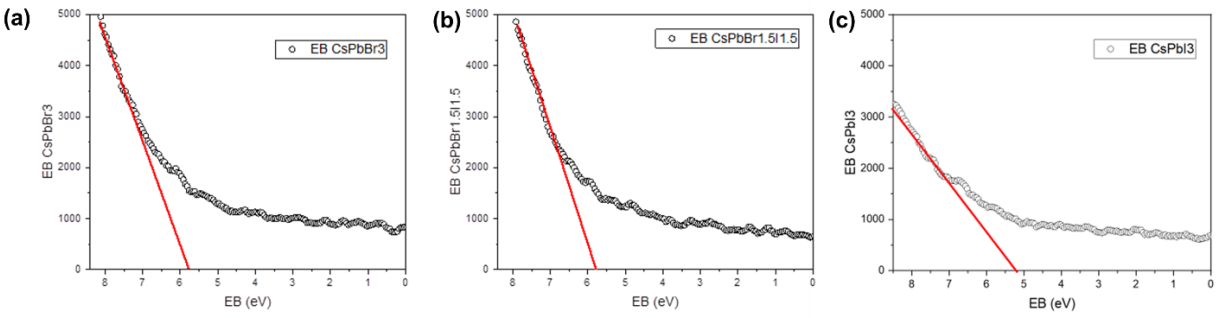

Figure S5. UPS for VB position determination.

Discussion about PL measurements to validate band positions

As shown in **Figure S6a**, type I alignment allows charge transfer of both carriers from the material with wider band gap (donor) to that with narrower band gap (acceptor), which should be reflected on increased PL emission of the acceptor and decreased emission of the donor. Conversely, type II alignment allows asymmetrical charge transfer between both systems and should result in the quenching of the PL emission of both components.[7-8] **Figures S6b-f** illustrate the change in emission properties of the different studied QDs, upon addition of a second chromophore. In **Figure S6b**, the emission from $CsPbI_3$ QDs was drastically decreased about 83% of initial emission intensity. However, PL from $CsPb_{0.4}Sn_{0.6}I_3$ remains unaltered after $CsPbI_3$ addition (**Figure S6b, inset**), indicating type I alignment if dilution effect is considered (discussed below). In contrast, as shown in **Figure S6c-d** and **Figure S6e-f**, emissions from both constituents were quenched when another QDs solution was added indicating type II alignment. It must be highlighted that in all cases, the PL measurements for the determination of the type-II alignment were carried out in a short term (few seconds) after addition of second QDs solution to clearly differentiate from long term process (few minutes), halide exchange between two different halide perovskite QDs (**Figure S7**).[9] As described earlier, the quenching of the emissions from both components reflects type-II alignment between $CsPb_{0.4}Sn_{0.6}I_3$/$CsPbBr_3$, and between $CsPbBr_3$/$CsPbI_3$.

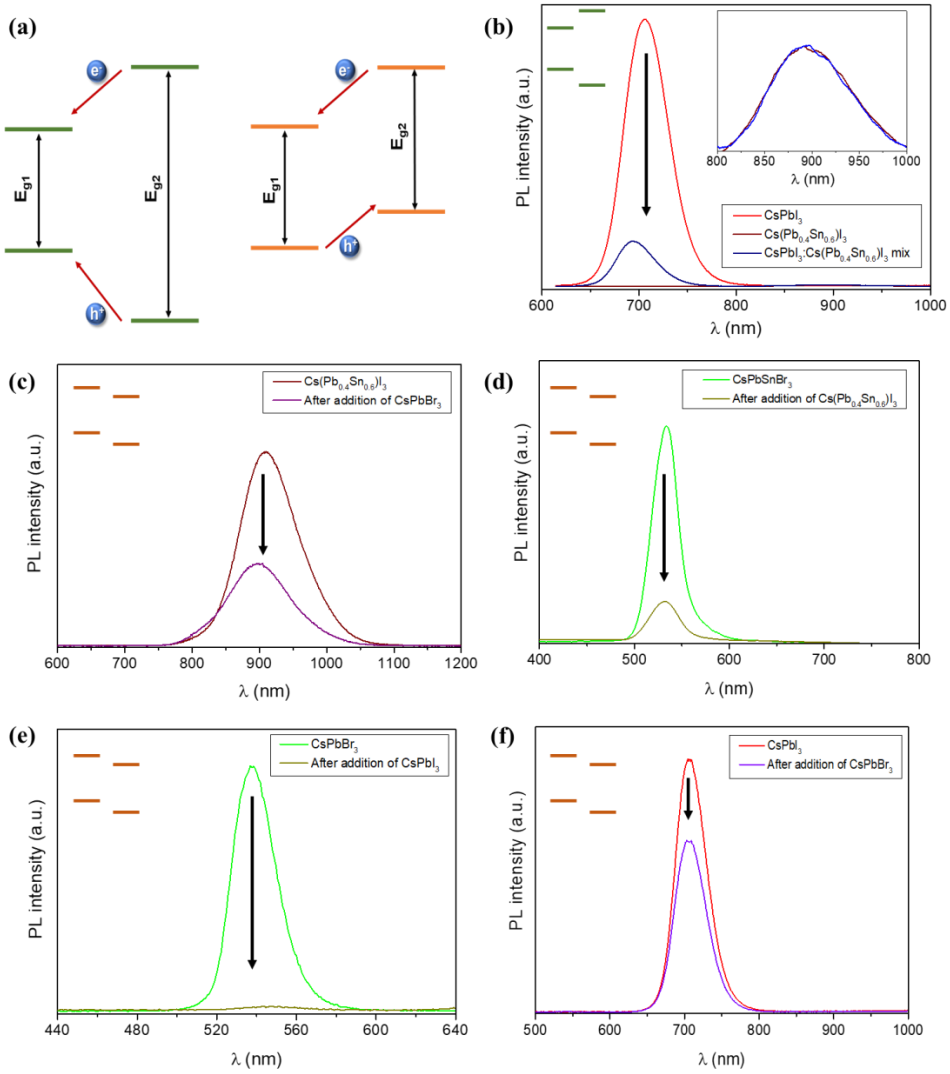

Figure S6. (a) Scheme indicating type I (left) and type II (right) interactions between two different chromophores. PL measurements showing the interaction between the studied perovskite QDs: **(b)** 'Type-I' interaction between $CsPbI_3/Cs(Pb_{0.4}Sn_{0.6})I_3$; **(c)-(d)** 'Type-II' interaction between $CsPbBr_3/Cs(Pb_{0.4}Sn_{0.6})I_3$. **(e)-(f)** 'Type-II' interaction between $CsPbBr_3/Cs(Pb_{0.4}Sn_{0.6})I_3$ and $CsPbBr_3/CsPbI_3$. In **(b)-(f)**, the relative band alignment for the corresponding system is schematically indicated.

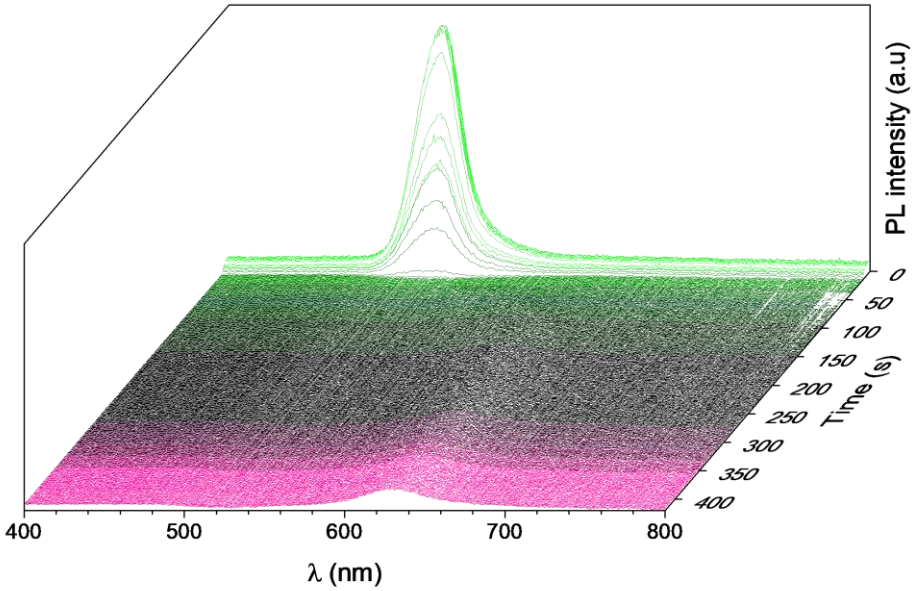

Figure S7. Kinetic PL measurement showing emission quenching and halide mixing ($CsPbBr_3$/$CsPbI_3$) in their respective time scales.

Dilution effect

To consider dilution effect, in an initial 0.8 mg mL^{-1} concentration of the $CsPbBr_3$ QDs dispersion, hexane was added to a final concentration of 0.4 mg mL^{-1}. By simply considering the dilution effect, the emission intensity should decrease less than 10% as shown in **Figure S8**.

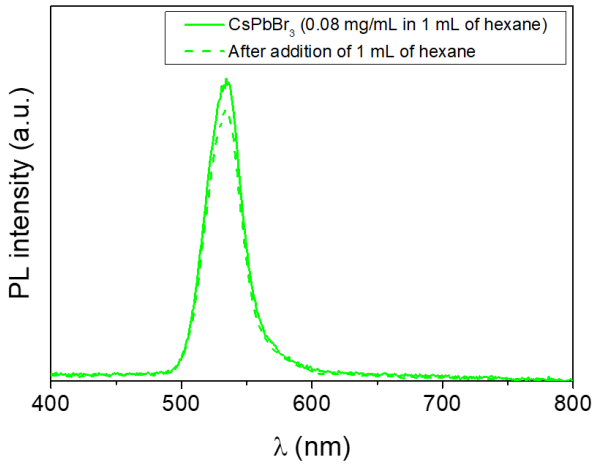

Figure S8. Effect of dissolution on PL emission when adding hexane.

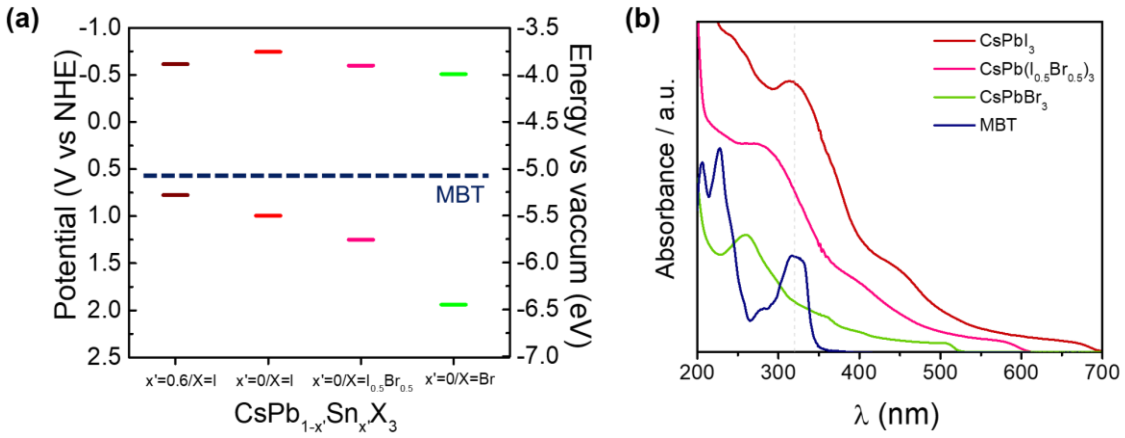

Figure S9. (a) Energy diagram obtained through CV of the QDs and the averaged redox potential reported for MBT. **(b)** Absorbance spectra of the QDs and the MBT, showing the optimal behavior of $CsPbBr_3$ for testing the photocatalytic activity through optical measurements.

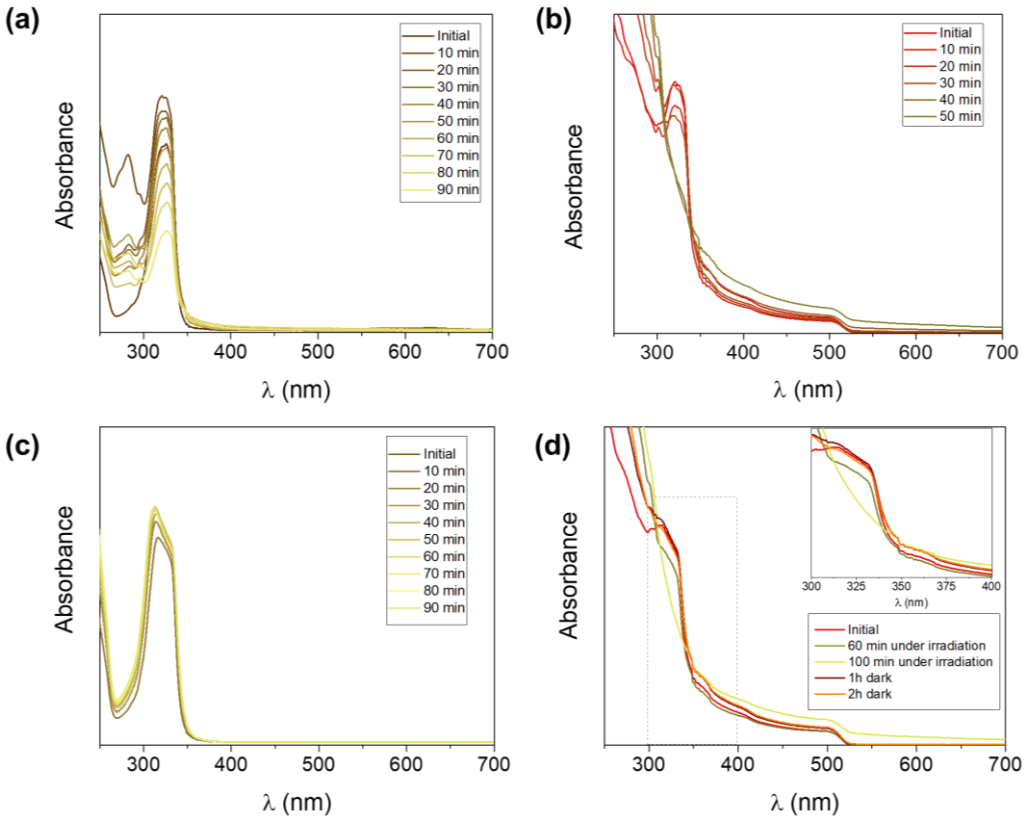

Figure S10. Absorbance spectra of MBT photodegradation under 100 mW cm^{-2} irradiation **(a)** MBT in hexane, **(b)** MBT and $CsPbBr_3$ QDs in hexane, **(c)** MBT in hexane and UV filter, **(d)** Control measurements with MBT and $CsPbBr_3$ QDs in hexane kept in dark condition.

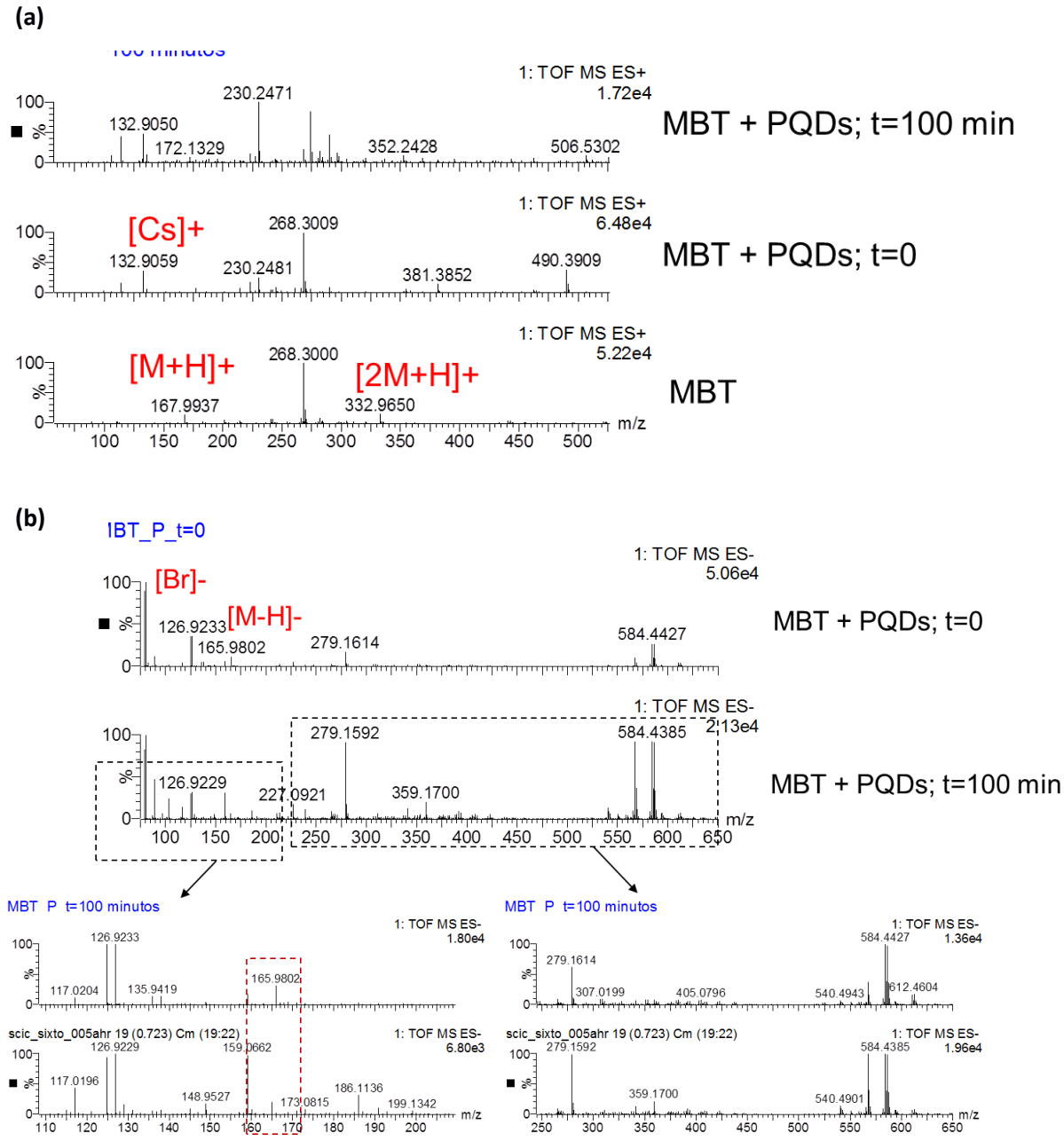

Figure S11. ESI-MS performed in a control sample of MBT in hexane, and then with the $CsPbBr_3$ QDs incorporated before (t=0) and after (t=100 min) 100 mW cm^{-2} irradiation using a UV filter. **(a)** $ESI^{(+)}$, **(b)** $ESI^{(-)}$

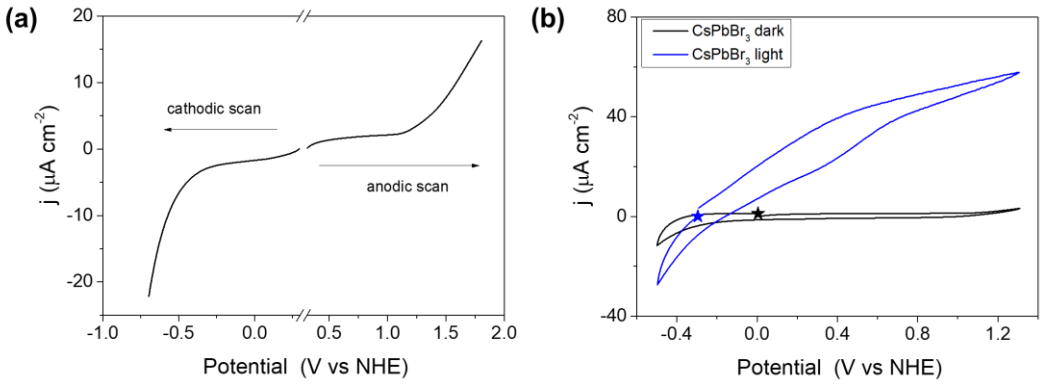

Figure S12. (a) Linear sweep voltammetry performed separately in anodic and cathodic directions in $CsPbBr_3$/c-TiO_2/FTO film in dark, to determine the optimal voltage window for PEC characterization preventing degradation of the $CsPbBr_3$ QDs. (**b)** Cyclic voltammetry in $CsPbBr_3$/c-TiO_2/FTO film in dark and under 1 sun illumination. The stars symbols mark the starting value of each scan, which is the OCP value.

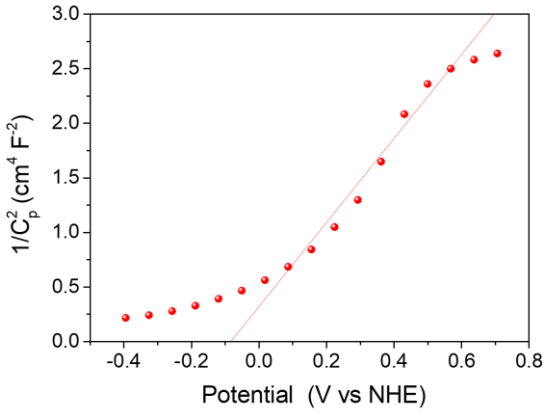

Figure S13. Mott-Schottky plot on $CsPbBr_3$/c-TiO_2/FTO film. (Performed at single frecuency; 500 Hz)

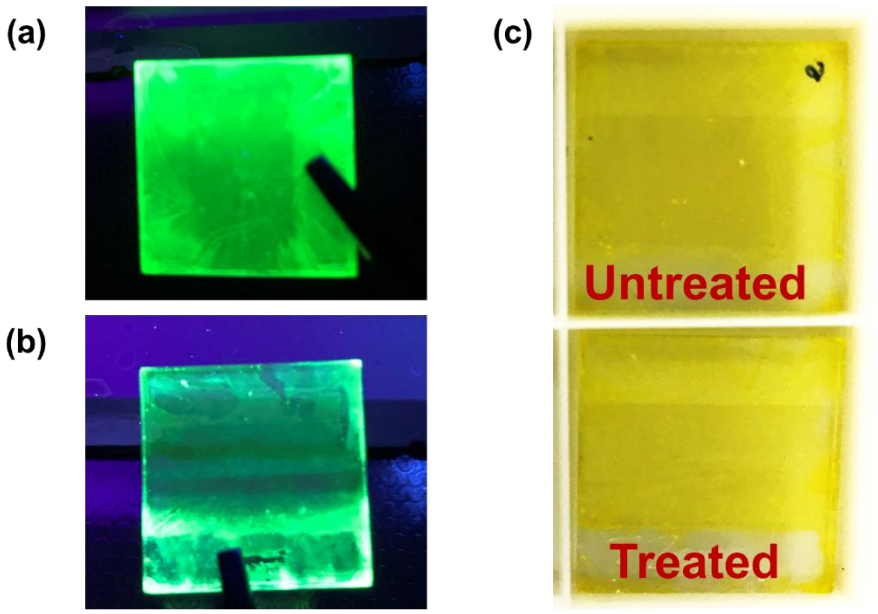

Figure S14. (a) Digital picture of the $CsPbBr_3$/c-TiO_2/FTO film under UV light before and (b) after several PEC measurements (linear and cyclic voltammetry and chronoamperometry in dark and under illumination conditions). (c) Comparison between and untreated sample and a treated one.

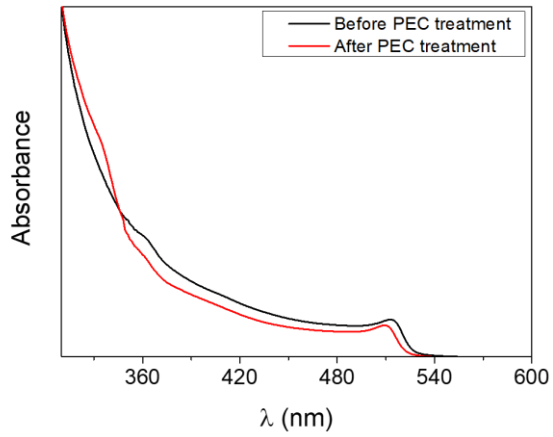

Figure S15. Absorbance spectra of the $CsPbBr_3$/c-TiO_2/FTO film before and after PEC measurements.

Table S1. Summary of the survey of the different salt support/solvent combinations tested to ascertain the stability of the QDs solutions during the photocatalytic/photoelectrochemical tests. Unstable combinations (☹) and stable combination (☺) are indicated.

Solvent / Support salt	Toluene/DCM	Hexane/DCM
TBA-TFB	☹	☹
TBA-P	☹	☹
TBA-DHP	☹	☹
TBA-HFP	☹	☺

TBA-TFB= Tetrabutylammonium tetrafluoroborate

TBA-P= Tetrabutylammonium perchlorate

TBA-DHP= Tetrabutylammonium dihydrogenphosphate

TBA-HFP= Tetrabutylammonium hexafluorophosphate

Table S2. Band structure parameters obtained from CV measurements of the investigated QDs.

QDs	Optical E_g (eV)	VB (V vs NHE)	CB (V vs NHE)	Electrochemical E_g (eV)	VB from UPS (V vs NHE)
$CsPbI_3$	1.7	0.995	-0.745	1.74	0.68
$CsPb_{1-x}Sn_xI_3$	1.4	0.775	-0.615	1.39	-
$CsPb(I_{0.5}Br_{0.5})_3$	1.77	1.25	-0.6	1.84	1.28
$CsPbBr_3$	2.4	2.145	-0.315	2.46	1.3

Table S3. Correlation between the band alignment estimated from electrochemical measurements (cyclic voltammetry) and optical measurements (photoluminescence).

Interacting materials	**Alignment from CV**	**Alignment from PL**
$CsPbI_3$ and $Cs(Pb_{0.4}Sn_{0.6})I_3$	I	I
$CsPbI_3$ and $CsPb(I_{0.5}Br_{0.5})_3$	II	N/A
$CsPbI_3$ and $CsPbBr_3$	II	II
$Cs(Pb_{0.4}Sn_{0.6})I_3$ and $CsPb(I_{0.5}Br_{0.5})_3$	I	N/A
$Cs(Pb_{0.4}Sn_{0.6})I_3$ and $CsPbBr_3$	II	II
$CsPb(I_{0.5}Br_{0.5})_3$ and $CsPbBr_3$	II	N/A

Table S4. Results of triexponential fitting ($y = A_1e^{-x/\tau_1} + A_2e^{-x/\tau_2} + A_3e^{-x/\tau_3}$) of the time-resolved PL from $CsPbBr_3$ PQD with MBT solution with subject to illumination time. A_i, τ_i, $<\tau>$, χ^2 represent amplitude, lifetime, average lifetime ($<\tau> = \frac{\Sigma A_i\tau_i^2}{\Sigma A_i\tau_i}$), chi square value, respectively.

Irradiation time	**A_1**	**τ_1 (ns)**	**A_2**	**τ_2 (ns)**	**A_3**	**τ_3 (ns)**	**$<\tau>$ (ns)**	**χ^2**
0 min	0.125	2.03	0.427	8.00	0.448	31.2	26.3	1.15
5 min	0.110	1.34	0.467	5.90	0.423	23.2	19.2	1.01
15 min	0.163	1.27	0.543	5.93	0.294	21.2	15.6	1.09
45 min	0.569	0.861	0.341	4.13	0.0901	19.4	11.0	1.55
90 min	0.661	0.785	0.312	3.37	0.0268	30.6	12.1	1.15

References

1. Protesescu, L.; Yakunin, S.; Bodnarchuk, M. I.; Krieg, F.; Caputo, R.; Hendon, C. H.; Yang, R. X.; Walsh, A.; Kovalenko, M. V. Nanocrystals of Cesium Lead Halide Perovskites ($CsPbX_3$, X = Cl, Br, and I): Novel Optoelectronic Materials Showing Bright Emission with Wide Color Gamut. *Nano Letters* **2015,** *15* (6), 3692-3696.
2. Liu, F.; Ding, C.; Zhang, Y.; Ripolles, T. S.; Kamisaka, T.; Toyoda, T.; Hayase, S.; Minemoto, T.; Yoshino, K.; Dai, S.; Yanagida, M.; Noguchi, H.; Shen, Q. Colloidal Synthesis of Air-Stable Alloyed $CsSn_{1-x}Pb_xI_3$ Perovskite Nanocrystals for Use in Solar Cells. *Journal of the American Chemical Society* **2017,** *139* (46), 16708-16719.
3. Sanehira, E. M.; Marshall, A. R.; Christians, J. A.; Harvey, S. P.; Ciesielski, P. N.; Wheeler, L. M.; Schulz, P.; Lin, L. Y.; Beard, M. C.; Luther, J. M. Enhanced mobility $CsPbI_3$ quantum dot arrays for record-efficiency, high-voltage photovoltaic cells. *Science Advances* **2017,** *3* (10).
4. Samu, G. F.; Scheidt, R. A.; Kamat, P. V.; Janáky, C. Electrochemistry and Spectroelectrochemistry of Lead Halide Perovskite Films: Materials Science Aspects and Boundary Conditions. *Chemistry of Materials* **2018,** *30* (3), 561-569.
5. Bard, A. J.; Faulkner, L. R. *Electrochemical Methods: Fundamentals and Applications*. Wiley: 2000.
6. Serdechnova, M.; Ivanov, V. L.; Domingues, M. R. M.; Evtuguin, D. V.; Ferreira, M. G. S.; Zheludkevich, M. L. Photodegradation of 2-mercaptobenzothiazole and 1,2,3-benzotriazole corrosion inhibitors in aqueous solutions and organic solvents. *Phys. Chem. Chem. Phys.* **2014,** *16* (45), 25152-25160.
7. Mashford, B. S.; Stevenson, M.; Popovic, Z.; Hamilton, C.; Zhou, Z.; Breen, C.; Steckel, J.; Bulovic, V.; Bawendi, M.; Coe-Sullivan, S.; Kazlas, P. T. High-efficiency quantum-dot light-emitting devices with enhanced charge injection. *Nature Photonics* **2013,** *7*, 407.
8. Giménez, S.; Rogach, A. L.; Lutich, A. A.; Gross, D.; Poeschl, A.; Susha, A. S.; Mora-Seró, I.; Lana-Villarreal, T.; Bisquert, J. Energy transfer versus charge separation in hybrid systems of semiconductor quantum dots and Ru-dyes as potential co-sensitizers of TiO_2-based solar cells. *Journal of Applied Physics* **2011,** *110* (1), 014314.
9. Ravi, V. K.; Scheidt, R. A.; Nag, A.; Kuno, M.; Kamat, P. V. To Exchange or Not to Exchange. Suppressing Anion Exchange in Cesium Lead Halide Perovskites with $PbSO_4$–Oleate Capping. *ACS Energy Letters* **2018,** *3* (4), 1049-1055.

Chapter 8: Conclusiones Generales y Perspectivas

La implementación de tecnologías basadas en la conversión y almacenamiento de la energía solar mediante sistemas foto-electrocatalíticos, exige grandes esfuerzos para el desarrollo de materiales efectivos y de bajo coste. En la presente tesis doctoral, se ha abordado la investigación de materiales semiconductores con potencial aplicación en la producción de combustibles solares. Para ello, se plantearon como estrategias la mejora funcional de los fotoelectrodos, la comprensión de mecanismos operacionales y la evaluación de nuevos materiales para aplicaciones fotocatalíticas y fotoelectroquímicas. Como resultado, se realizaron importantes contribuciones que incluyen: *(i)* la integración de materiales abundantes y de bajo coste para conseguir fotoánodos con desempeño y eficiencias significativamente mejoradas, *(ii)* la revelación de un nuevo método para elucidar mecanismos de operación en fotoelectrodos y *(iii)* la aportación de una metodología sistemática para la evaluación y utilización de materiales semiconductores con interés en aplicaciones foto-electrocatalíticas.

Del trabajo de investigación desarrollado resultaron las siguientes conclusiones y logros:

- ✓ Se mejoró significativamente el desempeño fotoelectroquímico del $BiVO_4$, (~ 4 veces de incremento de la fotocorriente) mediante el acoplamiento del CoO_x como co-catalizador altamente poroso. El CoO_x se obtuvo de la conversión de un precursor marco-metal-orgánico (ZIF-67). Además, se investigó la naturaleza de dicha mejora, sugiriendo los resultados obtenidos el papel catalítico del CoO_x para la oxidación del agua en la superficie del fotoánodo. Esta nueva propuesta para la aplicación de un co-catalizador derivado de un marco-metal-orgánico en la mejora del $BiVO_4$ sirve como un precedente para el diseño de dispositivos en celdas fotoelectroquímicas, mediante rutas de modificación simples con materiales basados en elementos abundantes.

- ✓ Se reveló un nuevo método para la determinación de mecanismos de operación específicos en sistemas fotoelectroquímicos. Se demostró experimentalmente que el valor negativo en el IMPS está asociado a la derivada de la fotocorriente con la intensidad de la luz, y no con el signo de la fotocorriente. Las medidas de fotocorriente estacionaria en función de la intensidad de luz incidente revelaron información significativa sobre los procesos de recombinación y atrapamiento en el $BiVO_4$. Con lo cual, se ha establecido un nuevo método para futuras investigaciones sobre mecanismos de operación de las celdas fotoelectroquímicas.

- ✓ Se consiguió, mediante un dispositivo integrado electrocatalítico-fotovoltaico basado en materiales abundantes, la separación eficiente del agua asistida con luz, alcanzando un 7.7.% de eficiencia de conversión solar-a-hidrógeno. Se desarrolló un electrocatalizador conformado por las fases NiO, α-Fe_2O_3 y $NiFe_2O_4$, catalíticamente activas para la reacción de oxidación de agua. La adecuada actividad catalítica del componente electrocatalizador, sumada a la idoneidad de las celdas solares basadas en películas delgadas de silicio para impulsar la reacción de oxidación del agua, permitió para el fotoánodo integrado

mostrar un rendimiento fotoelectroquímico eficiente y estable, competitivo con dispositivos y materiales similares. Estos resultados representan un avance significativo hacia el desarrollo de dispositivos para llevar a cabo la fotosíntesis artificial, al sustituir los costosos materiales actualmente empleados.

- ✓ Se estableció una metodología sistemática para la evaluación y la demostración práctica del alto potencial de los puntos cuánticos de perovskitas inorgánica en aplicaciones de fotocatalíticas y fotoelectroquímicas. En primer lugar, se establecieron las condiciones de operación estable para las posteriores medidas. Posteriormente, se determinó la alineación de bandas de puntos cuánticos con diferentes composiciones ($CsPb_{1-x'}Sn_{x'}X_3$; X = Br, I o $Br_{0.5}I_{0.5}$) a través de técnicas electroquímicas y espectroscópicas, lo que permitió evaluar su potencial para conducir una determinada reacción química. Dicho potencial se confirmó utilizando la degradación fotocatalítica y fotoelectroquímica de un contaminante orgánico como prueba de concepto. La aplicación futura de esta metodología abre perspectivas prometedoras en el estudio de nuevos materiales con potencial aplicación en sistemas foto-electrocatalíticos.

Los resultados obtenidos también revelan aspectos importantes que podrían ser abarcados en futuras líneas de investigación.

En primer lugar, se demostró que un material derivado de un marco-metal-orgánico puede ser aprovechado como co-catalizador de la reacción de oxidación de agua en una celda fotoelectroquímica. Sin embargo, se quiere una investigación más profunda, a través de técnicas espectroscópicas como TAS, PIAS o SEC, que proporcione detalles mecanísticos adicionales sobre la dinámica de las cargas en la interfase CoO_x-$BiVO_4$/solución. Además, y como se mostró en esta tesis, las medidas de IMPS y $j_{e-}j_{\phi}$ podrían proporcionar información relevante sobre los mecanismos de operación de los fotoelectrodos. No obstante, se requiere la validación detallada de los mecanismos revelados a través de este método. Esta investigación está actualmente en progreso.

En segundo lugar, los dispositivos integrados PV–EC a partir de celdas solares de películas delgadas de silicio y electrocatalizadores basados en elementos abundantes, han demostrado ser aplicados con éxito como fotoánodos para la oxidación del agua. No obstante, se puede abordar reacciones más complejas a partir de este enfoque, dada la capacidad de ajuste del voltaje suministrado por el componente fotovoltaico, sumado a la versatilidad de su diseño para impulsar reacciones tanto de oxidación o reducción. Además, mediante el uso de la electrocatalizadores adecuados y estrategias de recubrimiento apropiadas, se puede fabricar un dispositivo monolítico que actúa como una "hoja artificial" para la producción de combustible o síntesis de productos de valor añadido.

Finalmente, se demostró el aprovechamiento de las excelentes propiedades optoelectrónicas de los puntos cuánticos de perovskitas totalmente inorgánicas en aplicaciones fotocatalíticas y fotoelectroquímicas. Sin embargo, la inestabilidad de estos materiales en medio acuoso sigue siendo un gran inconveniente para la aplicación práctica en sistemas de fotoelectrólisis del agua o reducción de CO_2. En consecuencia, se debe implementar estrategias adicionales, como el uso de capas protectoras o encapsulación, para el despliegue futuro de aplicaciones foto-electrocatalíticas con estos materiales.

En resumen, los resultados logrados dentro de esta tesis doctoral van acompañados de contribuciones significativas en el desarrollo futuro de materiales semiconductores para

sistemas de conversión y almacenamiento de la energía solar. Hay además varios aspectos que deben abordarse para la implementación a gran escala de la producción de combustibles asistida por la energía solar, que puedan competir con las fuentes de energía líderes actuales.

General Conclusions and Outlooks

The widespread application of technologies based on solar conversion and storage with photo-electrocatalytic approaches still demands great efforts to target effective and low-cost semiconductor materials. In the present doctoral thesis, the research of advanced semiconductor materials with potential applications for solar fuel production, was addressed. Consequently, the functional improvement of photoelectrode devices, the comprehension of operational mechanisms, and the assessment of novel materials for PC and PEC applications, was carried out to accomplish the main goal. As a result, important contributions have been produced covering: *(i)* the integration of Earth-abundant and low-cost materials to achieve significantly enhanced PEC performance and efficiency in photoanodes for water splitting, *(ii)* the introduction of novel methods providing relevant information on the operational mechanism of photoelectrodes, and *(iii)* to provide a systematic methodology that allows the evaluation and exploitation of attractive semiconductor materials for photo-electrocatalytic applications.

From the developed research, the following conclusions and achievements were obtained:

- ✓ The PEC performance of the $BiVO_4$, was significantly improved (a ~four-times increased photocurrent) with the highly porous CoO_x as co-catalyst. The CoO_x was obtained from the conversion of a cobalt-based metal-organic framework (ZIF-67). Moreover, mechanistic insights about the nature of the enhanced PEC activity in the $CoO_x/BiVO_4$ photoanode suggested the "true" catalytic role towards water oxidation of CoO_x at the photoanode surface. This new application of a MOF converted co-catalyst improving the photoelectrochemical performance of $BiVO_4$ serves as a remarkable milestone for the future design of photoelectrodes devices for PEC devices through simple modification routes with Earth-abundant materials.

- ✓ A novel platform of valuable information about operational mechanisms in semiconductor materials for PEC applications was provided. It was experimentally demonstrated that the negative value of the IMPS transfer function is associated with the derivative of the photocurrent with the light intensity, rather than with the sign of the photocurrent. Therefore, the steady-state $j_e - j_\phi$ measurements revealed significant information about recombination and trapping processes in $BiVO_4$, establishing a new method for further mechanistic investigations in PEC cells.

- ✓ Robust and stable solar water splitting, up to a 7.7.% STH efficiency, was achieved with an integrated PV–EC photoanode, based on non-critical raw materials. An electrocatalyst consisting of water oxidation-actives NiO, α-Fe_2O_3 and $NiFe_2O_4$ phases was developed. The higher activity of the EC, added to the suitability of the thin-film silicon solar cells used to power the water oxidation reaction, allowed for the integrated device to show efficient and stable PEC operation. Such performance is competitive with the current PV–EC approaches based on similar materials. These results represent a significant step forward for

the practical realization of an "artificial leaf", by substituting the current expensive raw materials.

- ✓ A systematic methodology was established for the assessment and practical demonstration of the high potential of all-inorganic perovskites QDs in PC and PEC applications. First, the environmental conditions for the stable operation were established. Then, the band alignment of perovskites QDs with different compositions ($CsPb_{1-x}Sn_xX_3$; X=Br, I or $Br_{0.5}I_{0.5}$) was determined through electrochemical and spectroscopic techniques, which allows predicting their suitability to drive a certain chemical reaction. Such potential was further confirmed using the photocatalytic and photochemical degradation of organic contaminants as a proof of concept. Future application of this methodology opens promising perspectives in the study of new materials with potential for photo-electrocatalytic applications.

The obtained results also revealed important aspects that could be addressed in future research lines.

In first place, it was demonstrated that a porous MOF-converted compound can be harnessed as a highly efficient water oxidation co-catalyst in a PEC cell. However, a deeper investigation with spectroscopic techniques such as TAS, PIAS and SEC, could reveal further mechanistic insights about the charge dynamic at the CoO_x-$BiVO_4$/solution interface. In addition, as shown in this thesis, IMPS and $j_{e-}j_{\phi}$ measurements could provide relevant operational information of the photoelectrode. However, a detailed validation of the mechanisms revealed through these methods is required, which is currently in progress.

Secondly, PV–EC integrated devices from Earth-abundant EC and thin-film silicon solar cells, has proven to be successfully applied as photoanode for water splitting. Moreover, more challenging reactions can be addressed with this approach, given the tunability of the delivered voltage by the PV component, added to the versatility of its design to drive either oxidation or reduction reactions. Furthermore, by using suitable EC and appropriate isolation strategies, a monolithic device acting as an "artificial leaf" for fuel production or synthesis or added-value products, can be fabricated.

Finally, harnessing of the outstanding optoelectronic properties of the all-inorganic perovskites QDs in PC and PEC applications was demonstrated. However, the instability of these materials in aqueous media remains a major drawback for practical application in water splitting or CO_2 reduction systems. Consequently, further strategies such as the use of protective layer or encapsulation, need to be implemented for future deployment of photo-electrocatalytic applications with these materials.

In summary, the results achieved within this doctoral thesis represent significant contributions for the future development of semiconductor materials for solar energy conversion and storage systems. Nonetheless, several aspects need to be addressed for the practical implementation of solar-assisted solar fuel production, that can compete with the current leading energy sources.